Sofia University "St. Kliment Ohridski"
Faculty of Physics

Critical phenomena and quantum metrology with strongly correlated quantum-optical systems

ABSTRACT

for awarding THE SCIENTIFIC DEGREE DOCTOR OF SCIENCE (DSc) in PHYSICS

Code 4.1

Peter Aleksandrov Ivanov

May 25, 2022

ABSTRACT

The study of quantum systems that exhibit a quantum phase transition is of great interest to modern physics. Such models are usually non-integrable and analytical description is possible only within the thermodynamic limit. The quantum phase transition is related to the closing of the energy gap between the ground state energy and the first excited energy at the transition point. Typically, a quantum phase transition is described by an ordering parameter that varies nonanalytically at the transition point. The observation of a quantum phase transition requires low temperatures and control of the parameters characterizing the system. Such conditions are found in quantum optical systems, where low temperature is achieved by applying laser cooling, and control over the parameters is carried out by applying laser fields.

The idea of the quantum simulator can be applied here, namely the mathematical similarity between a model and the simulated in a controlled quantum optical system. One such system that can be used for quantum simulations is laser-cooled ions in Paul's trap. The internal states of the ion form an efficient spin system, and the external degrees of freedom are described by collective modes. Laser fields can create a connection between the spins and oscillations of the ionic crystal, which allows the simulation and study of various spin and spin-boson models that can show a quantum phase transition. Also, reading the information encoded in the spin and vibration states can be done with great precision using Ramsey spectroscopy.

Chapters 2, 3, 4, 5, 6, and 7 in this dissertation are devoted to the study of critical phenomena in quantum optical systems. It is proposed to simulate and study the phase diagram of the Jaynes-Cummings-Hubbard ion crystal model, which describes the quantum phase transition of polaritones between the Mott insulator phase and the superfluid phase. Chapter 4 proposes models in which a magnetic structural transition and spin-phonon condensate formation can be observed. They are based on the symmetric Jan-Teller connection between local transverse phonons and the spin states of Paul's trap ions. Chapter 5 is devoted to spin magnetism in a linear ionic crystal. Chapter 6 examines the creation of an artificial magnetic field for photons in a non planar resonator. The energy spectrum of the photons in the resonator is described by Landau levels. The interaction of photons and Rydberg atoms leads to the formation of polariton excitation, which can be considered as a quasiparticle. The strong Rydberg dipole-dipole interaction creates an interaction between the polaritons and thus between the photons in the resonator. It has been shown that the presence of a magnetic field and a strong repulsion interaction between photons can create a

photonic analogue of the Laughlin states in the fractional quantum Hall effect.

As noted, the presence of a quantum phase transition leads to a sharp change in the ground state of the system around the transition point. From the point of view of information geometry, this means that the distance between two close quantum states separated by a critical point can be large. Information geometry studies the geometry of quantum states that depend on a given parameter or set of parameters. Infinitesimally, the small change in the parameters leads to distinctness between the quantum states, which allows us to define a differentially small distance between them. In the most general case, the metric tensor in the information space describes Riemannian geometry. At the phase transition point, the metric tensor diverges, which can be used as a critical signal in quantum systems. The difference of quantum states and the metric tensor are closely related to quantum metrology, which studies the accuracy in determining an unknown parameter using a quantum system. Indeed, the more a quantum state is sensitive to a change in a parameter, the more accurately it can be determined. Therefore, the metric tensor and the measurement accuracy are closely related. Quantum Fisher information is used as a measure of sensitivity in quantum metrology. The statistical uncertainty in measuring a parameter is inversely proportional to the Fisher information. Therefore, the more Fisher information we have, the more accurately we have determined the unknown parameter. Quantum Fisher information can be shown to be proportional to the metric tensor. This close relationship shows that ultra-precise quantum metrology can be achieved in systems showing a quantum phase transition.

Chapter 9 proposes quantum metrology in Dicke's model, which describes a quantum phase transition of the second order between normal and superradiant phases. It is shown that the system is sensitive to parameters violating the symmetry of the model. Such parameters may be, for example, the frequency difference between the laser frequency and the atomic transition frequency or low electrical forces. The presence of a quantum phase transition leads to an increase in the signal, so that the unknown parameter can be determined with Heisenberg precision. Dicke's model can be realized with ions in Paul's trap, where the collective degrees of freedom are formed by the internal ionic states, and the bosonic degree of freedom by the vibrational mode. Chapter 10 proposes a quantum sensor of weak forces with one ion or a system of ions trapped by Paul. It is shown that forces of order 10^{-24}N can be measured by observing the time oscillations of the spin states of the ion. Chapter 11 proposes quantum metrology with systems showing dissipative phase transition. Such phase transitions can be observed in open edge systems. The balance between coherent and dissipative dynamics leads to the formation of an nonequilibrium state with a density matrix that can exhibit non-analytical behavior at the transition point. Remarkably, around the transition point the dissipative system is sensitive to perturbations violating its symmetry. This allows us to determine the two parameters characterizing the displacement operator with great accuracy.

Chapter 12 is devoted to the optimal measurement of low temperatures in a linear ionic crystal. After Doppler laser cooling, the vibrational state of the ions in Paul's trap is thermal with a temperature of the order of 100 μK.

The application of a laser field connects the oscillations of the crystal with the collective spin states of the ions, so that information about the temperature can be transferred to the atomic populations. The temperature is determined optimally by projective spin measurements.

Chapter 13 links the existence of a quantum phase transition to quantum chaos. Although quantum mechanics is a linear theory, quantum systems can exhibit quantum chaos. The presence of quantum chaos can be defined by the statistical distributions of the energy difference at the levels or by the exponential increase of the non-simultaneous correlation function. Rabi's quantum model describes the interaction between a photon and spin and can exhibit a quantum phase transition within the effective thermodynamic limit. It has been shown that in the super-radiant phase the system exhibits quantum chaos and can reach a state of equilibrium in which the spin time oscillations decrease.

CONTENTS

1. INTRODUCTION TO PHYSICS OF TRAPPED IONS

1.1 Classical Equation of Motion

The Gauss law states the impossibility of generating an electrostatic potential minimum in free space. Charged particles can be trapped either in a combination of electric and magnetic static fields- a Penning trap or in a radio-frequency electric field, a Paul trap, where a radio-frequency (rf) voltage U_{rf} with rf drive frequency ω_{rf} is applied to some of the ion-trap electrodes, see Fig. 1.1. Generate potential becomes [1]

$$\Phi(x,y,z,t) = \frac{U_{\mathrm{dc}}}{2}(\alpha_{\mathrm{dc}}x^2 + \beta_{\mathrm{dc}}y^2 + \gamma_{\mathrm{dc}}z^2) + \frac{U_{\mathrm{rf}}}{2}\cos(\omega_{\mathrm{rf}}t)(\alpha_{\mathrm{rf}}x^2 + \beta_{\mathrm{rf}}y^2 + \gamma_{\mathrm{rf}}z^2), \tag{1.1}$$

where U_{dc} is a constant trapping voltages applied to the electrodes. The Laplace equation in free space $\Delta\Phi(x,y,z,t) = 0$ puts an additional constraint on the coefficients: $\alpha_{\mathrm{dc}} + \beta_{\mathrm{dc}} + \gamma_{\mathrm{dc}} = 0$ and $\alpha_{\mathrm{rf}} + \beta_{\mathrm{rf}} + \gamma_{\mathrm{rf}} = 0$. One possibility to fulfill these conditions is to set $\alpha_{\mathrm{dc}} = \beta_{\mathrm{dc}} = \gamma_{\mathrm{dc}} = 0$ and $\alpha_{\mathrm{rf}} + \beta_{\mathrm{rf}} = -\gamma_{\mathrm{rf}}$. This produces a purely dynamic confinement of the ion and is realized by an electrode configuration as shown in Fig. 1.1(a), where the torus-shaped electrode is supplied with radio frequency and the spherical electrodes are grounded. An alternative solution would be the choice $-\alpha_{\mathrm{dc}} = \beta_{\mathrm{dc}} + \gamma_{\mathrm{dc}}$ and $\alpha_{\mathrm{rf}} = 0$, $\beta_{\mathrm{rf}} = -\gamma_{\mathrm{rf}}$ leading to a linear Paul trap with dc confinement along the x axis and dynamic confinement in the y-z plane. Figure 1.1(b) shows a possible setup with cylindrically shaped electrodes and segmented dc electrodes along the axial direction which we consider in the following. In this trapping geometry, the ions can crystallize into linear ion strings aligned along the x axis. The classical equation of motion for an ion with mass m and charge q is $m\frac{d^2\vec{r}}{dt^2} = -q\nabla\Phi(\vec{r},t)$ which is transformed into a set of two uncoupled Mathieu differential equations [1, 2]

$$\frac{d^2u(\tau)}{d\tau^2} + (a_u - 2q_u\cos(2\tau))u(\tau), \quad u = x, y, \tag{1.2}$$

where $2\tau = \omega_{\mathrm{rf}}t$. For linear Paul trap, the coefficients a_u and q_u are given by

$$q_y = \frac{2|q|U_{\mathrm{rf}}\beta_{\mathrm{rf}}}{m\omega_{\mathrm{rf}}^2}, \quad a_y = -\frac{4|q|U_{\mathrm{dc}}\beta_{\mathrm{dc}}}{m\omega_{\mathrm{rf}}^2}, q_z = -\frac{2|q|U_{\mathrm{rf}}\gamma_{\mathrm{rf}}}{m\omega_{\mathrm{rf}}^2}, \quad a_z = \frac{4|q|U_{\mathrm{dc}}\gamma_{\mathrm{dc}}}{m\omega_{\mathrm{rf}}^2}. \tag{1.3}$$

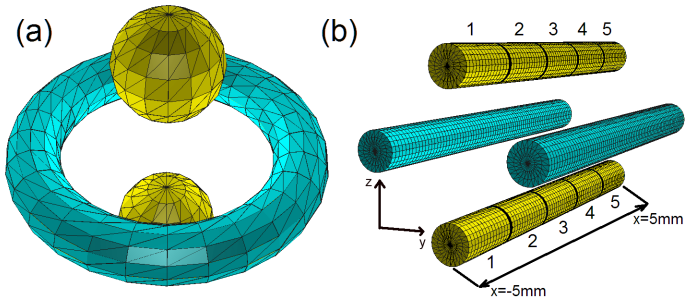

Fig. 1.1: Electrode geometries of ion traps: The rf electrodes (dark shading) and dc electrodes (bright shading), are depicted. (a) Typical electrode configuration for a 3d ring trap with dynamic rf confinement in all three dimensions. (b) Electrode arrangement for a linear Paul trap. The dc electrodes are divided into segments numbered from 1 to 5.

The general solution of the Mathieu differential equation can be expressed as

$$u(\tau) = Ae^{i\omega_u t}\sum_{n=-\infty}^{+\infty} C_{2n}e^{in\omega_{\rm rf}t} + Be^{-i\omega_u t}\sum_{n=-\infty}^{+\infty} C_{2n}e^{-in\omega_{\rm rf}t}, \qquad (1.4)$$

where $\omega_u = \beta_u\omega_{\rm rf}/2$ and the coefficients C_{2n} depend only on a_u and q_u. Using this we obtain the following equation [2]

$$-\sum_{n=-\infty}^{+\infty} C_{2n}e^{2ni\tau}(2n+\beta_u) + \{a_u - 2q_u\cos(2\tau)\}\sum_{n=-\infty}^{+\infty} C_{2n}e^{2ni\tau} = 0. \qquad (1.5)$$

Equalizing the terms in front of $e^{2ni\tau}$ for any n we obtain the following set of equations:

$$C_{2n+2} - D_{2n}C_{2n} + C_{2n+2} = 0, \quad D_{2n} = \frac{a_u - (2n+\beta_u)^2}{q_u}. \qquad (1.6)$$

Therefore, we have

$$C_{2n} = \frac{C_{2n+2}}{D_{2n} - \frac{1}{D_{2n-2} - \frac{1}{D_{2n-4} - \frac{1}{\cdots}}}}, \qquad (1.7)$$

or equivalent

$$C_{2n} = \frac{C_{2n-2}}{D_{2n} - \frac{1}{D_{2n+2} - \frac{1}{D_{2n+4} - \frac{1}{\cdots}}}}, \qquad (1.8)$$

For $n = 0$ we obtain

$$C_2 + \frac{a_u - \beta_u^2}{q_u}C_0 + C_{-2} = 0 \qquad (1.9)$$

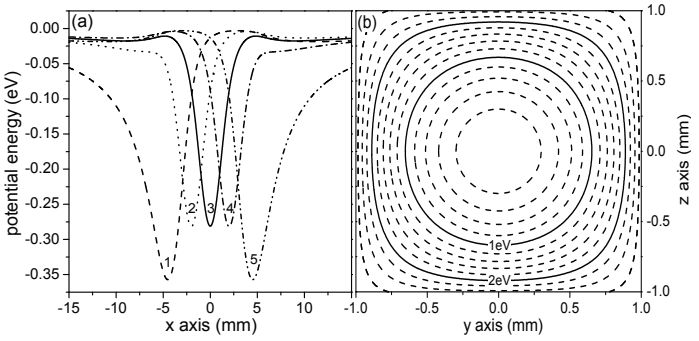

Fig. 1.2: a) Trapping potentials along the trap x-axis generated by each individual electrodes from the linear Paul trap geometry. Each curve corresponds to the respective electrode biased to -1 V and all others to 0V. b) Equipotential lines of the pseudo-potential in the radial plane.

and hence

$$\beta_u^2 = a_u - q_u \left(\frac{1}{D_2 - \frac{1}{D_4 - \frac{1}{D_6 - \frac{1}{\cdots}}}} + \frac{1}{D_{-2} - \frac{1}{D_{-4} - \frac{1}{D_{-6} - \frac{1}{\cdots}}}} \right). \tag{1.10}$$

The stable solutions are obtained for $0 < \beta_u < 1$, thereby in the low limit approximation we find

$$\beta_u^2 \approx a_u - q_u \left(\frac{1}{D_2} + \frac{1}{D_{-2}} \right) \approx a_u + \frac{q_u^2}{2}, \tag{1.11}$$

so that $\beta_u = \sqrt{a_u + \frac{q_u^2}{2}}$, which is valid as long as $q_u, a_u \ll 1$. For particle trajectory we obtain

$$u(t) = A\{e^{i\beta_u \frac{\omega_{\rm rf} t}{2}}(C_0 + C_2 e^{i\omega_{\rm rf} t} + C_{-2} e^{-i\omega_{\rm rf} t}) + e^{-i\beta_u \frac{\omega_{\rm rf} t}{2}}(C_0 + C_2 e^{-i\omega_{\rm rf} t} + C_{-2} e^{i\omega_{\rm rf} t})\}. \tag{1.12}$$

Using the relations $C_0 = C_{-2} D_{-2} = C_2 D_2$ as well as $D_2 \approx -\frac{4}{q_u} = D_{-2}$ in the low limit approximation the trajectory of the charge particle in linear Paul trap becomes [1, 2]

$$u(t) = 2AC_0 \cos\left(\beta_u \frac{\omega_r f t}{2}\right) \left(1 - \frac{q_u}{2} \cos(\omega_{\rm rf} t)\right). \tag{1.13}$$

The ion undergoes harmonic oscillations at the secular frequency $\omega_u = \beta_u \omega_{\rm rf}/2$ modulated by small oscillations near the rf-drive frequency (called micromotion). The static axial confinement along the x axis is harmonic with the oscillator frequency given by $\omega_x = \sqrt{|q| U_{\rm dc} \alpha_{\rm dc}/m}$. The axial confinement is generated by biasing the dc electrode segments appropriately, see Fig. (1.2)a.

The radial confinement is dominated by the rf potential which can be approximated by an *effective* harmonic potential $\Phi_{\text{eff}}(y,z) = |q||\nabla\Phi(y,z)|^2/4m\omega_{\text{rf}}^2$ where $\Phi(y,z)$ is the potential generated by setting the radio frequency electrodes to a constant viltage U_{ef}, see Fig. (1.2)b.

1.2 Ion String. Equilibrium positions

Let us now consider system of N ions in linear Paul trap with frequencies $\omega_{x,y,z}$. The potential energy of the system consists of harmonic potential and mutual Coloumb repulsion. We have

$$V = \frac{m}{2}\sum_{\alpha=x,y,z}\sum_{j=1}^{N}\omega_\alpha^2 r_{\alpha,j}^2 + \frac{q^2}{8\pi\epsilon_0}\sum_{j\neq k}\left(\sum_\alpha (r_{\alpha,j}-r_{\alpha,k})^2\right)^{-\frac{1}{2}}, \tag{1.14}$$

where $\vec{r}_j = (r_{x,j}, r_{y,j}, r_{z,j})$ is the radius vector of the jth ion. The equilibrium ion position is determined by the condition of balance between the harmonic confinement and Coloumb repulsion which is given by

$$\left(\frac{\partial V}{\partial r_{\alpha,j}}\right)_0 = 0, \quad j = 1,2,\ldots,N, \tag{1.15}$$

where the index 0 indicates that the partial derivative is evaluated at the equilibroim position $r_{\alpha,j}^0$. Equation (1.15) is a condition for the minimum of the potential energy, which determine the equilibrium positions of the ions. Using the expression for the potential energy we find

$$\frac{\partial V}{\partial r_{\alpha,j}} = m\omega_\alpha^2\left(r_{\alpha,j} - \frac{l^3\omega_z^2}{\omega_\alpha^2}\sum_{p\neq j}^{N}\frac{(r_{jp})_\alpha}{|r_{jp}|^3}\right). \tag{1.16}$$

Here we have defined $(r_{j,p})_\alpha = r_{\alpha,j} - r_{\alpha,p}$ and respectively $|r_{jp}| = \left(\sum_\alpha (r_{\alpha,j}-r_{\alpha,p})^2\right)^{\frac{1}{2}}$. The parameter $l = \left(\frac{e^2}{4\pi\varepsilon_0 m\omega_z^2}\right)^{\frac{1}{3}}$ has a units of meter and characterize the average ion distance. For standard parameters the average distance is approximatly of order of 10 μm, while the size of the ions wave function in the ground motional state is of order of 10 nm. Therefore, in a good approximation one can neglect the overlapping of the wave functions of two neighbor ions so that the quantum statistics (Bose/Fermi) does not play role in linear Paul trap. The condition (1.15) gives rise to a set of N algebraic equations for the equilibrium positions which in general is numerically solved. Depending on the ratio between the axial and radial trap frequencies the ion system can crystalize in linear, 2D, 3D configurations. In the case of strong radial frequencies, $\omega_z \ll \omega_{x,y}$ the ions are arranged in linear configuration. so that $\vec{r}_{\alpha,j}^0 = (0,0,lu_j)$, where u_j are dimensionless equilibrium positions. Hence, we have $(r_{jp}^0)_\alpha = l\delta_{\alpha,z}(u_j - u_p)$ and [3]

$$u_j - \sum_{n=1}^{j-1}\frac{1}{(u_j-u_n)^2} + \sum_{n=j+1}^{N}\frac{1}{(u_j-u_n)^2} = 0, \quad j = 1,2,\ldots,N. \tag{1.17}$$

At low temperature the ions can perform small oscillations around their equilibrium positions $r_{\alpha,j} = r^0_{\alpha,j} + \delta r_{\alpha,j}$, where $\delta r_{\alpha,j}$ is a small fluctuation. The Hamiltonian of the system is

$$\begin{aligned}\hat{H} &= \sum_{\alpha}\sum_{j}^{N}\frac{\hat{p}^2_{\alpha,j}}{2m} + \frac{m}{2}\sum_{\alpha}\sum_{j}^{N}(r^0_{\alpha,j} + \delta\hat{r}_{\alpha,j})^2 \\ &\quad + \frac{e^2}{2}\sum_{j\neq k}^{N}\left(\sum_{\alpha}(r^0_{\alpha,j} + \delta\hat{r}_{\alpha,j} - r^0_{\alpha,k} - \delta\hat{r}_{\alpha,k})^2\right)^{-\frac{1}{2}}. \qquad (1.18)\end{aligned}$$

This is the most general Hamiltonian describing the ion system, which contains infinite series of displacement terms. As can be expected the effect of high order terms can be neglected at low temperature limit which we will discuss in the following.

1.2.1 Harmonic Approximation

Let us now consider that the quantum displacement of each ion around it equilibrium position is small. This allows to expand the potential energy in Taylor series. We have

$$\hat{V} = V_0 + \frac{1}{2}\sum_{\alpha,\beta}\sum_{i,j}^{N}\left(\frac{\partial^2 V}{\partial r_{\alpha,i}\partial r_{\beta,j}}\right)_0 \delta\hat{r}_{\alpha,i}\delta\hat{r}_{\beta,j} + O(\delta r^3_{\alpha,i}), \qquad (1.19)$$

where V_0 is a constant term. Evaluating the second derivative we obtain the following Hamiltonian

$$\begin{aligned}\hat{H} &= \sum_{\alpha}\sum_{j=1}^{N}\left(\frac{\hat{p}^2_{\alpha,j}}{2m} + \frac{1}{2}m\omega^2_{\alpha}\delta\hat{r}^2_{\alpha,j}\right) + \frac{e^2}{8\pi\epsilon_0}\sum_{\alpha,\beta}\sum_{j=1}^{N}\left(\sum_{p\neq j}^{N}\frac{Q^{\alpha,\beta}_{jp}}{|r^0_{jp}|^5}\right)\delta\hat{r}_{\alpha,j}\delta\hat{r}_{\beta,j} \\ &\quad - \frac{e^2}{8\pi\epsilon_0}\sum_{\alpha,\beta}\sum_{i\neq j}^{N}\frac{Q^{\alpha,\beta}_{i,j}}{|r^0_{i,j}|^5}\delta\hat{r}_{\alpha,i}\delta\hat{r}_{\beta,j}, \qquad (1.20)\end{aligned}$$

where $Q^{\alpha,\beta}_{i,j} = 3(r^0_{i,j})_\alpha(r^0_{i,j})_\beta - \delta_{\alpha,\beta}|r^0_{i,j}|^2$.

The first term in (1.20) desribes the free oscillations of the ions alon the three spatial directions. The effect of the Coulomb interaction is derscibes by the last two terms in (1.20). In a harmonic approximation the oscillation of the ions can be viewed as a system of N coupled harmonic ossillators. Therefore, the system of N ions can oscillate in $3N$ different collective modes. The collective frequencies depend on the shape of the ion crystal, that is from the condition for the equilibrium positions.

1D ion chain

In the limit of strong radial frequencies the ions ara arranged in 1D configuration along the trap axis z. In that case the collective modes along the three

spatial directions are decoupled. This leads to significant simplification of the Hamiltonian (1.20), which can be written as follows:

$$\hat{H} = \hat{H}_x + \hat{H}_y + \hat{H}_z. \tag{1.21}$$

Each term describes the collective oscillation in the respective direction.

Collective modes along the trap axis z

The Hamiltonian can be written as

$$\hat{H}_z = \sum_{j=1}^{N} \frac{\hat{p}_{z,j}^2}{2m} + \frac{m\omega_z^2}{2} \sum_{i,j=1}^{N} B_{i,j}^z \delta\hat{r}_{z,i} \delta\hat{r}_{z,j}. \tag{1.22}$$

Here $B_{i,j}^z$ is a $(N \times N)$ matrix with elements

$$B_{i,j}^z = \begin{cases} 1 + 2\sum_{p\neq j}^{N} \frac{1}{|u_p - u_j|^3}, & (i = j), \\ -\frac{2}{|u_i - u_j|^3}, & (i \neq j), \end{cases} \tag{1.23}$$

The Hamiltonian (1.22) describes system of N coupled harmonic oscillators with spring couling $-2/|u_i - u_j|^3$. The collective modes can be found by diagonalization of matrix $B_{i,j}^z$, that is by solving

$$\sum_{i=1}^{N} B_{i,j}^z b_i^{(p)} = \gamma_{z,p} b_j^{(p)}. \tag{1.24}$$

The eigenvectors are orthonormal, $\sum_{j=1}^{N} b_j^{(n)} b_j^{(m)} = \delta_{n,m}$, and satisfy the condition $\sum_{p=1}^{N} b_i^{(p)} b_j^{(p)} = \delta_{i,j}$. The collective modes are defined by $\hat{Q}_p(t) = \sum_{j=1}^{N} b_j^{(p)} \delta\hat{r}_{z,j}(t)$ and the corresponding moments are $\hat{P}_p(t) = m\frac{d\hat{Q}_p(t)}{dt}$. Hence, the Hamiltonian becoms

$$\hat{H}_z = \sum_{p=1}^{N} \frac{\hat{P}_p^2}{2m} + \frac{m}{2} \sum_{p=1}^{N} \omega_p^2 \hat{Q}_p^2, \tag{1.25}$$

where $\omega_p = \omega_z\sqrt{\gamma_p}$ are the collective frequencies. In Fig. 2.1 we show the collective oscillations for ion chain with $N = 2$ and $N = 3$ ions. The lowest collective mode is the center-of-mass mode in which ions oscillate with equal amplitudes and frequency $\omega_{c.m.} = \omega_z$ which is independent on the number of ions. The next frequency collective mode is the breathing mode with frequency $\omega_b = \sqrt{3}\omega_z$ which is also independent on N. All other modes depend on N.

The canonical quantinization of $\hat{Q}_p$ and $\hat{P}_p$ imposes the commutation relation $[\hat{Q}_p, \hat{P}_k] = \mathrm{i}\hbar\delta_{pk}$. It is convinient to introduce the creation $\hat{a}_p^\dagger$ and anihilation $\hat{a}_p$ collective phonon operators. Using the standard relation

$$\hat{Q}_k = \sqrt{\frac{\hbar}{2m\omega_k}}(\hat{a}_k^\dagger + \hat{a}_k), \hat{P}_k = \mathrm{i}\sqrt{\frac{\hbar m\omega_k}{2}}(\hat{a}_k^\dagger - \hat{a}_k), \tag{1.26}$$

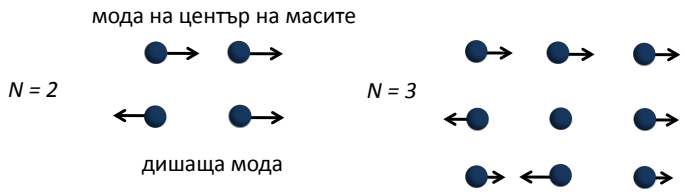

Fig. 1.3: Collective oscillations of ion chain with $N = 2$ and $N = 3$ ions.

we obtain

$$\hat{H}_z = \hbar \sum_{k=1}^{N} \omega_k \left(\hat{a}_k^\dagger \hat{a}_k + \frac{1}{2} \right). \tag{1.27}$$

The Hamiltonian $\hat{H}_z$ describes the collective vibrational modes of an ion chain along the z direction.

1.2.2 Transverse oscillations

Using the equilibrium position, the Hamiltonian which describes the transverse vibrations is give by

$$\begin{aligned} \hat{H}_\perp &= \hat{H}_x + \hat{H}_y, \\ \hat{H}_{\alpha'} &= \sum_{i=1}^{N} \frac{\hat{p}_{\alpha',i}}{2m} + \frac{m\omega_{\alpha'}^2}{2} \sum_{i,j=1}^{N} B_{i,j}^{\alpha'} \delta\hat{r}_{\alpha',i} \delta\hat{r}_{\alpha',j}, \end{aligned} \tag{1.28}$$

where $\alpha' = x, y$. The matrix $B_{i,j}^{\alpha'}$ has the following structure [4]:

$$B_{i,j}^{\alpha'} = \begin{cases} 1 - \frac{\omega_z}{\omega_{\alpha'}} \sum_{p \neq j}^{N} \frac{1}{|u_p - u_j|^3}, & (i = j), \\ \frac{\omega_z}{\omega_{\alpha'}} \frac{1}{|u_i - u_j|^3}, & (i \neq j), \end{cases} \tag{1.29}$$

Let represents the small displacements $\delta\hat{r}_{\alpha',j}$ and respectively the canonical momentums $\hat{p}_{\alpha',j}$ using the creation and anihhilation operators of vibrational quanta along the transverse direction, namely

$$\delta\hat{r}_{\alpha',j} = \sum_{p=1}^{N} \sqrt{\frac{\hbar}{2m\omega_{p,\alpha'}}} b_j^{(p)\alpha'} (\hat{a}_p^\dagger + \hat{a}_p), \quad \hat{p}_{\alpha',j} = i \sum_{p=1}^{N} \sqrt{\frac{\hbar m \omega_{p,\alpha'}}{2}} b_j^{(p)\alpha'} (\hat{a}_p^\dagger - \hat{a}_p). \tag{1.30}$$

Here $\vec{b}^{(p)\alpha'}$ $(p = 1, 2, \ldots, N)$ are the eigenvectors of the matrix $B_{i,j}^{\alpha'}$, that is $B_{i,j}^{\alpha'} b_j^{(p)\alpha'} = \mu_{p,\alpha'} b_i^{(p),\alpha'}$, where $\mu_{p,\alpha'}$ are the corresponding eigenvalues. The collective frequencies are $\omega_{p,\alpha'} = \omega_{\alpha'} \sqrt{\mu_{p,\alpha'}}$. Replacing (1.30) in (1.28) we obtain

$$\hat{H}_\perp = \hbar \sum_{p=1}^{N} \omega_{p,x} \left(\hat{a}_{p,x}^\dagger \hat{a}_{p,x} + \frac{1}{2} \right) + \hbar \sum_{p=1}^{N} \omega_{p,y} \left(\hat{a}_{p,y}^\dagger \hat{a}_{p,y} + \frac{1}{2} \right). \tag{1.31}$$

In the transverse direction the highest vibrational frequency is the center-of-mass mode frequency which is equal to $\omega_{\rm com} = \omega_{\alpha'}$. The next frequency is the rocking mode frequency $\omega_{\rm roc} = \sqrt{\omega_{\alpha'}^2 - \omega_z^2}$. Both vibtational frequencies are independent on N, whereas all other varie with N.

Important property of the transverse vibrational spectrum is that by increasing N the lowest vibrational frequncy vanishes which is signal for structural instability. This leads to the formation of $2D$ ion crystal.

1.3 Interaction with Laser Field

Consider that ion has to metastable electronic states which we denote $|\uparrow\rangle$, $|\downarrow\rangle$ with corresponding energies $E_\uparrow$, $E_\downarrow$ and transition frequency $\omega_0 = (E_\uparrow - E_\downarrow)/\hbar$. The Hamiltonian which describes the internal degrees of freedon then is given by

$$\hat{H}_{\rm spin} = E_\uparrow |\uparrow\rangle\langle\uparrow| + E_\downarrow |\downarrow\rangle\langle\downarrow| = \frac{\hbar\omega_0}{2}\sigma_z + \frac{E_\uparrow + E_\downarrow}{2}\hat{1}, \tag{1.32}$$

where $\sigma_z = |\uparrow\rangle\langle\uparrow| - |\downarrow\rangle\langle\downarrow|$ is the Pauli matrix and $\hat{1} = |\uparrow\rangle\langle\uparrow| + |\downarrow\rangle\langle\downarrow|$ identity operator. Second term commuts with all operators, thereby does not play any role.

Despite the internla states, ion has also vibrational degrees of freedom. Therefore, the interaction-free Hamiltonian becomes

$$\hat{H}_0 = \frac{\hbar\omega_0}{2}\sigma_z + \hbar \sum_{\alpha=x,y,z} \omega_\alpha \hat{a}_\alpha^\dagger \hat{a}_\alpha. \tag{1.33}$$

Consider that a coherent monohromatic laser field propagates along the trap axis z. Assume that the laser field excites dipole transition between the internlal electric states of the ion. Then the interaction Hamiltonian is given by

$$\hat{V} = -\hat{\mu} \cdot \vec{E}(z,t). \tag{1.34}$$

Here $\hat{\mu}$ is the operator of the electric dipole moment of the ion, $\vec{E}(z,t) = E_0\vec{\epsilon}\cos(kz - \omega_{\rm L}t + \phi)$ is the laser electric field component, where $\vec{\epsilon}$ is the vector of the laser polarization. $\vec{k}$ is the wave vector, $\omega_{\rm L}$ is the laser frequency, and ϕ is the laser phase. The interaction Hamiltonian becomes

$$\hat{V} = -q\left(\mu_{\uparrow\downarrow}\sigma_+ + \mu_{\downarrow\uparrow}\sigma_-\right) \cdot \frac{E_0\vec{\epsilon}}{2}\left(e^{i\{\eta(\hat{a}^\dagger + \hat{a}) - \omega_L t + \phi\}} + \text{h.c.}\right), \tag{1.35}$$

where $\mu_{\uparrow\downarrow} = \langle\uparrow|\hat{\mu}|\downarrow\rangle$, $\mu_{\downarrow\uparrow} = \langle\downarrow|\hat{\mu}|\uparrow\rangle$ are the matrix elements of the dipole moment between the corresponding electonic states and $\sigma_+ = |\uparrow\rangle\langle\downarrow|$, $\sigma_+ = |\downarrow\rangle\langle\uparrow|$. In the experession (1.35) we have represented the ion displacement as $\hat{z} = \sqrt{\frac{\hbar}{2m\omega_z}}(\hat{a}^\dagger + \hat{a})$ and $\eta = k\sqrt{\frac{\hbar}{2m\omega_z}}$ is the Lamb-Dicke parameter. The total Hamiltonian is given by

$$\hat{H} = \hat{H}_0 + \hat{V}. \tag{1.36}$$

It is convenient to transform the total Hamiltonian into the interaction picture via the unitary transformation $\hat{U} = e^{-\frac{i\hat{H}_0 t}{\hbar}}$. From the Schrodinger equation $i\frac{d}{dt}|\psi\rangle = \hat{H}|\psi\rangle$ we derive $i\frac{d}{dt}|\psi_{\rm int}\rangle = \hat{H}_{\rm int}|\psi_{\rm int}\rangle$, where $|\psi\rangle = \hat{U}|\psi_{\rm int}\rangle$ and the interaction Hamiltonian becomes

$$\hat{H}_{\rm int} = \hat{U}^\dagger \hat{V} \hat{U}. \tag{1.37}$$

Neglecting the fast oscillating terms with terms proportional to $\omega_L + \omega_0$ compared with the slowly oscillation terms propostional to $\omega_L - \omega_0$ we obtain [5]

$$\hat{H}_{\rm int} = \hbar\Omega\sigma_+ e^{i\{\eta(\hat{a}^\dagger e^{i\omega_z t} + \hat{a}e^{-i\omega_z t}) - \delta t + \phi\}} + \text{h.c.}, \tag{1.38}$$

where $\delta = \omega_L - \omega_0$ is the detuning between the laser frequency and the atomic transition frequency and Ω is the Rabi frequency.

The Hilbert space consists of the inernal states $|\uparrow\rangle$, $|\downarrow\rangle$ and the Fock states of the harmonic oscillator, $|n\rangle$ $(n = 0, 1, 2, \ldots)$. Therefore, the wave vector can be decomposed as

$$|\psi_{\rm int}\rangle = \sum_{m=\uparrow,\downarrow} \sum_{n=0}^{\infty} c_{m,n} \, |m, n\rangle \, , \tag{1.39}$$

where $c_{m,n}$ are the probability amplitudes. The equation (1.39) shows that in the most general case the system is in the entangled state between the internal and motion states of the ion. The Schrodinger equation becoms

$$i\hbar \frac{d}{dt} c_{m',n'}(t) = \sum_{m=\uparrow,\downarrow} \sum_{n=0}^{\infty} \langle m', n'|\hat{H}_{\rm int}|m, n\rangle c_{m,n}(t). \tag{1.40}$$

Assume that the detuning is $\delta = \omega_z k + \Delta$, where $k = 0, \pm 1, \pm 2...$ and $|\Delta| \ll \omega_z$. Using the equality $e^{\alpha\hat{a}^\dagger + \alpha^*\hat{a}} = e^{\alpha\hat{a}^\dagger} e^{\alpha^*\hat{a}} e^{-\frac{|\alpha|^2}{2}}$, we derive the following Hamiltonian [5]:

$$\hat{H}_{\rm int} = \hbar\Omega\sigma_+ e^{-\frac{\eta^2}{2}} \sum_{p,r=0}^{\infty} (i\eta)^{p+r} \frac{(\hat{a}^\dagger)^p}{p!} \frac{(\hat{a})^r}{r!} e^{i\omega_z(p-r-k)t} e^{-i\Delta t} + \text{H.c.} \tag{1.41}$$

We can distinguish three different transitions. For $k = 0$ the detuning is close to the frequency of the atomic transition. In that case the transitions between the ground and excited electronic states is realized without change of the vibrational state, namely $|\downarrow\rangle|n\rangle \leftrightarrow |\uparrow\rangle|n\rangle$. Such a transition is called *carrier transition.*

For $k = -1, -2, -3, ...$ the transition from the ground state to the exited state can be realized only by absorption of vibrational quanta, $|\downarrow\rangle|n\rangle \leftrightarrow |\uparrow\rangle|n - |k|\rangle$. Such a transition for given k is called *red-sideband transition.* Finally, for $k = 1, 2, 3, ...$ the transition between the ground and excited states can be realized only by creation of vibrational quanta, namely $|\downarrow\rangle|n\rangle \leftrightarrow |\uparrow\rangle|n + k\rangle$. Such a transition for given k is called *blue-sideband transition.*

Let us consider the Hamiltonians for the three different cases. The matrix elements of the operator are

$$D_{n',n} = \langle n'|e^{\alpha a^\dagger} e^{-\alpha^* a}|n\rangle, \tag{1.42}$$

where we assume that $n' > n$. Taylor expansition gives [6]

$$\begin{aligned} D_{n',n} &= \sum_{m'=0}^{\infty}\sum_{m=0}^{\infty}(\alpha)^{m'}(-\alpha^*)^m\langle n'|\frac{(a^\dagger)^{m'}(a)^m}{m'!m!}|n\rangle \\ &= \sum_{m'=0}^{n'}\sum_{m=0}^{n}\delta_{n'-m',n-m}\frac{(\alpha)^{m'}}{m'!}\frac{(-\alpha^*)^m}{m!}\sqrt{\frac{n'!}{(n'-m')!}}\sqrt{\frac{n!}{(n-m)!}} \\ &= \alpha^{n'-n}\sum_{m=0}^{n}\frac{(-1)^m|\alpha|^{2m}}{m!(n'-n+m)!}\frac{\sqrt{n'!n!}}{(n-m)!} \\ &= \alpha^{n'-n}\sqrt{\frac{n!}{n'!}}L_n^{n'-n}(|\alpha|^2), \end{aligned} \tag{1.43}$$

where we have introduced the generalized Laguerre polynomials

$$L_n^m(x) = \sum_{k=0}^{n}(-1)^k\left(\begin{array}{c} n+m \\ n-k \end{array}\right)\frac{x^k}{k!}. \tag{1.44}$$

Finally, for $n' < n$ we derive

$$D_{n',n} = \alpha^{n-n'}\sqrt{\frac{n'!}{n!}}L_{n'}^{n-n'}(|\alpha|^2). \tag{1.45}$$

From Eq. (1.38) it follows that $\alpha = i\eta e^{i\omega_z t}$ so that the matrix elements between the Fock states become

$$D_{n',n} = (i\eta)^{|n'-n|}e^{i\omega(n'-n)t}\sqrt{\frac{n_<!}{n_>!}}L_{n_<}^{|n'-n|}(\eta^2), \tag{1.46}$$

where $n_< = \min(n', n)$ and $n_> = \max(n', n)$

Carrier transition

For the carrier transition the laser detuning is set to $\omega_{\rm L} - \omega_0 = \Delta$ so that $k = n' - n = 0$. Such a coherent transition between the levels $|\uparrow\rangle|n\rangle$ and $|\downarrow\rangle|n\rangle$ do not change the vibrational state. The wave vector can be written as $\psi(t)\rangle = c_{\downarrow,n}|\downarrow, n\rangle + c_{\uparrow,n}|\uparrow, n\rangle$ and using (1.46) we obtain

$$\begin{aligned} i\frac{dc_{\uparrow,n}}{dt} &= \Omega_{n,n}e^{-i(\Delta t-\phi)}c_{\downarrow,n}, \\ i\frac{dc_{\downarrow,n}}{dt} &= \Omega_{n,n}e^{i(\Delta t-\phi)}c_{\uparrow,n}, \end{aligned} \tag{1.47}$$

where $\Omega_{n,n} = e^{-\eta^2/2}L_n(\eta^2)$ with $L_n^0(x) = L_n(x)$.

For constant Rabi frequency $\Omega_{n,n} = \text{const}$ and laser detuning $\Delta = \text{const}$ the system of differential equations can be solved exactly. Indeed, performing the

change of the variables $c_{\uparrow,n} = \tilde{c}_{\uparrow,n} e^{-i\Delta t/2}$ and $c_{\downarrow,n} = \tilde{c}_{\downarrow,n} e^{i\Delta t/2}$, it leads to

$$\begin{aligned} i\frac{d\tilde{c}_{\uparrow,n}}{dt} &= -\frac{\Delta}{2}\tilde{c}_{\uparrow,n} + \Omega_{n,n}\tilde{c}_{\downarrow,n}, \\ i\frac{d\tilde{c}_{\downarrow,n}}{dt} &= \frac{\Delta}{2}\tilde{c}_{\downarrow,n} + \Omega_{n,n}\tilde{c}_{\uparrow,n}. \end{aligned} \tag{1.48}$$

This is a system of differential equations with constant coefficients so that the solution is given by

$$\begin{aligned} c_{\uparrow,n}(t) &= e^{-i\frac{\Delta t}{2}}\left(\cos(\tilde{\Omega}_{n,n}t) + \frac{i\Delta}{2\tilde{\Omega}_{n,n}}\sin(\tilde{\Omega}_{n,n}t)\right)c^0_{\uparrow,n} - ie^{-i\frac{\Delta t}{2}+i\phi}\frac{\Omega_{n,n}}{\tilde{\Omega}_{n,n}}\sin(\Omega_{n,n}t)c^0_{\downarrow,n} \\ c_{\downarrow,n}(t) &= e^{i\frac{\Delta t}{2}}\left(\cos(\tilde{\Omega}_{n,n}t) - \frac{i\Delta}{2\tilde{\Omega}_{n,n}}\sin(\tilde{\Omega}_{n,n}t)\right)c^0_{\downarrow,n} - ie^{i\frac{\Delta t}{2}-i\phi}\frac{\Omega_{n,n}}{\tilde{\Omega}_{n,n}}\sin(\Omega_{n,n}t)c^0_{\uparrow,n} \end{aligned} \tag{1.49}$$

where $\tilde{\Omega}_{n',n} = \sqrt{\Omega^2_{n',n} + \left(\frac{\Delta}{2}\right)^2}$.

1.3.1 Red- and blue-sideband transitions

As we mention above the red- and blue-sideband transitions are accompanied by change of the vibrational state of the ion chain. For red-sidenand transition, the transition from ground to the excited state is only possible by decreasing the phonon number $|\downarrow, n\rangle -> |\uparrow, n'\rangle$ while for the blue-sidenand transition such a transition increases the vibrational state, $|\downarrow, n\rangle -> |\uparrow, n'\rangle$.

Let us write the arbitrary wave vector as $|\psi(t)\rangle = c_{\downarrow,n}(t)\,|\downarrow, n\rangle + c_{\uparrow,n'}(t)\,|\uparrow, n'\rangle$ and using Eq. (1.46) we obtain

$$\begin{aligned} \frac{dc_{\uparrow,n'}}{dt} &= -i^{1+|n'-n|}\Omega_{n',n}e^{-i(\Delta t-\phi)}c_{\downarrow,n}, \\ \frac{dc_{\downarrow,n}}{dt} &= -i^{1-|n'-n|}\Omega_{n',n}e^{i(\Delta t-\phi)}c_{\uparrow,n'}, \end{aligned} \tag{1.50}$$

where the Rabi frequency is $\Omega_{n',n} = \eta^{|n'-n|}\sqrt{\frac{n_<!}{n_>!}}L^{|n'-n|}_{n_<}(\eta^2)$ with $n_< = \min(n', n)$ and $n_> = \max(n', n)$. This system is similar to what we have obtained for the carrier transition. For constant Rabi frequency and detuning the general solution for the three cases can be written as $|\psi(t)\rangle = \hat{U}_{n',n}(t, 0)|\psi(0)\rangle$, where

$$\hat{U}_{n',n}(t,0) = \begin{bmatrix} e^{-i\frac{\Delta t}{2}}\left(\cos(\tilde{\Omega}_{n',n}t) + i\frac{\Delta}{2\tilde{\Omega}_{n',n}}\sin(\tilde{\Omega}_{n',n}t)\right) & -ie^{-i\left(\frac{\Delta t}{2}-\phi-\frac{\pi}{2}|n'-n|\right)}\frac{\Omega_{n',n}}{\tilde{\Omega}_{n',n}}\sin(\Omega_{n',n}t) \\ -ie^{i\left(\frac{\Delta t}{2}-\phi-\frac{\pi}{2}|n'-n|\right)}\frac{\Omega_{n',n}}{\tilde{\Omega}_{n',n}}\sin(\Omega_{n',n}t) & e^{i\frac{\Delta t}{2}}\left(\cos(\tilde{\Omega}_{n',n}t) - i\frac{\Delta}{2\tilde{\Omega}_{n',n}}\sin(\tilde{\Omega}_{n',n}t)\right) \end{bmatrix}. \tag{1.51}$$

1.3.2 Lamb-Dicke Approximation

Improrant experimental situation is when the amplitude of ion's motion along the laser wave vector is less than $\lambda/2\pi$, which correspond to the condition

$\langle\psi_{\rm motion}|k^2\delta\hat{z}^2|\psi_{\rm motion}\rangle^{1/2} \ll 1$. In that case the Lamb-Dicke condition is $\eta\sqrt{2\bar{n}+1} \ll 1$, where $\bar{n}$ is the mean phonon number. As long as this is satisfied then in lowest approximation with respect to η we obtain

$$\Omega_{n',n} = \Omega\eta^{|n'-n|}\sqrt{n_>!/n_<!}(|n'-n|)^{-1}. \tag{1.52}$$

Therefore for the first red-sideband transition, and for carrier and blue-sideband transitions we obtain

$$\Omega_{n-1,n} = \Omega\eta\sqrt{n}, \quad \Omega_{n,n} = \Omega, \quad \Omega_{n+1,n} = \Omega\eta\sqrt{n+1}. \tag{1.53}$$

In the Lamb-Dicke limit the Hamiltonian for the carrier transition becomes ($\Delta = 0$)

$$\hat{H}_{\rm c} = \hbar\Omega(\sigma^+ e^{i\phi} + \sigma^- e^{-i\phi}), \tag{1.54}$$

which describes continous oscillations between the ground and excitet states with Rabi frequency Ω

For the first red-sidenabd transition $k = -1$ we obtain

$$\hat{H}_{\rm r} = i\hbar\eta\Omega(\hat{a}\sigma^+ e^{i\phi} - \hat{a}^\dagger\sigma^- e^{-i\phi}). \tag{1.55}$$

This is a Jaynes-Cummings Hamiltonian, which describes the coherent interaction between the internal states of the ion and the quantum oscillation mode. The strength of the interaction between the levels $|\downarrow, n\rangle$ and $|\uparrow, n\rangle$ is characterized with Rabi frequency $\Omega_{n-1,n}$, which depends on the vibrational quantum number n. It follows that if the system is prepared in the state $|\psi(0)\rangle = |\downarrow, 0\rangle$ then the Rabi frequency vanishes and the system remains in this state, although the laser field is applied. Such a dynamics in which one system depends on the state of other quantum system is fundamental for all quantum operation using in the quantum information.

Finally, the Hamiltonian for the first blue-sidenabd transition $k = 1$ is

$$\hat{H}_{\rm b} = i\hbar\eta\Omega(\hat{a}^\dagger\sigma^+ e^{i\phi} - \hat{a}\sigma^- e^{-i\phi}), \tag{1.56}$$

with Rabi frequency $\Omega_{n+1,n}$. This is the so called anti-Jaynes-Cummings Hamiltonian. Here, even the system is prepared in the motion ground state $|\psi(0)\rangle = |\downarrow, 0\rangle$ the laser field would induce transition because $\Omega_{1,0} \neq 0$.

1.4 Bichromathic Interaction

The bichromatic interaction is used experimantally quite oftenly because creates entangled states and quantum gates with trapped ions. It is a combination of red- and blue-sidenabd detuned laser field with well defined laser detuning. Assuming that the Rabi frequencies of the both laser fields are equal the Hamiltonian of the system is

$$\hat{H}_{\rm int} = \hbar\Omega\sigma_+ e^{i\{\eta(\hat{a}^\dagger e^{i\omega_z t} + \hat{a}e^{-i\omega_z t}) - \delta_r t + \phi_r\}} + \hbar\Omega\sigma_+ e^{i\{\eta(\hat{a}^\dagger e^{i\omega_z t} + \hat{a}e^{-i\omega_z t}) - \delta_b t + \phi_b\}} + \text{h.c.}, \tag{1.57}$$

where $\delta_r = \omega_{L,r} - \omega_0 = -\omega_z + \delta$ and $\delta_b = \omega_{L,b} - \omega_0 = \omega_z - \delta$ ($|\delta| \ll \omega_z$) are the respective laser detunings of the both fields. Within the Lamb-Dicke approhimation one can expand the exponents and keeping the leading terms we have

$$\begin{aligned}\hat{H}_{\rm int} &= \hbar\Omega\sigma_+\{1 + i\eta(\hat{a}^\dagger e^{i\omega_z t} + \hat{a}e^{-i\omega_z t})\}e^{i(\omega_z-\delta)t+i\phi_r} \\ &\quad +\hbar\Omega\sigma_+\{1 + i\eta(\hat{a}^\dagger e^{i\omega_z t} + \hat{a}e^{-i\omega_z t})\}e^{-i(\omega_z-\delta)t+i\phi_b} + \text{h.c.} \quad (1.58)\end{aligned}$$

Assuming rotating wave approximation one can neglect the fast rotating terms. Therefore, if the conditions $\Omega \ll \omega_z$ and $\eta\Omega \ll \omega_z$ the Hamiltonian becomes

$$\hat{H}_{\rm int} = \hbar i\eta\Omega\sigma_+\hat{a}e^{-i\delta t}e^{i\phi_r} + \hbar i\eta\Omega\sigma_+\hat{a}^\dagger e^{i\delta t}e^{i\phi_b} + \text{h.c.}, \quad (1.59)$$

where we have neglected the terms $\Omega\sigma_+ e^{i\omega_z t} + \text{h.c.}$, $\Omega\sigma_+\hat{a}^\dagger e^{i2\omega_z t} + \text{h.c.}$. The coupling between the internal and vibrational states is $g = \eta\Omega$ so that

$$\hat{H}_{\rm int} = i\hbar g(\sigma_+ e^{i\phi_{\rm s}} - \sigma_- e^{-i\phi_{\rm s}})(\hat{a}^\dagger e^{i\delta t+i\phi_{\rm m}} + \hat{a}e^{-i\delta t-i\phi_{\rm m}}), \quad (1.60)$$

where

$$\phi_{\rm s} = \frac{1}{2}(\phi_b + \phi_r), \quad \phi_{\rm m} = \frac{1}{2}(\phi_b - \phi_r). \quad (1.61)$$

Similarly to Jaynes-Cummings model the the quantum evolution udner the action of the bichromatic laser fields can be exactly solved. Indeed, let us for simplicity set $\phi_b = \phi_r = -\pi/4$ so that

$$\hat{H}_{\rm int} = \hbar g\sigma_x(\hat{a}^\dagger e^{i\delta t} + \hat{a}e^{-i\delta t}). \quad (1.62)$$

For arbitrary initial state the solution of the Schrodinger equation can be written as

$$|\psi(t)\rangle = \hat{U}(t, t_0)\,|\psi(t_0)\rangle\,, \quad (1.63)$$

where the unitary operator is given by

$$\hat{U}(t, t_0) = T_{\leftarrow} e^{-\frac{i}{\hbar}\int_{t_0}^{t}\hat{H}(\tau)d\tau} \quad (1.64)$$

Here with $T_{\leftarrow}$ we denote the time hronological order in the exponent. Using the Magnus expression, the unitary operator becomes

$$\begin{aligned}\hat{U}(t, t_0) &= \exp\{-\frac{i}{\hbar}\int_{t_0}^{t} dt_1\hat{H}_1 - \frac{1}{2\hbar^2}\int_{t_0}^{t} dt_1\int_{t_0}^{t_1} dt_2[\hat{H}_1, \hat{H}_2] \\ &\quad +\frac{i}{6\hbar^3}\int_{t_0}^{t} dt_1\int_{t_0}^{t_1} dt_2\int_{t_0}^{t_2} dt_3\left([\hat{H}_1, [\hat{H}_2, \hat{H}_3]] + [\hat{H}_3, [\hat{H}_2, \hat{H}_1]]\right) + \ldots\} \quad (1.65)\end{aligned}$$

where $\hat{H}_k = \hat{H}(t_k)$. For the Hamiltonian (1.62) it is easy to see that the infinite sum is simplified to two terms. Indeed, we have

$$[\hat{H}_1, \hat{H}_2] = [\hat{a}^\dagger e^{i\delta t_1} + \hat{a}e^{-i\delta t_1}, \hat{a}^\dagger e^{i\delta t_2} + \hat{a}e^{-i\delta t_2}] = 2i\sin(\delta(t_2 - t_1)), \quad (1.66)$$

where we have used $\sigma_x^2 = 1$. The results show that the commutator is proportional to the identity operator, thereby the high order turms in the Magnus series are zero. Using this we derive

$$\hat{U}(t,0) = e^{\sigma_x(\alpha(t)\hat{a}^\dagger - \alpha^*(t)\hat{a})}, \quad \alpha(t) = -i\frac{g}{\delta}(e^{i\delta t} - 1), \tag{1.67}$$

where we set $t_0 = 0$.

1.5 Conclusion

In this introductory chapter, the basic concepts of Paul's trap ions were discussed. It has been shown that a quadrupole configuration of electrodes with a fast oscillating electric field applied leads to a stable harmonic minimum for the ion. The equilibrium positions of an ion system and the corresponding vibrational modes were considered. The interaction of an ion with a laser field was also considered. Depending on the frequency of the laser field, the transitions between atomic levels can occur with or without a change in the vibrational quantum number.

2. QUANTUM PHASE TRANSITION IN JAYNES-CUMMINGS-HUBBARD MODEL

In this Chapter we present a system for the simulation of quantum phase transitions of collective internal qubit and phononic states with a linear crystal of trapped ions. The laser-ion interaction creates an energy gap in the excitation spectrum, which induces an effective phonon-phonon repulsion and a Jaynes-Cummings-Hubbard interaction. This system shows features equivalent to phase transitions of polaritons in coupled cavity arrays. Trapped ions allow for easy tuning of the hopping frequency by adjusting the axial trapping frequency and the phonon-phonon repulsion via laser detuning and intensity. We propose an experimental protocol to access all observables of the system, which allows one to obtain signatures of the quantum phase transitions even with a small number of ions.

Furthermore, we discuss analytic approximations to the ground-state phase diagram of the homogeneous Jaynes- Cummings-Hubbard Hamiltonian with general short-range hopping. We derive approximate analytic expressions for the boundaries between Mott-insulating and superfluid phases and give explicit expressions for the critical value of the hopping amplitude within the different approximation schemes. In the case of an array of cavities, which is represented by the standard Jaynes-Cummings-Hubbard model, we compare both approximations to numerical data from density-matrix renormalization-group calculations.

Finally, we discuss the simulation of Heisenberg models with spins $s = 1/2$ and $s = 1$ with a linear crystal of trapped ions. We show that the laser-ion interaction induces a Jaynes-Cummings-Hubbard interaction between the atomic V-type level structure and the two phonon species. In the strong-coupling regime the collective atom and phonon excitations become localized at each lattice site and form an effective spin system with varying length. We show that the quantum-mechanical superexchange interaction caused by the second-order phonon hopping processes creates a Heisenberg-type coupling between the individual spins. Trapped ions allow control of the superexchange interactions by adjusting the trapping frequencies, the laser intensity, and the detuning.

2.1 Physical Realization of Jaynes-Cummings-Hubbard Model using Trapped Ions

Trapped ions are among the most promising physical systems for implementing quantum computation [7] and quantum simulation [8]. Long coherence times and individual addressing allow for the experimental implementation of quantum gates and quantum computing protocols such as the Deutsch-Josza algorithm, teleportation, quantum error correction, quantum Fourier transformation, and Grover search. Quantum simulation could be performed in the future by large-scale quantum computation [9].

In this Section, we propose a physical implementation of the Jaynes-Cummings-Hubbard (JCH) model using trapped ions. The JCH model was proposed in the context of an array of coupled cavities, each containing a single two-state atom and a photon [10, 11, 12, 13, 14]. Such a system is described by the combination of two well-known physical models: the Hubbard model, which describes the interaction and hopping of bosons in a lattice [15], and the Jaynes- Cummings model, which describes the interaction of an atom with a quantum field. The JCH model predicts a quantum phase transition of polaritons, which are collective photonic and atomic excitations. We shall show that the laser-driven ion chain in a linear Paul trap is described by a JCH Hamiltonian, wherein the ions and the phonons correspond to the atoms and the photons, respectively, in a coupled cavity array, see Fig. 2.1. As in [16], the position-dependent energy and the nonlocal hopping frequency of the phonons are controlled by the trapping frequencies, while the effective on-site repulsion is provided by the interaction of the phonons with the internal states of the ions and can be adjusted by the parameters of an external laser field, namely, the Rabi frequency and the detuning. This on-site interaction is analogous to the photon blockade (photon-photon repulsion), where the strong atom cavity coupling prevents the entering of additional photons into the optical cavity [17]. We shall show that many-body effects appear as a quantum phase transition between a localized Mott insulator (MI) and a delocalized superfluid (SF) state of the composite phononic and internal qubit states of the ions. Due to the collective nature of the excitations we distinguish between collective qubit and phononic SF and MI phases and the pure phononic SF phase, similar to the effects predicted in [18] for coupled cavity arrays.

Consider a chain of N ions confined in a linear Paul trap along the z axis with trap frequencies ω_q $q = x, y, z$, where the radial trap frequencies are much larger than the axial trap frequency $\omega_{x,y} \gg z$, so that the ions are arranged in a linear configuration and occupy equilibrium positions z_i^0 along the z axis. Making a Taylor expansion around the equilibrium position and neglecting x^3, y^3, zx^2, zy^2 and higher-order terms, the Hamiltonian in the radial direction x reads [3]

$$\hat{H}_x = \frac{1}{2M}\sum_{k=1}^{N}\hat{p}_k^2 + \frac{M\omega_x^2}{2}\sum_{k=1}^{N}\hat{x}_k^2 - \frac{M\omega_z^2}{2}\sum_{k>m}^{N}\frac{(\hat{x}_k-\hat{x}_m)^2}{|u_k-u_m|^3}. \tag{2.1}$$

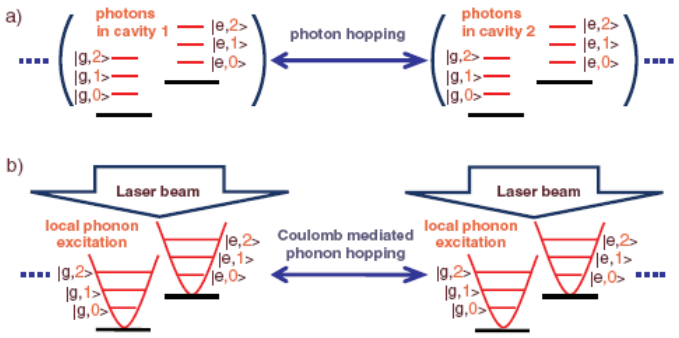

Fig. 2.1: (Color online) Analogy between phase transitions in coupled cavities and trapped ions: (a) coupled cavities each containing photons and single two-state atoms. Intercavity hopping is provided by an optical fiber. The strong coupling between the atoms and the photons leads to a photon-photon repulsion. (b) All ions are simultaneously interacting with a traveling wave in the radial direction. The laser-ion interaction creates an effective on-site interaction between the local phonons. The phonon hopping appears due to the Coulomb interaction and can be adjusted by the mutual distance of the ions.

Here $\hat{p}_k$ is the momentum operator, M is the ions mass, and $\hat{x}_k$ is the position operator of the kth ion about its dimensionless equilibrium position u_k. In Hamiltonian (2.1) the motion in the radial direction is decoupled from the axial motion. In terms of the normal modes ω_p, Hamiltonian (2.1) reads $\hat{H}_x = \hbar \sum_{p=1}^{N} \omega_p (\hat{\tilde{a}}_p^\dagger \hat{\tilde{a}}_p + 1/2)$. Here $\hat{\tilde{a}}_p^\dagger$ and $\hat{\tilde{a}}_p$ are the phonon creation and annihilation operators of the pth collective phonon modes. However, if $\hat{x}_k$ and $\hat{p}_k$ are written in terms of local creation $\hat{a}_k^\dagger$ and annihilation $\hat{a}_k$ operators, so that $\hat{x}_k = \sqrt{\hbar/2M\omega_x}(\hat{a}_k^\dagger + \hat{a}_k)$ and $p_k = i\sqrt{\hbar M\omega_x/2}(\hat{a}_k^\dagger - \hat{a}_k)$, Hamiltonian (2.1) reads

$$\hat{H}_x = \hbar \sum_{k=1}^{N} (\omega_x + \omega_k) \hat{a}_k^\dagger \hat{a}_k + \hbar \sum_{k>m}^{N} t_{km} (\hat{a}_k^\dagger \hat{a}_m + \hat{a}_k \hat{a}_m^\dagger), \tag{2.2}$$

where we have neglected higher-order (energy nonconserving) terms. The phonons are trapped with a position-dependent frequency

$$\omega_k = -\frac{\alpha\omega_z}{2} \sum_{s\neq k}^{N} \frac{1}{|u_k - u_s|^3}, \tag{2.3}$$

where $\alpha = \omega_z/\omega_x$ ($\alpha \ll 1$), and they may hop between different ions, with nonlocal hopping strengths

$$t_{km} = \frac{\alpha\omega_z}{2} \frac{1}{|u_k - u_m|^3}, \tag{2.4}$$

derived from the long-range Coulomb interaction.

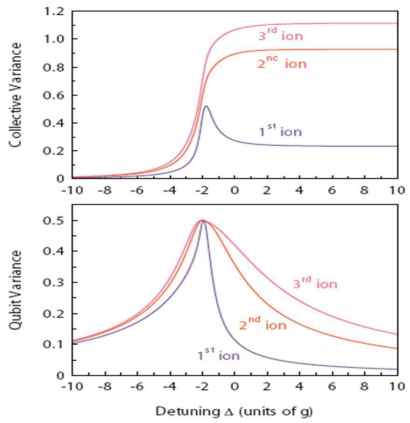

Fig. 2.2: (Color online) Total (qubit+phonon variance) DN_k (top) and the qubit variance $DN_{a,k}$ $(k = 1, 2, 3)$ (bottom) for a chain of five ions with five excitations as a function of the laser detuning Δ for fixed hopping $t = 0.3g$. Negative values of Δ correspond to blue detuning with respect to the red-sideband transition.

We shall show that the laser-ion interaction induces an effective repulsion between the local phonons. This interaction provides the phase transition from phononic SF state to composite SF and MI phases of the joint phononic and qubit excitations. Consider ion qubits with a transition frequency ω_0, which interact along the radial direction with a common traveling-wave laser light addressing the whole ion chain with frequency $\omega_{\rm L}$. The Hamiltonian of the system after the optical rotating-wave approximation is given by [5]

$$\hat{H} = \hat{H}_x + \hbar\Omega \left(\sum_{k=1}^{N} \sigma_k^+ e^{i\eta(\hat{a}_k^\dagger + \hat{a}_k) - i\delta t} + \text{H.c.} \right) \tag{2.5}$$

Here $\sigma_k^+ = |e_k\rangle\langle g_k|$ and $\sigma_k^- = |g_k\rangle\langle e_k|$ are the spin flip operators, $|e_k\rangle$ and $|g_k\rangle$ are the qubit states of the kth ion, Ω is the real-values Rabi frequency, $\delta = \omega_L - \omega_0$ is the laser detuning, and $\eta = |\mathbf{k}|x_0$ is the Lamd-Dicke parameter, where $\mathbf{k}$ is the laser wave vector and $x_0 = \sqrt{\hbar/3M\omega_x}$ is the spread of the ground-state wave function. The Hamiltonian, after transforming into the interaction picture by the unitary transformation $\hat{U} = e^{i\hat{H}_0 t/\hbar}$, with $\hat{H}_0 = -\hbar\omega_x \sum_{k=1}^{N} \hat{a}_k^\dagger \hat{a}_k + \hbar\Delta \sum_{k=1}^{N} |e_k\rangle\langle e_k|$, in the Lamb-Dicke limit and after the vibrational rotating-wave approximation, reads

$$\begin{aligned} H_I &= \hbar \sum_{k=1}^{N} \omega_k \hat{a}_k^\dagger \hat{a}_k + \hbar\Delta \sum_{k=1}^{N} |e_k\rangle\langle e_k| + \hbar g \sum_{k=1}^{N} (\sigma_k^+ \hat{a}_k + \sigma_k^- \hat{a}_k^\dagger) \\ &\quad + \hbar \sum_{k>m} t_{km} (\hat{a}_k^\dagger \hat{a}_m + \hat{a}_k \hat{a}_m^\dagger), \end{aligned} \tag{2.6}$$

where $\hat{H}_I = \hat{U}^\dagger \hat{H} \hat{U} - i\hbar \hat{U}^\dagger \partial_t \hat{U}$. We assume that the laser is tuned near the red motional sideband $\delta = -\omega_x - \Delta$, with a small detuning Δ ($\Delta \ll \omega_x$). The coupling between the internal qubit and local phonon states is $g = \eta\Omega$. Hamiltonian (2.6) is valid when $t_{km}, g \ll \omega_x$, which ensures that higher terms, which violate the conservation of the total number of excitations, can be neglected. The first three terms in Eq. (2.6) describe the Jaynes-Cummings model. The first two terms correspond to the energies of the local phonons and the ions, while the third term describes the laser-ion interaction. The fourth term in Eq. (2.6) describes the nonlocal hopping of phonons between different ions and allows the comparison to Hubbard systems. Hamiltonian (2.6) commutes with the total excitation operator $\hat{N} = \sum_{k=1}^{N} \hat{N}_k$, hence the total number of excitations is conserved. Here $\hat{N}_k = a_k a_k + |e_k\rangle\langle e_k|$ is the number operator of the total qubit and phononic excitations at the kth site. If the laser detuning δ is tuned near the blue motional sideband then the system is represented by the anti- Jaynes-Cummings dynamics, which shows equivalent behavior by redefinition of the excitation operator $\hat{N}_k = \hat{a}_k^\dagger \hat{a}_k + |g_k\rangle\langle g_k|$. In the following we only assume small detunings Δ around the red-sideband transition, so that the anti-Jaynes-Cummings interaction does not occur.

In the JCH model the effective on-site interaction is provided by the interaction of phonons and qubit states at each site. The strength of the on-site interaction depends on external parameters, such as the Rabi frequency Ω and the laser detuning Δ. This interaction creates an energy gap, which prevents the absorption of additional phonons by each ion. When the hopping frequency is increased the energy gap decreases and a quantum phase transition occurs between the SF and MI phases [19].

We describe the quantum phase transition between the MI and SF states by the variance $DN_k = (\langle \hat{N}_k^2 \rangle = \langle \hat{N}_k \rangle^2)^{1/2}$of the number operator $\hat{N}_k$ with respect to the ground state of Hamiltonian (2.6) for fixed number of excitations. If the on-site interaction between the phonons dominates the hopping, the ground-state wave function is a product of local qubit and phononic states for each site with a fixed number of excitations. Hence in the MI state, the variance DN_k for any k vanishes. When the hopping term dominates the onsite interaction, then the ground state consists of a superposition of qubit and phononic states with delocalized excitations over the entire chain. In this state the variance DN_k at each site is nonzero.

Figure 2.2 (top) shows the variance DN_k ($k = 1, 2, 3$) for a chain of five ions with five collective excitations versus the laser detuning Δ for fixed hopping frequency $t = \alpha\omega_z/2$ calculated by an exact diagonalization of Hamiltonian (2.6). Due to the symmetry of the trap with respect to the center it is not necessary to plot the phase diagrams for ions 4 and 5. For sufficiently large negative detuning Δ, there exists an energy gap, which prevents the absorption of additional phonons. Hence, the system is in the MI phase, where the qubit and phononic excitations are localized. When the detuning Δ increases, the energy gap decreases and the system makes a phase transition to the SF phase. The phase transition is stronger for the ions near the center of the trap due to stronger

Coulomb interaction and increased hopping strengths and weaker at the ends of the ion chain. The comparison between the variance at the different sites demonstrates two characteristic features. First, there is a range of detunings where the qubit and phononic excitations at ion 1 (end of the chain) are predominantly in a MI phase, whereas the other ions are in the SF phase. Second, there is a broad range of Δ along which the joint excitations at all ions are in the SF phase.

Figure 2.2 (bottom) shows the variance of the qubit excitations $DN_{a,k}$,k with $\hat{N}_{a,k} = |e_k\rangle\langle e_k|$. This allows us to distinguish the following phases: in the region of large negative detuning Δ the collective and the qubit variances are small, indicating that the system is in the qubit MI phase. Increasing the detuning, the collective variance stays small but the qubit variance increases, which shows that the system is indeed in a collective MI phase. Approaching $\Delta = 0$ the system makes a phase transitions into the collective qubit and phononic SF phases as now both collective and qubit variance are large. Finally, for sufficiently large positive detuning the qubit variance decreases but the collective variance stays large, which shows that the system is in the phononic SF phase.

In conclusion, we have proposed an implementation of the JCH model by trapped ions simulating polaritonic phase transitions in coupled cavity arrays. The system shows a MI to SF phase transition of the collective qubit and phononic excitations even with a small number of ions. The features can be easily measured by local addressing. Compared to atoms in optical cavities, our implementation is easier to manipulate, as all parameters can be tuned by changing the trap frequency, laser detuning, and intensity. Additionally, the system can be extended by adding impurities of ions with different masses, which allows for simpler addressing of the radial phonon modes and a separation of coexistent phases.

2.2 Analytic approximations to the phase diagram of the Jaynes-Cummings-Hubbard model

A large variety of analytic and numeric methods was applied to the JCH model and related models, providing profound results for the phase diagram and other ground-state quantities [20]. In this Section, we show that in the strong-interaction limit and near commensurate filling simple approximate analytic solutions of the JCH model can be found if there is translational invariance, i.e., for an infinite homogeneous system or periodic boundary conditions realizable, e.g., with ions in a race-track Paul trap design. These solutions provide a good analytic approximation to the full ground-state phase diagram.

In this Section, we will shortly review the main features of the JCH model

defined by the Hamiltonian

$$\begin{aligned}\hat{H} &= \omega\sum_j \hat{a}_j^\dagger\hat{a}_j + \Delta\sum_j \sigma_j^+\sigma_j^- + g\sum_j(\sigma_j^\dagger\hat{a}_j + \hat{a}_j^\dagger\sigma_j^-) \\ &\quad + \sum_d t_d\sum_j(\hat{a}_j^\dagger\hat{a}_{j+d} + \hat{a}_{j+d}^\dagger\hat{a}_j) \end{aligned} \tag{2.7}$$

In the limit of vanishing hopping t_d, the resulting Jaynes-Cummings model can easily be diagonalized. In this case, all sites j decouples and become independent. Since the total number of excitations on every site j is a constant of motion, the local JC Hamiltonian block diagonalizes. Within each tow-dimensional excitation subspace, the eigenstates can easily found. We have

$$\begin{aligned}|\pm, n\rangle &= \frac{[\chi_n \mp (\omega-\Delta)]|\uparrow, n-1\rangle \pm 2g\sqrt{n}|\downarrow, n\rangle}{\sqrt{2}\sqrt{\chi_n^2 \mp (\omega-\Delta)\chi_n)}} \\ &= \alpha_n^\pm|\uparrow, n-1\rangle \pm \beta_n^\pm|\downarrow, n\rangle, \end{aligned} \tag{2.8}$$

with $\chi_n = \sqrt{(\Delta-\omega)^2 + 4ng^2}$ and $n > 0$,and the eigenenergies are

$$E_n^\pm = n\omega + \frac{\Delta-\omega}{2} \pm \frac{1}{2}\chi_n. \tag{2.9}$$

For $n = 0$, the ground state is nondegenerate and given by $|-, 0\rangle = |\downarrow, 0\rangle$ with $E_0 = 0$. Here, the state $|\uparrow, n-1\rangle$ describes and atomic excitation together with $n-1$ bosonic excitations; $|\downarrow, n\rangle$ is the state with the atom in the ground state and n bosonic excitations. In the strong-interaction limit $g \gg |\Delta-\omega|$, the energy gap $\Delta E_n = E_n^+ - E_n^- = \chi_n \sim 2g\sqrt{n}$ is large compared to any other energy scale in the system and, thus the excited states $|+, n\rangle$ do not contribute to the ground state.

For the following discussion, it will be useful to consider the action of a single bosonic creation or annihilation operator on a given JC eigenstate $|\pm, n\rangle$. Defining

$$A_n^\pm = \begin{cases}\sqrt{n}\alpha_n^\pm\beta_{n+1}^- \pm \sqrt{n+1}\beta_n^\pm\alpha_{n+1}^-, & n > 0 \\ \alpha_1^-, & n = 0,\end{cases} \tag{2.10}$$

$$B_n^\pm = \begin{cases}\sqrt{n}\alpha_n^\pm\beta_{n+1}^+ \mp \sqrt{n+1}\beta_n^\pm\alpha_{n+1}^+, & n > 0 \\ -\alpha_1^+, & n = 0,\end{cases} \tag{2.11}$$

$$C_n^\pm = \begin{cases}\sqrt{n-1}\alpha_n^\pm\beta_{n+1}^- \pm \sqrt{n}\beta_n^\pm\alpha_{n-1}^-, & n > 1 \\ 0, & n \le 1,\end{cases} \tag{2.12}$$

$$D_n^\pm = \begin{cases}\sqrt{n-1}\alpha_n^\pm\beta_{n-1}^+ \mp \sqrt{n}\beta_n^\pm\alpha_{n-1}^+, & n > 1 \\ \pm\beta_1^\pm\delta_{n,1}, & n \le 1,\end{cases} \tag{2.13}$$

the action of $\hat{a}^\dagger$ and $\hat{a}$ on the state $|\pm, n\rangle$ can be seen to be

$$\hat{a}^\dagger|\pm,n\rangle = A_n^\pm|+,n+1\rangle + B_n^\pm|-,n+1\rangle, \quad \hat{a}|\pm,n\rangle = C_n^\pm|+,n-1\rangle + D_n^\pm|-,n-1\rangle, \tag{2.14}$$

i.e., $\hat{a}^\dagger$ and $\hat{a}$ connect the manifold of states $|\pm, n\rangle$ to the manifolds $|\pm, n+1\rangle$ and $n > 0$, respectively, as expected.

In order to calculate the phase boundaries of the Mott insulating lobes for the JCH model, we will follow the usual route. Since the total number of excitations in the system commutes with the full JCH Hamiltonian, it is enough to treat the system for a fixed number of excitations. The boundary of the nth Mott lobe can then be determined by calculating the total energy $E(N)$ for $N = nL - 1$, $N = nL$, and $N = nL + 1$ excitations in a system with L sites. The chemical potential then reads as

$$\mu_n^\pm = \pm\{E(nL \pm 1) - E(nL)\}, \tag{2.15}$$

where the plus sign belongs to the upper boundary of the Mott lobe and the minus sign to the lower one. For $t_d = 0$, $\mu_n^\pm$ can be calculates straightforwardly. Starting with the energy for $N = nL$ excitations with n being an integer, i.e., for a commensurate number of excitations, it can be seen that due to the nonlinear dependence of the single-site energy E_n^- on n, the excitations will distribute equally over the whole lattice. The ground state is therefore given by $\vec{n} = \{n, n, \ldots, n\}$. Now, when adding (removing) a single excitation from the whole system, the ground state is given by $\{n \pm 1, n, \ldots, n\}$, where we have ignored the degeneracy of the state since we are only interested in the energy and the system is homogeneous. With this, the energies at $t_d = 0$ can be written as

$$E(nL-1) = (L-1)E_n^- + E_{n-1}^-, \quad E(nL) = LE_n^-, \quad E(nL+1) = (L-1)E_n^- + E_{n+1}^-, \tag{2.16}$$

and the chemical potentials evaluate to

$$\mu_n^+ = E_{n+1}^- - E_n^- = \omega - \frac{\chi_{n+1}}{2} + (1+\delta_{n0})\frac{\chi_n}{2} + \delta_{n0}\frac{\Delta-\omega}{2}, \tag{2.17}$$

for any n and

$$\mu_n^- = E_n^- - E_{n-1}^- = \omega - \frac{\chi_n}{2} + (1+\delta_{n1})\frac{\chi_{n-1}}{2} + \delta_{n1}\frac{\Delta-\omega}{2}, \tag{2.18}$$

for $n > 0$. Thus, for a commensurate number of excitations the system displays particle-hole gaps. Since $\mu_{n+1}^- = \mu_n^+$, the chemical potential for noncommensurate total number of excitations between $N = nL$ and $N = (n+1)L$ is the same, corresponding to a critical point. For nonvanishing tunneling, the critical points extend to critical regions.

The simplest numerical method to obtain a qualitative phase diagram is the so-called mean-field theory. As described, for instance, in [21], the mean-field theory can be implemented by introducing an order parameter Ψ, which in our case is chosen to be homogeneous and real valued. Decoupling the hopping term by using

$$\hat{a}_j^\dagger \hat{a}_l \to \Psi(\hat{a}_j^\dagger + \hat{a}_l) - |\Psi|^2, \tag{2.19}$$

the whole JCH Hamiltonian in the grand-canonical ensemble uncouples in real space with a local Hamiltonian being

$$\hat{H}_{\mathrm{MF}} = (\omega-\mu)\hat{a}^\dagger\hat{a}+(\Delta-\mu)\sigma^+\sigma^-+g(\hat{a}^\dagger\sigma^-+\hat{a}\sigma^-)-2\tilde{J}\Psi(\hat{a}^\dagger+\hat{a})+2\tilde{J}|\Psi|^2. \quad (2.20)$$

At this point, we omitted the spatial index because the problem is purely local. The modified hopping amplitude $\tilde{J} = -\sum_d t_d$ gives the effective coupling within the mean-field scheme. The phase diagram is now found by diagonalizing the mean-field Hamiltonian (3.1) either exactly by means of perturbation theory or numerically, setting an upper bound for the maximal number of bosonic excitations in the system. The ground-state energy is then given by $\min_\Psi E[\Psi]$ and the MI is distinguished from the SF by the value of Ψ for the minimal energy. For $\Psi = 0$, the system is in a MI state, for $\Psi > 0$, the ground state is superfluid. This sets the point of the MI to SF transition. It should be mentioned at this point that this method gives inadequate results in one dimension ($D = 1$) but is exact for $D \to \infty$. Additionally, the effective hopping $\tilde{J}$ must be larger than zero to yield useful results.

2.2.1 Approximative Determination of the Phase Boundaries

Effective strong-coupling model

From the discussion above, it can be seen that the phase boundaries are defined by the closure of the particle-hole gap. In the present section, we will derive effective Hamiltonians in the strong-coupling limit for the calculation of the upper and lower chemical potentials of the nth Mott lobe, allowing to calculate the particle-hole gap in first order of the hopping amplitudes t_d. To do so, we employ degenerate perturbation theory using Kato's expansion as summarized in [22] up to first order with $H_{\mathrm{eff}} = PVP$. This procedure is equivalent to the polariton mapping considered in [12, 20]. First, we note that according to Eq. (2.9) the state $|+, n\rangle$ is separated by a large energy gap from the ground state $|-, n\rangle$. Thus, $|+, n\rangle$ can be completely neglected in the following as already mentioned in [12].

When looking for the energy of the ground state with $N = nL$, from perturbation theory, no first-order contributions are present. So, the Hilbert space per site is one dimensional, consisting of the single state $|-, n\rangle$. Thus, up to first order, the energy is given by $E(nL) = LE_n^-$. When adding an excitation, the local Hilbert space increases; now (locally), the two states $|-, n\rangle$ and $|-, n+1\rangle$ need to be taken into account. So, in this limit, the system for an additional particle can be understood as a system consisting of effective spin-1/2 particles. We will identify the states $|\Uparrow\rangle$ with the state $|-, n+1\rangle$ and $|\Downarrow\rangle$ with $|-, n\rangle$. In order to derive the effective spin-1/2 model, one has to look on the action of the hopping operator $\hat{a}_{j+1}^\dagger\hat{a}_j$ on the states in the Hilbert space. Neglecting the contributions from the states $|+, n\rangle$ and $|+, n+1\rangle$, the hopping operator acts as

$$\hat{a}_{j+1}^\dagger\hat{a}_j|\Downarrow\rangle_{j+1}|\Uparrow\rangle_j = B_n^- D_{n+1}^-|\Uparrow\rangle_{j+1}|\Downarrow\rangle_j, \quad (2.21)$$

within the considered subspace. Therefore, by introducing spin operators $\tilde{\sigma}_j^{\pm}$, the hopping term is equivalent to a nearest-neighbor spin-spin interaction with

$$\hat{a}_{j+1}^{\dagger}\hat{a}_j = B_n^- D_{n+1}^- \tilde{\sigma}_{j+1}^+ \tilde{\sigma}_j^- \tag{2.22}$$

Together with the energy of the system, one can thus write an effective Hamiltonian describing the upper boundary of the nth Mott lobe

$$\tilde{H} = E_n^- \sum_j \tilde{\sigma}_j^- \tilde{\sigma}_j^+ + E_{n+1}^- \sum_j \tilde{\sigma}_j^+ \tilde{\sigma}_j^- + B_n^- D_{n+1}^- \sum_d t_d \sum_j (\tilde{\sigma}_{j+d}^+ \tilde{\sigma}_j^- + \tilde{\sigma}_{j+d}^- \tilde{\sigma}_j^+). \tag{2.23}$$

This Hamiltonian is equivalent to

$$\tilde{H} = (L-1)E_n^- + E_{n+1}^- + B_n^- D_{n+1}^- + B_n^- D_{n+1}^- \sum_d t_d \sum_j (\tilde{\sigma}_{j+d}^+ \tilde{\sigma}_j^- + \tilde{\sigma}_{j+d}^- \tilde{\sigma}_j^+) \tag{2.24}$$

since we are at fixed magnetization with only one spin pointing upward. This Hamiltonian can be further simplified, by using a Jordan-Wigner transformation mapping the spin operators $\tilde{\sigma}_j^-$ onto fermionic operators $\hat{c}_j$ and, subsequently, performing a Fourier transformation

$$\hat{c}_j = \frac{1}{\sqrt{L}} \sum_k e^{-2\pi i k j/L} \hat{c}_k. \tag{2.25}$$

Then, the ground-state wave function factorizes since the Hamiltonian decouples in momentum space

$$\tilde{H} = (L-1)E_n^- + E_{n+1}^- + 2B_n^- D_{n+1}^- \sum_d t_d \sum_k \cos\left(\frac{2\pi k d}{L}\right) \hat{c}_k^{\dagger}\hat{c}_k. \tag{2.26}$$

This model is equivalent to free fermionic particles with hopping amplitudes given by t_d. In momentum space, a single fermion will occupy the mode with the lowest energy. Thus, the total energy of the single particle and therefore the total energy of an additional excitation on top of the nth Mott insulator in the JCH model is given by

$$E(nL+1) = (L-1)E_n^- + E_{n+1}^- + F_n(k), \quad F(k) = 2B_n^- D_{n+1}^- \sum_d t_d \sum_k \cos\left(\frac{2\pi k d}{L}\right) \tag{2.27}$$

and the momentum mode k is chosen such that $F_n(k)$ is minimal. It should be mentioned that the product $B_n^- D_{n+1}^-$ is positive for any (Δ, ω, n), so the momentum mode is purely determined by the minimum of $\sum_d t_d \cos(2\pi k d/L)$.

To calculate the energy for a hole in the nth Mott insulator, we follow exactly the same route. Now, the state $|\Downarrow\rangle$ is associated with $|-, n-1\rangle$ and $|\Uparrow\rangle$ with $|-, n\rangle$. The hopping operators act as

$$\hat{a}_{j+1}^{\dagger}\hat{a}_j |\Downarrow\rangle_{j+1} |\Uparrow\rangle_j = B_{n-1}^- D_n^- |\Uparrow\rangle_{j+1} |\Downarrow\rangle_j \tag{2.28}$$

and the effective Hamiltonian is given by

$$\tilde{H} = E_{n-1}^{-} \sum_j \tilde{\sigma}_j^{-} \tilde{\sigma}_j^{+} + E_n^{-} \sum_j \tilde{\sigma}_j^{+} \tilde{\sigma}_j^{-} + B_{n-1}^{-} D_n^{-} \sum_d \sum_j (\tilde{\sigma}_{j+d}^{+} \tilde{\sigma}_j^{-} + \tilde{\sigma}_j^{+} \tilde{\sigma}_{j+d}^{-}). \tag{2.29}$$

Here the magnetization consists of one spin pointing downward. Again, after making use of a Jordan-Wigner transformation and, subsequently, a Fourier transformation, the energy of a single hole is given by

$$E(nL-1) = (L-1)E_n^{-} + E_{n-1}^{-} + F_{n-1}(k), \tag{2.30}$$

where the same condition holds for k. Now, putting the calculated energies (2.27) and (2.30) together, the chemical potentials and therefore the boundaries of the nth Mott-insulating lobe can easily be derived. They are given by

$$\begin{aligned} \mu_n^{+} &= E_{n+1}^{-} - E_n^{-} + 2B_n^{-} D_{n+1}^{-} \sum_d t_d \cos\left(\frac{2\pi k' d}{L}\right), \\ \mu_n^{-} &= E_n^{-} - E_{n-1}^{-} - 2B_{n-1}^{-} D_n^{-} \sum_d t_d \cos\left(\frac{2\pi k'' d}{L}\right), \end{aligned} \tag{2.31}$$

where k' (k'') is chosen such that $\mu_n^{+}(k')$ ($\mu_n^{-}(k'')$) is minimal (maximal.)

Fermion approximation

In this section, we will apply an even simpler but not that obvious approximation. When looking at the JCH Hamiltonian, it can be seen that all terms are quadratic. These kinds of models are in general suited for an exact solution by means of a Fourier transform. The problem at this point is, however, that the commutation relations of spin operator $\sigma_j^{\pm}$ are not as simple as that of bosons or fermions. This limits the applicability of a Fourier transform since the operators in momentum space will not obey the same commutation relation as in real space. The usual step of a prior Jordan-Wigner transformation, transforming the spin operators to proper fermionic operators, is not applicable in this case since the interaction part is linear in the spin operators, so the Jordan-Wigner factors do not cancel out. Thus, both transformations cannot be carried out exactly without increasing the descriptional complexity of the problem. Nevertheless, the Hamiltonian can be diagonalized by a Fourier transform in an approximate way.

As said above, all modes decouple at $t_d = 0$. For this reason, the spin operators are in this limit equivalent to fermionic operators. If we assume that this replacement also holds for small values of t_d, the JCH model can be rewritten in a fermionic approximation

$$\hat{H} = \omega \sum_j \hat{a}_j^{\dagger} \hat{a}_j + \Delta \sum_j \hat{c}_j^{\dagger} \hat{c}_j + g \sum_j (\hat{c}_j^{\dagger} \hat{a}_j + \hat{a}_j^{\dagger} \hat{c}_j) + \sum_d t_d \sum_j (\hat{a}_j^{\dagger} \hat{a}_{j+d} + \hat{a}_{j+d}^{\dagger} \hat{a}_j). \tag{2.32}$$

Here the spin operators σ^+ (σ^-) are replaced by fermionic operators $\hat{c}^\dagger$ ($\hat{c}$). Within this approximation, a Fourier transform of both the bosonic and fermionic degree of freedom can be easily accomplished via

$$\hat{a}_j = \frac{1}{\sqrt{L}} \sum_k e^{-2\pi i k l/L} \hat{a}_k, \quad \hat{c}_j = \frac{1}{\sqrt{L}} \sum_k e^{-2\pi i k l/L} \hat{c}_k. \tag{2.33}$$

Here $\hat{a}_k$ and $\hat{c}_k$ are operators in momentum space. Doing so, the JCH Hamiltonian transforms to that of uncoupled JC systems

$$\hat{H} = \sum_k \omega_k \hat{a}_k^\dagger \hat{a}_k + \Delta \sum_k \hat{c}_k^\dagger \hat{c}_k + g \sum_k (\hat{c}_k^\dagger \hat{a}_k + \hat{a}_k^\dagger \hat{c}_k), \quad \omega_k = \omega + 2 \sum_d t_d \cos\left(2\pi \frac{kd}{L}\right). \tag{2.34}$$

The ground state in any mode is given by the JC ground state with frequency ω_k. The energy of mode k with n excitations is

$$E_k^n = (1 - \delta_{n0}) \left(n\omega_k + \frac{\Delta - \omega_k}{2} - \frac{1}{2}\sqrt{(\Delta - \omega_k)^2 + 4ng^2} \right). \tag{2.35}$$

Since the total number of excitations in the system

$$\hat{N} = \sum_k (\hat{a}_j^\dagger \hat{a}_j + \sigma_j^+ \sigma_j^-) \to \sum_k (\hat{a}_k^\dagger \hat{a} k + \hat{c}_k^\dagger \hat{c}_k) \tag{2.36}$$

commutes with the Hamiltonian (2.34), a common basis can be chosen. Thus, the full solution of Eq. (2.34) for a fixed total number of excitations $N = nL$ is given by the distribution $\vec{n} = \{n_{k_1}, n_{k_2}, \ldots\}$ of N excitations on L momentum modes with minimal energy $E_N[\vec{n}] = \sum_k E_k^{n_k}$ together with the constraint $\sum_k n_k = N$. Note that the number of momentum modes L is equal to the number of sites.

When constructing the phase diagram, the energy of $N = nL + 1$, $N = nL$, $N = nL - 1$ excitations needs to be calculated. In the limit of vanishing hopping ($t = 0$) and for commensurate filling, i.e., $N = nL$, the distribution of occupation numbers, which has the lowest energy, is again $\vec{n} = \{n, n, \ldots, n\}$. This corresponds to a MI state with an integer number of excitations on every lattice sites. The phase is gapped with a particle-hole gap. When t is increased, the ground state remains the same, but the gap closes and a quantum phase transition occurs from the MI to the SF phase at some critical value of t. The only remaining thing in order to calculate the chemical potentials is to find the momentum mode, where the addition (removal) of an excitation gives the maximum (minimum) reduction (increase) in the total energy. This yields

$$\mu_n^+ = E_{k'}^{n+1} - E_{k'}^n, \quad \mu_n^- = E_k^n - E_k^{n-1}, \tag{2.37}$$

where k' (k) is chosen such that $\mu_n^+(k')$ ($\mu_n^-(k)$) is minimal (maximal). The values of k and k' depend mainly on the sign of the hopping amplitudes t_d.

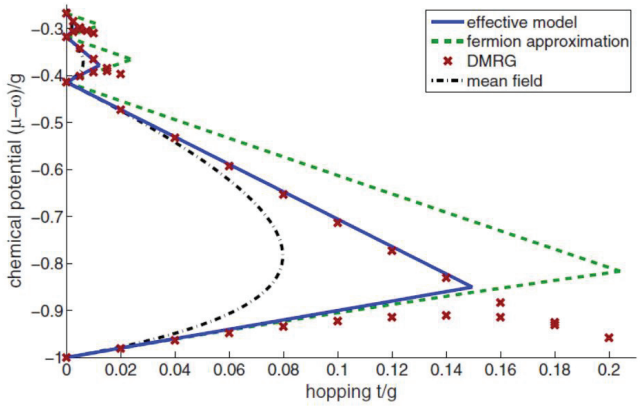

Fig. 2.3: (Color online) Comparison of ground-state phase diagram of the 1D JCH model obtained by DMRG as well as mean-field results (dot-dashed line) with the prediction from our approaches (solid line: strong-coupling effective Hamiltonian; dashed line: fermion approximation) for $\Delta = \omega = 1$ and $g = 1$. Taking into account the simplicity of both approaches, the agreement with the DMRG data is rather good while the mean-field predictions are rather poor, as expected for 1D systems. The critical hopping amplitudes estimated from the DMRG data agree surprisingly well with those predicted within the fermion approximation, although the shape of the Mott lobe is different.

2.2.2 Application to specific realizations of the JCH model

After having introduced the two approaches used in previous section, we will apply them to the case of the simple JCH model with positive effective-mass and nearest-neighbor hopping and to a modified model describing the physics of a linear ion chain. The case of the simple JCH model essentially serves as a testing ground for our approximation schemes, including a comparison of the analytic results to numerical data from density-matrix renormalization-group (DMRG) and mean-field calculations. Later on, the generalized JCHM will be treated by both approximations giving analytic results for the phase diagram in a wide range of parameters.

2.2.3 JCH model with positive effective-mass and nearest-neighbor hopping

The Hamiltonian of the JCH model in this case is given by

$$\hat{H} = \omega \sum_j \hat{a}_j^\dagger \hat{a}_j + \Delta \sum_j \sigma_j^+ \sigma_j^- + g \sum_j (\sigma_j^+ \hat{a}_j + \hat{a}_j^\dagger \sigma_j^-) - t \sum_j (\hat{a}_j^\dagger \hat{a}_{j+1} + \hat{a}_{j+1}^\dagger \hat{a}_j), \tag{2.38}$$

where the hopping amplitudes satisfy $t_d = -t\delta_{d1}$.

For the calculation of the chemical potentials, we first have to determine the momentum modes k' and k'', which contribute to the energy. For $\Delta = \omega$, the

coefficients are $\alpha_n^{\pm} = \beta_n^{\pm} = \frac{1}{\sqrt{2}}$ and therefore

$$B_n^- = D_{n+1}^- \begin{cases} \frac{\sqrt{n}+\sqrt{n+1}}{2}, & n > 0 \\ -\frac{1}{\sqrt{2}}, & n = 0. \end{cases} \tag{2.39}$$

Within this, the function $F_n(k)$ is given by

$$F_n(k) = -t\frac{\left(\sqrt{n}+\sqrt{n+1}\right)^2}{2-\delta_{n0}}\cos\left(2\pi\frac{k}{L}\right). \tag{2.40}$$

Both chemical potentials have its minimum (maximum) at $k = 0$. Putting everything together, the phase boundaries of the nth Mott lobe, calculated using the effective strong-coupling model read as

$$\mu_n^+ = \omega - \frac{1}{2}\chi_{n+1} + \frac{1-\delta_{n0}}{2}\chi_n - t\frac{\left(\sqrt{n}+\sqrt{n+1}\right)^2}{2-\delta_{n0}}, \tag{2.41}$$

for any n and

$$\mu_n^- = \omega - \frac{1}{2}\chi_n + \frac{1-\delta_{n1}}{2}\chi_{n-1} - t\frac{\left(\sqrt{n}+\sqrt{n+1}\right)^2}{2-\delta_{n1}}, \tag{2.42}$$

for $n > 0$. This allows for determination of the critical hopping amplitude t_{crit}, where $\mu_n^+ = \mu_n^-$, which is given by

$$\frac{t_{\mathrm{crit}}}{g} = 2\frac{2\sqrt{n}-\sqrt{n+1}-\sqrt{n-1}}{(\sqrt{n}+\sqrt{n+1})^2+(\sqrt{n+\delta_{n1}}+\sqrt{n-1})^2}. \tag{2.43}$$

Second, we apply the second approximation to this model. With the given system parameters, the momentum-dependent phonon energies are given by $\omega_k = \omega - 2t\cos(2\pi k/L))$ and the energy in the kth momentum mode for a given filling n reads as

$$E_k^n = (1-\delta_{n0})\left(n\omega - 2nt\cos\left(2\pi\frac{k}{L}\right) + t\cos\left(2\pi\frac{k}{L}\right) - \sqrt{t^2\cos^2\left(2\pi\frac{k}{L}\right)+ng^2}\right). \tag{2.44}$$

Finally, the momentum modes k' (k) which minimize (maximize) the chemical potentials need to be found. In the present case $t < 0$, these are $k' = 0$ and $k = L/2$. Thus, the resulting chemical potentials are

$$\mu_n^+ - \omega = -2t + t\delta_{n0} - \sqrt{t^2+(n+1)g^2} + (1-\delta_{n0})\sqrt{t^2+ng^2}, \tag{2.45}$$

for any n and

$$\mu_n^- - \omega = 2t - t\delta_{n1} - \sqrt{t^2+ng^2} + (1-\delta_{n1})\sqrt{t^2+(n-1)g^2}, \tag{2.46}$$

for $n > 0$. A closed form for the critical hopping can be found but is rather lengthy and will therefore be skipped.

We now compare our analytic results to various numerical calculations. Figure (2.3) shows both analytic approximations along with numerical data from DMRG [14] and mean-field [10] calculations, where the modified hopping amplitude in the mean-field Hamiltonian evaluates as $\tilde{J} = t$. From the figure, it can be seen that the effective model gives a much better agreement with the numerical DMRG data, especially, the slopes of the lobes agree perfectly at small hopping. The fermion approximation overestimates the size of the Mott lobe. In particular, while the lower boundaries are rather well reproduced, the upper boundaries have the wrong slope. Surprisingly though the critical hopping amplitudes seem to agree better with the DMRG data than the results obtained from the effective strong-coupling Hamiltonians. Although the fermion approximation is quantitatively worse than the effective strong-coupling Hamiltonians, it provides a simple approximative solution to the JCH model beyond the mean-field level, which has the advantage of giving a closed form of the ground state.

In summary, we have presented two simple analytic approximations to the phase diagram of the Jaynes-Cummings-Hubbard model. The first approximation describes the particle-hole excitations in the vicinity of the Mott-insulator to superfluid transition for a specific filling by a simple effective spin model, which generalizes the know results to arbitrary short range hopping. The second approximation treats the spins as fermions, which allows for a simple solution of the model by means of a Fourier transformation. A comparison of both methods to DMRG and mean-field data shows reasonable agreement to the numerics. The approximative description by effective strong-coupling Hamiltonians makes very good quantitative predictions for the phase boundaries of the Mott insulating lobes for small hopping and can be straightforwardly written down up to second order. The fermion approximation also performs very well for the lower boundaries but is less accurate for the upper ones. It does make, however, rather good predictions for the critical hopping at commensurate fillings and has the advantage of giving a closed form for the ground state in the whole parameter regime. Altogether, both methods provide quite reasonable results for the phase boundaries compared to numerical results from DMRG simulations.

2.3 Superexchange Magnetism. Jaynes-Cummings-Hubbard interaction between V-type level structure

In this chapter is presented a system for the simulation of Heisenberg models with spins $s = \frac{1}{2}$ and $s = 1$ with a linear crystal of trapped ions. The underlying idea is based on the mapping of the Jaynes-Cummings-Hubbard model in a V-type three-level system (JCHv) to an effective Heisenberg spin model using a linear ion crystal. The two-bosonic species in the JCHv model are represented by the two radial local phonon modes, while the long-range phonon hopping dynamics appear naturally due to the interaction. We shall show that the laser beams in two orthogonal directions tuned near the respective red sideband transition can be used to provide the JC couplings between the three internal states of the ion and the two radial phonon species. Another possible realization of the JCHv

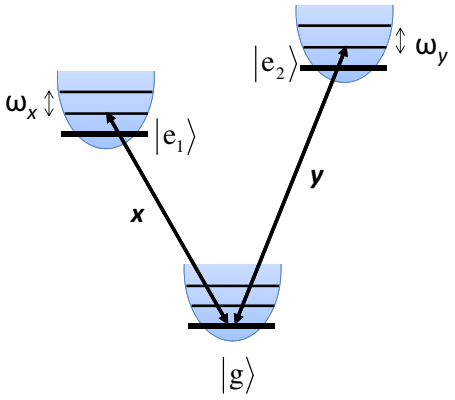

Fig. 2.4: (Color online) The V-type three-level system consists of the ground state $|g\rangle$ and two metastable excited states $|e_1\rangle$, $|e_2\rangle$. Two laser beams with properly chosen frequencies and polarizations create the JC couplings between the V-type level structure and the two radial x and y phonon species.

model is based on an oscillating magnetic field gradient, where the JC couplings are controlled by the magnetic gradient. When the phonon hopping dynamics is suppressed the second-order virtual processes can induce an effective Heisenberg exchange between the localized polaritonic excitations in different lattice sites. The nature of the conserved polariton quasiparticles can be transformed into atomic or phononic excitations by controlling the laser intensity and detuning. We will show that in the strongly coupled regime the Heisenberg spin models with $s = \frac{1}{2}$ and $s = 1$ can be realized. As for the ultracold two-component atoms in an optical lattice [23, 24], we show that a higher-order virtual phonon hopping processes in both radial directions mediate the spin-spin interactions. We calculate the respective tunneling matrix elements in the case of anisotropic spin-phonon couplings and detuned JC interaction. We consider two cases. (i) In the case of one excitation per lattice site the corresponding spin dynamics is described by the anisotropic XXZ Heisenberg model in the presence of external effective magnetic field. We show that the anisotropy in the system can be controlled by the external parameters such as the laser intensity and the detuning, which allows us to realize an easy-axis or easy-plane ferromagnet. (ii) For the two excitations per lattice site, the underlying lowest energy physics of the JCHv model is described by an effective spin $s = 1$ system. We show that the spin-spin interaction induced by the second-order hopping events is governed by the highly anisotropic spin $s = 1$ Heisenberg model. Such a spin-1 model can serve as a test bed to explore a novel topological orders.

2.3.1 Jaynes-Cummings-Hubbard Model in a V-Shape System

Trapped ions are a suitable system to implement JC interaction in a two-level system by driving a red-sideband transition with an external laser [5, 25] or

a magnetic-field gradient [26]. The two-level system typically consists of two metastable levels. The JC interaction can be created by a direct two-photon optical transition, as in the $4s^2S_{1/2} - 3d^2D_{5/2}$ transition in $^{40}Ca^+$ ion or alternatively one can use radio-frequency, or hyper-fine levels where the JC coupling is driven by Raman-type interaction. Here we consider an atomic V-type system, which consists of a ground state $|g\rangle$ and two metastable levels $|e_1\rangle$ and $|e_2\rangle$ with transition frequencies $\omega_{e,1}$ and $\omega_{e,2}$, which are depicted in Fig. 2.4. For example, such a level structure occurs in $^{40}Ca^+$ ion with ground state $|g\rangle = |S_{1/2}, m_J = -1/2\rangle$ and two excited levels $|e_1\rangle = |D_{5/2}, m_J = -5/2\rangle$ and $|e_2\rangle = |D_{5/2}, m_J = -3/2\rangle$. We assume that the linear ion crystal interacts with two laser beams along the two orthogonal radial directions with laser frequencies $\omega_{\mathrm{L},x}$ and $\omega_{\mathrm{L},y}$. The Hamiltonian describing the laser-ion interaction after making the optical rotating-wave approximation is given by [5, 25]

$$\begin{aligned}\hat{H} &= \hat{H}_{xy} + \Omega_x \sum_j \{|e_{1,j}\rangle\langle g_j| e^{i\eta_x(\hat{a}^\dagger_{x,j} + \hat{a}_{x,j}) - i\delta_x t} + \text{H.c.}\} \\ &\quad + \Omega_y \sum_j \{|e_{2,j}\rangle\langle g_j| e^{i\eta_y(\hat{a}^\dagger_{y,j} + \hat{a}_{y,j}) - i\delta_y t} + \text{H.c.}\}. \end{aligned} \tag{2.47}$$

Here Ω_β is the Rabi frequency and $\eta_\beta = |\vec{k}_\beta|/\sqrt{2m\omega_\beta}$ is the Lamb-Dicke parameters along the β axis, with $\vec{k}_\beta$ being the laser wave vector. $\delta_x = \omega_{\mathrm{L},x} - \omega_{e,1}$, $\delta_y = \omega_{\mathrm{L},y} - \omega_{e,2}$ are the laser detunings. We assume that the laser frequencies are tuned near the motional red sideband along the two radial directions,

$$\omega_{\mathrm{L},x} = \omega_{e,1} - \omega_0 - (\omega_x - \Delta_x), \quad \omega_{\mathrm{L},y} = \omega_{e,2} - \omega_0 - (\omega_y - \Delta_y), \tag{2.48}$$

where the conditions $\Delta_\beta, \omega_0 \ll \omega_\beta, \omega_{e,1(2)}$ are satisfied. The detunings $\Delta_\beta = \Delta - \delta\omega_\beta$ introduce effective trapping frequencies along the two orthogonal directions, while the detuning ω_0 introduces an effective spin frequency. The Hamiltonian (2.47) after transforming into a rotating frame with respect to

$$\hat{U}(t) = \exp\Big[i \sum_j \{\sum_{a=1}^{2} \omega_0 |e_{a,j}\rangle\langle e_{a,j}| - \sum_\beta (\omega_\beta - \Delta_\beta)\hat{a}^\dagger_{\beta,j}\hat{a}_{\beta,j}\} t\Big], \tag{2.49}$$

in the Lamb-Dike limit and the vibration rotating-wave approximation, reads

$$\begin{aligned}\hat{H}_{\mathrm{JCHv}} &= \hat{H}_{\mathrm{JC}} + \hat{H}_{\mathrm{b}}, \\ \hat{H}_{\mathrm{JC}} &= \sum_j \Big[\sum_\beta \Delta_{\beta,j} \hat{a}^\dagger_{\beta,j}\hat{a}_{\beta,j} + \omega_0(|e_{1,j}\rangle\langle e_{1,j}| + |e_{2,j}\rangle\langle e_{2,j}|) \\ &\quad + g_x(\hat{a}_{x,j}|e_{1,j}\rangle\langle g_j| + \text{H.c}) + g_y(\hat{a}_{y,j}|e_{2,j}\rangle\langle g_j| + \text{H.c})\Big], \end{aligned} \tag{2.50}$$

where $\hat{H}_{\mathrm{JCHv}} = \hat{U}^\dagger \hat{H} \hat{U} - i\hat{U}^\dagger \partial_t \hat{U}$. Here $g_\beta = \eta_\beta \Omega_\beta$ are the spin-phonon couplings and $\Delta_{\beta,j} = \Delta + \delta\omega_{\beta,j} - \delta\omega_\beta$. The term $\hat{H}_{\mathrm{JC}}$ describes the JC model in a V-type atomic system, where the first two terms correspond to the effective

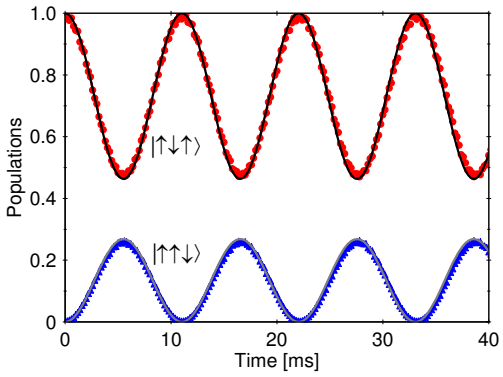

Fig. 2.5: (Color online) Superexchange interaction in a system of three ions couples the states $|\uparrow\downarrow\uparrow\rangle$, $|\uparrow\uparrow\downarrow\rangle$ and $|\downarrow\uparrow\uparrow\rangle$ according to the effective Hamiltonian (2.58). We compare the probability of finding the system in states $|\uparrow\downarrow\uparrow\rangle$ and $|\uparrow\uparrow\downarrow\rangle$ computed by the effective Hamiltonian (2.58) (red circles and blue triangles) and Hamiltonian (2.50) (solid lines). The population of state $|\downarrow\uparrow\uparrow\rangle$ is indistinguishable from that of $|\uparrow\uparrow\downarrow\rangle$ and it is not shown in the figure. We assume axial trap frequency $\omega_z/2\pi = 120$ kHz and aspect ratios $\omega_y/\omega_x = 1.8$ and $\omega_y/\omega_z = 100$. The parameters are set to $t^x_{1,2}/2\pi = 0.86$ kHz, $t^y_{1,2}/2\pi = 0.48$ kHz, $t^x_{1,3}/2\pi = 0.1$ kHz, $t^y_{1,3}/2\pi = 0.06$ kHz and $g_x/2\pi = 19$ kHz, $g_y/2\pi = 20$ kHz, $\delta/2\pi = -0.22$ kHz, which ensure that the system is in the strong-coupling regime. The phonon detuning is set to $\delta\omega_\beta = \omega_{\beta,1}$, such that we have $\delta\omega_{x,1} - \delta\omega_{x,2} = 2\pi \times 8$ Hz and $\delta\omega_{y,1} - \delta\omega_{y,2} = 2\pi \times 4$ Hz.

energies of the local phonons and ions, while the last two terms describe the couplings between the internal levels and the x and y local phonons. The term $\hat{H}_\mathrm{b}$ describes the nonlocal hopping of the two-phonon species between different lattice sites and allow us direct comparison with the case of two-component ultracold atom gas in an optical lattice. Finally we note that the continuous U(1) symmetry of the Hamiltonian (2.50) associated with the conservation of the total number of excitations is generated by the excitation operator $\hat{N} = \sum_j \hat{N}_j$ with $\hat{N}_j = \sum_\beta \hat{a}^\dagger_{\beta,j}\hat{a}_{\beta,j} + \sum_{a=1,2} |e_{a,j}\rangle\langle e_{a,j}|$.

2.3.2 Energy Scales

Similar to the two-level JCH model, the three-level JCHv model is not generally amenable to an exact solution. The particular limit, which we study in the present paper is the strong-coupling regime $g_\beta \gg t^\beta_{i,j}$, which allows us to diagonalize the term $\hat{H}_\mathrm{JC}$ in (2.50) and then treat the hopping term $\hat{H}_\mathrm{b}$ as a perturbation. Because the number of excitations $\hat{N}_j$ in each site j is a constant of motion the Hilbert space is decomposed in subspaces with well-defined numbers of excitations. In the following we consider the homogeneous limit $\Delta_{\beta,j} \approx \Delta$ ($\Delta \gg \delta\omega_{\beta,j} - \delta\omega_\beta$) but in the numerical simulations we take into account the finite-size effects. For null excitations the ground state of $\hat{H}_\mathrm{JC}$ is nondegenerate

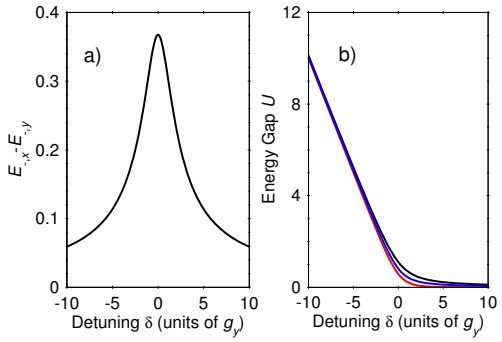

Fig. 2.6: (Color online) a) The energy splitting $E_{-,x} - E_{-,y}$ versus δ. The spin-phonon couplings satisfy $g_y = \sqrt{2.5} g_x$. b) The energy difference $U = E_{\rm exc} - 2E_{-,y}$, versus the detuning δ. Here $E_{\rm exc}$ is the energy for the state with two excitations in one site and none in another. The three curves are the energy differences with respect to the three low-energy states.

and given by $|g, 0_x, 0_y\rangle$ with $E_0 = 0$. Here the state $|l, n_x, n_y\rangle$ $(l = g, e_1, e_2)$ describes an ion in the internal state $|l\rangle$ together with n_x and n_y local phonons. For one excitation per lattice site (unit filling factor) the energy spectrum is

$$E_{\pm,\beta} = \Delta + \frac{\delta}{2} \pm \sqrt{\frac{\delta^2}{4} + g_\beta^2}, \tag{2.51}$$

with $\delta = \omega_0 - \Delta$. The dressed eigenstates corresponding to the two lowest eigenfrequencies are

$$\begin{aligned} |\uparrow\rangle &= |-\rangle_x = \cos\theta_x |g, 1_x, 0_y\rangle - \sin\theta_x |e_1, 0_x, 0_y\rangle, \\ |\downarrow\rangle &= |-\rangle_y = \cos\theta_y |g, 0_x, 1_y\rangle - \sin\theta_y |e_2, 0_x, 0_y\rangle, \end{aligned} \tag{2.52}$$

where the mixing angle is defined by

$$\theta_\beta = \tan^{-1} \frac{2g_\beta}{\delta + \sqrt{\delta^2 + 4g_\beta^2}}. \tag{2.53}$$

In the strong-coupling regime the energy splitting $E_{+,\beta} - E_{-,\beta}$ is large compared to any other energy scale in the system; hence the two low energy states (2.52) can be treated as an $s = \frac{1}{2}$ effective spin system with the energy difference shown in Fig. 2.6(a). The two states become degenerate for $g_x = g_y$, while for unequal couplings there is a finite energy difference, which tends to zero for large detuning δ. The eigenstates (2.52) describe the polaritonic excitation in the system caused by the strong spin-phonon coupling. The nature of the polaritonic excitations can be controlled by the external parameters, such as laser intensity and detuning. For instance, in the limit of large negative detuning ($|\delta| \gg g_\beta$) the polaritons are transformed into atomic excitations, $|\uparrow\rangle \approx |e_1, 0_x, 0_y\rangle$, $|\downarrow\rangle \approx |e_2, 0_x, 0_y\rangle$, while for large positive detuning ($\delta \gg g_\beta$) the excitations become purely phononic, $|\uparrow\rangle \approx |g, 1_x, 0_y\rangle$ and $|\downarrow\rangle \approx |g, 0_x, 1_y\rangle$.

We can extend the discussion to the case of integer filling of two excitations per site. In that case the lowest energy Hilbert space of a lattice site consists of three eigenstates given by

$$\begin{aligned}
|1\rangle &= \cos\theta_{2,x}|g,2_x,0_y\rangle - \sin\theta_{2,x}|e_1,1_x,0_y\rangle,\\
|0\rangle &= \cos\varphi|g,1_x,1_y\rangle - \sin\varphi(\sin\zeta|e_1,0_x,1_y\rangle + \cos\zeta|e_2,1_x,0_y\rangle),\\
|-1\rangle &= \cos\theta_{2,y}|g,0_x,2_y\rangle - \sin\theta_{2,y}|e_2,0_x,1_y\rangle,
\end{aligned} \tag{2.54}$$

where the mixing angles are defined as

$$\theta_{2,\beta} = \tan^{-1}\frac{\sqrt{2}g_\beta}{\frac{\delta}{2}+\sqrt{2g_\beta^2+\frac{\delta^2}{4}}}, \quad \varphi = \tan^{-1}\frac{\sqrt{g_x^2+g_y^2}}{\frac{\delta}{2}+\sqrt{g_x^2+g_y^2+\frac{\delta^2}{4}}}, \quad \zeta = \tan^{-1}\frac{g_x}{g_y}. \tag{2.55}$$

The corresponding energies of the states (2.54) are

$$\begin{aligned}
E_1 &= 2\Delta + \frac{\delta}{2} - \sqrt{2g_x^2+\frac{\delta^2}{4}},\\
E_0 &= 2\Delta + \frac{\delta}{2} - \sqrt{g_x^2+g_y^2+\frac{\delta^2}{4}},\\
E_{-1} &= 2\Delta + \frac{\delta}{2} - \sqrt{2g_y^2+\frac{\delta^2}{4}},
\end{aligned} \tag{2.56}$$

respectively. By using the same arguments as above, we conclude that in the strong-coupling regime the eigenstates (2.54) represent an effective spin $s = 1$ system. Again, the nature of the polaritonic excitations can be transformed into various kinds depending on the spin-phonon couplings g_β and the detuning δ. For large negative detuning ($|\delta| \gg g_\beta$) the spin states contain one atomic excitation and one phonon excitation, $|1\rangle \approx |e_1,1_x,0_y\rangle$, $|0\rangle \approx (\sin\zeta|e_1,0_x,1_y\rangle + \cos\zeta|e_2,1_x,0_y\rangle)/\sqrt{2}$ and $|-1\rangle \approx |e_2,0_x,1_y\rangle$, while in the limit $\delta \gg g_\beta$ the atomic transitions are suppressed so that the spin states contain only two phononic excitations, $|1\rangle \approx |g,2_x,0_y\rangle$, $|0\rangle \approx |g,1_x,1_y\rangle$ and $|-1\rangle \approx |g,0_x,2_y\rangle$. In general for n excitations the low energy manifold consists of $n+1$ eigenstates, which make it possible to simulate spin $\frac{1}{2}n$ particles [28].

Now we examine the effect of the finite hopping amplitudes $t_{i,j}^\beta$. First, we note that the energy spectrum of $\hat{H}_{\rm JC}$ displays a particle-hole gap, which implies that there exists an energy difference U between the states with n excitations per site and the states with $n+1$ excitations in one site and $n-1$ in another [29]. In Fig. 2.6(b), we plot these energy differences for $n = 1$. For large positive detuning the energy gap becomes vanishingly small, while in the limit of large negative detuning the gap scales as $U \sim |\delta|$ [30].

As long as the energy gap is much higher than the hopping strength $t_{i,j}^\beta$ ($U \gg t_{i,j}^\beta$) the excitations are strongly localized in each site, so that the system is in the Mott insulator phase. In this regime a single excitation jump changes the total on-site polaritonic excitations and therefore such processes are highly

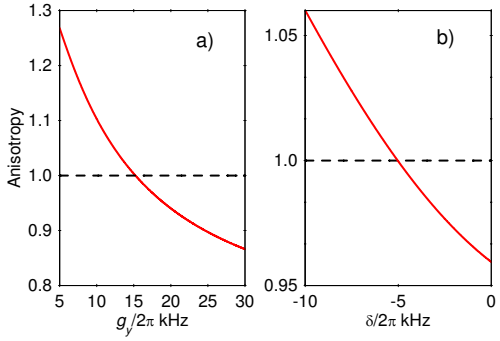

Fig. 2.7: (Color online) The anisotropy $\lambda_{1,2} = J^z_{1,2}/J^{xy}_{1,2}$ in a system of three ions. a) The anisotropy as a function of g_y. The parameter are set to $g_x/2\pi = 12$ kHz, and $\delta/2\pi = -0.5$ kHz. b) We fixed the coupling $g_y/2\pi = 18$ kHz and vary the detuning δ. The hopping amplitudes are set to $t^x_{1,2}/2\pi = 0.5$ kHz, $t^y_{1,2}/2\pi = 0.7$ kHz.

suppressed. Although the hopping events are frozen, the spin degrees of freedom can be coupled by an effective superexchange interaction. Indeed, the next high-lying states containing $n+1$ or $n-1$ excitations can be reached as virtual intermediate states in second-order hopping processes. Such second-order hopping events mediate the spin-spin interaction between the effective spin systems on different sites and can be studied using the expression

$$(\hat{H}_{\rm eff})_{r_j r'_k, d_j d'_k} = (\hat{H}_{\rm JC})_{r_j r'_k, d_j d'_k} + \frac{1}{2}\sum_{\chi}\langle r_j, r'_k|\hat{H}_{\rm b}|\chi\rangle\langle\chi|\hat{H}_{\rm b}|d_j, d'_k\rangle\left(\frac{1}{E_{r_j r'_k} - E_\chi} + \frac{1}{E_{d_j d'_k} - E_\chi}\right). \tag{2.57}$$

The matrix elements of the effective Hamiltonian (2.57) describe the coupling between the spin states $|r_j, r'_k\rangle \leftrightarrow |d_j, d'_k\rangle$ on sites j and k with energies E_{r_j,r'_k} and E_{d_j,d'_k}, respectively, created via hopping processes to state $|\chi\rangle$ with energy E_χ which contains $n+1$ excitations in one site, and $n-1$ in another. In the following we will consider only the spin-$\frac{1}{2}$ and spin-1 models; then the spin indices take values $r, d = \uparrow, \downarrow$ for $s = \frac{1}{2}$ or $r, d = 1, 0, -1$ for $s = 1$.

2.3.3 Spin-$\frac{1}{2}$ Anisotropic XXZ Heisenberg model

A second-order hopping process to a state with two excitations in one site and none in another creates an effective spin-spin interaction between spin-$\frac{1}{2}$ systems on different lattice sites. By calculating the matrix elements in Eq. (2.57) we find that the resulting spin dynamics is described by the anisotropic XXZ Heisenberg Hamiltonian in the presence of external magnetic field,

$$\hat{H}_{\rm eff} = \sum_{j<k} K^{xy}_{j,k}(\sigma^x_j\sigma^x_k + \sigma^y_j\sigma^y_k) + \sum_{j<k} K^z_{j,k}\sigma^z_j\sigma^z_k + \sum_j H_j\sigma^z_j, \tag{2.58}$$

where $\sigma_j^x = (|\uparrow_j\rangle\langle\downarrow_j| + \text{H.c})$, $\sigma_j^y = -i(|\uparrow_j\rangle\langle\downarrow_j| - \text{H.c})$ and $\sigma_j^z = |\uparrow_j\rangle\langle\uparrow_j| - |\downarrow_j\rangle\langle\downarrow_j|$ denote the corresponding spin operators of the system. The couplings in Eq. (2.58) derived by second-order perturbation theory in the phonon hopping are given by

$$
\begin{aligned}
K_{j,k}^{xy} &= -t_{j,k}^x t_{j,k}^y \frac{2(\tan\zeta + \cot\zeta) + 5}{8g_y(1+\tan\zeta)}, \\
K_{j,k}^{z} &= \frac{(t_{j,k}^x)^2(\tan\zeta - 6\cot\zeta - 4) + (t_{j,k}^y)^2(\cot\zeta - 6\tan\zeta - 4)}{16g_y(1+\tan\zeta)}, \\
H_j &= -\frac{5}{8}\sum_{k\neq j}\Big[\frac{(t_{j,k}^x)^2}{g_x} - \frac{(t_{j,k}^y)^2}{g_y}\Big],
\end{aligned}
\tag{2.59}
$$

where we take $\delta = 0$. Off resonance, the expressions are too long to be presented here. In Fig. 2.5 we show the comparison between the JCHv Hamiltonian (2.50) and the effective spin model (2.58) for a linear ion crystal with three ions. The superexchange couplings cause oscillation between the initial state $|\uparrow\downarrow\uparrow\rangle$ and states $|\uparrow\uparrow\downarrow\rangle$, $|\downarrow\uparrow\uparrow\rangle$ according to the spin model (2.58). Obviously, the effective spin model matches the exact dynamics very accurately.

Finally, we note that the couplings (11.0.6) can be tuned by adjusting the external parameters, namely, the axial trap frequency, the laser field intensities and the detuning. For example, one could control the amount of spin-exchange anisotropy $\lambda_{i,j} = K_{i,j}^z / K_{i,j}^{xy}$ by varying the spin-phonon couplings or the detuning, as demonstrated in Fig. 2.7. This allows us to choose the appropriate parameters such that an easy-axis $\lambda_{i,j} \geq 1$ or easy-plane $\lambda_{i,j} < 1$ ferromagnets are realized.

2.3.4 *Heisenberg-like model with spin-1*

A simple generalization of the interacting spin models with higher spins can be obtained by considering the case of two polaritonic excitations per site. Then the low-lying energy manifold of the Hamiltonian $\hat{H}_{\text{JC}}$ consists of three eigenstates (2.54), which in the following will represent an effective spin $s = 1$ system. The energies of these states are degenerate for $g_x = g_y$, while for unequal couplings $g_x \neq g_y$ the degeneracy is lifted and due to the non-linearity in the energy spectrum, the differences $E_1 - E_0$ and $E_0 - E_{-1}$ are not equidistant. In the strong-coupling regime, the second-order hopping processes to the states with three excitations in one site and one excitation in another create couplings between the states (2.54) at different lattice sites, which allow us to map the original Hamiltonian (2.50) to an effective spin $s = 1$ model. After calculating the matrix elements, we arrive to the following highly anisotropic effective Heisenberg-like

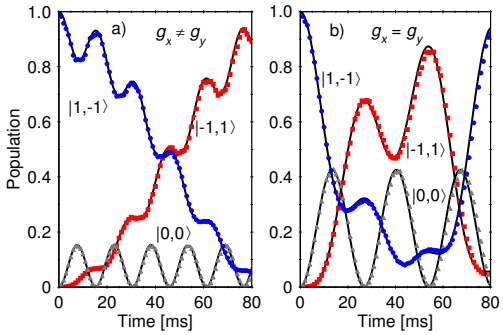

Fig. 2.8: (Color online) Coherent superexchange interaction in a system of two ions. a) We plot the time evolution of states $|1,-1\rangle$ (blue circles), $|-1,1\rangle$ (red squares) and $|0,0\rangle$ (grey triangles) according to the effective Heisenberg-like Hamiltonian (2.60) compared with the JCHv Hamiltonian (2.50) (solid lines). The parameter are set to $g_x/2\pi = 32$ kHz, $g_y/2\pi = 34$ kHz, $\delta = 0$, $t^x_{1,2}/2\pi = 0.1$ kHz and $t^y_{1,2}/2\pi = 0.17$ kHz. b) the same but the spin phonon couplings are set to $g_x/2\pi = 34$ kHz and $g_x = g_y$.

Hamiltonian

$$\begin{aligned}\hat{H}_{\rm eff} &= \sum_j [D_j(\hat{S}^z_j)^2 + B_j\hat{S}^z_j] + \sum_{j<k} J^{xy}_{j,k}(\hat{S}^x_j\hat{S}^x_k + \hat{S}^y_j\hat{S}^y_k) + \sum_{j<k} J^z_{j,k}\hat{S}^z_j\hat{S}^z_k \\ &+ \sum_{j<k} W_{j,k}[\hat{S}^z_j(\hat{S}^z_k)^2 + (\hat{S}^z_j)^2\hat{S}^z_k] + \sum_{j<k} V_{j,k}(\hat{S}^z_j\hat{S}^z_k)^2 \\ &+ \sum_{j<k}[v^{(1)}_{j,k}(\hat{S}^z_j\hat{S}^+_j\hat{S}^-_k\hat{S}^z_k + \text{H.c.}) + v^{(-1)}_{j,k}(\hat{S}^z_j\hat{S}^-_j\hat{S}^+_k\hat{S}^z_k + \text{H.c.})]. \quad (2.60)\end{aligned}$$

Here $\hat{S}^x_j = \frac{1}{2}(\hat{S}^+_j + \hat{S}^-_j)$, $\hat{S}^y_j = \frac{i}{2}(\hat{S}^-_j - \hat{S}^+_j)$, and $\hat{S}^z_j = -i[\hat{S}^x_j, \hat{S}^y_j]$ are the spin $s = 1$ operators at site j. The Hamiltonian (2.60) represents the spin $s = 1$ Heisenberg model with Ising-like and single-ion anisotropy terms [31]. Such an anisotropy of the spin-spin interactions occurs due to the non-equidistance in the energies of spin $s = 1$ system, which reflects into the matrix elements in Eq. (2.57). Indeed, for equal spin-phonon couplings ($g_x = g_y$) the degeneracy of the states (2.54) equalizes the superexchange interaction between the states and the effective Hamiltonian corresponds to the anisotropic ferromagnetic Heisenberg model in the presence of the external magnetic field,

$$\hat{H}_{\rm eff} = \sum_{j<k}\{J^{xy}_{j,k}(\hat{S}^x_j\hat{S}^x_k + \hat{S}^y_j\hat{S}^y_k) + J^z_{j,k}\hat{S}^z_j\hat{S}^z_k\} + \sum_j B_j\hat{S}^z_j. \quad (2.61)$$

In Fig. 2.8 we check the validity of the perturbative approach by comparing the effective Hamiltonian (2.60) with the JCHv Hamiltonian (2.50) in a system of two ions. For unequal couplings, Fig. 2.8(a), the probabilities of finding the system in the states $|1,-1\rangle$, $|0,0\rangle$, and $|-1,1\rangle$ evolve according to Eq. (2.60),

while in the case of equal couplings the spin evolution is governed by the effective Hamiltonian (2.61), Fig. 2.8(b).

The Heisenberg-like model (2.60) presented here can be considered as a generalization of the highly anisotropic spin-1 models recently investigated in a system of ultracold dipolar molecules loaded in a one-dimensional optical lattice [32, 33]. However, to the best of our knowledge, there is no extensive study of the entire phase diagram of our highly anisotropic spin-1 model. As was pointed out in Refs. [34, 35, 36], the gapped phases of any one-dimensional spin model can be classified by its symmetry group. An example of such topological phases is the Haldane phase, which appears in one-dimensional integer-spin chains [37]. The latter are characterized with nonzero excitation gaps and exponentially decaying spin correlation functions. The stability of the Haldane phase crucially depends on the protection of an appropriate set of symmetries. Since our model contains an odd number of spin operators, the only discrete symmetry of the Hamiltonian (2.60) is the rotation by π around the z axis, which takes $\hat{S}_j^{x,y} \to -\hat{S}_j^{x,y}$ and $\hat{S}_j^z \to \hat{S}_j^z$, while the Hamiltonian (2.61) obeys an additional symmetry, which is a rotation by π around the y axis and time-reversal such that $\hat{S}_j^{x,z} \to \hat{S}_j^{x,z}$ and $\hat{S}_j^y \to -\hat{S}_j^y$. As was pointed out in Ref. [32], such spin-1 models may exhibit novel nontrivial topological order.

Although the spin couplings $J_{j,k}^{xy} < 0$ and $J_{j,k}^z < 0$ support ferromagnetic ground-state order we may use the duality between ferro- and antiferromagnetic models, i.e. $\hat{H}_{\rm AF} = -\hat{H}_{\rm F}$ [38]. The latter implies that the highest energy state of the ferromagnetic model is in fact the ground state of the corresponding antiferromagnetic Hamiltonian. The key observation here is that one could switch between both spin models (2.60) and (2.61) by controlling the intensities of the laser beams. For example, the preparation can start by setting $g_x = g_y$ and $t_{j,k}^x \gg t_{j,k}^y$, which implies $|J_{j,k}^z| \gg |J_{j,k}^{xy}|$, and prepare the antiparallel spin configuration. Such a state can be realized by ground-state cooling of the radial vibrational modes and pumping the internal ion states to $|g\rangle_j$. The antiparallel configuration between states $|1\rangle$ and $|-1\rangle$ can be created by noting that for large negative detuning ($|\delta| \gg g_\beta$) the polaritonic nature of the states is reduced to $|1\rangle \approx |e_1, 1_x, 0_y\rangle$ and $|-1\rangle \approx |e_2, 0_x, 1_y\rangle$, see Eq. (2.54). The latter states can be created by π pulses that are resonant with the respective blue-sideband transitions. Once the initial state is prepared one could lower δ and induce unequal spin-phonon couplings. The superexchange interaction can be probed by letting the system to evolve and then measure either the local phonon number or the internal ion population.

In conclusion we have shown that a laser-driven linear ion crystal can realize the JCHv model. We have studied the strongly coupled regime where the JCHv model can be mapped to effective spin models. We have considered the case of one and two polaritonic excitations per site, which represent our effective spin-$\frac{1}{2}$ and spin-1 systems. The underlying mechanism that creates the spin-spin couplings is the Heisenberg superexchange interaction, which can be controlled by the trap frequencies, the laser intensity and the detuning .

3. QUANTUM SIMULATION OF MAGNETIC STRUCTURAL PHASE TRANSITION WITH TRAPPED IONS

In this Chapter we study theoretically the collective and cooperative $E \otimes e$ Jahn-Teller distortion in a system of trapped ions. We show that under suitable conditions the spin ensemble may interact only with a single vibrational mode in each radial direction with U(1) symmetric couplings. Our model is exactly solvable in the thermodynamical limit and it is amenable to be solved by exact numerical diagonalization for a moderate number of ions. We than extend the discussion by focusing on cooperative Jahn-Teller models consisting of an ensemble of effective spins coupled to a set of many vibrational modes. We show that the system undergoes a quantum magnetic structural phase transition which leads to a reordering of particle positions and the formation of a spin-phonon quasicondensate in mesoscopic ion chains. Furthermore, we discuss analytical approximations to the ground-state phase diagram and the collective low-energy excitations of the cooperative Jahn-Teller model. We determine existing of one gapless Goldstone mode and two gapped amplitude modes inside the symmetry-broken phase. We show that trapped ions are ideally suited to study the spontaneous breaking of a continuous symmetry as well as magnetic structural phase transitions in a mesoscopic spin-boson system.

3.1 Implementation of the Collective Jahn-Teller Model with Trapped Ions

Physical systems where bosonic modes interact with electronic or pseudospin degrees of freedom reveal a rich variety of phenomena in condensed matter and atomic physics. A prominent example is given by Jahn-Teller (JT) models [39, 40] which describe the interaction of electronic orbital degrees of freedom with vibrational modes either in molecules or solids. The JT effect is formulated as a structural instability of molecular configurations in electronically degenerate states. In particular, the electron-phonon coupling shifts the potential minima of the nuclei, which leads to position reordering and molecular distortion. Similar to molecular systems, the properties of some crystals are also strongly affected by the JT coupling that induces symmetry breaking and structural phase transitions [41]. Furthermore, the strong electron-phonon coupling in cooperative JT models is an important factor in the description of colossal magneto-resistance in manganites and high T_c-superconductivity [42, 43].

Atomic systems such as ultracold atoms and trapped ions allow experimen-

talists to implement JT models in a controllable way that is not possible in solid-state or molecular setups. This is a motivation to push the current quantum technology toward the realization of Analogical Quantum Simulators (AQS). The latter are controllable systems where interactions between particles can be tuned and quantum states can be accurately prepared and measured with high efficiency. Recently, physical realizations of JT couplings have been discussed in terms of two-level systems coupled to a bimodal cavity [57] and Bose-Einstein condensates in the presence of spatially dependent laser fields [45]. These systems pave the way for studying quantum phenomena such as ground-state entanglement [46, 47] and the creation of artificial non-Abelian magnetic fields [189]. Quantum chaotic behavior in the energy spectrum of multi-spin lattice JT model was discussed in [49].

In this Chapter we propose an implementation of AQS of an infinite range E⊗e Jahn-Teller model based on a trapped ion crystal. The doublet of electronic states is replaced here by two internal metastable states of the ions. The pair of molecular vibrational modes is represented by the two degenerate orthogonal center-of-mass (c.m.) modes, respectively, in the two radial directions. We show that the U(1) symmetric JT spin-phonon coupling can be provided by applying a magnetic field with time-oscillating gradient, which couples the collective spin ensemble to the two orthogonal c.m. modes. The JTD model is quasi-exactly solvable in the sense that the ground state can be found exactly in the thermodynamical limit [50], or even studied by exact numerical diagonalization with a moderate number of ions. The experimental implementation of the JTD model can be used for the controlled study of quantum phenomena such as symmetry breaking, as well as to benchmark trapped ion quantum simulators in a numerically tractable limit.

The E⊗e JTD model possesses a continuous symmetry associated with rotation in the plane orthogonal to the trap axis. There is a critical spin-phonon coupling above which the U(1) symmetry is spontaneously broken and the system evolves into one particular ground state which does not respect the same symmetry as the Hamiltonian. That broken symmetry is associated with a magnetic structural phase transition at zero temperature, where the equilibrium positions of the ions are displaced in an *arbitrary* direction within the radial x-y plane, together with the creation of macroscopic spin coherence. We show that the radial distortion of the ion crystal is accompanied with the creation of density of phonon excitations and macroscopic spin coherence, which is an analog to the normal-to-super-radiance phase transition in the Dicke model [51, 52].

Jahn-Teller E⊗e *spin-phonon coupling*

We describe the interaction of the trapped ion spin ensemble with the collective vibrational modes. Those interactions can be induced either by laser dipole forces or by magnetic field gradients. Here we focus on the latter technique since it naturally implements symmetric couplings in the x-y plane, and it also avoids undesired effects like high-order terms in the Lamb-Dicke expansion and the spontaneous emission decoherence [53, 179]. Let us assume that the ion

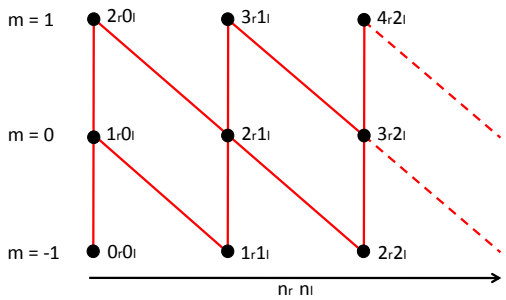

Fig. 3.1: (Color online) Coupling pattern of the relevant ionic and vibrational states $|j,m\rangle|n_r,n_l\rangle$ for j=1. Due to the symmetries in spin-phonon coupling and parity of the Hamiltonian (3.7), the quantum number $n_r - n_l - m$ is preserved and the Hilbert space is decomposed into subspaces of positive (negative) parity. Here we show the non-vanishing couplings (solid lines) between states with $n_r - n_l - m = 1$ and positive parity.

crystal interacts with an oscillating magnetic quadrupole of the form

$$\vec{B}(t;x,y) = Bf(t)(\vec{e}_x x - \vec{e}_y y). \tag{3.1}$$

Such a field can be created in a micro-structured planar ion trap, recently experimentally demonstrated [27], which contains two wires parallel to the linear ion crystal. The magnetic field affects only the radial motion of the ion crystal and thus the motion along the z axis can be safety neglected. We consider a time modulation $f(t) = (\cos\nu_b t + \cos\nu_r t)$ to control the couplings. The magnetic dipole interaction is described by the interaction Hamiltonian

$$\hat{H}_{\rm I} = -\sum_{i=1}^{N} \hat{\vec{\mu}}_i \cdot \vec{B}(t;\delta r_{x,i},\delta r_{y,i}), \tag{3.2}$$

where $\hat{\vec{\mu}}_i = \mu_x\sigma_i^x + \mu_y\sigma_i^y$ is the magnetic dipole moment operator of the ion i, and we assume the condition $\mu_x = \mu_y = \mu$. To control the spin-phonon couplings we choose driving frequencies

$$\nu_{b,r} = (\tilde{\omega}_0 - \omega_0) \pm (\omega_{\rm c.m.} - \omega). \tag{3.3}$$

The goal is to drive spin-flip transitions with detuning ω_0 as well as blue- and red-sideband transitions of the c.m. mode $\omega_{\rm c.m.}$ with detuning $\pm\omega$.

The applied bichromatic magnetic field in x-y plane, establishes Jaynes-Cummings and anti-Jaynes-Cummings interactions, which couple the internal and the motional states of the ions [27]. The Hamiltonian in the interaction

picture with respect to $\hat{H}_0$ is given by

$$\begin{aligned}\hat{H}_{\mathrm{I}} &= -\frac{\mu B}{2}\sum_{i=1}^{N}\delta\hat{r}_{x,i}(t)(\sigma_i^+ e^{\mathrm{i}\tilde{\omega}_0 t}+\sigma_i^- e^{-\mathrm{i}\tilde{\omega}_0 t})f(t)\\ &\quad -\mathrm{i}\frac{\mu B}{2}\sum_{i=1}^{N}\delta\hat{r}_{y,i}(t)(\sigma_i^+ e^{\mathrm{i}\tilde{\omega}_0 t}-\sigma_i^- e^{-\mathrm{i}\tilde{\omega}_0 t})f(t),\end{aligned} \tag{3.4}$$

where $\sigma_i^{\pm}$ are the Pauli spin-flip operators. The displacement operators $\delta\hat{r}_{\alpha,i}$ are recast in terms of collective operators such that we can in a controlled way choose the driving frequencies to pick the radial c.m. mode as the only resonant one. For this, the following set of conditions has to be satisfied,

$$\omega_n \ll \tilde{\omega}_0, \quad \lambda,\omega,\omega_0 \ll \Delta_{\mathrm{c.m.}}, \tag{3.5}$$

where $\lambda = -\mu q_0 B/\sqrt{2}$ is the spin-phonon coupling with $q_0 \equiv q_1^0$ being the size of the c.m. wave packet. The latter conditions ensures the approximation that any vibrational mode but the c.m. one can be neglected in a rotating wave approximation. Consider as an example Zeeman $^{40}Ca^+$ qubits with transition frequency $\tilde{\omega}_0 = 30$ MHz confined in a planar trap with radial trapping frequency $\omega_{\mathrm{r}}/2\pi = 4$ MHz, the first condition in Eq. (3.5) is justified. Assuming crystal with $N = 10$ ions the frequency splitting is approximately $\Delta_{\mathrm{c.m.}}/2\pi \approx 103$ kHz. With current ion-trap technology a spin-phonon coupling of order of $\lambda/2\pi \approx 5$ kHz is achieved by magnetic field gradient $b = 35$ Tm^{-1}, which allowed to neglect the contribution of the off-resonant terms in Eq. (3.4). Under those assumptions we can approximate the interaction Hamiltonian by

$$\begin{aligned}\hat{H}_{\mathrm{I}} &= \frac{\lambda}{\sqrt{2N}}(\hat{a}_x^\dagger e^{\mathrm{i}\omega t}+\hat{a}_x e^{-\mathrm{i}\omega t})(\hat{J}_+ e^{\mathrm{i}\omega_0 t}+e^{-\mathrm{i}\omega_0 t}\hat{J}_-)\\ &\quad +\mathrm{i}\frac{\lambda}{\sqrt{2N}}(\hat{a}_y^\dagger e^{\mathrm{i}\omega t}+\hat{a}_y e^{-\mathrm{i}\omega t})(\hat{J}_+ e^{\mathrm{i}\omega_0 t}-\hat{J}_- e^{-\mathrm{i}\omega_0 t}),\end{aligned} \tag{3.6}$$

Here $\hat{a}_\alpha$ and $\hat{a}_\alpha^\dagger$ correspond to the annihilation and creation operators of the c.m. phonon, respectively. Note that the factor $N^{-1/2}$ in (3.6) appears due to the excitation of the radial c.m. modes, wherein the spin-phonon coupling scales as $b_{j,1}^{\alpha} \sim N^{-1/2}$. Since the ions are equally coupled with the phonons we have introduced the collective spin operators $\hat{J}_+ = \sum_{i=1}^{N}\sigma_i^+$ ($\hat{J}_+^\dagger = \hat{J}_-$) and $\hat{J}_z = 1/2\sum_{i=1}^{N}\sigma_i^z$, which describe the combined ionic pseudospin of length $j = N/2$. The collective spin basis is spanned by the Dicke states $|j,m\rangle$, which are eigenvectors of $\hat{J}^2|j,m\rangle = j(j+1)|j,m\rangle$ and $\hat{J}_z|j,m\rangle = m|j,m\rangle$, respectively. The Hilbert space of the total system is spanned by the states $\{|j,m\rangle\otimes|n_x,n_y\rangle\}$, where $|n_{x,y}\rangle$ is the Fock state with $n_{x,y}$ phonons. After performing the time-dependent unitary transformation $\hat{F} = e^{\mathrm{i}\omega t(\hat{n}_x+\hat{n}_y)+\mathrm{i}\omega_0 t\hat{J}_z}$, such that $\hat{H}_{\mathrm{JTD}} =$

$\hat{F}^\dagger \hat{H}_{\rm I} \hat{F} - {\rm i}\hbar \hat{F}^\dagger \partial_t \hat{F}$, we express the Hamiltonian (3.6) as

$$\begin{aligned} \hat{H}_{\rm JTD} &= \omega(\hat{n}_x + \hat{n}_y) + \omega_0 \hat{J}_z + \frac{\lambda}{\sqrt{4j}}(\hat{J}_+ + \hat{J}_-)(\hat{a}_x^\dagger + \hat{a}_x) \\ &\quad + {\rm i}\frac{\lambda}{\sqrt{4j}}(\hat{J}_+ - \hat{J}_-)(\hat{a}_y^\dagger + \hat{a}_y). \end{aligned} \tag{3.7}$$

Hence we arrive at the realization of the collective JTD model, which describes a two-degenerate vibrational modes coupled to the effective spin ensemble by the symmetric JT coupling. The Hamiltonian (3.7) is a multi-particle extension of the E⊗e model in molecular and solid-state physics. The trapped ion realization of JTD model allows for easy tuning of the effective spin and phonon frequencies by adjusting the detuning and the spin-phonon coupling via the magnetic gradient.

It is convenient to rewrite the Hamiltonian (3.7) in terms of right and left chiral operators [55]

$$\hat{a}_{\rm r}^\dagger = \frac{1}{\sqrt{2}}(\hat{a}_x^\dagger + {\rm i}\hat{a}_y^\dagger), \quad \hat{a}_{\rm l} = \frac{1}{\sqrt{2}}(\hat{a}_x + {\rm i}\hat{a}_y), \tag{3.8}$$

which can be used to express the z component of the total angular momentum $\hat{L}_z = \sum_{j=1}^N \hat{L}_j^z = \hat{n}_{\rm r} - \hat{n}_{\rm l}$. Using (3.8), the Hamiltonian (3.7) is expressed in the form

$$\begin{aligned} \hat{H}_{\rm JTD} &= \omega(\hat{a}_{\rm r}^\dagger \hat{a}_{\rm r} + \hat{a}_{\rm l}^\dagger \hat{a}_{\rm l}) + \omega_0 \hat{J}_z + \frac{\lambda}{\sqrt{2j}} \hat{J}_+ (\hat{a}_{\rm r}^\dagger + \hat{a}_{\rm l}) \\ &\quad + \frac{\lambda}{\sqrt{2j}} \hat{J}_- (\hat{a}_{\rm r} + \hat{a}_{\rm l}^\dagger), \end{aligned} \tag{3.9}$$

which shows that in the JTD model the creation of collective atomic excitation is accompanied by the creation (annihilation) of right (left) quantum of angular momentum and vice versa.

Holstein-Primakoff representation

In order to study the critical behavior of a collective JTD model (3.7) in the thermodynamical limit $j \to \infty$, we use the Holstein-Primakoff transformation whereby the spin-$N/2$ degree of freedom is expressed in terms of single mode bosonic operators, namely $\hat{J}_+ = \hat{b}^\dagger \sqrt{2j - \hat{b}^\dagger \hat{b}}$, $\hat{J}_- = \sqrt{2j - \hat{b}^\dagger \hat{b}}\hat{b}$, and $\hat{J}_z = \hat{b}^\dagger \hat{b} - j$. This transformation preserves the spin algebra and allows to convert

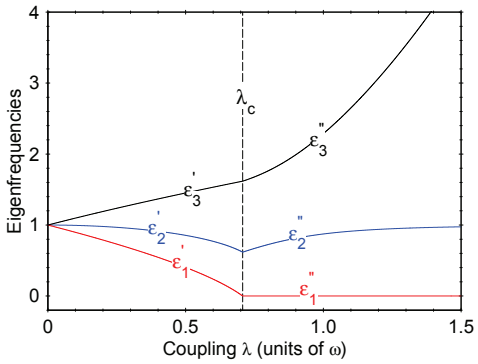

Fig. 3.2: (Color online) The excitation energy spectrum of the collective E⊗e JTD model in the limit $j \to \infty$ as a function of the spin-phonon coupling λ with $\omega = \omega_0$. For $\lambda \leq \lambda_c$ the eigenfrequencies ε'_p are given as a solution of Eq. (3.13). At $\lambda = \lambda_c$ the system undergoes a magnetic structural phase transition with broken U(1) symmetry. The new eigenfrequencies ε''_p for $\lambda \geq \lambda_c$ are given by Eq. (....).

the JTD Hamiltonian (3.7) into the Hamiltonian

$$\begin{aligned}\hat{H}_{\rm JTD} &= \omega(\hat{n}_x + \hat{n}_y) + \omega_0(\hat{b}^\dagger\hat{b} - j) + \frac{\lambda}{\sqrt{2}}\{\hat{b}^\dagger\sqrt{1 - \frac{\hat{b}^\dagger\hat{b}}{2j}} \\ &+\sqrt{1 - \frac{\hat{b}^\dagger\hat{b}}{2j}}\hat{b}\}(\hat{a}_x^\dagger + \hat{a}_x) + {\rm i}\frac{\lambda}{\sqrt{2}}\{\hat{b}^\dagger\sqrt{1 - \frac{\hat{b}^\dagger\hat{b}}{2j}} \\ &-\sqrt{1 - \frac{\hat{b}^\dagger\hat{b}}{2j}}\hat{b}\}(\hat{a}_y^\dagger + \hat{a}_y), \end{aligned} \tag{3.10}$$

which describes three coupled bosonic field modes. This approach is the basis for the theoretical discussion in the following section.

3.1.1 Magnetic Structural Phase Transition

We make a Taylor expansion of the square roots in the Hamiltonian (3.10) and assume $\langle b^\dagger b\rangle/j \ll 1$, which yields

$$\begin{aligned}\hat{H}^{(1)}_{\rm JTD} &= \omega(\hat{n}_x + \hat{n}_y) + \omega_0\hat{b}^\dagger\hat{b} + \frac{\lambda}{\sqrt{2}}(\hat{b}^\dagger + \hat{b})(\hat{a}_x^\dagger + \hat{a}_x) \\ &+{\rm i}\frac{\lambda}{\sqrt{2}}(\hat{b}^\dagger - \hat{b})(\hat{a}_y^\dagger + \hat{a}_y) + E^{(1)}_{\rm G}, \end{aligned} \tag{3.11}$$

where $E^{(1)}_{\rm G}/j = -\omega_0$ in the ground-state energy in the limit $j \to \infty$. The validity of the condition $\langle b^\dagger b\rangle/j \ll 1$ will be checked self-consistently below. We

diagonalize (3.11) by a Bogoliubov transformation, and get

$$\hat{H}^{(1)}_{\mathrm{JTD}} = \sum_{p=1}^{3} \varepsilon'_p \left(\hat{c}^{\dagger}_p \hat{c}_p + \frac{1}{2} \right) - \left(\omega + \frac{\omega_0}{2} \right) + E^{(1)}_{\mathrm{G}}. \tag{3.12}$$

The eigenfrequencies ε'_p can be found by solving the eigenvalue problem

$$\sum_{l=1}^{3} \mathcal{B}'_{il} v'^{(p)}_l = \varepsilon'^2_p v'^{(p)}_i, \tag{3.13}$$

with the matrix

$$\mathcal{B}'_{il} = \begin{bmatrix} \omega^2 & -\lambda\sqrt{\frac{\omega_0\omega}{m_+}} & \lambda\sqrt{\frac{\omega_0\omega}{m_-}} \\ -\lambda\sqrt{\frac{\omega_0\omega}{m_+}} & \frac{\omega^2+\omega_0^2}{2m_+} & \frac{\omega^2-\omega_0^2}{2\sqrt{m_+m_-}} \\ \lambda\sqrt{\frac{\omega_0\omega}{m_-}} & \frac{\omega^2-\omega_0^2}{2\sqrt{m_+m_-}} & \frac{\omega^2+\omega_0^2}{2m_-} \end{bmatrix}, \tag{3.14}$$

where $m_{\pm} = (1 \pm \lambda\sqrt{2/\omega_0\omega})^{-1}$. We obtain a non-negative real ε'_p $(p = 1, 2, 3)$ for $\lambda \leq \sqrt{\omega_0\omega/2}$, which allows us to define a critical coupling $\lambda_{\mathrm{c}} = \sqrt{\omega_0\omega/2}$. We note that the condition for the matrix (3.14) to be Hermitian holds for $\lambda \leq \lambda_{\mathrm{c}}$. The vacuum state $|0_1\rangle$ of Hamiltonian (3.12) is defined by the condition $\hat{c}_p |0_1\rangle = 0$.

In this phase the expectation values of the operators $\hat{a}_\alpha$ and $\hat{b}$ do not depend on the number of atoms and they grow as λ approach λ_{c} [56]. Thus, the mean value $\langle b^{\dagger} b \rangle$ is an intensive quantity, and in the thermodynamical limit we get $\langle b^{\dagger} b \rangle / j \to 0$, within the phase $\lambda < \lambda_{\mathrm{c}}$. In that limit, the phase is characterized with vanishing density of phonon excitations $\langle \hat{a}^{\dagger}_\alpha \hat{a}_\alpha \rangle / j = 0$ and collective spin pointing along the z axis, $\langle \hat{J}_z \rangle / j = -1$.

We may find a simple physical interpretation of the critical spin-phonon coupling λ_{c}. Indeed, it is well known that in the presence of spin-orbit coupling, the minima of the lower adiabatic potential surface APS (effective nuclei potential in the molecular physics) for $\lambda \leq \lambda_{\mathrm{c}}$ appears at the origin, while for $\lambda > \lambda_{\mathrm{c}}$ APS has a sombrero shape. Increasing the spin-phonon coupling, the energy is minimized by breaking some spatial symmetry and thus leads to a JT distortion.

In order to quantify amount of distortion and the spin ordering in the ion crystal above the critical coupling λ_{c}, we follow the general procedure introduced by Emary and Brandes in [50] for the quantum Dicke model. We displace each of the bosonic modes $\hat{a}^{\dagger}_x \to \hat{a}^{\dagger}_x + \sqrt{\alpha^*_x}$, $\hat{a}^{\dagger}_y \to \hat{a}^{\dagger}_y + \sqrt{\alpha^*_y}$, and $\hat{b}^{\dagger} \to \hat{b}^{\dagger} - \sqrt{\gamma^*}$, where α_x, α_y, and γ are generally complex parameters in the order of j. By using the Holstein-Primakoff representation and by substituting the displaced

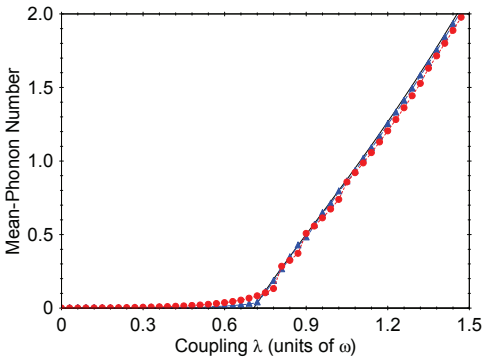

Fig. 3.3: The mean-phonon number $(\langle\hat{n}_x\rangle + \langle\hat{n}_y\rangle)/j$ as a function of the spin-phonon coupling λ. The numerical results for 10 (red circles) and 20 (blue triangles) ions are plotted together with the mean-field solution (solid line). For $\lambda \leq \lambda_c$ the phase is characterized with zero mean-phonon number. A position reordering is observed for $\lambda > \lambda_c$ accompanied with non-zero mean-phonon number. The magnetic structural transition becomes sharper with increasing N.

operators, the Hamiltonian (3.10) becomes

$$\begin{aligned}
\hat{H}^{(2)}_{\rm JTD} &= \omega(\hat{a}_x^\dagger\hat{a}_x + \sqrt{\alpha_x^*}\hat{a}_x + \sqrt{\alpha_x}\hat{a}_x^\dagger + |\alpha_x|) + \omega(\hat{a}_y^\dagger\hat{a}_y \\
&+\sqrt{\alpha_y^*}\hat{a}_y + \sqrt{\alpha_y}\hat{a}_y^\dagger + |\alpha_y|) + \omega_0(\hat{b}^\dagger\hat{b} - \sqrt{\gamma^*}\hat{b} \\
&-\sqrt{\gamma}\hat{b}^\dagger + |\gamma| - j) + \frac{\lambda}{\sqrt{2}}\sqrt{\frac{k}{2j}}(\hat{a}_x^\dagger + \hat{a}_x + \sqrt{\alpha_x^*} \\
&+\sqrt{\alpha_x})\{\hat{b}^\dagger\sqrt{\hat{\xi}} + \sqrt{\hat{\xi}}\hat{b} - \sqrt{\hat{\xi}}(\sqrt{\gamma^*} + \sqrt{\gamma})\} \\
&+\mathrm{i}\frac{\lambda}{\sqrt{2}}\sqrt{\frac{k}{2j}}(\hat{a}_y^\dagger + \hat{a}_y + \sqrt{\alpha_y^*} + \sqrt{\alpha_y})\{\hat{b}^\dagger\sqrt{\hat{\xi}} \\
&-\sqrt{\hat{\xi}}\hat{b} - \sqrt{\hat{\xi}}(\sqrt{\gamma^*} - \sqrt{\gamma})\},
\end{aligned} \tag{3.15}$$

where

$$k = 2j - |\gamma|;\ \sqrt{\hat{\xi}} = \sqrt{1 - \frac{\hat{b}^\dagger\hat{b} - \hat{b}^\dagger\sqrt{\gamma} - \hat{b}\sqrt{\gamma^*}}{k}}. \tag{3.16}$$

The parameters $\alpha_{x,y}$ and γ can be found from the condition that all terms linear in the bosonic field operators in Eq. (3.15) are canceled

$$\begin{aligned}
\sqrt{\alpha_x} &= \frac{\lambda}{\omega}\sqrt{j(1-s^2)}\cos\phi,\ \sqrt{\alpha_y} = \frac{\lambda}{\omega}\sqrt{j(1-s^2)}\sin\phi, \\
\sqrt{|\gamma|} &= \sqrt{j(1-s)},
\end{aligned} \tag{3.17}$$

with $s = \lambda_c^2/\lambda^2$. The phase $\phi = \arg(\sqrt{\gamma})$ remains undetermined which is a result of the arbitrariness in the choice of a direction in spontaneous symmetry

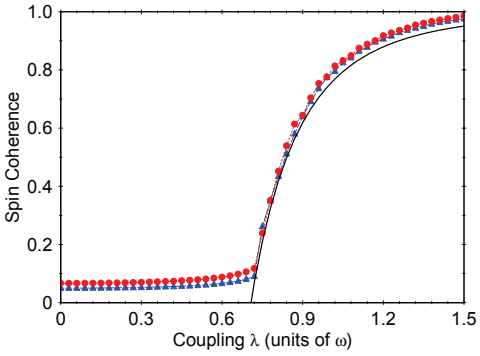

Fig. 3.4: The mean-field result for $(\langle \hat{J}_x^2 \rangle + \langle \hat{J}_y^2 \rangle)/j^2$ as a function of the spin-phonon coupling λ. The numerical results for 30 (red circles) and 40 (blue triangles) ions are compared with the mean-field solution (solid line). A creation of macroscopic spin-coherence is observed for $\lambda > \lambda_c$, which is an analog to the super-radiance phase in the Dicke model.

breaking. Again, making a Taylor expansion of $\sqrt{\hat{\xi}}$ and neglect, the terms with j in the denominator the Hamiltonian (3.15) can be brought to the diagonal form

$$\begin{aligned} \hat{H}^{(2)}_{\rm JTD} &= \sum_{p=2}^{3} \varepsilon''_p \left(\hat{r}^\dagger_p \hat{r}_p + \frac{1}{2} \right) - \omega - \frac{\omega_0}{4s}(1+s) \\ &\quad - \frac{\lambda^2}{2\omega}(1-s) + E^{(2)}_{\rm G}, \end{aligned} \tag{3.18}$$

where $E^{(2)}_{\rm G}/j = -\left(\frac{\lambda^2}{\omega} + \frac{\omega_0^2 \omega}{4\lambda^2} \right)$ is the ground-state energy in the limit $j \to \infty$. The new excitation frequencies ε''_p are solution of the eigenvalue problem

$$\sum_{l=1}^{3} \mathcal{B}''_{il} v''^{(p)}_l = \varepsilon''^2_p v''^{(p)}_i, \tag{3.19}$$

for the matrix

$$\mathcal{B}''_{il} = \begin{bmatrix} \xi^2 M_- & \lambda^2 \sqrt{2M_-} & \nu \sqrt{M_+ M_-} \\ \lambda^2 \sqrt{2M_-} & \omega^2 & -\lambda^2 \sqrt{2M_+} \\ \nu \sqrt{M_+ M_-} & -\lambda^2 \sqrt{2M_+} & \xi^2 M_+ \end{bmatrix}, \tag{3.20}$$

with $\xi^2 = \left(\frac{\omega^2}{2} + \frac{\omega_0^2}{2s^2} \right)$, $\nu = \left(\xi^2 - \frac{\omega_0^2}{s^2} \right)$ and $M_\pm = (1 \pm s)$, respectively. In contrast to (3.13), now the frequencies ε''_p remain positively defined in the region $\lambda \geq \lambda_c$, Fig. 3.2.

The mean-value phonon number with respect to the new vacuum state $|0_2\rangle$ of the Hamiltonian (3.18) with $\hat{r}_p |0_2\rangle = 0$ is $\langle \hat{n}_x \rangle / j = (\lambda^2/\omega^2)(1-s^2)\cos^2\phi$ and

$\langle \hat{n}_y \rangle / j = (\lambda^2/\omega^2)(1-s^2)\sin^2\phi$, indicating a non-zero radial phonon excitations, Fig. 3.3.

The collective displacement of the c.m. mode implies a position reordering of the ions' equilibrium positions in the radial x-y plane. It follows that the new radial equilibrium positions are $x_{i0} = q_0\sqrt{2\alpha_x/j}$ and $y_{i0} = q_0\sqrt{2\alpha_y/j}$. The structural transition also is accompanied with the ferromagnetic spin ordering, $\langle \hat{J}_x^2 \rangle / j^2 = (1-s^2)\cos^2\phi$, $\langle \hat{J}_y^2 \rangle / j^2 = (1-s^2)\sin^2\phi$, respectively, Fig. 3.4. We note that, the magnetic structural transition breaks the continuous U(1) symmetry of the JTD model, which reflects to the energy spectrum, namely one of the eigenfrequencies corresponds to the gapless Goldstone mode, $\varepsilon_1'' = 0$, see Fig. 3.2.

In conclusion we have presented a proposal for the physical realization of the collective JTD model based on a linear ion crystal. We have shown that the JTD model exhibits a magnetic structural phase transition in the thermodynamical limit. Beyond the critical coupling the continuous U(1) symmetry is spontaneously broken which leads to collective motional displacement of the radial coordinates and creation of macroscopic spin-coherence. The features of the magnetic structural transition can be easily measured in the mesoscopic ion crystal by laser induced fluorescence. All parameters can be tuned by changing the detuning and the magnetic field gradient. In future we will investigate the JT effects in 2D ion crystals, which are relevant to orbital physics in solids. Furthermore, the ion crystal also can serve as a platform for studying non-equilibrium phenomena and effects of decoherence in such complex many-body systems, which are computationally intractable.

3.2 Quantum Simulation of Cooperative Jahn-Teller Systems with Linear Ion Crystals

In this Section we propose the trapped ion analogical QS of a one dimensional cooperative Jahn-Teller (cJT) model of two-level systems coupled to bosonic modes by a symmetric $(E \otimes e)$ interaction. Our proposed QS allows to explore quantum effects relevant to orbital physics in solids and to use trapped ions as a testbed for theories to describe those systems. Previous theoretical works include related models with single-particle quantum optical setups [57] and spin-orbit coupled Bose-Einstein condensates [189]. We study the rich phenomenology of the many-body case and predict that the system undergoes a quantum magnetic structural phase transition with the formation of a spin-boson superfluid. The latter is a quantum magnetic version of the classical zig-zag phase observed in ion chains [59]. We focus on the quantum simulation of the symmetric $E \otimes e$ models, which show a particularly interesting phase diagram due to the breaking of a continuous U(1) symmetry, although or proposal can be generalized to asymmetric interactions.

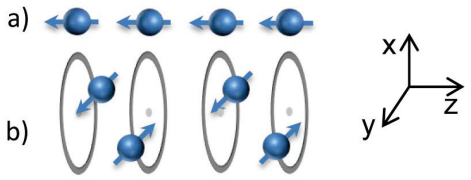

Fig. 3.5: Quantum magnetic structural phase transition with trapped ions. (a) Normal state ($g < g_c$). (b) Quantum magnetic zig-zag phase ($g > g_c$). For moderate chain lengths long-range zig-zag order appears together with an antiferromagnetic spin phase.

3.2.1 Cooperative Jahn-Teller Model

We consider a chain of N spins with levels $|0\rangle_j$, $|1\rangle_j$ at each site j, coupled to a chain with two boson species with operators $a_{\beta,j}$ ($\beta = x, y$ and $\hbar = 1$ from now on). The Hamiltonian of the cooperative Jahn-Teller model is given by

$$H_{\rm cJT} = H_{\rm s} + H_{\rm b} + H_{\rm c}, \tag{3.21}$$

where $H_{\rm s}(\omega_z) = (\omega_z/2)\sum_j \sigma_j^z$, and $H_{\rm b}$ is the free boson term,

$$H_{\rm b}(\{\Delta_j\},\{t_{j,l}\}) = \sum_{\beta,j} \Delta_j \; a^\dagger_{\beta,j} a_{\beta,j} + \sum_{\beta,j>l} t_{j,l} \left(\; a^\dagger_{\beta,j} a_{\beta,l} + \text{H.c.} \right), \tag{3.22}$$

where Δ_j is the on-site boson energy and $t_{j,l}$ are boson hopping matrix elements. Alternatively the boson bath can be described in terms of normal modes, $a_{\beta,n} = \sum_j b_{n,j} a_{\beta,j}$, with $b_{n,j}$ the normal mode wave-functions, such that $H_{\rm b} = \sum_{\beta,n} \Delta_n a^\dagger_{\beta,n} a_{\beta,n}$, with Δ_n the collective mode energies. The last term in (3.21) is a Jahn-Teller $E \otimes e$ spin-boson coupling

$$H_{\rm c}(g) = \frac{g}{\sqrt{2}} \sum_j \{\sigma_j^x (a_{x,j} + a^\dagger_{x,j}) + \sigma_j^y (a_{y,j} + a^\dagger_{y,j})\}, \tag{3.23}$$

that can be rewritten in terms of right and left chiral operators $a^\dagger_{r,j} = (a^\dagger_{x,j} + {\rm i} a^\dagger_{y,j})/\sqrt{2}$, $a^\dagger_{l,j} = (a^\dagger_{x,j} - {\rm i} a^\dagger_{y,j})/\sqrt{2}$, as follows

$$H_{\rm c}(g) = g \sum_j \sigma_j^+ (a_{r,j} + a^\dagger_{l,j}) + \text{H.c.}. \tag{3.24}$$

The Hamiltonian (3.21) is U(1)-symmetric under rotations in the xy plane, generated by $C = \sum_j (a^\dagger_{r,j} a_{r,j} - a^\dagger_{l,j} a_{l,j} + \sigma_j^z/2)$.

3.2.2 Mean-field theory

The Hamiltonian (3.21) and its particular trapped ion realization pose an intriguing quantum many-body problem that we approach first by a mean-field

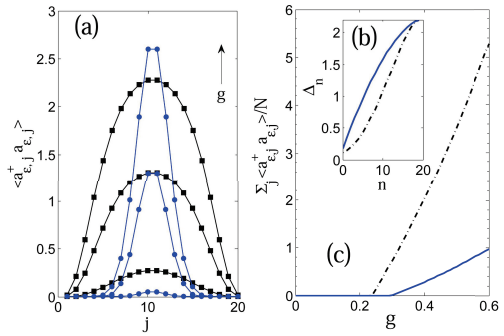

Fig. 3.6: Mean-field results with $N = 20$ ions. Energy units such that $\omega_z = 1$, $\Delta = 2.2$. (a) Phonons per site in the chiral base. Black squares: homogeneous chain with $g = 0.25, 0.3, 0.35$ and $t_{j,j+1} = 0.5$. Blue circles: Coulomb chain with $g = 0.4, 0.45, 0.5$, and distances scaled such that at the center, $t^{\rm coul}_{10,11} = 0.5$. In (b) and (c) we show results for a Coulomb (continuous line) and an homogeneous (dashed line). (b) Vibrational energies of the radial collective modes. (c) Mean number of phonons as a function of g. The phase transition point at $g \sim 0.25$ and 0.3 is visible for the Coulomb and homogeneous chain, respectively.

variational ansatz. We write that ansatz in terms of chiral operators, $a^\dagger_{\epsilon,n}$ ($\epsilon = \mathrm{r}, \mathrm{l}$ from now on), as a product state of spins and displaced bosons in the collective mode basis,

$$|\Psi_{\rm MF}\rangle = \prod_j |\theta_j, \phi_j\rangle \otimes e^{\sum_{\epsilon,n}(\alpha_{\epsilon,n} a^\dagger_{\epsilon,n} - \alpha^*_{\epsilon,n} a_{\epsilon,n})} |0\rangle_l |0\rangle_r, \tag{3.25}$$

where $|\theta_j, \phi_j\rangle = \cos(\theta_j/2)|0\rangle_j + e^{-i\phi_j}\sin(\theta_j/2)|1\rangle_j$ is a coherent spin state of the spin j, and $|0\rangle_\epsilon$ is the vacuum of each ϵ chiral mode. By minimizing the energy $E = \langle\Psi_{\rm MF}| H |\Psi_{\rm MF}\rangle$, we arrive to a set of coupled equations for the variational parameters θ_j, ϕ_j, and $\alpha_{\epsilon,n}$,

$$\alpha_{\epsilon,n} = -\frac{g}{2\Delta_n}\sum_j b_{n,j}\sin\theta_j, \quad \omega_z \tan\theta_j = -\sum_l J_{j,l}\sin\theta_l, \;\; J_{j,l} = 2\sum_n \Re\frac{g^2}{\Delta_n} b^*_{n,j} b_{n,l},$$

with condition $\phi_j = \phi_l = \phi$, and $\phi = 0$. The latter is an arbitrary choice for a direction of spontaneous symmetry breaking, such that spins are aligned in the xz plane.

To estimate the mean-field phase diagram let us consider first periodic boundary conditions, such that $b_{n,j} = \exp(-\mathrm{i}2\pi nj/N)/\sqrt{N}$, and couplings $J_{j,l} > 0$. This last condition is met if vibrational energies $\Delta_n > 0$, and have a minimum at the center-of-mass mode, $n = 0$. We find the homogeneous solution $\theta_j = \theta$, with value $\cos\theta = g_{\rm c}^2/g^2$ if ($g > g_{\rm c}$), and $\cos\theta = 1$ if ($g < g_{\rm c}$), where the critical coupling is $g_{\rm c}^2 = \Delta_0\omega_z/2$. The critical amplitude is $\alpha_{\epsilon,0} = -(g\sqrt{N}/2\Delta_0)\sin\theta$, showing condensation into the $n = 0$ mode for

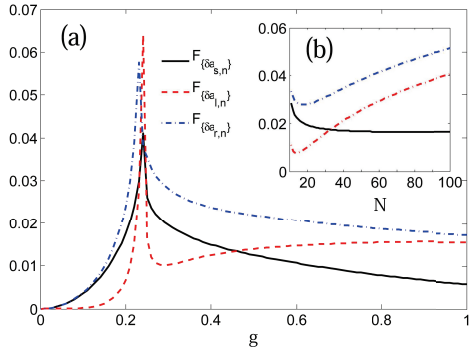

Fig. 3.7: Quantum Gaussian fluctuations $F_{\delta a_{\gamma,n}}$. Black, blue and red lines correspond to $\gamma = s$ (spin-waves), l (l-phonons) and r (r-phonons) respectively. We have considered homogeneous chains and units such that $\omega_z = 1$, $\Delta = 2.2$, $t_{j,j+1} = 0.5$ in homogeneous chains. (a) $N = 20$ ions and different g values. As expected fluctuations exhibit a peak at the critical point. Note that $F_{\{a_{s,n}\}}$ and $F_{\{a_{r,n}\}}$ are enhanced since spin and r-phonon operators are closer to resonance in (3.24). (b) $g = 0.3$ and different values of N. Fluctuations diverge with growing N in accordance with the Mermin-Wagner theorem.

$g > g_c$. Note that condensation above $g > g_c$ implies both ferromagnetic ordering of spins in the xz plane together with the collective displacement of the center-of-mass coordinate, thus implying a magnetic structural phase transition.

To predict the phases of the cJT model in an ion chain we have to include finite-size corrections. We consider: (i) *Coulomb ion chains* (inhomogeneous). The separation between ions in an harmonic linear trap, $d_j = r_j^0 - r_{j-1}^0$, increases from the center to the ends of the chain. As a result, both $t_{j,k}^{\text{coul}}$ and $\omega_{t,j}$ depend on the position. (ii) *Homogeneous ion chains*. This case corresponds to constant distance between ions. It may describe one dimensional arrays of microtraps and also approximates locally the description of an inhomogeneous chain. Figs. 3.6 show results for cases (i) and (ii), with $N = 20$ ions. We present results in the staggered basis such that we are studying the trapped ion cJT model with $t_{j,l}^{\text{stag}}$. Spin-phonon condensation appears first in the center of the chain, something that can be used to experimentally detect condensation. That effect is stronger in the Coulomb chain case due to the inhomogeneity in the local trapping frequencies. Note that uniform displacement in the staggered basis corresponds to zig-zag displacement in the original phonon basis.

3.2.3 Gaussian quantum fluctuations

Quantum fluctuations destroy long-range order in the thermodynamical limit of one-dimensional systems where a continuous symmetry is spontaneously broken as a result of infrared divergences. Still a mean-field theory remains a fair approximation in a range of mesoscopic sizes of the crystal length, thus in the most relevant parameter regime. To quantify fluctuations, we use a Gaussian ap-

proximation around the mean-field solution. Let us define first the fluctuation operators with respect to bosonic degrees of freedom, $\delta a_{\epsilon,n} = a_{\epsilon,n} - \alpha_{\epsilon,n}$. Spin fluctuations are defined by means of a Holstein-Primakoff approximation around the ferromagnetic order. For this, we define operators $U_{\theta,j}|\theta_j, 0\rangle_j = |0,0\rangle_j$, that rotate the coherent spin state to a product state of spins pointing in the $-z$ direction, $\sigma_j^z = \cos\theta_j \bar{\sigma}_j^z + \sin\theta_j \bar{\sigma}_j^x$, $\sigma_j^x = \cos\theta_j \bar{\sigma}_j^x - \sin\theta_j \bar{\sigma}_j^z$, with $\bar{\sigma}_j^{z,x} = U_{\theta_j} \sigma_j^{z,x} U_{\theta_j}^\dagger$. After the rotation, we can use the usual Holstein-Primakoff transformation where the reference state is taken in the $\bar{\sigma}^z$ basis, $\bar{\sigma}_j^+ \approx \delta a_{s,j}^\dagger$, $\bar{\sigma}_j^- \approx \delta a_{s,j}$, $\bar{\sigma}_j^z = 2\delta a_{s,j}^\dagger \delta a_{s,j} - 1$, valid in the limit $\langle \delta a_{s,j}^\dagger \delta a_{s,j} \rangle \ll 1$. Finally, we substitute spin and boson operators in the cJT Hamiltonian (3.21) and expand to second order in the fluctuation operators, such that we get

$$\begin{aligned} H_{\rm G} &= \sum_{n,\epsilon} \Delta_n \delta a_{\epsilon,n}^\dagger \delta a_{\epsilon,n} + \sum_j \omega_j \delta a_{s,j}^\dagger \delta a_{s,j} \\ &+ \frac{g}{2} \sum_{j,n} b_{n,j} \cos\theta_j (\delta a_{s,j} + \delta a_{s,j}^\dagger)(\delta a_{l,n} + \delta a_{l,n}^\dagger + \delta a_{r,n} + \delta a_{r,n}^\dagger) \\ &+ \frac{g}{2} \sum_{j,n} b_{n,j} (\delta a_{s,j} - \delta a_{s,j}^\dagger)(\delta a_{l,n} - \delta a_{l,n}^\dagger - (\delta a_{r,n} - \delta a_{r,n}^\dagger)), \end{aligned} \tag{3.26}$$

with $\omega_j = \omega_z / \cos\theta_j$. $H_{\rm G}$ is diagonalized by means of a Bogoliubov transformation to spin-phonon fluctuation operators c_m,

$$\delta a_{\gamma,n} = \sum_{m=1,\ldots,3N} \left(U_{n,m}^\gamma c_m + V_{n,m}^\gamma c_m^\dagger \right) \quad (\gamma = \mathrm{s,l,r}). \tag{3.27}$$

The matrices $U_{n,m}^\gamma$, $V_{n,m}^\gamma$, define a canonical transformation to a set of $3N$ bosonic operators c_m, such that $H_{\rm G} = \sum_m \omega_m c_m^\dagger c_m$. The low-energy modes c_m form an acoustic Goldstone branch in the condensed phase.

To compute quantum fluctuations we define the vacuum $|\Omega\rangle$, by the condition $c_m|\Omega\rangle = 0$ and define the variance per atom for a set of the original spin-phonon fluctuation modes,

$$F_{\{\delta a_{\gamma,n}\}} = \frac{1}{N} \sum_n \langle \Omega | \delta a_{\gamma,n}^\dagger \delta a_{\gamma,n} | \Omega \rangle, \tag{3.28}$$

and calculate $F_{\{\delta a_{r,n}\}}$ (r-phonon), $F_{\{\delta a_{l,n}\}}$ (l-phonon), and $F_{\{\delta a_{s,n}\}}$ (spin-wave) fluctuations. In Fig. 3.7(a) we show that quantum fluctuations are smaller for larger g couplings, in agreement with the intuition that $g \gg g_c$ corresponds to the classical limit. For mesoscopic trapped ion sizes ($N \approx 20$) condition $F_{\{a_{\gamma=s,r,l,n}\}} \ll 1$ is satisfied, consistent with the validity of Hamiltonian (3.26). In Fig. 3.7(b) we show the enhancement of quantum fluctuations a function of the system size N.

3.2.4 Numerical calculations with the DMRG method

To validate the results obtained within a mean-field theory approach, we have performed DMRG numerical calculations. We choose a maximum number of

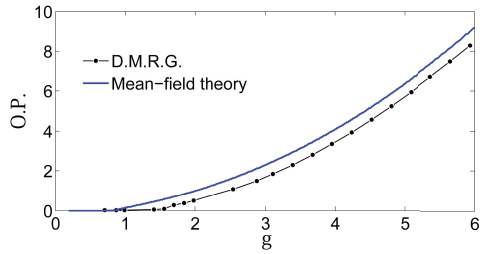

Fig. 3.8: Comparison for O.P. defined in the text in a short-range homogeneous cJT chain with $t = 0.2$, and units such that $\Delta = 2$, $\omega_z = 1$, and $N = 20$.

bosons per site $n_{\mathrm{b}} = 20$, which accounts for a local Hilbert space of 72 states. That local dimension makes our calculation computationally demanding even for short ion chains. The number of states kept in the reduced density matrix description (or bond-dimension) is $D = 20$, and we check that the solution has converged to an error of 10^{-3} in all quantities presented here.

To simplify the calculation we test the mean-field theory on a short range cJT model, with $t_{j,k} = -t\delta_{j,j-1}$. Also, we define an order parameter in terms of long-range order, O.P. $= \sum_{j,k}\sum_{\epsilon=r,l}\langle a^{\dagger}_{\epsilon,j}a_{\epsilon,k}\rangle/N^2$. That definition has the advantage to hold even without assuming spontaneous symmetry breaking. Fig. 3.8 shows that the mean-field prediction closely follows the quasi-exact DMRG result for a mesoscopic ion crystal with $N = 20$ ions.

In conclusion in this Section we have studied the trapped ion QS of a cJT model that describes the coupling of two-level systems to a bath of bosonic degrees freedom. We predict a quantum phase transition to a spin-boson condensate in the ground state. Experiments may allow us to explore non-equilibrium phenomena and the effect of decoherence. Our trapped ion QS involves a large number of spin-phonon degrees of freedom and may challenge current numerical methods for many-body problems. Our proposal is also relevant for other experimental setups such as cavity or circuit QED systems, where the coupling of emitters to arrays of cavities can be controlled to yield Jahn-Teller couplings

3.3 Collective Modes in the Cooperative Jahn-Teller Model: Path Integral Approach

In this Section we use path integral approach to describe analytically the quantum magnetic structural phase transition with the formation of bosonic condensates and magnetic ordering of the spins in the cJT model. Within the framework of the saddle-point approximation we determine the mean-field solution and then consider the quantum fluctuations around the mean-field result. We show that the energy spectrum of the cJT system consists of three collective excitations branches. In the symmetry broken phase we find a linear gapless Goldstone mode and two gapped amplitude modes.

3.3.1 Path integral approach to the cJT model

In the functional integral treatment, the second quantized Hamiltonian of the model is translated to the phase representation with the help of the path integral formalism. In this approach the boson operators are replaced with their associated fields, namely $\hat{a}_{\gamma,k} \to \alpha_{\gamma,k}(\tau)$, $\hat{a}^{\dagger}_{\gamma,k} \to \alpha^{*}_{\gamma,k}(\tau)$ where τ is the imaginary time [61]. For the spin-degrees of freedom we choose a spin-coherent representation with coherent-state parameterized by the independent polar θ_j and azimuthal φ_j angles, respectively,

$$|n_j\rangle = \cos\left(\frac{\theta_j}{2}\right)|\uparrow_j\rangle + e^{\mathrm{i}\varphi_j}\sin\left(\frac{\theta_j}{2}\right)|\downarrow_j\rangle\,. \tag{3.29}$$

The spin operators are replaced by the corresponding Bloch vector $\vec{n}_j = [n_{x,j}, n_{y,j}, n_{z,j}]$ whose components are the expectation values of the Pauli matrices with respect to the state (3.29) which gives

$$\vec{n}_j = [\sin(\theta_j)\cos(\varphi_j), \sin(\theta_j)\sin(\varphi_j), \cos(\theta_j)]. \tag{3.30}$$

The Bloch vector has a unit length $\vec{n}_j^2 = 1$ and specifies the orientation of spin at site j. Having this in hand the partition function for the cJT model can be expressed as

$$Z(\beta) = \int \prod_{\gamma,k}\prod_{j} D\alpha^{*}_{\gamma,k}(\tau) D\alpha_{\gamma,k}(\tau) D\vec{n}_j(\tau)\delta(\vec{n}_j^2 - 1)e^{-S}, \tag{3.31}$$

with the Euclidian action given by

$$\begin{aligned} S &= \int_0^{\beta} d\tau\{\sum_{\gamma,k}(\alpha^{*}_{\gamma,k}\frac{\partial\alpha_{\gamma,k}}{\partial\tau} + \Delta_k\alpha^{*}_{\gamma,k}\alpha_{\gamma,k}) + \frac{\omega_z}{2}\sum_j\cos(\theta_j) \\ &\quad + \frac{g}{2}\sum_{j,k}\sin(\theta_j)\{e^{\mathrm{i}\varphi_j}(b^{*}_{k,j}\alpha_{\mathrm{r},k} + b_{k,j}\alpha^{*}_{\mathrm{l},k}) + \mathrm{c.c}\}\} + S_{\mathrm{B}}, \end{aligned} \tag{3.32}$$

where $\beta = 1/T$ is the inverse temperature. The Berry phase contribution to the action (3.32) from the spin-degrees of freedom is given by

$$S_{\mathrm{B}} = \sum_j \int_0^{\beta}\langle n_j|\frac{\partial}{\partial\tau}|n_j\rangle = \mathrm{i}\sum_j\int_0^{\beta} d\tau\sin^2\left(\frac{\theta_j}{2}\right)\frac{\partial\varphi_j}{\partial\tau}. \tag{3.33}$$

Finally, we require that the corresponding bosonic fields have periodic boundary conditions $\alpha_{\gamma,k}(\beta) = \alpha_{\gamma,k}(0)$ and $\alpha^{*}_{\gamma,k}(\beta) = \alpha^{*}_{\gamma,k}(0)$. The same condition is hold and for the spin variables, where we have $\theta_j(\beta) = \theta_j(0)$ and $\varphi_j(\beta) = \varphi_j(0)$.

3.3.2 Saddle-Point Approximation

Next we consider the classical equation of motion, which are determined by the condition, that the variation of the action (3.32) with respect to the field

variables should vanish,

$$\frac{\delta S}{\delta \theta_j} = 0, \quad \frac{\delta S}{\delta \varphi_j} = 0, \quad \frac{\delta S}{\delta \alpha^*_{\gamma,k}} = 0. \tag{3.34}$$

Note that the same condition is also satisfied for the bosonic field $\alpha_{\gamma,k}$. The term classical refers to a mean-field solution, i.e., disregarding the quantum fluctuations. The variation of the action S with respect of the spin-degrees of freedom gives the following equations of motion

$$\begin{aligned} \mathrm{i}\sin(\theta_j)\frac{\partial \varphi_j}{\partial \tau} &= \omega_z \sin(\theta_j) - g\cos(\theta_j)\sum_k \{e^{\mathrm{i}\varphi_j}(b^*_{k,j}\alpha_{\mathrm{r},k} \\ &\quad + b_{k,j}\alpha^*_{\mathrm{l},k}) + \mathrm{c.c}\}, \\ \frac{\partial \theta_j}{\partial \tau} &= g\sum_k \{e^{\mathrm{i}\varphi_j}(b^*_{k,j}\alpha_{\mathrm{r},k} + b_{k,j}\alpha^*_{\mathrm{l},k}) - \mathrm{c.c}\}), \end{aligned} \tag{3.35}$$

where the dynamics follow from the Berry phase term (3.33). The third condition in (3.34) reads

$$\begin{aligned} \frac{\partial \alpha_{\mathrm{r},k}}{\partial \tau} &= -\Delta_k \alpha_{\mathrm{r},k} - \frac{g}{2}\sum_j b_{k,j}(n_{x,j} - \mathrm{i}n_{y,j}), \\ \frac{\partial \alpha_{\mathrm{l},k}}{\partial \tau} &= -\Delta_k \alpha_{\mathrm{l},k} - \frac{g}{2}\sum_j b_{k,j}(n_{x,j} + \mathrm{i}n_{y,j}). \end{aligned} \tag{3.36}$$

We note that because the action S (3.32) is invariant with respect to $U(1)$ transformation, the corresponding equations of motion (3.35) and (3.36) obey the same symmetry. Although the Eq. (3.35) describes the dynamics of the spin-degree of freedom it is not expressed in terms of $\vec{n}_j$. One way to remedy this is to introduce a new set of two orthogonal to $\vec{n}_j$ vectors, namely $\vec{\theta}_j = [\cos(\theta_j)\cos(\varphi_j), \cos(\theta_j)\sin(\varphi_j), -\sin(\theta_j)]$ and $\vec{\varphi}_j = [-\sin(\varphi_j), \cos(\varphi_j), 0]$ which form an orthogonal triad $\vec{\theta}_j \times \vec{\varphi}_j = \vec{n}_j$. Then the Eq. (3.35) is rewritten as follows

$$\begin{aligned} \frac{\mathrm{i}}{2}\vec{\varphi}_j \cdot \frac{\partial \vec{n}_j}{\partial \tau} &= \frac{\omega_z}{2}(\vec{\varphi}_j + \vec{\theta}_j)\cdot \frac{\partial \vec{n}_j}{\partial \varphi_j} - g\vec{\theta}_j \cdot \vec{\alpha}_j, \\ \frac{\mathrm{i}}{2}\vec{\theta}_j \cdot \frac{\partial \vec{n}_j}{\partial \tau} &= g\vec{\varphi}_j \cdot \vec{\alpha}_j. \end{aligned} \tag{3.37}$$

Here we have introduce the vector notation $\vec{\alpha}_j = \sqrt{2}[\Re\alpha_{x,j}, \Re\alpha_{y,j}, 0]$ for the two bosonic fields. Finally, one can combine the two equations in (3.37) in a vector form which yield

$$\frac{\mathrm{i}}{2}\frac{\partial \vec{n}_j}{\partial \tau} = \frac{\omega_z}{2}\vec{B} \times \vec{n}_j + g\vec{\alpha}_j \times \vec{n}_j, \tag{3.38}$$

where we use $\frac{\partial \vec{n}_j}{\partial \varphi_j} = \vec{B} \times \vec{n}_j$. Now we are in position to interpret the dynamical equation for the spins. The first term in (3.38) represent the effect of the

externally applied magnetic field along the z direction, $\vec{B} = [0, 0, 1]$, such that for $g = 0$ the spins will perform precession with frequency determined by ω_z. On the other hand the spin-boson interaction gives rise to an effective magnetic field $\vec{\alpha}_j$ experienced by the spin at lattice site j. In the case when the bosonic fields describe the motional degrees of freedom of the spins in two orthogonal directions, the effective magnetic field $\vec{\alpha}_j$ becomes position-dependent, which is in close analogy with the Rashba spin-orbit coupling in the quantum spin Hall effect [62]. Because the vectors $\vec{B}$ and $\vec{\alpha}_j$ are always orthogonal, the spins execute precession along the axis 45^0 to both magnetic fields. We note that although Eq. (3.38) is purely local in a sense that it only depends on the lattice index j, the components of $\vec{\alpha}_j$ depend on the boson fields at different sites due to the tunneling elements $t_{j,l}$. As we will see below such a tight-binding lattice dynamics of the two bosonic species strongly coupled to the spins are capable of forming magnetic ordering and bosonic condensates.

The stationary saddle-point is obtained by the solution of Eq. (3.34) with the requirement that $\alpha_{\gamma,k}(\tau) = \bar{\alpha}_{\gamma,k}$ and $\vec{n}_j(\tau) = \vec{\bar{n}}_j$. Then we derive the following set of algebraic equations for the spin-degrees of freedom

$$\begin{aligned}
\omega_z \sin(\bar{\theta}_j) &= -\cos(\bar{\theta}_j) \sum_l J_{j,l} \sin(\bar{\theta}_l) \cos(\bar{\varphi}_j - \bar{\varphi}_l), \\
\sum_l J_{j,l} \sin(\bar{\theta}_l) \sin(\bar{\varphi}_j - \bar{\varphi}_l) &= 0,
\end{aligned} \tag{3.39}$$

where $J_{j,l} = 2\sum_k \frac{g^2}{\Delta_k} \Re\{b_{k,j} b^*_{k,l}\}$ and respectively for the bosonic fields

$$\begin{aligned}
\bar{\alpha}_{\mathrm{r},k} &= -\frac{g}{2\Delta_k} \sum_j b_{k,j} \sin(\bar{\theta}_j) e^{-\mathrm{i}\bar{\varphi}_j}, \\
\bar{\alpha}_{\mathrm{l},k} &= -\frac{g}{2\Delta_k} \sum_j b_{k,j} \sin(\bar{\theta}_j) e^{\mathrm{i}\bar{\varphi}_j}.
\end{aligned} \tag{3.40}$$

Apparently, the system (3.39) has a trivial solution $\sin(\bar{\theta}_j) = 0$ for $(j = 1, 2, \ldots, N)$ which implies $\bar{\alpha}_{\gamma,k} = 0$. Assuming $\sin(\bar{\theta}_j) \neq 0$, the condition $\bar{\varphi}_j = \bar{\varphi}_l = \bar{\varphi}$ solved the second equation in (3.39). The latter is the arbitrary choice for a direction of spontaneous symmetry breaking where the system chooses a direction along which to order. Hear after we assume $\bar{\varphi} = 0$, such that the Bloch vector becomes $\vec{\bar{n}}_j = [\sin(\bar{\theta}_j), 0, \cos(\bar{\theta}_j)]$ indicating that the spins are aligned in the xz plane. Let us now discuss the homogenous limit $\bar{\theta}_j = \bar{\theta}$ neglecting any boundary effect. In this limit Eqs. (3.39) and (3.40) can be solved exactly, which yield

$$\begin{aligned}
&\cos(\bar{\theta}) = -1, \quad \bar{\alpha}_{\gamma,k} = 0, \quad g < g_{\mathrm{c}}, \\
&\cos(\bar{\theta}) = -\frac{g_{\mathrm{c}}^2}{g^2}, \quad \bar{\alpha}_{\gamma,k} = -\frac{g\sqrt{N}}{2\Delta_k} \sin(\bar{\theta}) \delta_{k,0}, \quad g > g_{\mathrm{c}}
\end{aligned} \tag{3.41}$$

The solution (3.41) corresponds to the classical ground-state of the cJT model. For a coupling smaller than the critical value of $g_{\mathrm{c}} = \sqrt{\Delta_0 \omega_z / 2}$ $(g < g_{\mathrm{c}})$ the system is in a normal state where the Bloch vector for each spin points along

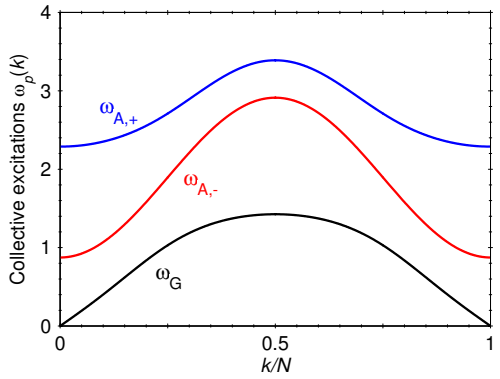

Fig. 3.9: The dispersions of the three branch frequencies versus k. We set $\Delta/g = 1$, $t/g = 0.5$, and $\omega_z/g = 1$. We have assumed position independent bosonic frequency $\Delta_j = \Delta + 2t$.

the $-z$ direction and $\bar{\alpha}_{\gamma,k} = 0$. Increasing the coupling through g_c ($g > g_c$) drives the system to undergo a quantum phase transition to a ferromagnetic ordering of spins in xz plane and condensation of the two boson species in the lowest energy mode $k = 0$. Here we emphasize that for a linear ion crystal with positive hopping amplitude the saddle-point approximation is not applied straightforward. This problem can be overcome by applying a canonical transformation to the operators $\hat{a}_{\epsilon,j} \to (-1)^j \hat{a}_{\epsilon,j}$ and $\sigma_j^\epsilon \to (-1)^j \sigma_j^\epsilon$ in (3.21). After this transformation to the staggered spin-boson basis the cJT model (3.21) is unchanged, but the tunneling is modified to $t_{j,l}^{\text{stagg}} = (-1)^{j-l} t_{j,l}$. The ferromagnetic spin order in the new basis, corresponds to an antiferromagnetic order in the physical basis, in which ions alternate spin direction and position.

In the following section we study the low-energy spectra of the cJT model in terms of collective excitations. We expand the action of the system around its saddle-point up to second order in the spin and bosonic fields. This leads to a Gaussian integral which can be evaluated.

3.3.3 Quantum Fluctuations around the saddle-point

Linear parametrization

Having described the saddle-point solution, we now consider the low-energy excitations of the cJT model in the symmetry-broken phase. For the bosonic fields we can use the standard linear parametrization

$$\alpha_{\gamma,k} = \bar{\alpha}_{\gamma,k} + \delta\alpha_{\gamma,k}, \tag{3.42}$$

where $\delta\alpha_{\gamma,k}$ describes the quantum fluctuations around the order parameter $\bar{\alpha}_{\gamma,k}$. In order to account the spin fluctuations around the state $\vec{\bar{n}}_j$ for each spin at site j we first perform rotation of the Bloch vector $\vec{n}_j = \hat{R}(\bar{\theta})\vec{n}'_j$ with rotation

matrix given by

$$\hat{R}(\bar{\theta}) = \begin{bmatrix} \cos(\bar{\theta}) & 0 & \sin(\bar{\theta}) \\ 0 & 1 & 0 \\ -\sin(\bar{\theta}) & 0 & \cos(\bar{\theta}) \end{bmatrix}. \tag{3.43}$$

Note that transformation of the Bloch vector implies rotation of the spin-coherent state specified by $|n'_j\rangle = e^{\mathrm{i}\frac{\bar{\theta}}{2}\sigma^y_j}|n_j\rangle$. The rotation matrix $\hat{R}(\bar{\theta})$ is determined in a such a way that transform $\vec{\bar{n}}_j$ to a new reference Bloch vector $\vec{\bar{n}}'_j = [0,0,1]$ which points along the z direction. Assuming that the spin and bosonic fluctuations are small in a sense that one can keep only the quadratic terms, such that $n'_{z,j} = \sqrt{1-n'^2_{x,j}-n'^2_{y,j}} \approx 1-(n'^2_{x,j}+n'^2_{y,j})/2$ we obtain

$$\begin{aligned} S &= S'_{\mathrm{B}} + \int_0^\beta d\tau \{ \sum_{\epsilon,k} (\delta\alpha^*_{\epsilon,k} \frac{\partial \delta\alpha_{\epsilon,k}}{\partial\tau} + \Delta_k \delta\alpha^*_{\epsilon,k}\delta\alpha_{\epsilon,k}) \\ &\quad + \frac{\Omega}{4}\sum_j (n'^2_{x,j}+n'^2_{y,j}) + \frac{g}{\sqrt{2}}\sum_{j,k} n'_{y,j}\{b^*_{k,j}\delta\alpha_{y,k} + b_{k,j}\delta\alpha^*_{y,k}\} \\ &\quad + \frac{g}{\sqrt{2}}\cos(\bar{\theta})\sum_{j,k} n'_{x,j}\{b^*_{k,j}\delta\alpha_{x,k} + b_{k,j}\delta\alpha^*_{x,k}\}\}, \end{aligned} \tag{3.44}$$

where the linear terms in the field fluctuations vanishes due to the conditions Eqs. (3.39) and (3.40) for $g > g_{\mathrm{c}}$. Here $\Omega = \omega_z/|\cos(\bar{\theta})|$ is the renormalised spin frequency and S'_{B} is the Berry phase term in the rotating basis. Note that the S'_{B} is invariant with respect to the rotation transformation, which implies that $S'_{\mathrm{B}} = \sum_j \int_0^\beta \langle n'_j|\frac{\partial}{\partial\tau}|n'_j\rangle$. Up to quadratic terms in the spin fluctuation fields the Berry phase can be written as

$$S'_{\mathrm{B}} = \frac{\mathrm{i}}{4}\sum_j \int_0^\beta d\tau \left(n'_{x,j}\frac{\partial n'_{y,j}}{\partial\tau} - n'_{y,j}\frac{\partial n'_{x,j}}{\partial\tau}\right). \tag{3.45}$$

We emphasize that in order to describe the collective excitations around the mean-field solution one needs to identify the number of conjugate pairs. In our model presented here the bosonic fields $\delta\alpha_{\epsilon,k}$ and $\delta\alpha^*_{\epsilon,k}$ in (3.44) are canonically conjugate variables, which leads to two independent degree of freedom. On the other hand the pairs $n'_{+,j} = (n'_{x,j}+\mathrm{i}n'_{y,j})/2$ and $n'_{-,j} = (n'_{x,j}-\mathrm{i}n'_{y,j})/2$ represent conjugate quantities corresponding to the spin fluctuations, which implies that one can expect in total three collective modes. In order to obtain the low-energy excitations, it is convenient to transform the spin fields in the momentum representation using $n'_{+,j} = \sum_k b_{k,j}n'_{+,k}$ and $n'_{-,j} = \sum_k b^*_{k,j}n'_{-,k}$, which yield

$$\begin{aligned} S &= \int_0^\beta \sum_k \{ n'_{-,k}\frac{\partial n'_{+,k}}{\partial\tau} + \sum_\epsilon (\delta\alpha^*_{\epsilon,k}\frac{\partial\delta\alpha_{\epsilon,k}}{\partial\tau} + \Delta_k\delta\alpha^*_{\epsilon,k}\delta\alpha_{\epsilon,k}) \\ &\quad + \Omega n'_{+,k}n'_{-,k} - \frac{g}{\sqrt{2}}(n'_{+,k}-n'_{-,-k})(\delta\alpha^*_{y,-k}-\delta\alpha_{y,k}) \\ &\quad + \frac{g}{\sqrt{2}}\cos(\bar{\theta})(n'_{+,k}+n'_{-,-k})(\delta\alpha^*_{x,-k}+\delta\alpha_{x,k})\}. \end{aligned} \tag{3.46}$$

The action (3.46) is quadratic in the field fluctuations, which lead to Gaussian functional integral. To diagonalize (3.46) one can introduce harmonic oscillator degrees of freedom for each pair of conjugate variables, such that we obtain

$$\begin{aligned} S &= \int_0^\beta d\tau \sum_k \{\mathrm{i}\sum_{a=1}^{3} \frac{\partial p_{a,k}}{\partial \tau} q_{a,k} + \frac{1}{2}\sum_{a=1}^{3} p_{a,k}p_{a,-k} \\ &\quad + \frac{1}{2}\sum_{a,a'=1}^{3} B^{(k)}_{a,a'} q_{a,k}q_{a',-k}\}, \end{aligned} \tag{3.47}$$

where the coupling matrix $B^{(k)}_{a,a'}$ is given by

$$B^{(k)}_{a,a'} = \begin{bmatrix} \Delta_k^2 & -g_{\mathrm{c}}^2\sqrt{\frac{2\Delta_k}{\Delta_0 m_+(k)}} & -g_{\mathrm{c}}^2\sqrt{\frac{2\Delta_k}{\Delta_0 m_-(k)}} \\ -g_{\mathrm{c}}^2\sqrt{\frac{2\Delta_k}{\Delta_0 m_+(k)}} & \frac{\varepsilon_k^2}{m_+(k)} & \frac{\varepsilon_k^2-\Delta_k^2}{\sqrt{m_+(k)m_-(k)}} \\ -g_{\mathrm{c}}^2\sqrt{\frac{2\Delta_k}{\Delta_0 m_-(k)}} & \frac{\varepsilon_k^2-\Delta_k^2}{\sqrt{m_+(k)m_-(k)}} & \frac{\varepsilon_k^2}{m_-(k)} \end{bmatrix}, \tag{3.48}$$

with $\varepsilon_k^2 = (\Delta_k^2 + \Omega^2)/2$ and $m_\pm(k) = (1 \pm \sqrt{\Delta_0/\Delta_k})^{-1}$. The dispersion relation of field fluctuations around the ground-state configuration, i.e., the collective spin-boson excitations, can be found by solving the eigenvalue problem $\sum_a B^{(k)}_{a,a'} u^{(p)}_a(k) = \omega_p^2(k) u^{(p)}_{a'}(k)$ with $p = 1, 2, 3$. The result is summarized in Fig. 3.9 where are shown the three branches of collective excitations, assuming periodic boundary conditions with nearest-neighbours bosonic tunneling $t_{j,l} = -t(\delta_{j,l+1} + \delta_{j,l-1})$ and bosonic dispersion $\Delta_k = \Delta + 2t\{1 - \cos(2\pi k/N)\}$. The lowest-lying branch correspond to the gapless Goldstone mode ω_{G}, which is linear for small k, i.e., $\omega_{\mathrm{G}} = c_{\mathrm{s}} 2\pi k/N + O(k^2)$ with characteristic slope $c_{\mathrm{s}} = 2g^2 \sin(\bar{\theta})\sqrt{t\Delta/(\Delta^4 + 4g^4\sin^2(\bar{\theta}))}$. The other two excitations, the so-called amplitude modes, remain gapped with $\omega_{\mathrm{A},\pm} = \Delta_\pm + O(k^2)$, where the gaps are given by

$$\Delta_\pm^2 = \frac{\Omega^2}{2} + \Delta^2 \pm \sqrt{\frac{\Omega^4}{4} + 4g_{\mathrm{c}}^4}. \tag{3.49}$$

So far, we have discussed the quantum fluctuations of the bosonic fields $\alpha_{\gamma,k}$ around their classical configuration. Because, in the symmetry broken phase the saddle-point solution predicts formation of bosonic condensates, it is naturally to express the cJT action in terms of density and phase of the respective condensate. Such a treatment allows us to connect the density fluctuations and the local phase of the condensates with the creation of the energy gaps in the spectra of cJT model. A convenient way to do this is to adopt the polar parametrization of the bosonic fields.

Polar decomposition

Let us choose the nonlinear polar parametrization

$$\alpha_{\gamma,j} = \sqrt{\bar{\rho} + \delta\rho_{\gamma,j}}\, e^{\mathrm{i}\zeta_{\gamma,j}}, \tag{3.50}$$

of the bosonic fields entering the path integral (3.32). Here the conjugate variables $\zeta_{\gamma,j}$ and $\delta\rho_{\gamma,j}$ describe, respectively, the local phase and the density fluctuation of the bosonic condensates around the mean-field solution $\bar{\rho} = (g/2\Delta_0)^2 \sin^2(\bar{\theta})$. In the limit of $\delta\rho_{\gamma,j}/\bar{\rho} \ll 1$ one can expand the square root in Eq. (3.50) and keep only the quadratic terms of the density fluctuations. The latter condition can be fulfilled for large coupling $g \gg g_{\rm c}$ ($\bar{\rho} \gg 1$), where the quantum fluctuations are suppressed. Assuming that the spin and bosonic fields vary smoothly on the scale of lattice constant a in a d dimensional cubic lattice one can perform gradient expansion, such that in the symmetry broken phase $g > g_{\rm c}$ the continuum action becomes

$$\begin{aligned} S &= a^{-d}\int_0^\beta d\tau \int d^d x\{S'_{\rm B} + \sum_\gamma \{{\rm i}\delta\rho_\gamma \frac{\partial\zeta_\gamma}{\partial\tau} + t\bar{\rho}a^2(\nabla\zeta_\gamma)^2 \\ &+ \frac{ta^2}{4\bar{\rho}}(\nabla\delta\rho_\gamma)^2 + \sqrt{\bar{\rho}}\frac{g\sin(\bar{\theta})}{2}(\zeta_\gamma^2 + \frac{\delta\rho_\gamma^2}{4\bar{\rho}^2})\} + \Omega n'_+ n'_- \\ &- \frac{g\cos(\bar{\theta})}{2\sqrt{\bar{\rho}}} n'_x(\delta\rho_{\rm r} + \delta\rho_{\rm l}) + g\sqrt{\bar{\rho}} n'_y(\zeta_{\rm r} - \zeta_{\rm l})\}. \end{aligned} \tag{3.51}$$

Observe that the term $t\bar{\rho}a^2(\nabla\zeta_\gamma)^2$ corresponds to the kinetic energy of a free particle with quadratic dispersion relation $\sim k^2$. Additionally, the spontaneous symmetry breaking gives rise to terms proportional to ζ_γ^2 such that the system gain an energy gaps which are not vanish in the limit $k \to 0$. As a result of that the conjugate pairs $(\zeta_{\rm r}, \delta\rho_{\rm r})$ and $(\zeta_{\rm l}, \delta\rho_{\rm l})$ lead to two gapped amplitude modes in the spectra of cJT model. Indeed, the subsequent diagonalization of the action (3.51) in the position-momentum representation gives an identical to $B^{(k)}_{a,a'}$ matrix Eq. (3.48) where the bosonic dispersion is replaced by its long-wave length limit, $\Delta_k \approx \Delta - td + t(ka)^2$.

In conclusion, we have provided the path-integral formalism of the cJT model. Within the saddle-point approximation we have obtained the classical ground-state of the cJT model. The solution predicts a quantum magnetic structural phase transition with formation of ferromagnetic spin order and condensations of the two bosonic species in the lowest energy mode. We have calculated the elementary excitations of our model and found a linear gapless Goldstone mode and two gapped amplitude modes in the symmetry-broken phase.

4. QUANTUM MAGNETISM IN MIXED SPIN SYSTEMS WITH IMPURITY DOPED ION CRYSTAL

In this chapter we propose the realization of linear crystals of cold ions which contain different atomic species for investigating quantum phase transitions and frustration effects in spin system beyond the commonly discussed case of $s = \frac{1}{2}$. Mutual spin-spin interactions between ions can be tailored via the Zeeman effect by applying oscillating magnetic fields with strong gradients. Further, collective vibrational modes in the mixed ion crystal can be used to enhance and to vary the strength of spin-spin interactions and even to switch those forces from a ferro- to an antiferromagnetic character. We consider the behavior of the effective spin-spin couplings in an ion crystal of spin-$\frac{1}{2}$ ions doped with high magnetic moment ions with spin $S = 3$. We analyze the ground state phase diagram and find regions with different spin orders including ferrimagnetic states. In the most simple non-trivial example we deal with a linear $\{Ca^+, Mn^+, Ca^+\}$ crystal with spins of $\{\frac{1}{2}, 3, \frac{1}{2}\}$. To show the feasibility with current state-of-the-art experiments, we discuss how quantum phases might be detected using a collective Stern-Gerlach effect of the ion crystal and high resolution spectroscopy. Here, the state-dependent laser-induced fluorescence of the indicator spin-$\frac{1}{2}$ ion, of species $^{40}Ca^+$, reveals also the spin state of the simulator spin-3 ions, $^{50}Mn^+$ as this does not possess suitable levels for optical excitation and detection.

4.1 Realization of Mixed spin-spin interaction

Going beyond spin-$\frac{1}{2}$ systems and trapping different ion species with spin $S > \frac{1}{2}$ will allow the study of novel aspects of quantum magnetism in a mixed spin chains [63, 64]. Such impurity doped systems might model effects which are of interest in solid state physics [65]. Our proposal is inspired by the outstanding progress in quantum logic spectroscopy [66, 67], where a single clock ion and a single readout ion are simultaneously confined and coupled through the mutual Coulomb repulsion, such that one can transfer the clock ion electronic state to the readout ion for high fidelity quantum state detection [68]. A different, new type of quantum logic readout technique enables us to propose quantum simulation in mixed ion crystals. For the case of neutral interacting atoms, the high magnetic moment of $6\mu_B$ of chromium has led to a wealth of novel effects [69, 70], made possible by the tuning of its spin interactions. ^{50}Mn, with an atomic number which is +1 higher as compared to Cr, shows a similar electronic structure and magnetic moment when singly ionized to Mn^+ for being trapped

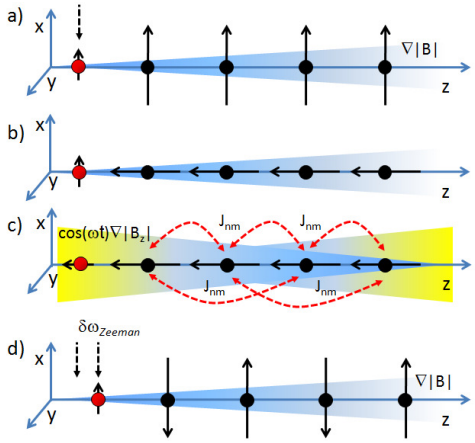

Fig. 4.1: Sketch of the proposed experimental sequence which a) initialization in the static magnetic gradient field, followed by a b) RF $\pi/2$ pulse on the Mn^+ ions and the c) creation of the spin-spin interactions by using an oscillating magnetic gradient field, and finally concluded by the d) collective spin readout on the Ca^+ ion using the position-dependent Stern-Gerlach effect. This leads to a bight or dark state of the Ca^+ ion which is imaged on a CCD camera as state-dependent fluorescence.

in the ion crystal.

In this section, we propose an efficient method for the creation of effective spin-spin interactions in ion crystals of spin-$\frac{1}{2}$ ions doped with different ion species with spin $S = 3$. An oscillating magnetic field gradient can be used to implement coupling between the spin states of both ion species and the collective motional states of the impurity doped crystal, (see Fig.4.1). The advantage to use an oscillating magnetic field instead of a laser field is due to avoiding the technical difficulties such as sideband cooling of the many vibrational modes and the necessity to use additional lasers to provide the spin-spin couplings. We show that by proper choice of the frequencies and the direction of the magnetic field gradient, the anisotropic Heisenberg model can be realized with tunable spin-spin couplings. We investigate the particular case of a field gradient applied along the trapping axis such that the spin-spin interactions are described by the transverse Ising model with *single-ion anisotropy*. We consider the ground state phase diagram for a small system consisting of two spin-$\frac{1}{2}$ ions and one spin-3 ion placed at the center, which is realizable with the current ion-trap technology. Due to the complex competition between the spin-spin couplings and the single-ion anisotropy we distinguish four regions with different spin orders. We find that for sufficiently strong antiferromagnetic nearest-neighbor coupling the spin order is *ferrimagnetic* wherein the two different spins are arranged in opposite directions. We show that the ferrimagnetic order can be frustrated due to competing next-nearest-neighbor coupling and the single-ion anisotropy which give rise to a highly entangled ground state.

We consider a harmonically confined impurity doped ion crystal with $N-K$ spin-$\frac{1}{2}$ ions with mass m and K spin-3 ions with mass M. For instance, this is the case of $^{40}Ca^{+}$ ion crystal doped with $^{50}Mn^{+}$ ions, which have $^{7}S_3$ electronic ground state. If the radial trap frequencies are much larger than the axial trap frequency ($\omega_{x,y} \gg \omega_z$), the ions arrange in a linear configuration along the axial z axis and occupy equilibrium positions. The axial trap potential is independent of the mass, so that the equilibrium position of the ions are independent of the composition of the ion crystal. A static magnetic field B_0 along the trap axis defines the quantization axis. The spin-$\frac{1}{2}$ sublevels $|\uparrow\rangle$ and $|\downarrow\rangle$ are Zeeman split by the applied magnetic field with a resonance frequency $\omega_0 = (g_J\mu_B/\hbar)B_0$. Here g_J denotes the Landé g-factor and μ_B is the Bohr magneton. The spin sublevels of spin-3 ions possess seven Zeeman states which we index as $|m\rangle$ with magnetic quantum number $m = -3, -2, \ldots, +3$ and resonance frequency $\tilde{\omega}_0$. In the case of ion crystal consisting of $^{40}Ca^{+}$ ions with electronic ground state $^{2}S_{1/2}$ doped with $^{50}Mn^{+}$ ions the Landé g-factor is $g_J \approx 2$ such that the resonance frequencies ω_0 and $\tilde{\omega}_0$ of both ion species are equal.

4.1.1 Magnetic field gradient along the z-direction

We assume that the impurity doped ion crystal interact collectively with oscillating magnetic gradient field with frequency ω applied along the z direction (for simplicity we omit the constant magnetic offset)

$$\vec{B} = \vec{e}_z z B_z \cos\omega t. \tag{4.1}$$

The Hamiltonian for N ions interacting with the magnetic field is $\hat{H} = \hat{H}_0 + \hat{H}_I$. Here

$$\hat{H}_0 = \frac{\hbar\omega_0}{2}\sum_{j=1}^{N-K}\sigma_j^z + \hbar\omega_0\sum_{k=1}^{K}S_k^z + \hbar\sum_{n=1}^{N}\omega_{n,z}\hat{a}_{n,z}^{\dagger}\hat{a}_{n,z}, \tag{4.2}$$

is the interaction-free Hamiltonian, with σ_j^z being the Pauli matrix for the j^{th} spin-$\frac{1}{2}$ ion and S_k^z is the spin operator for the k^{th} spin-3 ion with $S_z|m\rangle = m|m\rangle$. $\hat{a}_{n,z}^{\dagger}$ and $\hat{a}_{n,z}$ are, respectively, the creation and annihilation operators of collective phonons along the z axis with frequency $\omega_{n,z}$. The displacement $\hat{z}_j$ of the j^{th} ion from its equilibrium position can be expressed in terms of these set of operators as $\hat{z}_j = \sum_{n=1}^{N} b_{j,n}^z \Delta z_n(\hat{a}_{n,z}^{\dagger} + \hat{a}_{n,z})$. Here $\Delta z_n(a) = \sqrt{\hbar/2a\omega_{n,z}}$ with $a = m, M$ is the spread of the ground state wave function and $b_{j,n}^z$ $(n = 1, 2, \ldots, N)$ are the normal mode eigenvectors in the z direction. The interaction between the magnetic dipole moment of the ion species and the magnetic gradient is described by $\hat{H}_I = -\hat{\vec{\mu}}.\vec{B}$. The z-component of the magnetic-dipole moment for spin-$\frac{1}{2}$ ion is $\hat{\mu}_z = (\gamma/2)\sigma_z$ and, respectively, for spin-3 $\hat{\mu}_z = \gamma S_z$ with $\gamma = \mu_B g_L$. We may transform the Hamiltonian in the interaction picture with respect to $\hat{H}_0$ to obtain

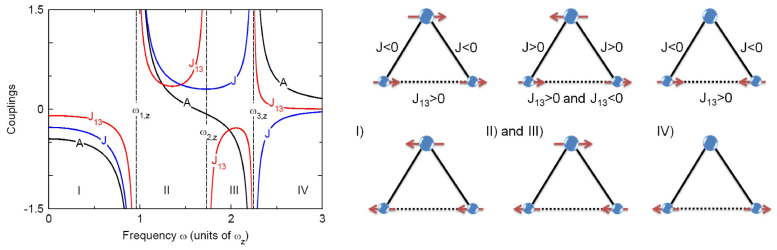

Fig. 4.2: The nearest-neighbor $J_{12} = J_{23} = J$, the next-nearest-neighbor J_{13} spin-spin couplings and the single-ion anisotropy A as a function of ω for ion crystal consisting of two spin-$\frac{1}{2}$ ions and one spin-3 ion placed at the center, (see Eq. (9.34)). The couplings J, J_{13} and A are normalized to $\varepsilon = (\Delta z \partial_z \omega_0)^2/(2\omega_z)$, which quantifies the change of the spin resonance frequency ω_0 due to the shift of the equilibrium position of the ion with trap frequency ω_z by an amount equal to the spread of the ground state wavefunction, $\Delta z = \sqrt{\hbar/2m\omega_z}$. right). Quantum phases differ in the regions (I) to (IV).

$$\hat{H}_I^z = -\hbar \sum_{n=1}^{N} \left(\sum_{j=1}^{N-K} \frac{\Omega_{j,n}^z}{2} \sigma_j^z + \sum_{k=1}^{K} \Omega_{k,n}^z S_k^z \right) \left(\hat{a}_{n,z}^\dagger e^{i(\omega+\omega_{n,z})t} + \hat{a}_{n,z} e^{-i(\omega+\omega_{n,z})t} \right)$$
$$-\hbar \sum_{n=1}^{N} \left(\sum_{j=1}^{N-K} \frac{\Omega_{j,n}^z}{2} \sigma_j^z + \sum_{k=1}^{K} \Omega_{k,n}^z S_k^z \right) \left(\hat{a}_{n,z}^\dagger e^{-i(\omega-\omega_{n,z})t} + \hat{a}_{n,z} e^{i(\omega-\omega_{n,z})t} \right). \quad (4.3)$$

The function $\Omega_{j,n}^z = b_{j,n}^z \Delta z_n B_z \gamma / 2\hbar$ is the Rabi frequency of the j^{th} ion, which quantifies the coupling to the n^{th} vibrational mode. Hence, the oscillating magnetic gradient field mediates a coupling between the internal states of the ions and the external (motional) states of the ion crystal. Indeed, the two terms in the Hamiltonian (4.3) describe a time-varying spin-dependent displacement with frequencies $(\omega + \omega_{n,z})$ and $(\omega - \omega_{n,z})$. If the frequency ω is not resonant to any vibrational mode and the condition $|\omega_{n,z} - \omega| \gg \Omega_{j,n}^z$ is satisfied for any n then we can perform time-averaging of the rapidly oscillating terms in (4.3). Hence, we arrive at the following time-averaged effective Hamiltonian

$$\hat{H}_{eff}^z = \hbar \sum_{\substack{j,j'=1 \\ j>j'}}^{N-K} J_{j,j'}^{(1,z)} \sigma_j^z \sigma_{j'}^z + \hbar \sum_{\substack{k,k'=1 \\ k>k'}}^{K} J_{k,k'}^{(2,z)} S_k^z S_{k'}^z$$
$$+\hbar \sum_{j,k=1}^{N} J_{j,k}^{(3,z)} \sigma_j^z S_k^z + \hbar \sum_{k=1}^{K} A_k^z (S_k^z)^2. \quad (4.4)$$

Therefore, the off-resonant oscillating magnetic gradient creates effective spin-spin interaction between the identical and different ion species in the crystal.

The first two terms in (4.4) quantify the spin-spin coupling between the spin-$\frac{1}{2}$ ions and the spin-3 ions. The third term in (4.4) describes the spin-spin coupling between the different ion species. Surprisingly, the adiabatic elimination of the vibrational modes for a ion crystal with $s > \frac{1}{2}$ ions gives rise to single-ion anisotropy term A_j^z which quantifies the non-linear Zeeman shift of the spin-3 magnetic sublevels. We note that the non-linear Zeeman shift for spin-$\frac{1}{2}$ ions is equal for the both magnetic sublevels, thereby it is proportional to the unit matrix. The couplings in (4.4) are given by

$$J_{j,j'}^{(1,z)} = \frac{B_z^2\gamma^2}{8\hbar m}\sum_{n=1}^{N}\frac{b_{j,n}^z b_{j',n}^z}{\omega^2-\omega_{n,z}^2},\; J_{k,k'}^{(2,z)} = \frac{B_z^2\gamma^2}{2\hbar M}\sum_{n=1}^{N}\frac{b_{k,n}^z b_{k',n}^z}{\omega^2-\omega_{n,z}^2},$$
$$J_{j,k}^{(3,z)} = \frac{B_z^2\gamma^2}{4\hbar\sqrt{mM}}\sum_{n=1}^{N}\frac{b_{j,n}^z b_{k,n}^z}{\omega^2-\omega_{n,z}^2},\; A_k^z = \frac{B_z^2\gamma^2}{4\hbar M}\sum_{n=1}^{N}\frac{(b_{k,n}^z)^2}{\omega^2-\omega_{n,z}^2}. \tag{4.5}$$

The main advantage of using an oscillating magnetic field gradient instead of constant is that we may engineer a variety of interactions between the ions. Fig. 4.2 shows the spin-spin couplings and the single-ion anisotropy (9.34) for a chain of two spin-$\frac{1}{2}$ ions and one spin-3 ion place at the center versus the frequency ω. In contrast with the constant magnetic field gradient applied along the trapping axis z wherein the spin-couplings can be only ferromagnetic, now as ω is varied the magnitude and the sign of the couplings are changed which allows the creation of ferromagnetic, antiferromagnetic or frustrated interaction between the ions. The ground state of Hamiltonian (4.4) highly depends from the sign of the single-ion anisotropy terms A_k^z. Indeed, for sufficiently large positive single-ion anisotropy ($A_k^z \gg 0$), the spin-3 ions have magnetic quantum number $m = 0$ for the ground state, while in the opposite limit ($|A_k^z| \gg 0$) the spin-3 ground state projection is $m = \pm 3$.

4.1.2 Magnetic field along xyz-direction

Consider the magnetic gradient applied along the xyz direction

$$\vec{B}(x,y,z) = \vec{e}_z z B_z \cos\omega t + \vec{e}_x x B_x f(t) - \vec{e}_y y B_y f(t), \tag{4.6}$$

with $f(t) = (\cos\omega_b t + \cos\omega_r t)$. Such a field can be created in a micro structured planar ion trap, which contains a central wire loop. The oscillating field in x-y direction provides additional coupling $\Omega_{j,n}^q = b_{j,n}^q \Delta q_n B_q \gamma/2\hbar$ ($q = x, y$) between the internal and motional degree of freedom of the ion crystal. We assume that the frequencies $\omega_b - \omega_0 = \delta$ and $\omega_r - \omega_0 = -\delta$ are tuned to the blue- and red- sideband transition with detuning $\pm\delta$. After applying an optical rotating-wave approximation (neglecting the terms $\omega_0 + \omega_{b,r}$) and assuming that $|\omega_{n,q} - \delta| \gg \Omega_{j,n}^q$ is fulfilled for any vibrational mode in the x-y-direction, the

time-averaged effective Hamiltonian is given by

$$\hat{H}_{eff} = \hbar \sum_{q=x,y,z} \{ \sum_{\substack{j,j'=1 \\ j>j'}}^{N-K} J_{j,j'}^{(1,q)} \sigma_j^q \sigma_{j'}^q + \sum_{\substack{k,k'=1 \\ k>k'}}^{K} J_{k,k'}^{(2,q)} S_k^q S_{k'}^q + \sum_{j,k=1}^{N} J_{j,k}^{(3,q)} \sigma_j^q S_k^q + \sum_{k=1}^{K} A_k^q (S_k^q)^2 \}. \quad (4.7)$$

The spin-spin couplings in x-y direction are identical in form to (9.34) by replacing $\omega \to \delta$ and $z \to x, y$. Hence, the magnetic field (4.6) creates an anisotropic Heisenberg (XYZ) interaction between the effective spins.

4.1.3 Transverse Ising Model

The quantum transverse Ising Hamiltonian is given by

$$H_{TI} = H_{eff}^z - \hbar B_x^0 \{ \sum_{j=1}^{N-K} \frac{\sigma_j^x}{2} + \sum_{k=1}^{K} S_k^x \}. \quad (4.8)$$

The last term in (4.8) can be simulated by driving transitions between the ion spin states employing radio frequency field $\vec{B}_0 = \vec{e}_x B_0 \cos\tilde{\omega} t$. Assuming the resonance condition is fulfilled, i.e., $\tilde{\omega} = \omega_0$ we obtain the effective transverse field $B_x^0 = \gamma B_0 / 2\hbar$.

The simplest non-trivial case is to consider ion chain with two spin-$\frac{1}{2}$ ions and one spin-3 ion placed at the center. Such ordering of ions is consistent with the natural behavior, as observed in Ref. [71]. When applying the oscillating gradient field, the resulting spin-spin couplings are shown in Fig. (4.2) as a function of the drive frequency ω. We may distinguish four different regions wherein the spin-spin interactions are ferromagnetic, antiferromagnetic, or frustrated. The presence of the single-ion anisotropy A in (4.8) changes substantially the ground state phase diagram compared to the case of spin-$\frac{1}{2}$ ion chain. In contrast to the spin-$\frac{1}{2}$ string, the ground state of the mixed $(S, s) = (3, \frac{1}{2})$ spin system can be frustrated due to the complex competition between the spin-spin couplings J and J_{13} and the single-ion anisotropy A.

In region I), see Fig. (4.2), all interactions are ferromagnetic ($J, J_{13} < 0$) and the resulting ground state of the Hamiltonian (4.8) as $B_x^0 \to 0$ is a coherent superposition of two ferromagnetic states $|\uparrow\uparrow\rangle |3\rangle$ and $|\downarrow\downarrow\rangle |-3\rangle$. Because the single-ion anisotropy is negative ($A < 0$), the ground state energy is minimized for spin-3 state with magnetic quantum number $m = \pm 3$. The ferromagnetic population $P_{fm,3} = P_{\uparrow\uparrow 3} + P_{\downarrow\downarrow -3}$ as a function of the effective magnetic field and the frequency ω is shown in Fig. (4.3)a. In the region II) the spin interactions are antiferromagnetic ($J, J_{13} > 0$). This is the case of ferrimagnetism in which spins of two types interact by nearest-neighbor antiferromagnetic coupling, (see Fig. (4.3)b). However, the ferrimagnetic interaction is frustrated due to the competing next-nearest-neighbor antiferromagnetic coupling $J_{13} > 0$ which disturbs

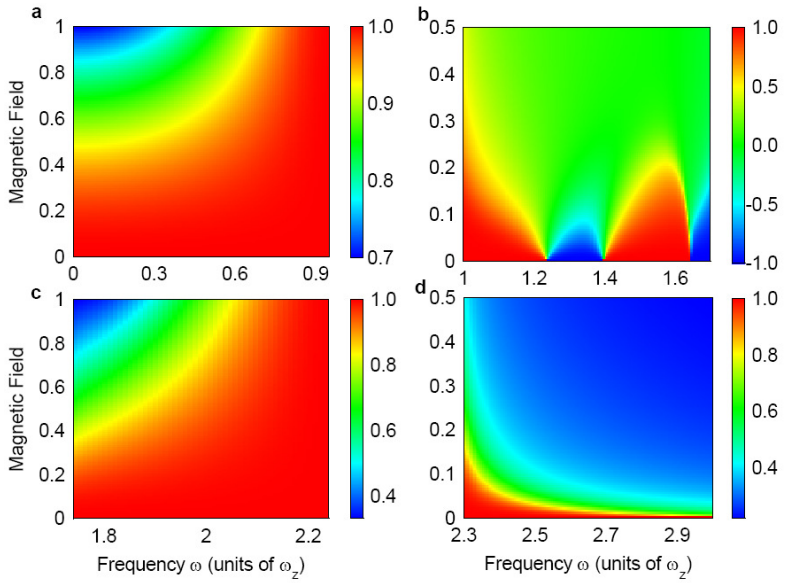

Fig. 4.3: The ground state phase diagram calculated by an exact diagonalization of Hamiltonian (4.8). a) The ferromagnetic population $P_{fm,3}$ as a function of the normalized transverse magnetic field B_x^0/ε and the frequency ω. In region I) the spin-spin couplings are ferromagnetic $J, J_{13} < 0$ and the single-ion anisotropy is $A < 0$. b) The population difference $P_{f,1} - P_{f,2} + P_{f,3} - P_{a,3}$ as a function of the normalized transverse magnetic field B_x^0/ε and the frequency ω. In region II) the spin-spin couplings are antiferromagnetic $J, J_{13} > 0$ and the single-ion anisotropy is $A > 0$. By increasing ω as $B_x^0 \to 0$ the system undergoes transition $|\psi_{f,1}\rangle \to |\psi_{f,2}\rangle \to |\psi_{f,3}\rangle \to |\psi_{a,3}\rangle$. c) The ferrimagnetic population $P_{f,3}$ as a function of the normalized transverse magnetic field B_x^0/ε and the frequency ω. In region III) the spin-spin couplings are, respectively, $J > 0$, $J_{13} < 0$ and the single-ion anisotropy is $A < 0$. d) The antiferromagnetic population $P_{a,0}$ as a function of the normalized transverse magnetic field B_x^0/ε and the frequency ω. In region IV) the spin-spin couplings are $J < 0$, $J_{13} > 0$, respectively, and the single-ion anisotropy is $A > 0$.

the ferrimagnetic order and tends to align the two spins-$\frac{1}{2}$ in a antiferromagnetic state. Additionally, the ferrimagnetic interaction is also frustrated due to the strong positive single-ion anisotropy $A > 0$ which attempts to project the spin-3 state $|m\rangle$ in a quantum number $m = 0$. In the beginning of region II) $A > 0$ is high but the ferrimagnetic configuration is still energetically favorable such that the ground state of Hamiltonian (4.8) as $B_x^0 \to 0$ is a superposition of two ferrimagnetic states $|\psi_{f,1}\rangle = (|\uparrow\uparrow\rangle\,|-1\rangle + |\downarrow\downarrow\rangle\,|1\rangle)/\sqrt{2}$, wherein the spins $S = 3$ and $s = \frac{1}{2}$ are aligned anti-parallel with each other. By increasing ω the single-ion anisotropy A decreases which allows the quantum number m to increase and the resulting ground state is $|\psi_{2,f}\rangle = (|\uparrow\uparrow\rangle\,|-2\rangle + |\downarrow\downarrow\rangle\,|2\rangle)/\sqrt{2}$. For $A/J = 2/3$ which occurs at $\omega \approx 1.24\omega_z$ the ground state for $B_x^0 = 0$ is an entangled superposition of four ferrimagnetic states $|\uparrow\uparrow\rangle\,|-1\rangle$, $|\downarrow\downarrow\rangle\,|1\rangle$, $|\uparrow\uparrow\rangle\,|-2\rangle$, and $|\downarrow\downarrow\rangle\,|2\rangle$. By decreasing A the ferrimagnetic state $|\psi_{2,f}\rangle$ undergoes a transition to $|\psi_{3,f}\rangle = (|\uparrow\uparrow\rangle\,|-3\rangle + |\downarrow\downarrow\rangle\,|3\rangle)/\sqrt{2}$. At the transition point $\omega = 1.4\omega_z$ and $A/J = 0.4$ the resulting ground state for $B_x^0 = 0$ is an entangled superposition of four ferrimagnetic states, $|\uparrow\uparrow\rangle\,|-2\rangle$, $|\downarrow\downarrow\rangle\,|2\rangle$, $|\uparrow\uparrow\rangle\,|-3\rangle$, and $|\downarrow\downarrow\rangle\,|3\rangle$. For sufficiently high positive J_{13} the ferrimagnetic arrangement is not favorable and the two spin-$\frac{1}{2}$ ions are arranged in an antiferromagnetic state. Hence, the ferrimagnetic configuration is broken and the ground state is $|\psi_{a,3}\rangle = (|\uparrow\downarrow\rangle + |\downarrow\uparrow\rangle)(|3\rangle + |-3\rangle)/2$. At the transition point $\omega \approx 1.65\omega_z$, the ground state of the Hamiltonian (4.8) is an entangled superposition of six states: two ferrimagnetic states $|\uparrow\uparrow\rangle\,|-3\rangle$ and $|\downarrow\downarrow\rangle\,|3\rangle$, and four antiferromagnetic states $|\uparrow\downarrow\rangle\,|3\rangle$, $|\uparrow\downarrow\rangle\,|-3\rangle$, $|\downarrow\uparrow\rangle\,|3\rangle$, and $|\downarrow\uparrow\rangle\,|-3\rangle$. In region III) the nearest-neighbor spin coupling is antiferromagnetic ($J > 0$) such that the ferrimagnetic configuration is favorable. In contrast with the region II), no frustration exist because the next-nearest-neighbor coupling is ferromagnetic $J_{13} < 0$ and $A < 0$. In the entire region the ground state is a ferrimagnetic $|\psi_{f,3}\rangle$, which minimizes all interactions. In Fig. (4.3)c the ferrimagnetic population $P_{f,3} = P_{\uparrow\uparrow-3} + P_{\downarrow\downarrow 3}$ versus the effective magnetic field and the frequency ω is shown . In region IV) the single-ion anisotropy is positive ($A > 0$) which causes the spin-3 being projected into quantum number $m = 0$. Additionally, the next-nearest-neighbor coupling is antiferromagnetic $J_{13} > 0$ and the resulting ground state as $B_x^0 \to 0$ is antiferromagnetic $|\psi_{a,0}\rangle = (|\uparrow\downarrow\rangle\ + |\downarrow\uparrow\rangle)\,|0\rangle\,/\sqrt{2}$. The antiferromagnetic population $P_{a,0} = P_{\uparrow\downarrow 0} + P_{\downarrow\uparrow 0}$ is shown in Fig. (4.3)d.

In conclusion we have proposed a method for the creation and manipulation of the spin-spin interactions in spin-$\frac{1}{2}$ ion crystal doped with high magnetic moment ions with spin $S = 3$. It is shown that by tuning the frequency and direction of the oscillating magnetic field gradients various fundamental models in quantum magnetism of mixed spin systems can be realized. Because of the competing long-range spin-spin couplings the spin orders are extremely numerous even for spin system consisting of a small number of ions. We have proposed a technique for spin preparation and readout based on the frequency addressing of an indicator spin-$\frac{1}{2}$ ion in the presence of spatially varying magnetic field.

5. TRAPPED-ION EMULATION OF THE ELECTRIC DIPOLE MOMENT OF NEUTRAL RELATIVISTIC PARTICLES

In this Chapter, we propose the simulation of a neutral relativistic particle with an intrinsic electric dipole moment (EDM) by means of the Dirac equation. This allows us to experimentally emulate the behavior of an EDM in an electrostatic field and two ensuing effects, which have not been measured so far: (i) lifting of spin degeneracy by an electrostatic field, and (ii) Larmor-like precession of a particle spin in an electrostatic field. In addition, we explore a few relativistic properties of these effects and propose their emulation with trapped ions.

5.1 Dirac Hamiltonian

The Dirac Hamiltonian for a neutral particle with electric dipole and magnetic moments in an external electromagnetic field is given by

$$\begin{aligned} \hat{H} &= c\hat{\alpha}\cdot\hat{\mathbf{p}} + \hat{\beta}mc^2 + d_a(ic\hat{\beta}\hat{\alpha}\cdot\mathbf{B} + 2\hat{\beta}\hat{\mathbf{S}}\cdot\mathbf{E}) \\ &\quad +\mu_a(i\hat{\beta}\hat{\alpha}\cdot\mathbf{E}/c - 2\beta\hat{\mathbf{S}}\cdot\mathbf{B}) \end{aligned} \tag{5.1}$$

where c is the speed of light, m is the particle mass, $\hat{\alpha}$ and $\hat{\beta}$ are the Dirac matrices, $\hat{S} = -\frac{i}{4}\hat{\alpha}\times\hat{\alpha}$ is the spin vector operator in relativistic theory, $\mathbf{E}$ is the electric field, $\mathbf{B}$ is the magnetic field, d_a is the electric dipole moment of the relativistic particle, and μ_a is its magnetic dipole moment. The extended Dirac Hamiltonian (5.1) is written in its standard form in the laboratory reference frame. For $d_a =\neq 0$, the Hamiltonian is not invariant with respect to space inversion and time reversal. For a neutral particle, such as neutrons, neutrinos, or some hypothetical dark matter particles, moving in a constant electrostatic field with respect to the laboratory reference frame, we have $\mathbf{B} = 0$, which simplifies the Hamiltonian to the block matric form

$$\hat{H} = \begin{bmatrix} mc^2 + d_a\hat{\sigma}\cdot\mathbf{E} & c\hat{\sigma}\cdot\hat{\mathbf{p}} + i\mu_a\hat{\sigma}\cdot\mathbf{E}/2 \\ c\hat{\sigma}\cdot\hat{\mathbf{p}} - i\mu_a\hat{\sigma}\cdot\mathbf{E}/2 & -mc^2 - d_a\hat{\sigma}\cdot\mathbf{E} \end{bmatrix}. \tag{5.2}$$

where $\hat{\sigma}$ is a vector of the Pauli matrices. In this fully relativistic Hamiltonian, the term $i\mu_a\hat{\sigma}\cdot\mathbf{E}/c$ coupling the magnetic dipole moment μ_a to the electrostatic field $\mathbf{E}$ in the laboratory frame of reference bears some resemblance to the spin-orbit coupling term which appears in the nonrelativistic limit of the Dirac equation. Classically the spin-orbit coupling term is induced from the Joules-Bernoulli equations as proportional to $\mathbf{B}\sim\mathbf{v}\times\mathbf{E}$, where $\mathbf{v}$ is the speed of the

particle. However, the term $i\mu_a\hat{\sigma}\cdot\mathbf{E}/c$ from the fully relativistic Hamiltonian is not the spin-orbit coupling term, which, although it is relativistic in nature, appears in the nonrelativistic Pauli equation. The eigenvectors of $\hat{H}$ are sought in the form of plane waves $|\psi_l\rangle = |l(\mathbf{p})\rangle e^{-i(\mathbf{p}\cdot\mathbf{r})/\hbar}$, where $|l(\mathbf{p})\rangle$ are four-component spinors with eigenvalue E_l. The general solution of the time-dependent Dirac equation $i\hbar\partial\Psi/\partial t = \hat{H}\Psi$ is given by $|\Psi\rangle = \sum_l b_l|l(\mathbf{p})\rangle e^{-i(\mathbf{p}\cdot\mathbf{r}-E_l t)/\hbar}$, where b_l are complex-values coefficients.

Recently, simulation of the 3D Dirac equation in its supersymmetric representation without external potential has been proposed for simulation of *Zitterbewegung* of a free electron [73]. Following this work, we propose here how to simulate Eq. (5.2) in the standard representation. The simulation of the 3D Dirac equation requires a single ion trapped in a Pual trap, in which the ion oscillates in the three spatial directions x, y, z with frequencies ν_j ($j = x, y, z$). The Dirac bispinor $|l(p)\rangle$ is implemented as a linear combination of four internal ion levels $|a\rangle$, $|b\rangle$, $|c\rangle$, and $|d\rangle$, which represent the internal degrees of freedom of the relativistic particle: $|l(\mathbf{p})\rangle = u_a|a\rangle + u_b|b\rangle + u_c|c\rangle + u_d|d\rangle$. The motional degrees of freedom of the simulated particle can me mapped to the ion vibrations using the relations $\hat{p}_j = i\hbar(\hat{a}_j^\dagger - \hat{a}_j)/2\Delta_j$, where $\hat{a}_j$ and $\hat{a}_j^\dagger$ are the phonon creation and annihilation operators, $\Delta_j = \sqrt{\hbar/2M\nu_j}$ is the spread in the position of the ground-state wave function, and M is the ion mass.

The Hamiltonian (5.2) can be implemented by simultaneous application of detuned red-sideband (Jaynec-Cummings (JC)), blue-sideband (anti-Jaynec-Cummings (AJC)), and carrier interactions between appropriately chosen pairs of the ion levels $|a\rangle$, $|b\rangle$, $|c\rangle$, and $|d\rangle$.

The detuned JC and AJC Hamiltonians read

$$\begin{aligned}\hat{H}_j^{JC} &= \hbar\eta_j\tilde{\Omega}_j(\hat{\sigma}^+\hat{a}_j e^{i\phi_r} + \hat{\sigma}^-\hat{a}_j^\dagger e^{-i\phi_r}) + \hbar\delta_j\hat{\sigma}_z,\\ \hat{H}_j^{AJC} &= \hbar\eta_j\tilde{\Omega}_j(\hat{\sigma}^+\hat{a}_j^\dagger e^{i\phi_r} + \hat{\sigma}^-\hat{a}_j e^{-i\phi_r}) + \hbar\delta_j\hat{\sigma}_z\end{aligned} \tag{5.3}$$

where ϕ_r and ϕ_b are the red- and blue-sideband phases, δ_j is the detuning, $\tilde{\Omega}_j$ are the Rabi frequencies, σ^+ and σ^- are the raising and lowering operators between two pairs of internal ion levels, and $\eta_j = k\Delta_j$ is the Lamb-Dicke parameter, where k is the wave number of the driving field. Homogeneity of space requires setting the trap frequencies in the three spatial directions equal to each other, $\nu_x = \nu_y = \nu_z$. This ensures that $\tilde{\Omega}_j = \tilde{\Omega}$, $\Delta_j = \Delta$, and $\eta_j = \eta$ for all spatial directions j.

In our proposal, the mass term $\beta m_0 c^2$ is implemented by the Stark shift part of two JC and two AJC interactions applied simultaneously on the transitions $|a\rangle \leftrightarrow |d\rangle$ and $|b\rangle \leftrightarrow |c\rangle$, i.e., we have the mapping $\beta m_0 c^2 \to 2\hbar\delta\hat{\sigma}_z^{ad} + 2\hbar\delta\sigma_z^{bc}$. The momentum term $c\hat{\alpha}\cdot\hat{\mathbf{p}}$ maps to the three terms $2\eta\Delta\tilde{\Omega}(\hat{\sigma}_x^{ad} + \hat{\sigma}_x^{bc})\hat{p}_x$, $2\eta\Delta\tilde{\Omega}(\hat{\sigma}_y^{ad} - \hat{\sigma}_y^{bc})\hat{p}_y$, and $2\eta\Delta\tilde{\Omega}(\hat{\sigma}_x^{ac} - \hat{\sigma}_x^{bd})\hat{p}_z$, where the superscripts in the Pauli matrices indicate the internal ion levels between which the coupling are applies.

The term describing the interaction between the EDM and the electrostatic field $2d_a\beta\hat{\mathbf{S}}\cdot\mathbf{E}$ in the Dirac Hamiltonian (5.1) is implemented by the carrier interaction $\hat{H}_j^{c(1)} = \hbar\Omega_j^{(1)}(\hat{\sigma}^+ e^{i\phi} + \hat{\sigma}^- e^{-\phi})$ with Rabi frequency $\Omega_j^{(1)}$, using

the mapping $2d_a\beta\hat{\mathbf{S}}\cdot\mathbf{E} \rightarrow 2\hbar\Omega^{(1)}[\hat{\sigma}_x^{ab}-\hat{\sigma}_x^{cd},\hat{\sigma}_y^{ab}-\hat{\sigma}_y^{cd},\hat{\sigma}_z^{ab}-\hat{\sigma}_z^{cd}]$. The term describing the coupling of the electrostatic field to the MDM is implemented with the help of carrier interaction with Rabi frequency $\Omega_j^{(2)}$, using the mapping $i\mu_a\hat{\beta}\hat{\alpha}\cdot\mathbf{E}/c \rightarrow 2\hbar\Omega^{(2)}[-\hat{\sigma}_y^{ad}-\hat{\sigma}_y^{bc},\hat{\sigma}_x^{bc}-\hat{\sigma}_x^{ad},\hat{\sigma}_y^{bd}-\hat{\sigma}_y^{ac}]$. The above terms can be implemented by setting appropriately the phases of the carrier interactions. This establishes the following relationship between the parameters of the Hamiltonian (5.2) and the trapped ion:

$$(\mu_a/c)E_j = 2\hbar\Omega_j^{(2)}, \quad d_aE_j = 2\hbar\Omega_j^{(1)}, \quad c = 2\eta\Delta\tilde{\Omega}, mc^2 = 2\hbar\delta. \tag{5.4}$$

While it is possible to implement the Hamiltonian (5.2) in supersymmetric representation, this has the drawback of establishing a correlation between the sizes of the emulated mass term and the emulated EDM term. The presented proposal for emulation of Eq. (5.2) has the advantage of independent experimental control of the emulated mass and the EDMterms.

To simplify the experimental requirements, we consider a model which can be regarded as either a 1D limit of Eq. (5.2) or a 3D variant in which the direction of propagation is along the direction of an externally applied electric field. When the external electric field and the direction of propagation are aligned, no spin-orbit coupling term can arise due to the invariance of the longitudinal components of the electromagnetic field with respect to Lorentz transformations. The choice of the direction is arbitrary and does not change the experimental observables. For the sake of convenience, we work with the x direction. The model is

$$\hat{H}_{1D} = c\alpha_x\hat{p}_x + \hat{\beta}mc^2 + 2d_a\hat{\beta}\hat{S}_xE_x + i(\mu_a/c)\hat{\beta}\hat{\alpha}_xE_x. \tag{5.5}$$

Note that the terms $2d_a\hat{\beta}\hat{S}_xE_x$ and $i(\mu_a/c)\hat{\beta}\alpha_xE_x$ are invariant with respect to Lorentz boosts in the x direction, and therefore there is no effective magnetic field seen by the particle in its stationary reference frame. This is another point which differentiates the $i(\mu_a/c)\hat{\beta}\alpha_xE_x$ term from the spin-orbit coupling or $\mathbf{v}\times\mathbf{E}$ term which will disappear in the 1D limit. Eq. (5.5) maps to the trapped-ion Hamiltonian

$$\begin{aligned}\hat{H}_{1D} &= 2\eta\Delta\tilde{\Omega}(\hat{\sigma}_x^{ad}+\hat{\sigma}_x^{bc})\hat{p}_x + 2\hbar\delta(\hat{\sigma}_z^{ad}+\hat{\sigma}_z^{bc}) \\ &\quad +2\hbar\Omega^{(1)}(\hat{\sigma}_x^{ab}-\hat{\sigma}_x^{cd}) - 2\hbar\Omega^{(2)}(\hat{\sigma}_y^{ad}+\hat{\sigma}_y^{bc}).\end{aligned} \tag{5.6}$$

The momentum terms and the mass term in Eq. (5.6) can be implemented by applying simultaneously two pairs of detuned AJC and JC interactions on the transitions $|a\rangle \leftrightarrow |c\rangle$ with $\phi_r = 3\pi/2$ and $\phi_b = \pi/2$,

$$\begin{aligned}2\eta\tilde{\Omega}\Delta\hat{\sigma}_x^{ad}\hat{p}_x + 2\hbar\delta\hat{\sigma}_z^{ad} &= \hat{H}_x^{JC,ad} + \hat{H}_x^{AJC,ad}, \\ 2\eta\tilde{\Omega}\Delta\hat{\sigma}_x^{bc}\hat{p}_x + 2\hbar\delta\hat{\sigma}_z^{bc} &= \hat{H}_x^{JC,bc} + \hat{H}_x^{AJC,bc},\end{aligned} \tag{5.7}$$

with $\beta_x = \beta$. The implementation of the EDM term $2d_a\hat{\beta}\hat{S}_xE_x$ requires two carrier interactions with Rabi frequency $\Omega^{(1)}$ on the transitions $|a\rangle \leftrightarrow |b\rangle$ and $|c\rangle \leftrightarrow |d\rangle$: $2\hbar\Omega^{(1)}(\hat{\sigma}_x^{ab}-\hat{\sigma}_x^{cd}) = \hat{H}_{ab}^{c(1)}(\phi=0)+\hat{H}_{cd}^{c(1)}(\phi=\pi)$. Using independently

and simultaneously two more carrier interactions with Rabi frequency $\Omega^{(2)}$ on the transitions $|a\rangle \leftrightarrow |d\rangle$ and $|b\rangle \leftrightarrow |c\rangle$, the MDM term $i(\mu_a/c)\hat{\beta}\hat{\alpha}_x E_x$ can be implemented : $-2\hbar\Omega^{(2)}(\hat{\sigma}_y^{ad} + \hat{\sigma}_y^{bc}) = \hat{H}_{ad}^{c(2)}(\phi = \pi/2) + \hat{H}_{bc}^{c(2)}(\phi = \pi/2)$.

The presence of the EDM term $2d_a\hat{\beta}\hat{S}_x E_x$ in the Hamiltonian (5.2) causes two interlinked effects. First it leads to a lifting of spin degeneracy in the spectrum of the Hamiltonian (5.2), which is caused just by the electrostatic field. This effect is technically similar to the lifting of spin degeneracy by a static magnetic field, which underpins the anomalous Zeeman and Paschen-Back effects in atomic physics. This is explained naturally because the electric dipole moment of any particle is aligned with its spin. However, conceptually it is different from SU(2) breaking by magnetic field since the lifting of spin degeneracy due to magnetic field involves only the breaking of time-reversal invariance, while the lifting of spin-degeneracy by EDM–electric field coupling breaks both time- and spacereversal symmetries. An alternative explanation can be sought in the fact that the electric dipole term $2d_a\hat{\beta}\hat{S}_x E_x$ breaks the space inversion symmetry while preserving the translational invariance in an electrostatic field. The second effect is a consequence of the first: the precession of the EDM and the associated spin around the electrostatic field, similar to the Larmor precession of a particle spin around a static magnetic field.

While these two effects can also be modeled within a nonrelativistic limit, the simulation of the 1D Dirac equation presents the opportunity to study two unusual purely relativistic features of spin splitting by electrostatic field. The first is the disappearance of spin splitting when the mass in the Dirac equation tends to zero. The second is the reduction in the size of the spin splitting caused by the coupling of the electrostatic field to the MDM embodied in the term $i(\mu_a/c)\hat{\beta}\hat{\alpha}_x E_x$. The mathematical analysis follows.

For a free Dirac Hamiltonian $E_x = 0$, the positive and negative energy eigenvalues $E_\pm = \pm\sqrt{c^2p_x^2 + m^2c^4}$ are doubly degenerate, reflecting the spin degeneracy. For a nonzero electrostatic field ($E_x \neq 0$), there is no degeneracy in the spectrum of the Hamiltonian (5.2),

$$E_\pm^\uparrow = \pm\sqrt{c^2p_x^2 + E_x^2(\mu_a/c)^2 + (mc^2 + E_x d_a)^2}, \quad E_\pm^\downarrow = \pm\sqrt{c^2p_x^2 + E_x^2(\mu_a/c)^2 + (mc^2 - E_x d_a)^2}. \tag{5.8}$$

The splitting $\Delta E = E_+^\uparrow - E_+^\downarrow = -(E_-^\uparrow - E_-^\downarrow)$ is

$$\Delta E = \sqrt{c^2p_x^2 + E_x^2(\mu_a/c)^2 + (mc^2 + E_x d_a)^2} - \sqrt{c^2p_x^2 + E_x^2(\mu_a/c)^2 + (mc^2 - E_x d_a)^2}. \tag{5.9}$$

First, in the limit $m = 0$ the spin splitting vanishes, $\Delta E = 0$, despite the fact that the EDM and electrostatic field are nonzero. This is in stark contrast to the nonrelativistic model, in which the spin splitting does not depend in any way on the mass term. Second, the term $i(\mu_a/c)\hat{\beta}\hat{\alpha}_x E_x$ does not lead to a lifting of the degeneracy as $\Delta E = 0$ for $d_a = 0$ and $\mu_a \neq 0$ and $E_x \neq 0$ by itself. Estimates of the EDM and MDM of several electrically neutral particles show that $mc^2 \ll E_x d_a, (\mu_a/c)E_x$. Expanding Eq. (5.9) in Taylor series with respect to the small variable $(\mu_a/c)E_x$ and making the approximations $E_+^\uparrow \sim E_+^\downarrow \sim mc^2$, we get for

the energy splitting to second order $\Delta E \approx 2E_x d_a - \frac{\mu_a^2 E_x^2}{m^2 c^4} d_a E_x$. Therefore, the effect of the term $i(\mu_a/c)\hat{\beta}\hat{\alpha}_x E_x$ is to decrease the energy splitting caused by the EDM-E_x coupling term. This consequence of $i(\mu_a/c)\hat{\beta}\hat{\alpha}_x E_x$ again stresses its distinction from the spin-orbit coupling term, which has the completely different effect of lifting spin degeneracy by itself and thus increasing the size of spin splitting on top of this from the EDM-E_x coupling. Furthermore, again the mass of the particle m plays a role in the spin splitting by being one of the determinants of its splitting. The amount of the decrease of ΔE due to the MDM-E_x coupling term depends on the ratio $\lambda = \left(\frac{(\mu_a/c)E_x}{mc^2}\right)^2$. For practically achievable strengths of E_x, $\lambda < 10^{-30}$, and thus for conventional experimental setups, its effect can be neglected and the energy splitting can be written in the form $\Delta E = \sqrt{c^2 p_x + (mc^2 + E_x d_a)^2} - \sqrt{c^2 p_x + (mc^2 - E_x d_a)^2}$. However, the effect of $i(\mu_a/c)\hat{\beta}\hat{\alpha}_x E_x$ on ΔE can be emulated and explored in an ion trap setup.

When $i(\mu_a/c)\hat{\beta}\hat{\alpha}_x E_x$ is neglected, the eigenspinors corresponding to $E_\pm^\downarrow$ and $E_\pm^\uparrow$ are given by $|\pm,\downarrow\rangle = (v_\pm^\downarrow, -v_\pm^\downarrow, -1, 1)^T/N_\pm^\downarrow$ and $|\pm,\uparrow\rangle = (v_\pm^\uparrow, v_\pm^\uparrow, 1, 1)^T/N_\pm^\uparrow$, with $N_\pm^\downarrow = \sqrt{2 + 2|v_\pm^\downarrow|^2}$, $N_\pm^\uparrow = \sqrt{2 + 2|v_\pm^\uparrow|^2}$, $v_\pm^\downarrow = w^\downarrow \pm \sqrt{1 + w^{\downarrow 2}}$ and $v_\pm^\uparrow = w^\uparrow \pm \sqrt{1 + w^{\uparrow 2}}$, where $w^\downarrow = (mc^2 - E_x d_a)/(cp_x)$ and $w^\uparrow = (mc^2 + E_x d_a)/(cp_x)$. The expectation values of the components $\hat{S}_y$ and $\hat{S}_z$ are zero for all four eigenspinors. The expectation value of $\hat{S}_x$ for the four-component spinors $|\pm,\uparrow\rangle$ is $1/2$ while the one for $|\pm,\downarrow\rangle$ is $-1/2$.

Consider an initial state which is a linear combination of positive energy solutions $|\Psi(0)\rangle = e^{-ip_x x/\hbar}(b_+^\uparrow|+\uparrow\rangle + b_+^\downarrow|+\downarrow\rangle)$. Then the general solution of the time-dependent problem will not involve negative energy eigenfunctions. The expectation value of the spin component $\hat{S}_j$ with respect to $|\Psi(t)\rangle$ is

$$\langle \hat{S}_j(t)\rangle = |b_+^\uparrow|^2\langle\uparrow + |\hat{S}_j|+\uparrow\rangle + |b_+^\downarrow|^2\langle\downarrow + |\hat{S}_j|+\downarrow\rangle + 2\mathrm{Re}\{(b_+^\uparrow)^* b_+^\downarrow \langle\uparrow + |\hat{S}_j|+\downarrow\rangle e^{\omega t}\}, \tag{5.10}$$

The overall behavior of $\langle\hat{\mathbf{S}}\rangle$ is a precession around E_x with an angular frequency ω, similar to the Larmor precession of a spin in an external magnetic field. It is interesting to note that despite using the Dirac four-component spinors, the resulting behavior is similar to the nonrelativistic case because of the properties of the spin operators.

The experimental signature of the lifting of spin degeneracy by an external electrostatic field is the Larmor-like precession of the spin expectation value. Using the mapping between the relativistic particle and the ion trap parameters, the simulated precession frequency becomes

$$\omega = 2\sqrt{\eta^2\Delta^2\tilde{\Omega}^2 p_x^2/\hbar^2 + (\delta + \Omega^{(1)})^2} - 2\sqrt{\eta^2\Delta^2\tilde{\Omega}^2 p_x^2/\hbar^2 + (\delta - \Omega^{(1)})^2}. \tag{5.11}$$

The simulation requires initialization of the trapped ion in state $|\Psi(0)\rangle = e^{-ip_x x/\hbar}(b_+^\uparrow|+\uparrow\rangle + b_+^\downarrow|+\downarrow\rangle)$. The construction of the initial state can be done using the same toolbox which is employed for the simulation of the Hamiltonian (5.6). The system should first be cooled to its ground state. Then the motional

degrees of freedom should be excited representing certain values of the simulated momentum through the relationship $\hat{p}_x = i\hbar(\hat{a}_x^\dagger - \hat{a}_x)/(2\Delta)$. Then using a combination of carrier interactions with appropriate timing for the desired values of the parameters $\Omega, \eta, \Delta, \tilde{\Omega}, \delta$ one can populate the four ionic levels with the required probabilities.

The dynamics of the system can be driven by the application of the described combination of AJC and JC stemming from a single bichromatic source, and carrier interactions will simulate the Dirac Hamiltonian (5.6). Controlling the transitions between four energy levels is not trivial, but is certainly feasible. Current experiments with trapped ions involve even more than four levels, for optical pumping, storage, ancillas, ionization. In the proposed experimental implementation, we need two pairs of JC and AJC fields for the simultaneous implementation of the momentum and mass term, which couple levels $|a\rangle$ and $|d\rangle$ and $|b\rangle$ and $|c\rangle$. The EDM-E term is implemented by a pair of carrier interactions on the transitions $|a\rangle \leftrightarrow |b\rangle$ and $|c\rangle \leftrightarrow |d\rangle$.

There are many possibilities for selection of the exact transitions, depending on the chosen atomic ion, technical details, and capabilities in different experimental setups. One possibility is to identify the four internal degrees of freedom with different hyperfine levels. For example, one can make the identification $|a\rangle = |F = 2, m = 0\rangle$, $|b\rangle = |F = 1, m = 1\rangle$, $|c\rangle = |F = 2, m = 1\rangle$, and $|d\rangle = |F = 1, m = 0\rangle$ as in the case of $^9Be^+$. The transitions $|a\rangle \leftrightarrow |d\rangle$ and $|b\rangle \leftrightarrow |c\rangle$ can each be addressed separately by a π-polarized detuned bichromatic field (JC + AJC) with sufficiently different frequencies due to the difference in the transition frequencies between $|a\rangle \leftrightarrow |d\rangle$ and $|b\rangle \leftrightarrow |c\rangle$ stemming from the applied weak magnetic field. The frequency offset can easily be controlled experimentally. The transitions $|a\rangle \leftrightarrow |b\rangle$ and $|c\rangle \leftrightarrow |d\rangle$ can be addressed separately by a pair of resonant carrier interactions with the opposite polarizations: σ_+ and σ_-. Thus the difference between the frequencies and polarizations ensures that no unwanted interference or shifts will be produced if the Zeeman splitting is large enough.

Because of the multitude of fields needed, it is important to estimate the induced light shift on a certain transition by laser fields driving the other transitions. The magnitude of the light shift is approximately equal to $\Omega^2/(2\Delta)$, where Ω is the Rabi frequency of the transition and Δ is the frequency detuning of the perturbing field. For such a light shift to be negligible, it is necessary that it must be much less than the Rabi frequency Ω. . The typical values of the Rabi frequency in a linear Paul trap are of the order of a few hundred kHz because Ω must be much less than the trap frequency (typically a few MHz). Of the four different transitions in the example, light shifts have to be accounted for only for the transitions $|a\rangle \leftrightarrow |d\rangle$ and $|b\rangle \leftrightarrow |c\rangle$, because the other two transitions $|a\rangle \leftrightarrow |b\rangle$ and $|c\rangle \leftrightarrow |d\rangle$ are driven by fields of different (circular) polarizations. A back-of-the-envelope estimate then shows that for a Rabi frequency of 200 kHz, the light shift will be below 2 kHz if the Zeeman splitting exceeds 5 MHz.

The dynamics of the system is manifested in a precession of the emulated relativistic particle spin embodied in oscillations of the relative phase between the two eigenspinors $|+\uparrow\rangle$ and $|+\downarrow\rangle$ with frequency ω. The two eigenspinors

$|+\uparrow\rangle$ and $|+\downarrow\rangle$ map to the four internal levels of the trapped ion and the emulated dynamics of EDM precession maps to periodic population transfer between the four internal ion levels with frequency $\omega = (E_+^{\uparrow} - E_+^{\downarrow})/\hbar$. This frequency ω which is the signature of the emulated dynamics can be measured by standard ion trap technology such as an electron shelving from any one of the internal ion levels.

Supposing a realistic electrostatic field $E_x = 10$ MV/cm, a neutron with an experimentally set upper EDM value of around $d_n \approx 10^{-26}e$ cm will lead to spin splitting $\Delta E \approx 10^{-19}$ eV corresponding to a precession frequency of $\omega = 10^{-4}$ Hz; for a neutron with an SM predicted EDM value of $d_n \approx 10^{-32}e$ cm, the corresponding spin splitting $\Delta E \approx 10^{-25}$ eV, and $\omega = 10^{-10}$ Hz, the precession frequency is so small that it would take of the order of 300 years for one full precession of the spin. These values present a considerable challenge to present and future conventional experiments. The emulation of the Dirac equation with the EDM term, Eq. (5.6), provides the possibility for emulation of the discussed effects, since they allow for emulated precession frequencies in the range $\omega \approx 10 - 10^7$ Hz.

In conclusion, we have proposed a scheme for simulating the EDM of neutral relativistic particles within Dirac theory in ion traps. We have described the lifting of spin degeneracy caused by an electrostatic field for a particle possessing EDM, and the consequent Larmor-like precession of the particle spin. We have predicted a few unusual relativistic features of the considered effects, and we proposed how they can be emulated in an ion trap. Furthermore, this can serve as a stepping stone toward more involved experimental studies of the physics of combined space inversion and time-reversal violation as well as CP violation. The CP violation in the effective model stems partially from the magnetic field in the ion traps, which breaks T symmetry. The validity of the total CPT symmetry then requires the breaking of CP symmetry in such a way as to compensate for the breaking of T symmetry. This mechanism is similar to the mechanism by which while C and P symmetry are separately broken, the combined CP symmetry is preserved.

6. ADIABATIC FLUX INSERTION AND GROWING OF LAUGHLIN STATES OF CAVITY RYDBERG POLARITONS

In this chapter we propose a scheme to adiabatically transfer flux quanta in multiples of $3\hbar$ simultaneously to all cavity photons by coupling the photons through flux-threaded cones present in such cavity setup. The flux transfer is achieved using external light fields with orbital angular momentum and a near-resonant dense atomic medium as mediator. Furthermore, coupling the cavity fields to a Rydberg state in a configuration supporting electromagnetically induced transparency, fractional quantum Hall states can be prepared. To this end a growing protocol is used consisting of a sequence of flux insertion and subsequent single-photon insertion steps. We discuss specifically the growing of the $\nu = 1/2$ bosonic Laughlin state, where we first repeat the flux insertion twice creating a double quasi-hole excitation. Then, the hole is refilled using a coherent pump and the Rydberg blockade.

6.1 Motivation

A key feature of the scheme is the controlled insertion of single photon and magnetic flux quanta into the cavity system. The latter creates a quasi-hole excitation in the center of the system and subsequently transfers the right amount of angular momentum. Then the hole is refilled by a coherent laser field creating a LN-type ground state. Besides being efficient our growing scheme has the advantage as compared e.g. to that suggested in [74] that quasi-holes created by photon decay are continuously pumped to the periphery of the LN-droplet, allowing to prepare a quantum-Hall liquid which is almost defect free in the center. The main challenge of the scheme is to insert an integer amount of flux quanta. For this we propose an adiabatic method for transferring external orbital angular momentum (OAM) from classical light beams to the cavity photons by using light-matter interaction as a mediator. Specifically we consider the interaction between an ensemble of four-level atoms coupled to the cavity field and classical light and show that the adiabatic transfer of OAM to the cavity photons can be achieved by using stimulated Raman adiabatic passage (STIRAP) with Laguerre-Gauss laser beams. The transfer is facilitated by an infinite set of cavity dark-state polaritons which are a superposition of light and collective matter excitations.

In order to realize a single photon coherent pump, the photonic cavity modes are coupled to a high lying Rydberg state of an atomic medium under conditions

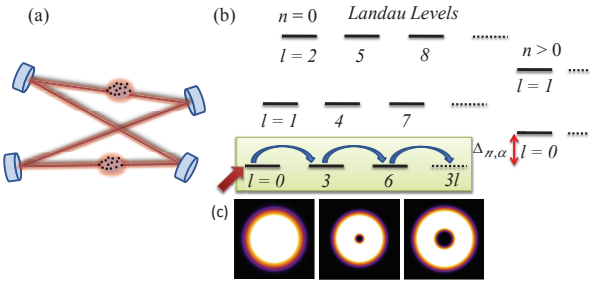

Fig. 6.1: (a) Non-planar resonator consisting of four mirrors creating an artificial magnetic field for cavity photons. Two clouds of atoms are used for adiabatic flux insertion and strong interactions mediated by Rydberg atoms. (b) Structure of the photonic Landau levels labeled by orbital angular quantum number l and radial quantum number n. Here $\Delta_{n,\alpha}$ is the frequency of the mode (n, α). The green box indicates the lowest Landau level (LLL). Initially, photons are pumped into the cavity mode with $n = l = 0$ (red arrow). Then, adiabatic flux insertion transfers orbital angular momentum from a classical light beam to cavity photons increasing the total angular momentum (blue arrow). (c) The density plot of the first three cavity modes in the LLL with angular momentum $l = 0$, $l = 3$ and $l = 6$.

of electromagnetically induced transparency [89, 90], which leads to a strong photon nonlinearity. Employing the resulting photon blockade, a single photon can be inserted into the system. Repeating a sequence of magnetic flux and subsequent photon insertion leads to a growing of the liquid while keeping it in the LN ground state.

6.1.1 Photon Cavity Setup

The artificial magnetic field in the photonic cavity setup of Ref. [91] is created by using the similarity between the Lorentz force on a charged particle in a magnetic field and the Coriolis force. Consider a ring resonator as indicated in Fig. 6.1(a) which confines the photon gas to a two-dimensional plane and leads to an effective mass. The mirror curvature modifies the mass and creates an additional harmonic potential in the two-dimensional plane. Using a non-planar geometry leads to an image rotation of the transverse mode profile in a single roundtrip. This is equivalent to the action of an effective magnetic field pointing in the direction of propagation plus an anti-binding centrifugal potential [92]. For sufficiently strong rotation the anti-binding potential can compensate the harmonic confinement and Landau levels emerge. Such a configuration is however unstable and sensitive to astigmatism, which drives transitions between angular momentum states with difference $\Delta\ell = \pm 2$. Increasing the effective rotation even further eventually leads to another configuration with large degeneracy that is stable, containing angular momentum states which differ by multiples of $3\hbar$ - the *photonic Landau levels*. The corresponding spectrum is il-

lustrated in Fig. 6.1(b). Now, within each photonic Landau level with frequency $\Delta_{n,\alpha}$ labeled by the radial quantum number n and a fixed value of $\alpha = 0, 1, 2$, the photon angular momentum $\ell\hbar = (3m+\alpha)\hbar$ increases in multiples of $3\hbar$. The corresponding Hamiltonian is

$$H_0 = \hbar \sum_{\alpha=0}^{2} \sum_{n=0}^{\infty} \Delta_{n,\alpha} \sum_{m=0}^{\infty} a^{\dagger}_{n,3m+\alpha} a_{n,3m+\alpha}. \tag{6.1}$$

Here, $a^{\dagger}_{n,l}$ and $a_{n,l}$ are the creation and annihilation operators of a cavity photon in spatial mode $f_{n,l}(r,\phi)$, described by the Laguerre-Gauss (LG) eigenmodes

$$f_{n,l}(r,\phi) = \sqrt{\frac{2^{|l|+1} n!}{\pi(|l|+n)! w_0^2}}\, x^{|l|} e^{il\phi} e^{-x^2} L_n^{|l|}\left(2x^2\right). \tag{6.2}$$

Here we defined $x = r/w_0$, with w_0 being the cavity waist and $L_n^{|l|}(x)$ are the LG polynomials. We use the term lowest Landau level (LLL) referring to the degenerate modes with radial quantum number $n = 0$ and $\alpha = 0$ (i.e. $l = 0, 3, 6, \ldots$). It is convenient to express the cavity field operator $\mathcal{E} = \sum_{\alpha=0}^{2} \sum_n \mathcal{E}_{n,\alpha}$ according the photonic Landau level structure as

$$\mathcal{E}_{n,\alpha}(r,\phi) = \sum_{m=0}^{\infty} f_{n,3m+\alpha}(r,\phi) a_{n,3m+\alpha}. \tag{6.3}$$

We note that all modes except $l = 0$ have a vanishing amplitude at the origin $r = 0$ and thus do not couple to atoms in the center of the transverse mode profile. More details of the experimental setup and mode functions can be found in Ref. [91, 92].

The frequencies of all cavity modes with $n \neq 0$ (see Fig.6.1(b)) are assumed to be far away from all atomic resonances and coupling to them is thus disregarded in what follows and we use the short-hand notation $a_{0,3m} \to a_{3m}$ etc.

6.1.2 Adiabatic Flux Insertion without interaction

6.1.3 Principle

The idea of adiabatically inserting flux quanta was introduced by Laughlin and provides an explanation of the quantized Hall current [94]. In the case of the photonic Landau levels we insert *photonic flux quanta* in multiples of $3\hbar$. This leads to a controlled *parallel* transfer of photons from modes a_{3m} to a_{3m+3} within the LLL. To avoid any direct coupling between these two modes, which would lead to errors, we split the process into two successive steps:

$$\text{i)} \quad a_{3m} \to a_{3m+1}, \qquad \text{ii)} \quad a_{3m+1} \to a_{3m+3}. \tag{6.4}$$

Light beams with OAM have already been successfully used to transfer angular momentum to an atomic medium [95]. Here we transfer OAM from an external

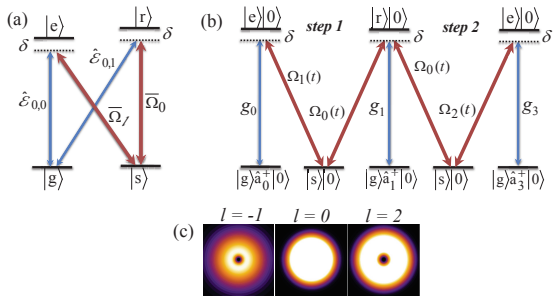

Fig. 6.2: (a) The atomic level structure consists of two meta-stable levels $|g\rangle$, $|s\rangle$ and two excited levels $|e\rangle$ and $|r\rangle$. (b) System initially prepared in state with $l = 0$. In the first stage of the protocol, the cavity modes $l = 0$ and $l = 1$ drives the transitions $|g\rangle \leftrightarrow |e\rangle$, $|g\rangle \leftrightarrow |r\rangle$ with coupling strength g_0 and g_1, while the laser fields $\Omega_1(t)$, $\Omega_0(t)$ couple the transitions $|e\rangle \leftrightarrow |s\rangle$, $|s\rangle \leftrightarrow |r\rangle$. We assume that the laser field Ω_1 has an OAM $-1\hbar$. As a consequence of this the initial photon in the $l = 0$ mode is transferred to the $l = 1$ mode using STIRAP technique. In the second step, the photon in the $l = 1$ mode is transferred to the $l = 3$ mode which belongs to the LLL manifold. This transition is performed by using the same atomic level structure, but with new Rabi frequency Ω_2 which carriers OAM $2\hbar$. (c) Density plots of the classical driving fields. We assume that Ω_0 Rabi frequency has a Gaussian shape with $l = 0$. The other two classical laser fields carry OAM, and thus have vanishing intensity at the center.

light beam to the cavity photons utilizing an atomic medium as a mediator. We consider atoms with four relevant states as depicted in Fig. 6.2(a). The atomic states are coupled via the cavity fields and external coherent driving fields carrying OAM l and with Rabi frequencies $\bar{\Omega}_l$. In order to be able to switch on and off the coupling of the cavity modes to the atomic medium, we assume that these transitions are sufficiently far away from single-photon resonance but that all Raman transitions are in two-photon resonance. In this way there is no interaction of the cavity field with the atomic medium in the absence of the classical driving fields.

In the first step (i) two classical laser fields, $\bar{\Omega}_1(r,\phi,t)$ and $\bar{\Omega}_0(r,t)$, which carry a net OAM of $1\hbar$ are applied to the atomic system. As a result a set of dark states is created in the subspace of states with $n=0$ which are mixtures essentially between the cavity field operators a_{3m} and a_{3m+1}, see Fig. 6.2(b). By using time-varying laser fields in a STIRAP counterintuitive pulse order, photons are absorbed from modes a_{3m} and successively created in modes a_{3m+1}. In this step an OAM of $1\hbar$ is transferred to each cavity photon in parallel.

In the second step (ii) classical light fields $\bar{\Omega}_0(r,t)$ and $\bar{\Omega}_2(r,\phi,t)$ with net OAM of $2\hbar$ are used. This leads to the formation of a new set of dark states now involving photonic modes a_{3m+1} and a_{3m+3}, see Fig. 6.2(b). In this step adiabatic following of the dark state transfers OAM of $2\hbar$ to each cavity photon. By successively repeating the processes one can increase the angular momentum of all occupied cavity modes in the LLL in parallel by multiples of $3\hbar$.

6.1.4 Atom-Field Interaction

Consider a dense ensemble of atoms with a four-level atomic structure as shown in Fig. 6.2(a). Besides a ground state $|g\rangle$ and a metastable state $|s\rangle$, we consider two excited states $|e\rangle$, $|r\rangle$ with finite lifetime. The atoms interact with the cavity field as well as with an external classical light beam with OAM. Here the transitions $|g\rangle \leftrightarrow |e\rangle$ and $|g\rangle \leftrightarrow |r\rangle$ are coupled to the cavity fields $\mathcal{E}_{0,0}$ and $\mathcal{E}_{0,1}$, while the atomic transitions $|s\rangle \leftrightarrow |e\rangle$ and $|s\rangle \leftrightarrow |r\rangle$ are driven by classical light fields with time-dependent Rabi frequencies $\bar{\Omega}_l(r,\phi,t)$ and $\bar{\Omega}_0(r,t) = \Omega_0(t)$. We assume an almost constant atomic density $n(r)$ in the central region of the light-matter interaction. As mentioned above, all transitions are assumed to be away from single-photon resonance with detuning δ but in respective two-photon resonance. In this case turning off the classical light fields amounts to switching off the interaction of the cavity modes with the atoms altogether. The atom-light coupling Hamiltonian is given by

$$\begin{aligned} H_\phi &= \hbar\delta \int d^2r\ (\sigma_{ee}+\sigma_{rr}) \\ &-\hbar \int d^2r\ \Big[\sum_{m=0}^{\infty} g_{3m} f_{0,3m}(r,\phi) a_{3m}\sigma_{eg} + \bar{\Omega}_l \sigma_{es} \\ &\quad +\bar{\Omega}_0\sigma_{sr} + \sum_{m=0}^{\infty} g_{3m+1} f_{0,3m+1}(r,\phi) a_{3m+1}\sigma_{rg} + \text{h.c.}\Big]. \end{aligned} \tag{6.5}$$

The coupling strength g_l are given by the atomic transition dipole matrix elements d_{eg} and d_{rg} of the $\mathcal{E}_{0,0}$ and $\mathcal{E}_{0,1}$ transitions, respectively, and overlap integrals with the mode functions

$$\begin{aligned} g_{3m} &\sim d_{eg} \int_0^{2\pi} d\phi \int_0^{\infty} dr \;\; r f_{n,3m}(r,\phi)\, n(r), \\ g_{3m+1} &\sim d_{rg} \int_0^{2\pi} d\phi \int_0^{\infty} dr \;\; r f_{n,3m+1}(r,\phi)\, n(r). \end{aligned} \tag{6.6}$$

In Eq. (6.5) we have introduced the standard continuous atomic flip operators $\sigma_{\mu,\nu}(\vec{r},t) = \frac{1}{\Delta V}\sum_{j\in\Delta V} |\mu_j\rangle\langle\nu_j|$ defined on a small volume ΔV centered around position $\vec{r}$ containing $\Delta N \gg 1$ atoms which fulfill the commutation relations $[\sigma_{\alpha,\beta}(\vec{r}), \sigma_{\mu,\nu}(\vec{r}')] = \delta(\vec{r}-\vec{r}')(\delta_{\beta,\mu}\sigma_{\alpha,\nu}(\vec{r}) - \delta_{\alpha,\nu}\sigma_{\mu,\beta}(\vec{r}))$.

Initially, all atoms are in the ground state. We assume weak cavity fields and discuss the linear response regime. Then, we can approximately set $\sigma_{gg} \approx 1$. Thus, the only relevant operators for our discussion are the coherences of excited and ground states, $P = \sigma_{ge}$ and $R = \sigma_{gr}$ and the coherence between the ground state and metastable state $S = \sigma_{gs}$. Within this approximation the operators $A = P, R, S$ fulfill the commutation relation $[A(\vec{r}), A^\dagger(\vec{r}')] = \delta(\vec{r}-\vec{r}')$. It is convenient to decompose them also into the LG basis (6.2),

$$A(r,\phi) \;\; = \;\; \sum_{n,l=0}^{\infty} A_{n,l}\, f_{n,l}(r,\phi). \tag{6.7}$$

First step

In the first step of the flux insertion scheme we assume that the laser field $\bar{\Omega}_l(r,\phi,t)$ in Eq. (6.5) has $l = 1$, i.e. carries an OAM of $-1\hbar$ such that

$$\bar{\Omega}_1(r,\phi,t) = \Omega_1(t)\,\kappa_1(x)\, e^{-i\phi}. \tag{6.8}$$

Now, using the decomposition of the atomic modes Eq. (6.7) and the photonic cavity modes Eq. (6.3) we can easily evaluate the Hamiltonian Eq. (6.5). Including the photonic Landau level Hamiltonian (6.1), we derive the Heisenberg-

Langevin equations in the linear response regime

$$\begin{aligned}
\frac{d}{dt}P_{n,3m} &= -(i\delta+\gamma)P_{n,3m} + i\Omega_1 \sum_{n'=0}^{\infty} \chi_{3m}^{n,n'} S_{n',3m+1} \\
&\quad + ig_{3m}a_{3m}\delta_{n,0}, \\
\frac{d}{dt}S_{n,3m+1} &= i\Omega_1^* \sum_{n'=0}^{\infty} \left(\chi_{3m}^{n',n}\right)^* P_{n',3m} + i\Omega_0 R_{n,3m+1}, \\
\frac{d}{dt}R_{n,3m+1} &= -(i\delta+\gamma)R_{n,3m+1} + i\Omega_0^* S_{n,3m+1} \\
&\quad + ig_{3m+1}a_{3m+1}\delta_{n,0}, \\
\frac{d}{dt}a_{3m} &= ig_{3m}P_{0,3m}, \\
\frac{d}{dt}a_{3m+1} &= ig_{3m+1}R_{0,3m+1},
\end{aligned} \tag{6.9}$$

with coupling coefficients determined by

$$\chi_{3m}^{n,n'} = \int_0^{2\pi} d\phi \int_0^{\infty} dr\, r\kappa_1(r) e^{-i\phi} f_{n,3m}^*(r,\phi)\, f_{n',3m+1}(r,\phi). \tag{6.10}$$

Here γ is the spontaneous decay rate from the excited states $|e\rangle$ and $|r\rangle$ which we assume for simplicity to be equal. Note that in the linear response regime the population of the excited states is negligible, which allows us to neglect Langevin noise terms here. We also disregard the cavity decay in our description for now but include it later.

One recognizes from Eqs. (6.9) that there is in general a coupling between modes with different radial index n, which is a problem. For that reason we now choose the spatial profile $\kappa_1(x)$ in such a way that couplings from the $n=0$ spin modes $S_{0,3m+1}$ to higher modes with $n'>0$ are highly suppressed, i.e. such that $\chi_{3m}^{n',0} \sim \delta_{n',0}$. This can be achieved for $\kappa_1(x) = 1/x$ with $\chi_{3m}^{0,0} = \sqrt{\frac{2}{3m+1}}$, see Eq. (6.10). Then, one can directly construct a dark state for an OAM transfer of $\Delta\ell = 1$,

$$\begin{aligned}
\Psi_m^{(1)} &= \frac{1}{N_m}\Bigg\{ g_{3m+1}\sqrt{\frac{2}{3m+1}}\Omega_1\, a_{3m} + g_{3m}\Omega_0 a_{3m+1} \\
&\qquad - g_{3m}g_{3m+1}S_{0,3m+1} \Bigg\},
\end{aligned} \tag{6.11}$$

which is a superposition of cavity-field operators a_{3m}, a_{3m+1} and corresponding collective ground-state coherences. It is straightforward to show that the dark state is a constant of motion in the adiabatic limit, i.e. $\partial_t \Psi_m^{(1)} = 0$. Here $N_m(t)$ is a normalization factor. We note that there is no choice of spatial profile $\kappa_1(x)$ that simultaneously perfectly suppresses also the couplings $\chi_{3m}^{0,n'}$ of the $n=0$ optical polarization modes $P_{0,3m}$ to modes with $n'>0$. However, this is not

a necessary condition to construct a dark state. Indeed, the couplings $\chi_{3m}^{0,n'}$ between the LLL ($n = 0$) with higher Landau level ($n' \geq 1$) are all of order unity for $\kappa_1(x) \sim 1/x$, i.e. $\chi_{3m}^{0,n'} = \mathcal{O}(1)$.

The ideal spatial profile $\kappa_1 \sim 1/x$ cannot be realized experimentally, however, since $\bar{\Omega}_1$ carries a non-vanishing OAM and thus must vanish for $r \to 0$. Instead we choose

$$\kappa_1(x) = \frac{x^2}{a^3 + x^3}, \tag{6.12}$$

with $a = r_0/w_0$ and $r_0 \ll w_0$ is some cut-off length. In the limiting case $a \to 0$, this approaches the ideal profile. For $a \ll 1$ the couplings $|\chi_{3m}^{n',0}| \sim a^2 \ll \chi_{3m}^{0,0}$ are strongly suppressed and we approximately obtain the dark state Eq. (6.11). The small residual couplings to collective atomic modes with higher radial index $n' > 0$ will lead to some losses, which will be discussed latter on.

Now a fully adiabatic transfer of excitations can be performed using a STIRAP protocol. As long as $\Omega_1 \gg \left\{\Omega_0(t_i)\sqrt{\frac{3m+1}{2}}\frac{g_{3m}}{g_{3m+1}}, g_{3m}\right\}$ the dark states coincide with the initial state $\Psi_m^{(1)} \simeq a_{3m}$. Adiabatic following transfers the dark states into $\Psi_m^{(1)} \simeq a_{3m+1}$ if $\Omega_0 \gg \left\{\Omega_1\sqrt{\frac{2}{3m+1}}\frac{g_{3m+1}}{g_{3m}}, g_{3m+1}\right\}$ which concludes the first step of the protocol at time t_1, and the population from all modes a_{3m} of the LLL is transferred in parallel to modes a_{3m+1} which belong to an excited Landau level manifold with $\alpha = 1$.

In order to return the population back to the LLL manifold we repeat the same procedure as above using the same atomic structure but with new Rabi frequency $\bar{\Omega}_2$ as we explain in the following.

Second step

The goal of the second step is to increase angular momentum of all photons by $2\hbar$. In order to perform this we assume that the transition $|e\rangle \leftrightarrow |s\rangle$ is driven with Rabi frequency

$$\bar{\Omega}_2(r, \phi, t) = \Omega_2(t)\kappa_2(x)e^{2i\phi}, \tag{6.13}$$

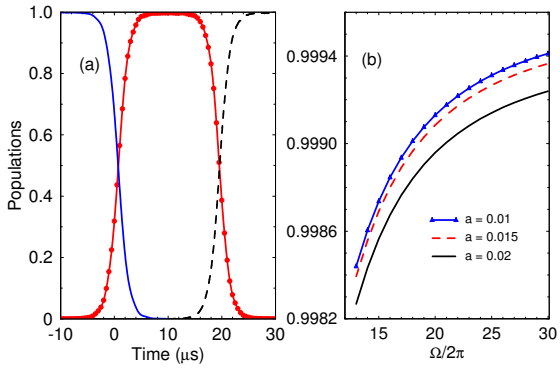

Fig. 6.3: (a) The expectation values of $a_{0,l}$ $(l = 0, 1, 3)$ versus time. The exact result for $a_{0,0}$ and $a_{0,1}$ (blue lines) according the coupled system Eq. (6.9) including the residual couplings for $a = 10^{-2}$. The red lines show the time-evolution of $a_{0,1}$ and $a_{0,3}$ according the coupled system Eq. (6.14). We choose a time-dependent Rabi frequencies with $\Omega = 2\pi \times 12.4$ MHz and cavity couplings $g = 2\pi \times 0.45$ MHz. The other parameters are set to $\gamma = 0$, $\delta = 2\pi \times 0.13$ MHz and $T = 1$ μs. (b) The expectation value of $a_{0,1}$ at time t_1 against Ω for $a = 0.01$ (blue line), $a = 0.015$ (red line), $a = 0.02$ (black line)

which carriers OAM $2\hbar$. Consequently, we obtain similar Heisenberg-Langevin equation to Eq. (6.9)

$$\begin{aligned}
\frac{d}{dt}P_{n,3m+3} &= -(i\delta+\gamma)P_{n,3m+3} + i\Omega_2 \sum_{n'=0}^{\infty} \widetilde{\chi}^{n,n'}_{3m+3} S_{n',3m+1} \\
&\quad + ig_{3m+3}a_{3m+3}\delta_{n,0}, \\
\frac{d}{dt}S_{n,3m+1} &= i\Omega_2^* \sum_{n'=0}^{\infty} \left(\widetilde{\chi}^{n',n}_{3m+3}\right)^* P_{n',3m+3} + i\Omega_0 R_{n,3m+1}, \\
\frac{d}{dt}R_{n,3m+1} &= -(i\delta+\gamma)R_{n,3m+1} + i\Omega_0^* S_{n,3m+1} \\
&\quad + ig_{3m+1}a_{3m+1}\delta_{n,0}+, \\
\frac{d}{dt}a_{3m+3} &= ig_{3m+3}P_{0,3m+3}, \\
\frac{d}{dt}a_{3m+1} &= ig_{3m+1}R_{0,3m+1},
\end{aligned} \tag{6.14}$$

with new coupling coefficients,

$$\widetilde{\chi}^{n,n'}_{3m} = \int_0^{2\pi} d\phi \int_0^{\infty} dr\, r\kappa_2(x) e^{2i\phi} f^*_{n,3m}(r,\phi)\, f_{n',3m-2}(r,\phi). \tag{6.15}$$

We now choose the spatial profile of $\kappa_2(x)$ in such a way that couplings from the $n = 0$ spin modes $S_{0,3m+1}$ to higher modes with $n' > 0$ are highly suppressed, i.e. that $\widetilde{\chi}^{n',0}_{3m+3} \sim \delta_{n',0}$. This can be achieved for $\kappa_2(x) = x^2$ with $\widetilde{\chi}^{0,0}_{3m+3} =$

$\frac{1}{2}\sqrt{\frac{(3m+3)!}{(3m+1)!}}$. Note that with this experimentally feasible choice of the spatial profile all couplings of spin coherences $S_{0,3m+1}$ to higher states with $n' > 0$ are exactly canceled such that there are no undesired residual couplings.

Similarly, we can directly construct an infinite set of dark states,

$$\Psi_m^{(2)} = \frac{1}{\tilde{N}_m}\Bigg\{ g_{3m+1}\frac{\Omega_2}{2}\sqrt{\frac{(3m+3)!}{(3m+1)!}}a_{3m+3} + g_{3m+3}\Omega_0 a_{3m+1} - g_{3m+3}g_{3m+1}S_{0,3m+1}\Bigg\}, \tag{6.16}$$

which are a constant of motion in the adiabatic limit, i.e. $\partial_t \Psi_m^{(2)} = 0$.

Starting at time t_1 which is now the initial time for the second step the dark state (6.16) coincides with $\Psi_m^{(2)} \simeq a_{3m+1}$ as long as $\Omega_0 \gg \left\{\Omega_2 \frac{1}{2}\sqrt{\frac{(3m+3)!}{(3m+1)!}}\frac{g_{3m+1}}{g_{3m+3}},\, g_{3m+1}\right\}$. Adiabatically increasing $\Omega_2(t)$ drives the system into $\Psi_m^{(2)}(t_f) \simeq a_{3m+3}$ if at $t = t_f$: $\Omega_2 \gg \left\{2\sqrt{\frac{(3m+1)!}{(3m+3)!}}\Omega_0\frac{g_{3m+3}}{g_{3m+1}},\, g_{3m+3}\right\}$ which concludes the second step. In total, the flux insertion protocol transfers OAM in multiples of $3\hbar$ to all cavity modes of the LLL in parallel.

6.1.5 Laughlin state preparation

Now, we discuss the preparation of Laughlin-type states in a setup of cavity Rydberg polaritons. Following Refs. [96, 97], a Laughlin state can be grown by the successive repetition of adiabatic flux insertion and a single-photon coherent pump, discussed below.

6.1.6 Rydberg Cavity Polaritons and Laughlin State

To realize a fractional quantum Hall system requires besides the artifical magnetic field, strong interactions between the photonic cavity modes in the lowest photonic Landau level,

$$H_{\text{int}} = \sum_{l_1,l_2}\sum_{l_3,l_4} V_{l_3,l_4}^{l_1,l_2}\, a_{l_1}^\dagger a_{l_2}^\dagger a_{l_3} a_{l_4}, \tag{6.17}$$

where $l_i = 3m$ and $m = 0, 1, \ldots$. This Hamiltonian can be realized by coupling the cavity field $\mathcal{E}_{0,0}$ to a high-lying Rydberg state in an EIT configuration. In recent cavity experiments the strong nonlinearity on the single photon level was demonstrated [98, 99]. The Rydberg cavity polaritons have an effective interaction potential $V(r) = C_6/(r^6 + a_B^6)$. Here, C_6 is the effective interaction strength and a_B is the Rydberg blockade radius. Although the opposite regime is very interesting on its own right [100], we assume in the following the case where the magnetic length $l_B = w_0/2$ is much larger than a_B. In this limit the dominant interaction contribution comes from the zero's Haldane pseudo

potential [100]

$$V_0 \simeq \frac{3C_6}{8l_B^2 a_B^4}, \tag{6.18}$$

which determines all interaction coefficients [101]

$$\begin{aligned} V_{l_3,l_4}^{l_1,l_2} &= \langle l_1, l_2|V|l_3, l_4\rangle \\ &\simeq \frac{V_0}{2}(l_1+l_2)!\sqrt{\frac{2^{-2(l_1+l_2)}}{l_1!l_2!l_3!l_4!}}\delta_{l_1+l_2,l_3+l_4}. \end{aligned} \tag{6.19}$$

We assume for the interaction coefficients $V_{l_3,l_4}^{l_1,l_2} \ll |\Delta_{0,1} - \Delta_{0,0}|$, i.e. they are small compared to the energy gap between the Landau levels to avoid mixing of states in different Landau level.

The combination of the photonic Landau level Eq. (6.1) and the strong photon nonlinearity Eq. (6.17) lead to a set of degenerate low energy states with total angular momentum L depending on the photon number N. For a given photon number N the zero energy state with lowest total angular momentum,

$$\langle z_1, \ldots, z_N|\mathrm{LN}, N\rangle = \prod_{i<j}(z_i^3 - z_j^3)^2, \tag{6.20}$$

is a unique ground state of the system, which resembles a Laughlin-type state. We here have dropped the ubiquitous Gaussian factor and the normalization constant. The two-dimensional coordinate is $z_j = x_j - iy_j$. The total angular momentum of the state (6.20) with N photons is $L|\mathrm{LN}, N\rangle = 3N(N-1)|\mathrm{LN}, N\rangle$. In addition, we consider here the mth quasi-hole states with N photons

$$\langle z_1, \ldots, z_N|m\mathrm{qh}\rangle = \prod_k z_k^{3m}\prod_{i<j}(z_i^3 - z_j^3)^2, \tag{6.21}$$

having total angular momentum $L|m\mathrm{qh}, N\rangle = \frac{3}{2}mN(N+1)|m\mathrm{qh}, N\rangle$. It is straightforward to show that the Laughlin-type state with $N+1$ photons has the same total angular momentum as the 2-quasi-hole state with N photons.

6.1.7 Full Protocol

Single Photon Pump. – We consider a coherent pump which injects a single photon into the mode a_0. This implies that there is no transfer of angular momentum into the system. We assume that an external laser field is applied with mode profile matching the $l = 0$ angular momentum state,

$$H_{\Omega_p} = \Omega_p(a_0^\dagger e^{-i\omega t} + a_0 e^{i\omega t}). \tag{6.22}$$

Here Ω_p is the driving pump Rabi frequency into the cavity and ω is the oscillation frequency which we assume to be in resonance with respect to the energy of the LLL, i.e. $\omega = \Delta_{0,0}$. Without the interaction Eq. (6.17) the Hamiltonian (6.22) creates a coherent amplitude of the photonic mode which contains

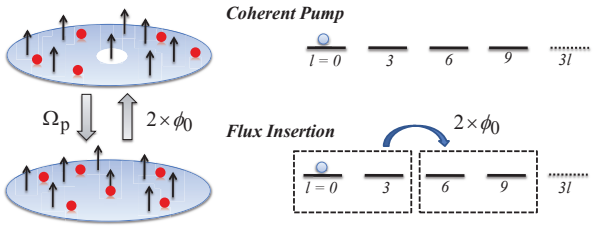

Fig. 6.4: The growing scheme which is used for the preparation of the Laughlin-type states consists of two steps. (i) Coherent pump of a single photon in the ground state of the cavity by using the non-linear photon-photon interaction. (ii) Increase of angular momentum per particle by 6 (flux insertion). Repeating the two steps lead to growing of the photonic Laughlin-type state.

a superposition of many photons. However, strong photon blockade ensures the insertion of a single photon requiring $\Omega_p \ll V_0, \Delta_{\rm LN}$, where $\Delta_{\rm LN} \simeq 0.2V_0$ is the many body gap of the system. Note that the Laughlin gap only slightly depends on the photon number N. Starting from a 2-quasi-hole state $|2{\rm qh}, N\rangle$, we use a π-pulse of time $\tau_p = \pi/2\Omega^{(N)}$ where

$$\Omega^{(N)} = \Omega_p \langle {\rm LN}, N+1 | a_0^\dagger | 2{\rm qh}, N\rangle \tag{6.23}$$

is the coupling between the quasi-hole and Laughlin state [96, 97], to insert a single photon.

Adiabatic Flux Insertion.– In the interacting case we require adiabaticity $\Delta_{\rm LN}\tau_f \gg 1$, where the many-body gap $\Delta_{\rm LN}$ should not vanish during flux insertion. To this end we couple the photonic cavity field $\mathcal{E}_{0,1}$ in the first Landau level using an EIT scheme to a Rydberg state as well. This ensures to maintain a finite many-body gap $\Delta_{\rm LN}$. For simplicity we assume the same interaction potential $V(r)$ as before. Now, in Eq. (6.17) we sum over all photonic modes in the lowest and first Landau level.

Protocol.– The growing scheme is depicted in Fig. 6.4. It starts by preparing the cavity with no photon. Then in the first step a single photon in mode a_0 is pumped into the cavity $|0\rangle \to a_0^\dagger|0\rangle$ by using the non-linear interaction Eq. (6.17). This state obviously has total angular momentum $L = 0$. Next we repeat the flux insertion scheme two times which realizes the transition $a_0^\dagger|0\rangle \to a_6^\dagger|0\rangle$ with $L = 6$. The latter state is a 2-quasi-hole state with one photon. Now a second photon is pumped into the cavity. The finite overlap $\Omega^{(1)}/\Omega_p = \sqrt{10/11}$ with the Laughlin state ensures that we pump into the ground state of the system. This step creates a Laughlin state with $N = 2$ photons. By repeating these two steps we grow a Laughlin-type state (6.20) with N photons.

To numerically simulate the full growing protocol is rather involved, since taking into account all different atomic excitations leads to fast growing of the relevant Hilbert space even for few excitations. Therefore we simplify the

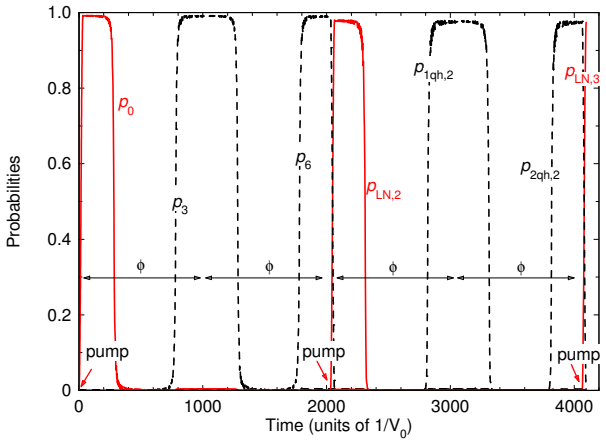

Fig. 6.5: Numerical simulation of growing scheme for creation of Laughlin states with $N = 2$ and $N = 3$ photons. The system is prepared initially in a state with no photon. The red arrow indicates the time at which the coherent pump is applied. The angular momentum per photon is increased by repeating twice the flux insertion. The probabilities are $p_m = |\langle\psi|a_m^\dagger|0\rangle|^2$, and respectively $p_{\mathrm{LN},N}$ and $p_{m\mathrm{qh},N}$ are the probabilities for Laughlin state and mth quasi-hole state. The parameters are set to $\Delta_0/V_0 = 10$, $\Omega_p/V_0 = 1/20$, $g_a/V_0 = g_b/V_0 = 1/5$.

protocol reducing it to the essential components, namely the adiabatic increase of angular momentum of the cavity modes by flux insertion and subsequent photon insertion. The simplified flux insertion method used for the simulation relies solely on the photonic cavity modes and is therefore amenable to numerical simulations by exact diagonalization. Specifically we consider a direct coupling between the lowest and first Landau level and change the energies of the Landau levels in time. This resembles a rapid adiabatic passage sweep. In Fig. 6.5 we show a numerical simulation of the full protocol for the preparation of Laughlin states up to three photons. After three steps of the protocol we obtain a LN state with three photons with probability $|\langle\psi|\mathrm{LN},3\rangle|^2 \approx 0.97$.

Finally, let us comment on the fidelity of our scheme. On the one hand, in the flux insertion process, the imperfections come from non adiabatic transitions, which requires $\Omega_l\tau_f \gg 1, \Delta_{\mathrm{LN}}\tau_f \gg 1$. On the other hand, in the coherent pump the imperfections come from coupling to higher photon number states which require $\Delta_{\mathrm{LN}}\tau_p \gg 1$. While both favor large timescales $\tau = 2\tau_f + \tau_p$ for each step in the growing protocol, losses limit the timescale τ. We take into account the effect of cavity losses as well as the finite lifetime of the Rydberg state by an effective loss rate γ_{eff}. As shown in Ref. [96, 97], the fidelity for the creation of an N-photon Laughlin state then scales as

$$\mathcal{F}_N \simeq \exp\left[-\frac{1}{2}N\left(\frac{1}{2}\gamma_{\mathrm{eff}}\tau(N+1) + \frac{\Lambda_N^2}{(\Delta_{\mathrm{LN}}\tau)^2}\right)\right], \tag{6.24}$$

where Λ_N depends on photon number N. Note that our protocol first creates a hole excitation in the center and then refills the hole. Repeating the steps of the protocol photons are pumped continuously into the center of the system. Defects created by losses will be continuously pumped to the periphery of the system and we expect that a much higher fidelity can be achieved in the steady state in the center of the cavity.

6.1.8 Discussion and Outlook

In summary, we discussed an adiabatic transfer protocol to insert flux quanta in a photonic twisted cavity setup. The scheme relies on a robust STIRAP technique transferring OAM of an external classical laser beam to the photonic cavity modes. A dense atomic ensemble hereby acts as a mediator. We show that the transfer can be described by a set of dark states between cavity modes with different angular momentum. Furthermore, we discuss imperfections of the protocol and estimate the fidelity. In addition we discuss the preparation of Laughlin-type states based on the growing protocol of Refs. [96, 97]. To this end, we discuss a single photon pump coupling the cavity field to a high-lying Rydberg state in an EIT configuration. We show that by successive repetition of flux insertion and coherent pump a Laughlin-type state can be prepared with high fidelity. Since as compared to alternative growing protocols [74] in our scheme photons and thus also loss-induced defects are continuously pumped from the center to the periphery of the system, we expect to create Laughlin-type states with much higher fidelity in the center of the cavity.

The non-local character of the interaction between Rydberg polaritons may lead to other interesting states such as the Moore-Read Pfaffian in the regime of large magnetic fields, where the magnetic length becomes comparable or smaller than the blockade radius. Furthermore, the coherent control may allow to investigate bilayer quantum Hall phases exploring different photonic Landau levels.

7. COMPENSATION OF THE TRAP-INDUCED QUADRUPOLE INTERACTION IN TRAPPED RYDBERG IONS

In this chapter the quadrupole interaction between the Rydberg electronic states of a Rydberg ion and the radio frequency electric field of the ion trap is analyzed. Such a coupling is negligible for the lowest energy levels of a trapped ion but it is important for a trapped Rydberg ion due to its large electric quadrupole moment. This coupling cannot be neglected by the standard rotating-wave approximation because it is comparable to the frequency of the trapping electric field. We investigate the effect of the quadrupole coupling by performing a suitable effective representation of the Hamiltonian. For a single ion we show that in this effective picture the quadrupole interaction is replaced by rescaled laser intensities and additional Stark shifts of the Rydberg levels. Hence this detrimental quadrupole coupling can be efficiently compensated by an appropriate increase of the Rabi frequencies. Moreover, we consider the strong dipole-dipole interaction between a pair of Rydberg ions in the presence of the quadrupole coupling. In the effective representation we observe reducing of the dipole-dipole coupling as well as additional spin-spin interaction.

7.1 Motivation

The strongly interacting Rydberg atoms offer a promising platform for quantum computation and simulation [75, 76, 77, 78]. The long-range Rydberg-Rydberg interaction between the neutral atoms can be controlled and enhanced by applying radio-frequency electric field [79, 80]. One hope that one may use the advantages of *both* trapped ions (individual addressability, entanglement operations with small errors, etc.) *and* the strong *long* range interaction of Rydberg ions. However this novel system suffers from some disadvantages. For example, stray electric and magnetic fields due to the trap could induce electric dipole moment of the Rydberg ion. Despite that, trapped Rydberg ions have been recently experimentally accomplished [81]. The Floquet sidebands due to quadrupole interaction as well as modification of the trapping potential due to the strong polarisability of the $^{88}Sr^{+}$ Rydberg ion have been observed [82] .

In Ref. [81, 83] the Rydberg levels are excited using a single-photon excitation with vacuum ultraviolet laser light at 122 nm. However, this is quite difficult to handle experimentally. Another experimental approach is to use $^{88}Sr^{+}$ Rydberg ions [82]. In that case the Rydberg ions are excited by two-photon transitions at

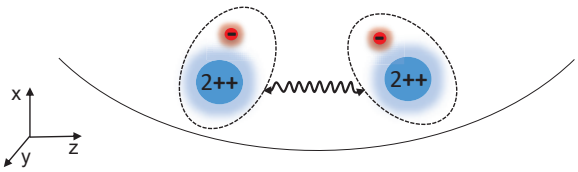

Fig. 7.1: Two Rydberg ions in a Paul trap. Due to the huge dipole moment the electron interacts with the radio-frequency electric field potential. This gives rise to the quadrupole interaction between the Rydberg levels of each individual ion. The ions are coupled due to the large electric dipole moment which is also altered by the quadrupole interaction.

243 and 309 nm respectively. Though the $^{88}Sr^{+}$ ions are excited more easily to Rydberg levels, the $nD_{3/2}$ Rydberg states are coupled by the quadrupole field of the trap. These undesirable transitions may transfer population out of the Rydberg state.

In this chapter we consider the effect of the quadrupole coupling on the coherent dynamics of Rydberg trapped ions. Such an effect arises due to the huge electric dipole moment of the Rydberg ion and causes undesired excitation of electronic transitions driven by the radio-frequency electric field of the Paul trap, see Fig. 7.1. We consider single Rydberg ion with one and two Rydberg state manifolds subject to the quadrupole coupling. We show that as long as the radio trap frequency ω of these quadrupole transitions is *sufficiently large*, the negative effect is averaged and traced out. To see that, we perform a suitable unitary transformation and investigate the system into a different picture. We show that the effect of the quadrupole coupling is merely to *rescale* the Rabi frequencies Ω_i which drive the transition between the Rydberg levels. The quandrupole interaction also induces an energy shift of the respective Rydberg levels. Moreover, we consider the strong dipole-dipole interaction between the Rydberg ions in the presence of quadrupole coupling. We show that the effect of the coupling is to reduce the strength of the dipole-dipole interaction. We also find that the quadrupole coupling induces residual dipole-dipole interaction which can be neglected only in the rotating-wave approximation.

7.2 The level system of $^{88}Sr^{+}$ trapped ion

Our quantum system consists of a single trapped Rydberg ion. Although the method is applicable for any Rydberg ion we consider for concreteness Rydberg $^{88}Sr^{+}$ ion with the level structure shown on Fig. 7.2. The Rabi frequency Ω_1 drives the two-photon transition between the states $|1\rangle$ and $|2\rangle$. State $|2\rangle$ belongs to a Rydberg $nD_{3/2}$ manifold with detuning Δ_2. We apply an additional laser field with Rabi frequency Ω_2 which couples level $|2\rangle$ and level $|3\rangle$ with detuning Δ_3. The latter is part of $n'P_{1/2}$ manifold. The interaction Hamiltonian becomes

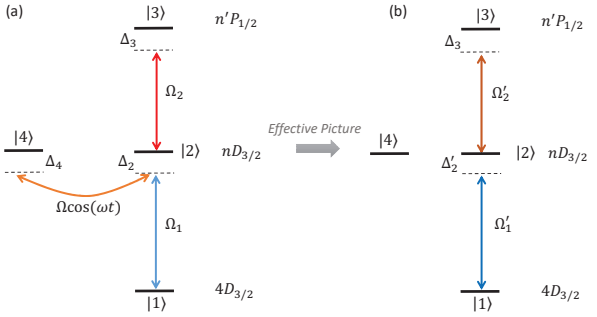

Fig. 7.2: (a) Level scheme of the Rydberg $^{88}Sr^+$ ion. The levels $nD_{3/2}$ and $n'P_{1/2}$ are Rydberg levels. Two laser fields are applied which drive the transitions $|1\rangle \leftrightarrow |2\rangle$ and $|2\rangle \leftrightarrow |3\rangle$ with Rabi frequencies $\Omega_{1,2}$ and detunings $\Delta_{2,3}$. The quadrupole field couples the levels $|2\rangle$ and $|4\rangle$ with peak Rabi frequency Ω. This transition oscillates with radio trap frequency ω. The level $|4\rangle$ has an energy shift Δ_4. (b) Using the effective picture, the system is reduced to three state ladder system with rescaled Rabi frequencies $\Omega'_{1,2}$ and detunings Δ'_2.

$(\hbar = 1)$

$$\hat{H}_0 = \Delta_2|2\rangle\langle 2| + \Delta_3|3\rangle\langle 3| + \Delta_4|4\rangle\langle 4| + (\Omega_1|1\rangle\langle 2| + \Omega_2|2\rangle\langle 3| + \text{H.c.})\,. \tag{7.1}$$

Let us consider the typical length scales of the trapped Rydberg ion. The external trapping frequency is of the order of MHz. To this frequency there corresponds a so called oscillator length a_o, which is roughly the *localization length* of the ion around its *equilibrium* position. For $\omega \sim$ MHz we have $a_o \sim$ 10 nm. On the other hand, the size of the Rydberg *orbit* a_{Ry} is proportional to n^2, where n is the principal quantum number. For Rydberg states $a_{Ry} \sim 100$ nm. Thus, it follows that $a_{Ry} \gg a_o$. Therefore the Rydberg ion can no longer be considered as a point-like particle but rather as a *composite* object [84] and its internal structure *must* be taken into account. Indeed, as shown in Refs. [82, 84, 85], the electric field of the Paul trap may excite *internal electronic* transitions which are no longer negligible contrary to the ordinary trapped ions.

The Paul trap electric field can be written as

$$\Phi(\mathbf{r}, t) = \alpha \cos(\omega t)(x^2 - y^2) - \beta\left(x^2 + y^2 - 2z^2\right), \tag{7.2}$$

where α and β are electric field gradients and ω is the radio-frequency of the Paul trap. In the customary ion traps, this electric field does *not* couple internal electronic states. The ion in that case can be considered as a point particle. However, in the case of Rydberg ions, it will couple electronic transitions. The coupling $\hat{H}_e$ of the above electric field is given by $\hat{H}_e = e\Phi(\mathbf{r}, t)$, where e is the electronic charge. Generally, this quadrupole coupling *cannot* couple (to first order) states in the manifold nX_J for $J = 1/2$ for any $X = S, P, D, \ldots$. Such

transitions are only allowed for $J > 1/2$ due to selection rules. However, states in the manifold nD_J ($J = 3/2$ or $J = 5/2$) are coupled even to first order by the quadrupole field. It turns out, that the time dependent interaction with the quadrupole is [82]

$$\hat{V}(t) = \hbar\Omega \cos(\omega t) \sum_{m_J=1/2}^{3/2} \{|nLJ(m_J - 2)\rangle\langle nLJm_J| + \text{H.c.}\}, \tag{7.3}$$

where Ω is the effective Rabi frequency for the quadruple coupling which oscillates with the trap frequency ω. This transition may lead to a leak of population to an undesirable state $|4\rangle$ as is shown in Fig. 7.2. Unfortunately rotating wave approximation is not applicable because the effective Rabi frequency Ω is comparable with the trap frequency ω [82]. In the next section we shall propose solution to this problem.

7.3 General theory of the effective picture

First, let us rewrite Eq. (7.3) for the $^{88}Sr^+$ ion,

$$\hat{V}(t) = \hat{v}e^{i\omega t} + \hat{v}^\dagger e^{-i\omega t}, \tag{7.4}$$

where

$$\hat{v} = \frac{\Omega}{2}\left(|2\rangle\langle 4| + |4\rangle\langle 2|\right). \tag{7.5}$$

Including the quadrupole interaction the total Hamiltonian becomes

$$\hat{H} = \hat{H}_0 + \hat{V}(t). \tag{7.6}$$

As we mentioned above the interaction $\hat{V}(t)$ may lead to leak of population out of Rydberg state $|2\rangle$ which spoils the single as well as the two qubit operators. In the following we perform a suitable unitary transformation. We shall designate this new quantum picture as an effective picture.

In order to derive the effective picture we perform a time dependent unitary transformation $\hat{U}(t) = e^{i\hat{K}(t)}$ to the state vector $|\psi\rangle$ such that $|\tilde{\psi}\rangle = \hat{U}(t)|\psi\rangle$, where $\hat{K}(t)$ is an Hermitian operator. Our goal is to choose $\hat{K}(t)$ such that the effective Hamiltonian $\hat{H}_{\text{eff}} = \hat{U}\hat{H}\hat{U}^\dagger + i(\partial_t\hat{U})\hat{U}^\dagger$ becomes time-independent to *any* desired order of ω^{-1}. Method for averaging of the rapidly oscillating terms was proposed in [86], which however is not suitable for our case since it requires knowledge of the spectrum of $\hat{H}_0$. We derive $\hat{K}(t)$ following the method presented in [87, 88]. Here we simply state the result

$$\hat{K}(t) = \omega^{-1}\hat{K}_1(t) + \omega^{-2}\hat{K}_2(t) + O(\omega^{-3}), \tag{7.7}$$

where

$$\hat{K}_1(t) = 2\hat{v}\sin(\omega t), \quad \hat{K}_2(t) = -2i[\hat{v}, \hat{H}_0]\cos(\omega t). \tag{7.8}$$

We find that the effective Hamiltonian becomes

$$\hat{H}_{\text{eff}} = \hat{H}_0 + \omega^{-2}[[\hat{v}, \hat{H}_0], \hat{v}] + O(\omega^{-4}), \tag{7.9}$$

which is indeed time-independent to $O(\omega^{-4})$.

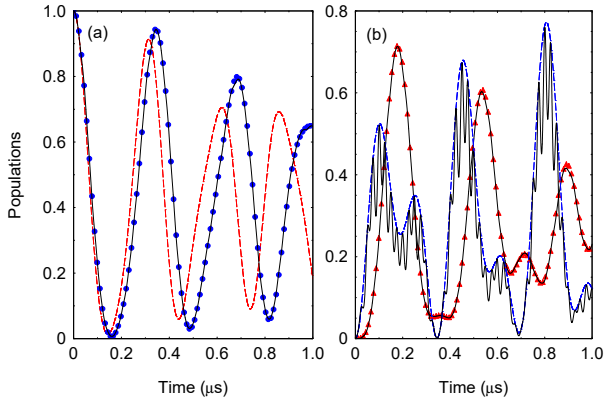

Fig. 7.3: (a) Time evolution of the probability $P_1(t)$ for the four-level system. We compare the probabilities derived from the original Hamiltonian (7.6) (solid lines) and the effective Hamiltonian (7.10) (blue dots). The red dashed line is the solution for $P_1(t)$ assuming rotating wave approximation. The parameters are set to $\Omega/2\pi = 12$ MHz, $\omega/2\pi = 20$ MHz, $\Omega_i/2\pi = 2$ MHz, $\Delta_2/2\pi = \Delta_3/2\pi = 2.0$ MHz, $\Delta_4/2\pi = 1.0$ MHz. (b) Probabilities $P_2(t)$ (dashed blue line) and $P_3(t)$ (red triangles) compared with the exact solution (solid lines).

7.4 Single Trapped Rydberg Ion

7.4.1 Single manifold coupled by the quadrupole interaction

In this subsection we consider the single trapped Rydberg ion with *one* Rydberg manifold coupled by the quadrupole coupling, see Fig. 7.2.

Substituting Eqs. (7.1) and (7.5) into Eq. (7.9), we obtain the following effective Hamiltonian,

$$\hat{H}_{\text{eff}} = \Delta_2'|2\rangle\langle 2| + \Delta_3|3\rangle\langle 3| + \Delta_4'|4\rangle\langle 4| + \left(1 - \frac{\Omega^2}{4\omega^2}\right)(\Omega_1|1\rangle\langle 2| + \Omega_2|2\rangle\langle 3| + \text{H.c.})\,. \tag{7.10}$$

Interestingly, we observe that the quadrupole interaction between states $|2\rangle$ and $|4\rangle$ is removed. However the new Rabi frequencies in the effective picture are rescaled (renormalized) with the same factor $\left(1 - \Omega^2/(4\omega^2)\right)$. Therefore in order to compensate the quadrupole interaction one needs to merely increase the laser intensities with the factor $\left(1 - \Omega^2/(4\omega^2)\right)^{-1}$. Additionally, we find that the quadrupole interaction caused an energy shift of the states $|2\rangle$ and $|4\rangle$ such that the laser detuning becomes $\Delta_2' = \Delta_2\{1 - \frac{\Omega^2}{2\omega^2}\left(1 - \frac{\Delta_4}{\Delta_2}\right)\}$ and respectively $\Delta_4' = \Delta_4\{1 - \frac{\Omega^2}{2\omega^2}\left(1 - \frac{\Delta_2}{\Delta_4}\right)\}$.

In Fig. 7.3 we compare the exact dynamics governed by the full Hamiltonian (7.6) and the effective Hamiltonian (7.10). As can be seen very good agreement is observed. For comparison, we also show the effective dynamics which is obtained by standard rotating-wave approximation (RWA), where the effect of the fast

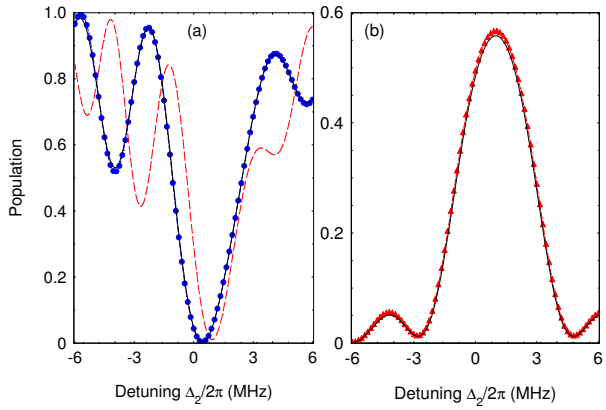

Fig. 7.4: (a) Probability $P_1(t)$ at time $t = 0.5$ μs versus the laser detuning Δ_2. The exact solution with the Hamiltonian (7.6) (solid lines) is compared with the solution with the effective Hamiltonian (7.10) (blue circles). The red dashed line is the solution for $P_1(t)$ assuming rotating wave approximation. (b) Same but for population $P_3(t)$. Solid line is the exact result and the red triangle is the effective solution.

oscillating terms is neglected, $\hat{v}e^{i\omega t} \approx 0$. As expected, RWA significantly deviates from the exact solution. This is due to the fact that Ω and ω are of the same order of magnitude, namely $\Omega = 0.6\omega$. In Fig. 7.3(b) we plot the population of the level $|2\rangle$ which is subject of the strong quadrupole interaction. Because of that the time evolution of the population contains fast and slow components where the latter can be described within the effective picture. Figure 7.4 shows the frequency scan of the populations $P_{1,3}$ at fixed interaction time. The exact and the effective solutions are almost indiscernible. Lastly, we point out that our analysis is correct as long as the trap frequency is larger than the effective quadrupole coupling, $\omega \gtrsim \Omega$. When the coupling increases more than the driving trap frequency one observes that it cannot be neglected in a sense that the level structure is no longer decoupled.

After a lengthy calculation it can be shown that the next correction to the effective Hamiltonian Eq. (7.9) is *not* $O(\omega^{-3})$ but is $O(\omega^{-4})$. This explains why the agreement in Fig. 7.3 is quite accurate.

7.4.2 Two Rydberg manifolds coupled by the quadrupole coupling

We extend the discussion by including higher angular momentum Rydberg states such as $n'P_{3/2}$ states, see Fig. 7.5(a). In that case the quadrupole Hamiltonian couples not only states $|2\rangle$ and $|4\rangle$ but also states $|3\rangle$ and $|5\rangle$. We shall show that in the effective picture the quadrupole coupling is again removed. In this

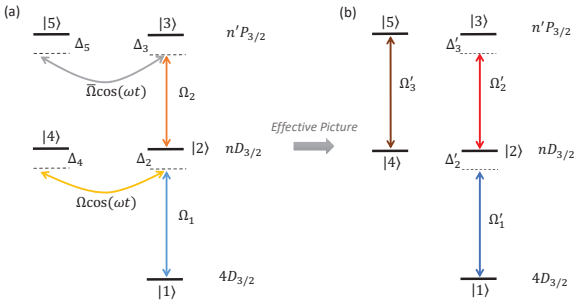

Fig. 7.5: (a) Rydberg levels for a quadrupole coupling when *both* Rydberg manifolds, $nD_{3/2}$ and $n'P_{3/2}$ are coupled by the quadrupole trap field with Rabi frequencies Ω and $\bar{\Omega}$. Both quadrupole couplings oscillate with radio trap frequency ω. (b) Effective quantum system is reduced into two *uncoupled* systems. The first system consists of the levels $|4\rangle$ and $|5\rangle$ which are driven by Rabi frequency $\Omega_3' = \frac{\Omega\bar{\Omega}\Omega_2}{2\omega^2}$. The other system is formed by the states $|i\rangle$ $i = 1, 2, 3$ in a ladder configuration driven by the rescaled Rabi frequencies $\Omega_1' = \Omega_1\left(1 - \frac{\Omega^2}{4\omega^2}\right)$ and $\Omega_2' = \Omega_2\left(1 - \frac{\Omega^2}{4\omega^2} - \frac{\bar{\Omega}^2}{4\omega^2}\right)$ and detunings Δ_2', Δ_3'.

case the Hamiltonian is again of the type $\hat{H} = \hat{H}_0 + \hat{V}(t)$. However, here

$$\begin{aligned}\hat{H}_0 =&\Delta_2|2\rangle\langle 2| + \Delta_3|3\rangle\langle 3| + \Delta_4|4\rangle\langle 4| + \Delta_5|5\rangle\langle 5| \\ &+ (\Omega_1|1\rangle\langle 2| + \Omega_2|2\rangle\langle 3| + \text{H.c.})\end{aligned} \tag{7.11}$$

and $\hat{V}(t) = \hat{v}e^{i\omega t} + \text{H.c.}$, where $\hat{v}$ is given by

$$\hat{v} = \frac{\Omega}{2}|2\rangle\langle 4| + \frac{\bar{\Omega}}{2}|3\rangle\langle 5| + \text{H.c.}, \tag{7.12}$$

with Ω and $\bar{\Omega}$ being the effective Rabi frequencies for the quadrupole interaction.

The expression Eq. (7.9) for the effective Hamiltonian as well as Eqs. (7.7) and (7.8) for $\hat{K}$ remain valid. Thus, we obtain

$$\hat{H}_{\text{eff}} = \hat{H}_1 + \hat{H}_2. \tag{7.13}$$

Here

$$\hat{H}_1 = \Delta_4'|4\rangle\langle 4| + \Delta_5'|5\rangle\langle 5| + \Omega_3'\left(|4\rangle\langle 5| + |5\rangle\langle 4|\right), \tag{7.14}$$

and

$$\begin{aligned}\hat{H}_2 \quad = \quad & \Delta_2'|2\rangle\langle 2| + \Delta_3'|3\rangle\langle 3| + \Omega_1\left(1 - \frac{\Omega^2}{4\omega^2}\right)\left(|1\rangle\langle 2|\right. \\ & \left.+|2\rangle\langle 1|\right) + \Omega_2\left(1 - \frac{\Omega^2}{4\omega^2} - \frac{\bar{\Omega}^2}{4\omega^2}\right)\left(|2\rangle\langle 3| + |3\rangle\langle 2|\right).\end{aligned} \tag{7.15}$$

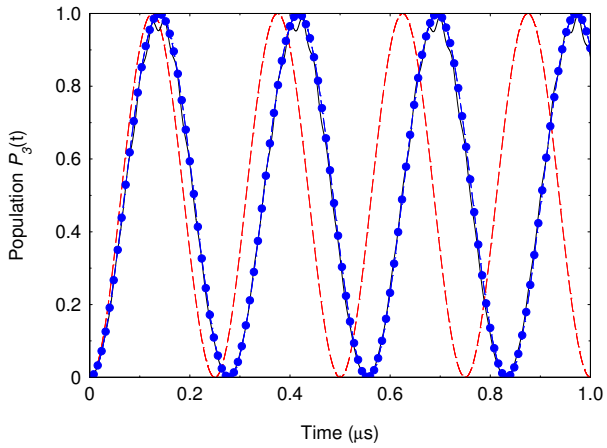

Fig. 7.6: Time evolution of the probability $P_3(t)$. The Rydberg states $|2\rangle$ and $|3\rangle$ are coupled by quadrupole interaction with the states $|4\rangle$ and $|5\rangle$ with coupling strengths $\Omega/2\pi = 12$ MHz and $\bar{\Omega}/2\pi = 4$ MHz. The trap radio frequency is set to $\omega/2\pi = 20$ MHz. The other parameters are $\Omega_2/2\pi = 2$ MHz, $\Omega_1 = 0$, $\Delta_i = 0$ $(i = 2, 3, 4)$. The solid line is the exact result and the dashed blue circles is the solution using the effective Hamiltonian (7.13). The red dashed line is the solution using rotating-wave approximation.

This result means that the initial five-level coupled system is reduced to two uncoupled ladders, see Fig. 7.5(b). The first ladder is a two level system consisting of states $|4\rangle$ and $|5\rangle$ driven by effective Rabi frequency $\Omega_3' = \frac{\Omega\bar{\Omega}\Omega_2}{2\omega^2}$. This transition is caused by the virtual chain of transitions between the states $|4\rangle \leftrightarrow |2\rangle \leftrightarrow |3\rangle \leftrightarrow |5\rangle$. This explains why $\Omega_3' \propto \Omega\Omega_2\bar{\Omega}$. Additionally, the quadrupole interaction causes energy shift of the level $|5\rangle$ such that we have $\Delta_5' = \Delta_5\{1 - \frac{\bar{\Omega}^2}{2\omega^2}\left(1 - \frac{\Delta_3}{\Delta_5}\right)\}$. The second ladder consists of three states $|1\rangle$, $|2\rangle$ and $|3\rangle$. The effect of the quadruple interaction is to rescale the respective Rabi frequencies and detunings Δ_2', $\Delta_3' = \Delta_3\{1 - \frac{\bar{\Omega}^2}{2\omega^2}\left(1 - \frac{\Delta_5}{\Delta_3}\right)\}$ as is shown in Fig. 7.5(b). As long as the initial population is in state $|1\rangle$, the population will remain in the second ladder, described by $\hat{H}_2$.

In Fig. 7.6 we show the resonance oscillations of the probability $P_3(t)$. We observe that the initial prepared population in state $|2\rangle$ exhibits Rabi oscillations where the exact solution is very closed to the effective picture. Although the quadrupole coupling between the states $|2\rangle$ and $|4\rangle$ is very strong and comparable with the radio trap frequency the corresponding probability is slightly affected.

7.5 Two Rydberg ions interacting with dipole-dipole interaction

In this section, we extend the discussion including the dipole-dipole interaction. We consider an ion chain consisting of two Rydberg ions. The generalization for

chain with N ions is straightforward. The full Hamiltonian is quite complicated, see for example Ref. [84]. However, under certain rather plausible approximations the Hamiltonian can be reduced to [84]

$$\hat{H} = \hat{H}_0 + \hat{V}(t) + \hat{H}_{\rm dd}. \tag{7.16}$$

Here $\hat{H}_0$ is given by

$$\begin{aligned}\hat{H}_0 = \sum_{j=1}^{2} \{ &\Delta_2 |2_j\rangle\langle 2_j| + \Delta_3 |3_j\rangle\langle 3_j| + \Delta_4 |4_j\rangle\langle 4_j| \} \\ &+ (\Omega_1 |1_j\rangle\langle 2_j| + \Omega_2 |2_j\rangle\langle 3_j| + \text{H.c.})\}. \end{aligned} \tag{7.17}$$

This is the single-ion Hamiltonian without the quadrupole interaction, see Eq. (7.1).

The quadrupole interaction is again of the type $\hat{V}(t) = \hat{v}e^{i\omega t} + \text{H.c.}$, where

$$\hat{v} = \frac{\Omega}{2} \left(|2_1\rangle\langle 4_1| + |2_2\rangle\langle 4_2| + \text{H.c.} \right). \tag{7.18}$$

Lastly, the term $\hat{H}_{\rm dd}$ is the dipole-dipole interaction. It is given by [84]

$$\hat{H}_{\rm dd} = \frac{\hat{d}_1^{(x)}\hat{d}_2^{(x)} + \hat{d}_1^{(y)}\hat{d}_2^{(y)} - 2\hat{d}_1^{(z)}\hat{d}_2^{(z)}}{8\pi\epsilon_0 |z_0^{(1)} - z_0^{(2)}|^3}. \tag{7.19}$$

Here $\hat{d}_j^{(\alpha)},\ \alpha = x, y, z$ is the α component of the operator of the dipole moment for the jth ion, ϵ_0 is the permittivity of the vacuum and $z_0^{(j)}$ is the equilibrium position of the jth ion along the z axis. We can project this dipole-dipole interaction upon the basis states. Next we perform an optical RWA which is fulfilled as long as the Bohr transition frequencies of the Rydberg levels are much higher than the all Rabi frequencies, such that we obtain

$$\hat{H}_{\rm dd} = \lambda \left(|2_1 3_2\rangle\langle 3_1 2_2| + |3_1 2_2\rangle\langle 2_1 3_2| \right), \tag{7.20}$$

where

$$\lambda = \frac{|\langle 2|\hat{d}_x|3\rangle|^2 + |\langle 2|\hat{d}_y|3\rangle|^2 - 2|\langle 2|\hat{d}_z|3\rangle|^2}{8\pi\epsilon_0 |z_0^{(1)} - z_0^{(2)}|^3}. \tag{7.21}$$

Here λ is the strength of the Rydberg dipole-dipole interaction. Only the matrix elements of $\hat{d}_\alpha,\ \alpha = x, y, z$ between *Rydberg* states (state $|2\rangle$ and state $|3\rangle$) have been used, since the other matrix elements are negligible. The reason is that the overlap between the wave-function of the ground state $|1\rangle$ and a Rydberg wave-function is negligible. The dipole-dipole coupling resembles the XX Heisenberg spin-spin interaction. Indeed, setting $\Omega_1 = 0$ one can introduce the spin rising $\sigma_j^+ = |3_j\rangle\langle 2_j|$ and lowering $\sigma_j^- = |2_j\rangle\langle 3_j|$ operators such that the dipole-dipole interaction can be rewritten as $\hat{H}_{\rm dd} = \lambda(\sigma_1^x\sigma_2^x + \sigma_1^y\sigma_2^y)$, where σ_j^α are the Pauli matrices.

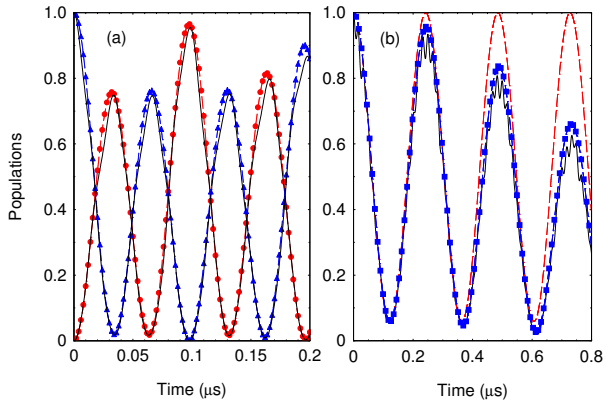

Fig. 7.7: (a) Coherent exchange of spin excitation versus the interaction time. We compare the exact solution for the probabilities to observe states $|2_1 3_2\rangle$ and $|3_1 2_2\rangle$ (solid lines) with the effective Hamiltonian for $P_{23}(t)$ (blue triangles) and $P_{32}(t)$ (red circles). The parameters are set to $\Omega/2\pi = 8.0$ MHz, $\omega/2\pi = 30$ MHz, $\Delta_2/2\pi = 1.0$ MHz, $\lambda/2\pi = 7.0$ MHz, and $\Omega_2/2\pi = 2.0$ MHz. (b) The same but initially the system is prepared in the state $|3_1 4_2\rangle$. The solid line is the exact solution and the dashed blue squares is the solution with the effective Hamiltonian. The dashed line shows the probability $P_{34}(t)$ assuming rotating wave approximation.

Combining $\hat{\tilde{H}}_0 = \hat{H}_0 + \hat{H}_{\rm dd}$, the total Hamiltonian becomes again of the type $\hat{H} = \hat{\tilde{H}}_0 + \hat{V}(t)$. Therefore the expression (7.9) for the effective Hamiltonian as well as Eqs. (7.7) and (7.8) for $\hat{K}$ remain valid. Using Eq. (7.9) the effective Hamiltonian becomes

$$\begin{aligned}\hat{H}_{\rm eff} = &\sum_{j=1}^{2}\{\Delta_2'|2_j\rangle\langle 2_j| + \Delta_3'|3_j\rangle\langle 3_j| + \Delta_4'|4_j\rangle\langle 4_j|\} \\ &+ \left(1 - \frac{\Omega^2}{4\omega^2}\right)(\Omega_1|1_j\rangle\langle 2_j| + \Omega_2|2_j\rangle\langle 3_j| + \text{H.c.})\} \\ &+ \lambda\left(1 - \frac{\Omega^2}{2\omega^2}\right)(|2_1 3_2\rangle\langle 3_1 2_2| + |3_1 2_2\rangle\langle 2_1 3_2|) \\ &+ \frac{\lambda\Omega^2}{2\omega^2}(|3_1 4_2\rangle\langle 4_1 3_2| + |4_1 3_2\rangle\langle 3_1 4_2|)\,. \end{aligned} \tag{7.22}$$

In Fig. 7.7, we compare the exact solution with Hamiltonian (7.16) with the solution using the effective Hamiltonian (7.22). Due to the strong dipole-dipole interaction the system exhibits coherent exchange of spin excitations described by the XX Heisenberg spin model. The quadropule interaction leads to rescaling of the dipole-dipole coupling by the factor $\left(1 - \Omega^2/(2\omega^2)\right)$, i.e., $\lambda \to \lambda\left(1 - \frac{\Omega^2}{2\omega^2}\right)$. The single ion Rabi frequencies are again renormalized with the same factor $\left(1 - \Omega^2/(4\omega^2)\right)$, i.e., $\Omega_i \to \Omega_i\left(1 - \frac{\Omega^2}{4\omega^2}\right)$, $i = 1, 2$. Additionally, the quadrop-

ule interaction induces residual dipole-dipole coupling between the states $|3_i 4_j\rangle$ and $|4_i 3_j\rangle$ described by the last term in (7.22). This coupling spoils the XX-type Heisenberg interaction between the Rydberg levels $|2_i 3_j\rangle$ and $|3_i 2_j\rangle$. In general, the residual dipole-dipole interaction can not be ignored except in the limit $\omega \gg \Omega$ where the RWA can be applied. Finally, we consider the dipole-dipole interaction between microwave dressed Rydberg ions. Such a dressing creates additional term in the dipole-dipole interaction (7.20) which couples the states $|2_i 2_j\rangle\langle 2_i 2_j|$ with coupling strengths μ. Because of that we find that the residual terms due to the quadrupole interaction are of order of $\mu(\Omega^2/2\omega^2)$.

Note that the whole technique is valid so long as $\omega \gtrsim \Omega_i,\ i = 1, 2$ *as well as* $\omega \gtrsim \lambda$. The last condition $\lambda \lesssim \omega$ puts a lower limit on the frequency ω. However the experimenter can increase ω above this limit. In addition, numerical simulations show that even for $\lambda = \omega/2$, the effective Hamiltonian remains quite correct. Therefore a long ranged dipole-dipole interaction of strength of $\sim 10 \div 20$ MHz is still viable. In addition, by increasing the radio frequency ω more powerful interaction λ can be used and the effective Hamiltonian is still applicable. For instance for $\omega = 2\pi \times 40$ MHz dipole-dipole interaction of the order of 20 MHz can be achieved.

7.6 Conclusion

In this chapter we have shown that the quadrupole interaction which causes a reduction in the dipole moment in a trapped Rydberg ion can be dealt with by increasing the Rabi frequencies. To show that we have applied an unitary transformation. In this new picture, dubbed 'effective picture', the Rabi frequencies are renormalized with the same factor $\left[1 - \Omega^2/(4\omega^2)\right]$. Therefore by increasing the laser intensities with the factor $\left[1 - \Omega^2/(4\omega^2)\right]^{-1}$, the negative effect of the quadrupole interaction $\Omega \cos \omega t$ can be removed. In addition, we have extended the discussion, when *both* Rydberg manifolds are coupled by the quadrupole part of the trapping electric field. We observes that the effective five level system is *decoupled* and the Rabi frequencies are altered by *different* factors. Therefore even in that case, the negative effect of the quadrupole interaction can be removed. One merely has to rescale the laser intensities by different magnitudes. We have extended the discussion to an ion chain of two ions and we have shown that the Rabi frequencies are renormalized as well as the dipole-dipole coupling is modified. The latter is out of experimental control. However the reduction of the dipole-dipole coupling is only a few per cent for reasonable experimental parameters [82], while the renormalization can be dealt with by increasing the Rabi frequency as was shown in the single ion case.

8. INTRODUCTION TO QUANTUM INFORMATION GEOMETRY

8.1 Distance Between Quantum States

8.1.1 Quantum Geometric Tensor

The goal of this chapter is to introduce the background of the quantum information geometry and its connection with the theory of quantum parameter estimation. In order to define geometry between the quantum states one need to introduce the concept of distance as a measure of distinguishingly. Let us define the fidelity between two quantum states as follows

$$F(\lambda, \lambda + d\lambda) = |\langle \Psi_0(\lambda) | \Psi_0(\lambda + d\lambda) \rangle|, \tag{8.1}$$

where $|\Psi_0(\lambda)\rangle$ is the state vector which describes the quantum system. We assume that $|\Psi_0(\lambda)\rangle$ depends on parameter λ and with $d\lambda$ we denote the small variation of λ. Then one can expand the scalar product in Taylor series

$$\langle \Psi_0(\lambda) | \Psi_0(\lambda + d\lambda) \rangle = 1 + \langle \Psi_0 | \partial_\lambda \Psi_0 \rangle d\lambda + \frac{1}{2} \langle \Psi_0 | \partial_\lambda^2 \Psi_0 \rangle d\lambda^2 + O(d\lambda^3). \tag{8.2}$$

Using (8.2) it is straightforward to show that

$$F(\lambda, \lambda + d\lambda) = \{1 + (\langle \Psi_0 | \partial_\lambda \Psi_0 \rangle \langle \partial_\lambda \Psi_0 | \Psi_0 \rangle + \frac{1}{2} \langle \Psi_0 | \partial_\lambda^2 \Psi_0 \rangle + \frac{1}{2} \langle \partial_\lambda^2 \Psi_0 | \Psi_0 \rangle) d\lambda^2 + O(d\lambda^3)\}^{1/2}. \tag{8.3}$$

We can simplify the last two terms in (8.3) using the relation $\langle \partial_\lambda^2 \Psi_0 | \Psi_0 \rangle + \langle \Psi_0 | \partial_\lambda^2 \Psi_0 \rangle = -2 \langle \partial_\lambda \Psi_0 | \partial_\lambda \Psi_0 \rangle$. Therefore, the distance between two infinitesimally close quantum states is given by

$$ds^2 = 1 - F(\lambda, \lambda + d\lambda)^2 = (\langle \partial_\lambda \Psi_0 | \partial_\lambda \Psi_0 \rangle - \langle \partial_\lambda \Psi_0 | \Psi_0 \rangle \langle \Psi_0 | \partial_\lambda \Psi_0 \rangle) d\lambda^2. \tag{8.4}$$

Remarkably, the term $g(\lambda) = \langle \partial_\lambda \Psi_0 | \partial_\lambda \Psi_0 \rangle - \langle \partial_\lambda \Psi_0 | \Psi_0 \rangle \langle \Psi_0 | \partial_\lambda \Psi_0 \rangle$ has a meaning of metric tensor characterizes the distance between the two states. As can be expected the metric tensor is invariant under arbitrary λ-dependent U(1) gauge transformation of the state wave functions. Indeed, since the global phase of the wave function is not observable the metric tensor and thus the distance have to be gauge invariant.

Although we have considered here only the single parameter dependence of the state vector one can generalize the result of the metric tensor for multiparameter case. Indeed, suppose that the state vector depends on a set of parameters $\vec{\lambda} = \{\lambda_1, \lambda_2, \ldots, \lambda_n\}$. Then, a natural measure of the distance between

the wave functions separated by infinitesimal $d\vec{\lambda}$ is

$$ds^2 = 1 - F(\vec{\lambda}, \vec{\lambda} + d\vec{\lambda})^2 = \sum_{\mu\nu} g_{\mu\nu} d\lambda_\mu d\lambda_\nu. \tag{8.5}$$

The metric tensor is given by $g_{\mu\nu} = \Re[\mathcal{G}_{\mu\nu}]$ where

$$\mathcal{G}_{\mu\nu} = \langle \partial_\mu \Psi_0 | \partial_\nu \Psi_0 \rangle - \langle \partial_\mu \Psi_0 | \Psi_0 \rangle \langle \Psi_0 | \partial_\nu \Psi_0 \rangle \tag{8.6}$$

is the quantum geometric tensor whose real symmetric part defines the metric tensor. For sake of completeness we also introduce the Berry curvature, which is given by the imaginary (antisymmetric) part of the geometric tensor: $F_{\mu\nu} = -2\Im[\mathcal{G}_{\mu\nu}] = \partial_\mu A_\nu - \partial_\nu A_\mu$, where $A_\mu = i\langle \Psi_0 | \partial_\mu | \Psi_0 \rangle$ is the Berry connection.

8.1.2 Fidelity Susceptibility

Let us now assume that the state vector $|\Psi_0(\lambda)\rangle$ is the ground state of Hamiltonian $\hat{H}(\lambda)$ with spectral equation $\hat{H}(\lambda)|\Psi_n(\lambda)\rangle = E_n(\lambda)|\Psi_n\rangle$. Then, it is straightforward to show that

$$\langle \Psi_n | \partial_\lambda \Psi_0 \rangle = \frac{\langle \Psi_n | \partial_\lambda \hat{H} | \Psi_0 \rangle}{E_0 - E_n}, \quad n \neq 0. \tag{8.7}$$

Using the spectral decomposition $\sum_{n=0} |\Psi_n\rangle\langle\Psi_n| = \hat{\mathbf{1}}$ we obtain for the fidelity F

$$F^2 = 1 - \langle \partial_\lambda \Psi_0 | (\hat{\mathbf{1}} - |\Psi_0\rangle\langle\Psi_0|) | \partial_\lambda \Psi_0 \rangle d\lambda^2 = 1 - \sum_{n\neq 0} \langle \partial_\lambda \Psi_0 | \Psi_n \rangle \langle \Psi_n | \partial_\lambda \Psi_0 \rangle d\lambda^2. \tag{8.8}$$

Using Eq. (8.7) we derive

$$F^2 = 1 - \sum_{n\neq 0} \frac{|\langle \Psi_n(\lambda) | \partial_\lambda \hat{H} | \Psi_0(\lambda) \rangle|^2}{(E_n(\lambda) - E_0(\lambda))^2}. \tag{8.9}$$

Finally, the fidelity susceptibility is defined by

$$\chi_F(\lambda) \lim_{\delta\lambda \to 0} \frac{-2\ln(F)}{\delta\lambda^2} = \sum_{n\neq 0} \frac{|\langle \Psi_n(\lambda) | \partial_\lambda \hat{H} | \Psi_0(\lambda) \rangle|^2}{(E_n(\lambda) - E_0(\lambda))^2}, \tag{8.10}$$

which is equal to the single parameter metric tensor.

For multi-parameter case the quantum geometric tensor becomes

$$\mathcal{G}_{\mu\nu} = \sum_{n\neq 0} \frac{\langle \Psi_0(\lambda) | \partial_\mu \hat{H} | \Psi_n(\lambda) \rangle \langle \Psi_n(\lambda) | \partial_\lambda \hat{H} | \Psi_0(\lambda) \rangle}{(E_n(\lambda) - E_0(\lambda))^2}. \tag{8.11}$$

This expression suggests that at the critical points λ_c, where the energy gap $\Delta_n = E_n(\lambda_c) - E_0(\lambda_c)$ vanishes the quantum geometric tensor might show a

singular behavior. Quantum models in which the ground state energy gap closes at some critical point in the thermodynamical limit may exhibit a quantum phase transition. Thus the singularity of the quantum geometric tensor can be used as a signal of criticality.

Moreover as we will show later on the metric tensor is related with the quantum Fisher information which gives the ultimate precision of the estimation of parameter λ. Since the larger quantum Fisher information the better estimation using probe systems which exhibit critical behaviour may significantly improve the estimation precision. Indeed, the estimation of a physical quantity driving a quantum phase transitions can be dramatically improved at the quantum critical point where the energy gap vanishes.

Up to now we have only considered the distance between pure quantum states. In the following we extend the discussion for mixed states.

8.1.3 Bures Distance

Let us generalized the definition of distance for mixed states. Suppose that we have two quantum states which is described by the density matrices $\hat{\rho}_A$ and $\hat{\rho}_B$. The Uhlmann fidelity between the quantum statistical distributions is defined by

$$\mathcal{F}(\hat{\rho}_A, \hat{\rho}_B) = \mathrm{Tr}\sqrt{\sqrt{\hat{\rho}_A}\hat{\rho}_B\sqrt{\hat{\rho}_A}}. \tag{8.12}$$

Then the Bures distance between two infinitesimally close density matrices $\hat{\rho}_A = \hat{\rho}$ and $\hat{\rho}_B = \hat{\rho} + \delta\hat{\rho}$ is given by

$$ds_B^2 = 2(1 - \mathcal{F}(\hat{\rho}_A, \hat{\rho}_B)). \tag{8.13}$$

In order to obtain a close expression for the Bures distance we expand the Uhlmann fidelity up to $\delta\hat{\rho}^2$. We have

$$\sqrt{\hat{\rho}^2 + \sqrt{\hat{\rho}}\delta\hat{\rho}\sqrt{\hat{\rho}}} = \hat{\rho} + \hat{\mathcal{X}} + \hat{\mathcal{Y}} + O(\delta\hat{\rho}^3), \tag{8.14}$$

where we assume that $\hat{\mathcal{X}} \sim \delta\hat{\rho}$ and $\hat{\mathcal{Y}} \sim \delta\hat{\rho}^2$. Therefore, we obtain the following conditions

$$\sqrt{\hat{\rho}}\delta\hat{\rho}\sqrt{\hat{\rho}} = \hat{\rho}\hat{\mathcal{X}} + \hat{\mathcal{X}}\hat{\rho}, \quad \hat{\rho}\hat{\mathcal{Y}} + \hat{\mathcal{Y}}\hat{\rho} = -\hat{\mathcal{X}}^2. \tag{8.15}$$

Note that because $\mathrm{Tr}\hat{\rho} = 1$ we have $\mathrm{Tr}\delta\hat{\rho} = 0$ and therefore $\mathrm{Tr}\hat{\mathcal{X}} = 0$.

The spectral decomposition of the density matrix is $\hat{\rho} = \sum_n p_n|\psi_n\rangle\langle\psi_n|$ where p_n are the eigenvalues ($\sum_n p_n = 1$) and $|\psi_n\rangle$ are the corresponding eigenvectors. Using this we obtain

$$\hat{\mathcal{X}}_{nm} = \frac{\sqrt{p_n p_m}}{p_n + p_m}\langle\psi_n|\delta\hat{\rho}|\psi_m\rangle, \quad \hat{\mathcal{Y}}_{nm} = -\frac{\hat{\mathcal{X}}^2_{nm}}{p_n + p_m}. \tag{8.16}$$

Finally, the Bures distance can be expressed as

$$ds_B^2 = \frac{1}{2}\sum_{nm}\frac{\langle\psi_m|\delta\hat{\rho}|\psi_n\rangle\langle\psi_n|\delta\hat{\rho}|\psi_m\rangle}{p_n + p_m} \tag{8.17}$$

Let us now assume that the density matrix depends on a set of parameters $\vec{\lambda}$ such as $\hat{\rho}(\vec{\lambda}) = \sum_n p_n|\psi_n(\vec{\lambda})\rangle\langle\psi_n(\vec{\lambda})|$. Then the variation becomes $\delta\hat{\rho}(\vec{\lambda}) = \sum_n p_n(|d\psi_n\rangle\langle\psi_n| + |\psi_n\rangle\langle d\psi_n|)$. Inserting this into Eq. (8.17) we obtain $ds_B^2 = \sum_{\mu\nu} g_{\mu\nu} d\lambda_\mu d\lambda_\nu$ where

$$g_{\mu\nu} = \frac{1}{2}\sum_{n\neq m} \frac{(p_n - p_m)^2}{p_n + p_m}\langle\psi_m|\partial_\mu\psi_n\rangle\langle\partial_\nu\psi_n|\psi_m\rangle \tag{8.18}$$

is the metric tensor.

8.2 Quantum Estimation Theory

The goal of a parameter estimation problem is to find an estimator $\lambda = \lambda(x_1, x_2, \ldots)$ from set n of measurement outcomes into the space of parameters. The classical Fisher information which quantifies the amount of information on the parameter λ is given by

$$F_{\mathrm{CL}}(\lambda) = \int dx \frac{1}{p(x|\lambda)}\left(\frac{\partial p(x|\lambda)}{\partial\lambda}\right)^2, \tag{8.19}$$

where $p(x|\lambda)$ is the conditional probability of obtaining the value x when the parameter has the value λ. Then the statistical uncertainty in the estimation of λ is given by the classical Cramér-Rao inequality

$$V(\lambda) \geq \frac{1}{F_{\mathrm{CL}}(\lambda)}, \tag{8.20}$$

where $V(\lambda)$ is the mean square error of estimator of the parameter λ.

According the Born roles of quantum mechanics the probability $p(x|\lambda)$ can be expressed as $p(x|\lambda) = \mathrm{Tr}(\hat{\Pi}_x\hat{\rho}_\lambda)$, where $\hat{\Pi}_x$ are the elements of a positive operator values measure (POVM) which satisfy the condition $\int dx\hat{\Pi}_x = \hat{\mathbf{1}}$ and $\hat{\rho}_\lambda$ is the density operator which depends on the parameter we wish to estimate. Let us now introduce the Symmetric Logarithmic Derivative (SLD) operator $\hat{\mathcal{L}}_\lambda$ by the equation

$$2\partial_\lambda\hat{\rho}_\lambda = \hat{\mathcal{L}}_\lambda\hat{\rho}_\lambda + \hat{\rho}_\lambda\hat{\mathcal{L}}_\lambda. \tag{8.21}$$

Therefore, we have $\partial_\lambda p(x|\lambda) = \mathrm{Tr}(\hat{\Pi}_x\partial_\lambda\hat{\rho}_\lambda) = \Re(\mathrm{Tr}\hat{\Pi}_x\hat{\rho}_\lambda\hat{\mathcal{L}}_\lambda))$. Using this one can rewrite the classical Fisher information as follows

$$F_{\mathrm{CL}}(\lambda) = \int dx \frac{\Re(\mathrm{Tr}\hat{\Pi}_x\hat{\rho}_\lambda\hat{\mathcal{L}}_\lambda))^2}{\mathrm{Tr}(\hat{\Pi}_x\hat{\rho}_\lambda)}. \tag{8.22}$$

Since the $F_{\mathrm{CL}}(\lambda)$ depends on the measurement basis a natural question arise whether one can maximize the Fisher information over the quantum measurements? Indeed, such a upper limit of $F_{\mathrm{CL}}(\lambda)$ exists and can be derived using

the following chain of inequalities

$$\begin{aligned} F_{\rm CL}(\lambda) &= \int dx \frac{\Re({\rm Tr}\hat{\Pi}_x\hat{\rho}_\lambda\hat{\mathcal{L}}_\lambda))^2}{{\rm Tr}(\hat{\Pi}_x\hat{\rho}_\lambda)} \leq \int dx \left|\frac{{\rm Tr}(\hat{\Pi}_x\hat{\rho}_\lambda\hat{\mathcal{L}}_\lambda)}{\sqrt{{\rm Tr}(\hat{\Pi}_x\hat{\rho}_\lambda)}}\right|^2 \\ &= \int dx \left|{\rm Tr}\left(\frac{\sqrt{\hat{\rho}_\lambda}\sqrt{\hat{\Pi}_x}}{\sqrt{{\rm Tr}(\hat{\Pi}_x\hat{\rho}_\lambda)}}\sqrt{\hat{\Pi}_x}\hat{\mathcal{L}}_\lambda\sqrt{\hat{\rho}_\lambda}\right)\right|^2 \\ &\leq \int dx {\rm Tr}\left(\sqrt{\hat{\Pi}_x}\hat{\mathcal{L}}_\lambda\sqrt{\hat{\rho}_\lambda}\sqrt{\hat{\rho}_\lambda}\hat{\mathcal{L}}_\lambda\sqrt{\hat{\Pi}_x}\right) = {\rm Tr}\left(\hat{\rho}_\lambda\hat{\mathcal{L}}_\lambda^2\right), \end{aligned} \tag{8.23}$$

where we use Schwartz inequality $|{\rm Tr}(A^\dagger B)|^2 \leq {\rm Tr}(A^\dagger A){\rm Tr}(B^\dagger B)$. The result show that the Fisher information is upper bounded by the so called quantum Fisher information

$$F_{\rm Q}(\lambda) = {\rm Tr}\left(\hat{\rho}_\lambda\hat{\mathcal{L}}_\lambda^2\right), \tag{8.24}$$

with $F_{\rm CL}(\lambda) \leq F_{\rm Q}(\lambda)$. Therefore the *fundamental precision* of any quantum estimation is bounded by the quantum Cramér-Rao inequality

$$V(\lambda) \geq \frac{1}{F_{\rm Q}(\lambda)}. \tag{8.25}$$

This inequality provides the ultimate bound of precision and does not depend on the measurement. Among the all measurement there exist the so called *optimal* measurement in which the classical Fisher information is equal to the quantum Fisher information.

One can explicitly find the optimal measurement for the single parameter estimation by defining the operator

$$\hat{O}_\lambda = \hat{\mathbf{1}} + \frac{\hat{\mathcal{L}}_\lambda}{F_{\rm Q}(\lambda)}. \tag{8.26}$$

Therefore we have $\langle\hat{O}_\lambda\rangle = {\rm Tr}(\hat{\rho}_\lambda\hat{O}_\lambda) = \lambda$ and $\langle\hat{O}_\lambda^2\rangle = {\rm Tr}(\hat{\rho}_\lambda\hat{O}_\lambda^2) = \lambda^2 + \frac{1}{F_{\rm Q}^2(\lambda)}$. The shot noise limited sensitivity in the estimation of the parameter λ from the measured signal $\langle\hat{O}_\lambda\rangle$ is given by

$$\delta\lambda^2 = \frac{\langle\hat{O}_\lambda^2\rangle}{\partial_\lambda\langle\hat{O}_\lambda\rangle} = \frac{1}{F_{\rm Q}(\lambda)}. \tag{8.27}$$

The result shows that the optimal measurement basis which saturates the quantum Cramér-Rao bound is given by the eigenvectors of the Symmetric Logarithmic Derivative operator $\hat{\mathcal{L}}_\lambda$.

The operator equation for the SLD operator can be solved as follows:

$$\hat{\mathcal{L}}_\lambda = 2\int_0^\infty du e^{-\hat{\rho}_\lambda u}\partial_\lambda\hat{\rho}_\lambda e^{-\hat{\rho}_\lambda u}. \tag{8.28}$$

Therefore, the basis independent form of the quantum Fisher information is given by

$$F_{\rm Q}(\lambda) = 2\int_0^\infty du {\rm Tr}(\partial_\lambda\hat{\rho}_\lambda e^{-\hat{\rho}_\lambda u}\partial_\lambda\hat{\rho}_\lambda e^{-\hat{\rho}_\lambda u}). \tag{8.29}$$

Usually, the explicit calculation requires to specify a given basis. It is convenient to choose the eigenbasis of the density matrix. Then the integration can be performed so that we obtain

$$F_{\rm Q}(\lambda) = 2\sum_{n,m}\frac{\langle\psi_m|\partial_\lambda\hat{\rho}_\lambda|\psi_n\rangle}{p_n+p_m}{\rm Tr}(\partial_\lambda\hat{\rho}_\lambda|\psi_m\rangle\langle\psi_n|) = 2\sum_{n,m}\frac{|\langle\psi_m|\partial_\lambda\hat{\rho}_\lambda|\psi_n\rangle|^2}{p_n+p_m}. \tag{8.30}$$

Furthermore, let us assume that the eigenvalues p_n are independent on the parameter λ. Then we have

$$\partial_\lambda\hat{\rho}_\lambda = \sum_k p_k(|\partial_\lambda\psi_k\rangle\langle\psi_k| + |\psi_k\rangle\langle\partial_\lambda\psi_k|). \tag{8.31}$$

Then using this it is straightforward to show that the quantum Fisher information is given by

$$F_{\rm Q}(\lambda) = 2\sum_{n,m}\frac{(p_n-p_m)^2}{p_n+p_m}|\langle\psi_n|\partial_\lambda\psi_m\rangle|^2. \tag{8.32}$$

Remarkably, this expression provides equivalence between the quantum Fisher information and the metrix tensor elements, namely

$$F_{\rm Q}(\lambda) = 4g_{\lambda\lambda}. \tag{8.33}$$

Therefore, the maximal amount of information on the parameter λ that can be extracted by performing an optimal measurement is intimately related with the measure of distinguishably between two infinitesimally close quantum states. This provide fundamental relation between quantum estimation theory and quantum information geometry!

8.3 Parameter Estimation of Unitary Perturbation

Let us now consider the case where the parameter of interest is the amplitude of a unitary perturbation which act on a given initial state with density matrix $\hat{\rho}_0$ whose spectral decomposition is $\hat{\rho}_0 = \sum_n p_n|\varphi_n\rangle\langle\varphi_n|$. The unitary propagator takes the form $\hat{U}_\lambda = e^{-i\lambda\hat{G}}$ where $\hat{G}$ is hermitian operator and λ is the parameter we wish to estimate. Then the density matrix after the action of the unitary perturbation is $\hat{\rho}_\lambda = \hat{U}_\lambda\hat{\rho}_0\hat{U}_\lambda^\dagger$ so that we have

$$\partial_\lambda\hat{\rho}_\lambda = i\hat{U}_\lambda[\hat{\rho}_0,\hat{G}]\hat{U}_\lambda^\dagger. \tag{8.34}$$

Uisng this we obtain for SLD operator the following expression

$$\hat{L}_\lambda = \hat{U}_\lambda\hat{L}_0\hat{U}_\lambda^\dagger, \quad \hat{L}_0 = 2i\sum_{nm}\langle\varphi_m|\hat{G}|\varphi_n\rangle\frac{p_m-p_n}{p_n+p_m}|\varphi_m\rangle\langle\varphi_n|. \tag{8.35}$$

Therefore, the quantum Fisher information becomes

$$F_{\mathrm{Q}}(\lambda) = \mathrm{Tr}(\hat{\rho}_\lambda \hat{L}_\lambda^2) = \mathrm{Tr}(\hat{U}_\lambda \hat{\rho}_0 \hat{U}_\lambda^\dagger \hat{U}_\lambda \hat{L}_0 \hat{U}_\lambda^\dagger \hat{U}_\lambda \hat{L}_0 \hat{U}_\lambda^\dagger) = \mathrm{Tr}(\hat{\rho}_0 \hat{L}_0^2). \tag{8.36}$$

Furthermore, using the spectral decomposition of $\hat{\rho}_0$ we obtain

$$\hat{L}_0 = -4 \sum_{m,k,p} A_{mk} A_{kp} |\varphi_m\rangle\langle\varphi_p|, \tag{8.37}$$

where

$$A_{mn} = \langle\varphi_m|\hat{G}|\varphi_n\rangle \frac{p_m - p_n}{p_m + p_n}. \tag{8.38}$$

Finally, the quantum Fisher information is given by

$$F_{\mathrm{Q}}(\lambda) = 4 \sum_{s,k} \frac{(p_s - p_k)^2}{p_s + p_k} |\langle\varphi_s|\hat{G}|\varphi_k\rangle|^2, \tag{8.39}$$

where the sum includes only terms with $p_s + p_k > 0$.

For a pure quantum state $\hat{\rho}_0 = |\varphi\rangle\langle\varphi|$ the quantum Fisher information assumes the simple form of a connected correlation function

$$F_{\mathrm{Q}}(\lambda) = \langle\varphi|\hat{G}^2|\varphi\rangle - \langle\varphi|\hat{G}|\varphi\rangle^2. \tag{8.40}$$

Since, the larger quantum Fisher information the better estimation precision of λ, the natural question arise whether one can maximaze $F_{\mathrm{Q}}(\lambda)$ over the initial quantum state $|\varphi\rangle$. As we will see below the maximal precision achievable in quantum parameter estimation can break classical limits if the system is initially prepared in a strongly entangled N-particle state.

8.4 Enhanced parameter estimation using entangled states

Let us now assume that the generator of unitary transformation is $\hat{G} = \hat{S}_z$, where $\hat{S}_\alpha = \frac{1}{2}\sum_{k=1}^N \sigma_k^\alpha$ ($\alpha = x, y, z$) are the collective spin operators and σ_k^α is the Pauli operator which describes the spin of the kth particle. Consider that the system of N spin-1/2 particles is prepared in the initial state

$$|\varphi_{\mathrm{GHZ}}\rangle = \frac{1}{\sqrt{2}} \left(|\uparrow_1 \uparrow_2 \ldots \uparrow_N\rangle + |\downarrow_1 \downarrow_2 \ldots \downarrow_N\rangle \right), \tag{8.41}$$

where $\sigma_k^z |\uparrow_k\rangle = +|\uparrow_k\rangle$ and $\sigma_k^z |\downarrow_k\rangle = -|\downarrow_k\rangle$. This state is a highly entangled *Greenberger-Horne-Zeilingler* (GHZ) state between N particles. Then it is straightforward to calculate the quantum Fisher information so that we obtain

$$F_{\mathrm{Q}}(\lambda) = N^2. \tag{8.42}$$

Hence using entangled GHZ state, the corresponding quantum Fisher information grows quadratically with the number of particles. The ultimate uncertainty in the estimation of the parameter λ is then given by

$$\delta\lambda^2 \geq \frac{1}{N^2}. \tag{8.43}$$

The result indicates that the estimation precision is amplified by a factor of N with respect to the case of using uncorrelated initial quantum states.

9. CRITICAL QUANTUM METROLOGY WITH STRONGLY CORRELATED QUANTUM OPTICAL SYSTEMS

The goal of this chapter is to investigate a novel quantum metrology schemes for enhanced parameter estimation using quantum critical systems. First we show that the quasi-adiabatic evolution of a systems governed by the Dicke and quantum Rabi Hamiltonians can be described in terms of a self-induced quantum many-body metrological protocol. This effect relies on the sensitivity of the ground state to a small symmetry-breaking perturbation at the quantum phase transition, that leads to the collapse of the wavefunciton into one of two possible ground states. The scaling of the final state properties with the number of atoms and with the intensity of the symmetry breaking field, can be interpreted in terms of the precession time of an effective quantum metrological protocol. We show that our ideas can be tested with spin-phonon interactions in trapped ion setups. Our work points to a classification of quantum phase transitions in terms of the capability of many-body quantum systems for parameter estimation.

We also propose a quantum metrology protocol for measuring frequencies and weak forces based on a periodic modulating quantum Jahn-Teller system composed of a single spin and two bosonic modes. We show that in the first order of the frequency drive the time-independent effective Hamiltonian describes spin-dependent interaction between the two bosonic modes. In the limit of high-frequency drive and low bosonic frequency the quantum Jahn-Teller system exhibits critical behaviour which can be used for high-precision quantum estimation. A major advantage of our scheme is the robustness of the system against spin decoherence which allows to perform parameter estimation with measurement time not limited by spin dephasing.

9.1 Estimation of frequency with Heisenberg limited precision using Dicke Hamiltonian

Experimental progress in the last years has provided us with setups in Atomic, Molecular an Optical physics in which interactions between many particles can be controlled and quantum states can be accurately initialized and measured. Those experimental systems have an exciting outlook for the analogical quantum simulation of many-body models [102, 6, 103]. For example trapped ion setups can be used to simulate the physics of quantum magnetism [104, 105, 106] and quantum structural phase transitions [107] by means of spin-dependent forces. A more established practical application of atomic systems is in precision mea-

surements for atomic clocks and frequency standards. The effect of quantum correlations on the accuracy of interferometric experiments has been investigated in the field of quantum metrology [108, 109]. Here, entangled states may yield a favorable scaling in the precision of a frequency measurement compared to uncorrelated states [110, 111, 112, 113]. In view of this perspective a question arises, namely, whether we can find applications of strongly correlated states of quantum simulators for applications in quantum metrology.

A natural direction to be explored is the use of quantum phase transitions [114] in atomic systems. Intuition suggests that close to a phase transition a system becomes very sensitive to small perturbations. In particular, if there is a phase transition to a phase with spontaneous symmetry breaking, we may expect that any tiny perturbation leads the system to collapse to one of several possible ground states. Actually, quantum states typically considered for quantum metrology, such as NOON states, have a close relation to ferromagnetic phases of mesoscopic Ising models. However, frequency measurements typically rely on dynamical processes, for example in Ramsey spectroscopy [110]. Thus the conditions under which an atomic system remains close to the ground state of a many-body Hamiltonian must be carefully studied in view of possible metrological applications.

In this work we present a proposal to fully exploit the spontaneous symmetry breaking of a discrete $\mathbb{Z}_2$ symmetry to implement a quantum metrology protocol with a system described by the Dicke Hamiltonian [115]. The latter is the simplest model showing a quantum phase transition, and remarkably it can be implemented in a variety of experimental setups in atomic physics, from trapped ions to ultracold atoms. Our scheme relies on an adiabatic evolution which takes the system across a quantum phase transition where $\mathbb{Z}_2$ is spontaneously broken. We show that the system is very sensitive to the presence of a symmetry breaking field, δ, such that it self-induces a many-body Ramsey spectroscopy protocol which can be read out at the end of the process. Within the adiabatic approximation, we show that the ground state multiplet of the Dicke model can be approximated by an effective two-level system, something that allows us to obtain an analytical result for the measured signal as a function of the number of atoms N.

Our proposal can work in two different ways: *(i) Quasi-adiabatic method.-* Non-adiabatic effects within the two-level ground state multiplet lead to variations in the final magnetization. By reading out the final state we recover the scalings corresponding to the Heisenberg limit of parameter estimation. *(ii) Full adiabatic method.-* Here we consider the information that is obtained by a single-shot measurement of the final magnetization. The system collapses into one of the possible symmetry broken states, and this allows to get the sign of the symmetry breaking field within a measurement time that scales inversely proportional to the number of particles, $t_m \propto 1/N$.

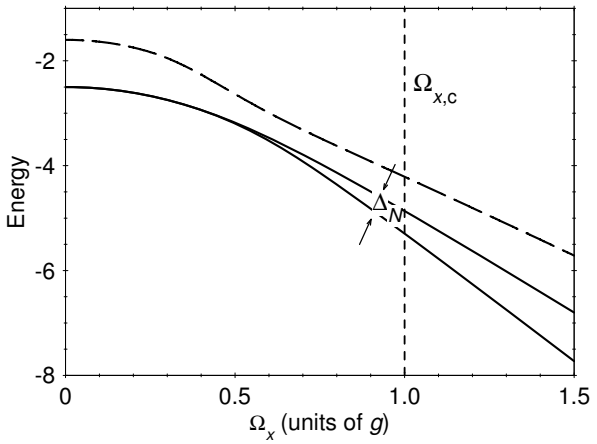

Fig. 9.1: Low energy spectrum (in units of g) of the single mode Dicke model for $\omega = 4g$ and $N = 10$ atoms as a function of Ω_x. The two lowest lying states are separated by energy splitting Δ_N. In a superradiant phase $\Omega_x < \Omega_{x,\mathrm{c}}$ the gap Δ_N can be calculated analytically by N-order perturbation theory. The dashed line is the third excited energy level.

9.1.1 Dicke model for quantum spectroscopy

We start by reviewing the celebrated Dicke Hamiltonian describing an ensemble of N two-level atoms coupled to a single bosonic mode ($\hbar = 1$ from now on),

$$\begin{aligned} H &= H_{\mathrm{D}} + H_{\delta}, \\ H_{\mathrm{D}} &= \omega a^{\dagger} a + \Omega_x J_x + \frac{2g}{\sqrt{N}}(a^{\dagger} + a) J_z, \\ H_{\delta} &= \delta J_z. \end{aligned} \tag{9.1}$$

H_{D} is the Dicke Hamiltonian, whereas H_{δ} is an additional symmetry breaking perturbation. $a^{\dagger}$ and a are creation and annihilation operators corresponding to an oscillator with frequency ω. Collective spin operators $\vec{J} = (J_x, J_y, J_z)$ are defined by

$$J_{\beta} = \frac{1}{2} \sum_{i=1}^{N} \sigma_i^{\beta}, \tag{9.2}$$

where σ_i^{β} ($\beta = x, y, z$) is the Pauli operator for each atom i. g and Ω_x are the intensive spin-boson coupling and transverse field, respectively. The term H_{δ} describes the coupling to a longitudinal field δ, where we assume the latter to be small in a sense to be precisely defined below.

The Dicke Hamiltonian is the simplest many-particle model with a discrete

$\mathbb{Z}_2$ symmetry. The latter is implemented by the parity operator defined by

$$\begin{aligned} &\Pi = \Pi_{\rm s} \otimes \Pi_{\rm b}, \\ &\Pi_{\rm s} = \sigma_1^x \otimes \cdots \otimes \sigma_N^x, \quad \Pi_{\rm b} = (-1)^{a^\dagger a}. \end{aligned} \tag{9.3}$$

Since $\Pi H_{\rm D} \Pi = H_{\rm D}$, parity is a good quantum number. The discrete $\mathbb{Z}_2$ symmetry plays a decisive role in the discussion below.

In the limit $N \to \infty$ the mean-field solution becomes exact [116, 117]. In this work we consider the evolution of the system with fixed g, ω, and varying values of the transverse field, Ω_x. In this case mean-field theory predicts a quantum phase transition at the critical point $\Omega_{x,{\rm c}} = 4g^2/\omega$. The latter separates a normal, or weak coupling phase ($\Omega_x \gg \Omega_{x,{\rm c}}$) with $\langle J_z \rangle, \langle a \rangle = 0$, from the superradiant, or strong coupling phase, ($\Omega_x \ll \Omega_{x,{\rm c}}$) with $\langle J_z \rangle, \langle a \rangle \neq 0$.

Since $\Pi a \Pi = -a$, $\Pi J_z \Pi = -J_z$, the mean-field solution breaks the parity symmetry. This effect can be understood in the following way. Consider $|\Psi_\delta\rangle$, the ground state of the Hamiltonian (9.1) with a finite longitudinal field δ. In the superradiant phase ($\Omega_x < \Omega_{x,{\rm c}}$) the following limit holds,

$$\lim_{\delta \to 0} \lim_{N \to \infty} \langle \Psi_\delta | a | \Psi_\delta \rangle \neq 0, \tag{9.4}$$

which implies that in the thermodynamical limit, an infinitesimal perturbation breaks the parity symmetry. Below we give an explicit proof of this result, which however is implicit in the fact that mean-field theory becomes exact as $N \to \infty$.

9.1.2 Low-energy spectrum of the Dicke model

In this section we show an effective description of the adiabatic quantum dynamics of $H_{\rm D} + H_\delta$ in terms of an effective two-level system.

First, we note that $H_{\rm D}$ commutes with the total angular momentum operator $\vec{J}^2$. Let us consider the eigenstates of $H_{\rm D} + H_\delta$ in the basis $\{|j,m\rangle |n\rangle_{\rm b}\}$, where $|j,m\rangle$ are the eigenstates of $\vec{J}^2$, J_z, and $|n\rangle_{\rm b}$ are the Fock states of the harmonic oscillator. We will study the evolution of the system starting with a fully polarized state with $j = N/2$, such that conservation of $\vec{J}^2$ ensures that we remain within the $j = N/2$ subspace. The dimension of the spin Hilbert space is thus $N + 1$, and the system is amenable to be studied with numerical diagonalization.

In the following we study the low-energy spectrum of $H_{\rm D}$ as a function of Ω_x, something that will allow us to get an effective description of the full Hamiltonian $H = H_{\rm D} + H_\delta$ in the superradiant phase. We define the two lowest eigenstates of $H_{\rm D}$, $|\Psi_{{\rm gs},\mp}\rangle$, with energies $E_{{\rm gs},\mp}$. The energy gap is $\Delta_N(g,\omega,\Omega_x) = E_{{\rm gs},+} - E_{{\rm gs},-}$, for clarity in the calculations below we write it explicitly as a function of the parameters in the Dicke Hamiltonian.

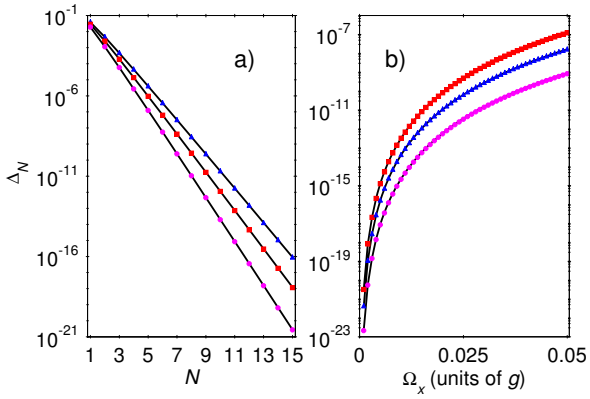

Fig. 9.2: a) The energy gap $\Delta_N(g,\omega,\Omega_x)$ of the Dicke Hamiltonian as a function of the number of atoms N with $\omega = 6g$ for various Ω_x. The numerical results for $\Omega_x = 0.02g$ (circles), $\Omega_x = 0.03g$ (square), $\Omega_x = 0.04g$ (triangle) are compared with the analytical solution (9.12) (solid lines). b) Numerical result for $\Delta_N(g,\omega,\Omega_x)$ as a function of Ω_x for $N = 8$ atoms and $\omega = 4g$ (black circles), $\omega = 6g$ (blue triangles), $\omega = 8g$ (red squares) compared with (9.12) (solid lines). Values for Δ_N are given in units of g.

Non-interacting limit ($\Omega_x \gg \Omega_{x,\mathrm{c}}$)

We study first the limit $\Omega_x \to \infty$, or alternatively $g = 0$. Assuming $\Omega_x > 0$, the lowest energy state is the fully polarized spin-state in the x direction,

$$|\Psi^{[\mathrm{g=0}]}_{\mathrm{gs},-}\rangle = \bigotimes_k |-\rangle_{x,k}|0\rangle_{\mathrm{b}}, \tag{9.5}$$

where $|\pm\rangle_{x,k}$ are the eigenstates of σ^x_k and $|n\rangle_{\mathrm{b}}$ is the Fock state of the bosonic mode with occupation n. The second lowest energy state is either a spin-wave if $\Omega_x < \omega$,

$$|\Psi^{[\mathrm{g=0}]}_{\mathrm{gs},+}\rangle = \frac{1}{\sqrt{N}} \sum_k |-\rangle_{x,1} \ldots |+\rangle_{x,k} \ldots |-\rangle_{x,N}|0\rangle_{\mathrm{b}}, \tag{9.6}$$

or an excitation of the harmonic oscillator if $\omega < \Omega_x$,

$$|\Psi^{[\mathrm{g=0}]}_{\mathrm{gs},+}\rangle = \bigotimes_k |-\rangle_{x,k}|1\rangle_{\mathrm{b}}, \tag{9.7}$$

being the gap $\Delta_N(0,\omega,\Omega_x) = \Omega_x$, or ω, respectively. In any case the two lowest energy states have opposite parity.

Strong-interacting limit ($\Omega_{x,\mathrm{c}} \gg \Omega_x$)

We discuss in more detail the superradiant phase, which is the most relevant for our quantum metrology protocol.

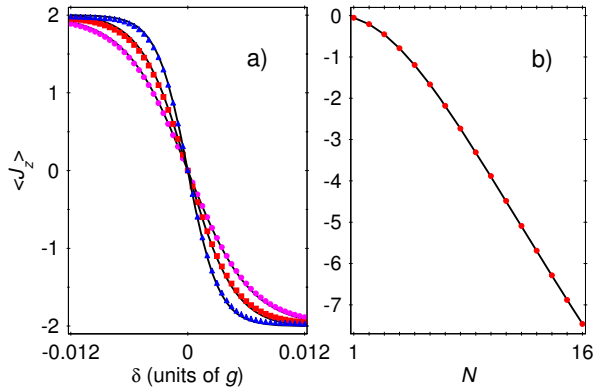

Fig. 9.3: a) The mean-value of J_z as a function of δ for $\omega = 3g$, $\Omega_x(0) = 9g$ and $N = 4$ for various γ. We compare the numerical solution of the time-dependent Schrödinger equation for $\gamma = 0.02g$ (triangle), $\gamma = 0.03g$ (square) and $\gamma = 0.04g$ (circle) with the solution of the two-state problem Eq. (9.28) (solid lines). b) The scaling of the measured signal as a function of N, for $\gamma = 0.03g$, $\omega = 10g$ and $\delta = 2.0 \times 10^{-3} g$. The red circles represent the numerical result, while the solid curve is the analytical solution, Eq. (9.29).

Consider first the limit $\Omega_x = 0$. Within the $j = N/2$ subspace, the spectrum of $H_{\rm D}$ corresponds to a set of Fock states of the harmonic oscillator, displaced by an amplitude proportional to the quantum number $m = -N/2, \ldots, N/2$,

$$|\Phi_{n,m}\rangle = D\left(-\frac{2g}{\omega\sqrt{N}}m\right)|\frac{N}{2}, m\rangle|n\rangle_{\rm b}, \tag{9.8}$$

where we have defined the displacement operator $D(\alpha) = e^{\alpha a^\dagger - \alpha^* a}$. The eigenenergies are

$$E_{n,m} = n\,\omega - \frac{g^2 N}{\omega}\left(\frac{m}{N/2}\right)^2. \tag{9.9}$$

We find two degenerate ground states, corresponding to $m = \pm N/2$,

$$|\Psi^{[\Omega_{\rm x}=0]}_{{\rm gs},\pm}\rangle = D\left(\mp\sqrt{N}g/\omega\right)|\frac{N}{2}, \pm\frac{N}{2}\rangle|0\rangle_{\rm b}, \tag{9.10}$$

with energies $E_{{\rm gs},\pm} = -(g^2/\omega)N$.

Let us consider now the effect of a small transverse field, Ω_x, in the low-energy spectrum. We expect the energy gap, $\Delta_N(g, \omega, \Omega_x)$, to be lifted by the coupling of the two degenerate states by the term $\Omega_x J_x$ in $H_{\rm D}$. However, note that the operator J_x has to flip all spins to bring $|\Psi^{[\Omega_x=0]}_{{\rm gs},+}\rangle$ to $|\Psi^{[\Omega_x=0]}_{{\rm gs},-}\rangle$, such that

$$\langle\Psi^{[\Omega_{\rm x}=0]}_{{\rm gs},+}|J_x^M|\Psi^{[\Omega_{\rm x}=0]}_{{\rm gs},-}\rangle = 0, \tag{9.11}$$

if $M \leq N-1$. The first nonzero contribution is thus of order N. Nth order perturbation theory allows us to estimate the following scaling

$$\Delta_N(g,\omega,\Omega_x) = f_N\left(g/\omega\right)\Omega_x\left(\frac{\Omega_x}{\Omega_{x,c}}\right)^{N-1}, \tag{9.12}$$

where $f_N(g/\omega)$ is a scaling function that describes the dependence of the gap on the ratio g/ω. An explicit expression for $f_N(g/\omega)$ can be found in the particular case $g \ll \omega$,

$$f_N(g/\omega) = 2e^{-2\left(\frac{g}{\omega}\right)^2}\frac{N^{N+1}}{2^N N!}. \tag{9.13}$$

The latter corresponds to the limit in which the harmonic oscillator can be adiabatically eliminated, such that $H_{\rm D}$ is equivalent to an infinite range Ising spin Hamiltonian. For other values of g/ω, one can use numerical calculations to estimate the exact form of the energy gap. Note that the effect of a finite gap, Δ_N, is to restore the parity symmetry by creating ground states that are linear combinations of $|\Psi_{\rm gs,-}^{[\Omega_x=0]}\rangle$, $|\Psi_{\rm gs,+}^{[\Omega_x=0]}\rangle$.

The most important feature of the superradiant phase, is thus the vanishing of the gap in the thermodynamical limit, analogously to the situation found, for example, in the short-range quantum Ising model [114]. In a finite size system, $\Delta_N(g,\omega,\Omega_x)$ monotonically decreases as we decrease Ω_x from the value $\Omega_{x,\rm c}$, see Fig. 9.2. The monotonic behavior of the gap with respect to the transverse field is actually valid along the whole phase diagram, and not only within the superradiant phase. This is shown in Fig. 9.1, where we present the evolution of the low-energy spectrum of $H_{\rm D}$.

Within the superradiant phase we can thus project the Hamiltonian $H = H_{\rm D} + H_\delta$ into the ground state multiplet to get the effective Hamiltonian,

$$H_{\rm eff} = \frac{\Delta_N(g,\omega,\Omega_x)}{2}\sigma^x + \frac{N\delta}{2}\sigma^z, \tag{9.14}$$

where Pauli operators act over the Hilbert subspace $\{|-\rangle,|+\rangle\} = \{|\Psi_{\rm gs,-}^{[\Omega_x=0]}\rangle, |\Psi_{\rm gs,+}^{[\Omega_x=0]}\rangle\}$. The perturbation δ appears in the $H_{\rm eff}$ multiplied by N. This effect is the backbone of our quantum metrology protocol, and it signals the amplification effect due to the spontaneous symmetry breaking that we will use to detect the δ field.

We note that the term $\Omega_x J_x$ couples the state $|\Psi_{\rm gs,\mp}^{[\Omega_x=0]}\rangle$ to the next excited states $|\Phi_{0,\mp(N/2-1)}\rangle$. In the superradiant phase this coupling perturbs the ground state multiplet, such that

$$|\Psi_{\rm gs,\mp}^{[\Omega_x=0]}\rangle \to |\Psi_{\rm gs,\mp}^{[\Omega_x=0]}\rangle + e^{-\frac{2}{N}\left(\frac{g}{\omega}\right)^2}\frac{\Omega_x}{2\Omega_{x,\rm c}}\frac{\sqrt{N}}{1-1/N}|\Phi_{0,\mp(N/2-1)}\rangle, \tag{9.15}$$

up to normalization factor. This perturbation, eventually gives a correction to the last term in (9.14),

$$\frac{N\delta}{2}\sigma^z \to \frac{N\delta}{2}\left(1 - e^{-\frac{4}{N}\left(\frac{g}{\omega}\right)^2}\frac{\Omega_x^2}{2\Omega_{x,\rm c}^2}\frac{1}{(1-1/N)^2}\right)\sigma^z, \tag{9.16}$$

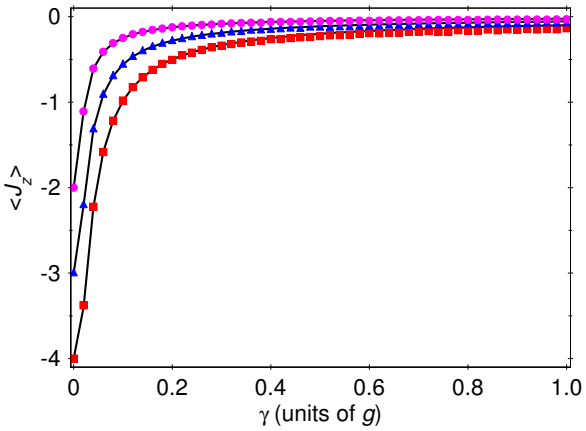

Fig. 9.4: The expectation value of J_z as a function of γ for $\omega = 10g$, $\Omega_x(0) = 9g$, $\delta = 2.0 \times 10^{-3} g$ and various N. The exact solution for $N = 4$ (circle), $N = 6$ (triangle) and $N = 8$ (square) is compared with Eq. (9.28) (solid lines).

which can be neglected in the strongly coupled phase ($\Omega_x \ll \Omega_{x,\mathrm{c}}$).

Finally, we also note that the validity of H_{eff}, together with the scaling given by Eq. (9.12), is an indirect proof of the symmetry breaking of the parity symmetry anticipated by the expression (9.4).

9.1.3 *Separation of time-scales for preparation and measurement*

Our scheme relies on the adiabatic evolution of the system by considering a time-dependent transverse field $\Omega_x(t)$. Alternative versions of this scheme may consider the time variation of the coupling constant, g. We assume that the system can be prepared in a linear superposition of low-energy states during an initial preparation stage (i), which subsequently evolves quasi-adiabatically to perform a self-induced quantum many-body metrological stage (ii):

(i) Preparation stage.- We consider an exponential decay

$$\Omega_x(t) = \Omega_x(0) e^{-t/\tau_{\mathrm{ev}}^{(1)}}, \tag{9.17}$$

with $\Omega_x(0) \gg \Omega_{x,\mathrm{c}}$, such that the system can be prepared initially in the ground state of the non-interacting phase, given by Eq. (9.5)

$$|\Psi(0)\rangle = |\Psi_{\mathrm{gs},-}^{[\mathrm{g}=0]}\rangle. \tag{9.18}$$

The system evolves from $t = 0$ up to $t = t_i$, the latter being the initial time for the subsequent stage. The transverse field varies up to $\Omega_x(t_i) = \Omega_{x,i}$, with $\Omega_{x,i} \ll \Omega_{x,\mathrm{c}}$, such that the system evolves into the strongly coupled regime. Within the preparation stage the gap is bounded by

$$\Delta_i = \Delta_N \left(g, \omega, \Omega_{x,i}\right). \tag{9.19}$$

We impose full adiabaticity of the evolution of the system during the preparation stage,

$$1/\tau_{\rm ev}^{(1)} \ll \Delta_i. \tag{9.20}$$

Finally, we also need the condition,

$$\Delta_i \gg N\delta, \tag{9.21}$$

such that the system enters into the superradiant phase as an eigenstate of the $\Delta_N(g,\omega,\Omega_x)$ term in Hamiltonian (9.14). A crucial observation is that conditions (9.20) and (9.21) imply that the preparation rate $1/\tau_{\rm ev}^{(1)}$ is not bounded by the parameter δ. Thus increasing the precision in measuring δ does not require increasingly longer $\tau_{\rm ev}^{(1)}$.

(ii) Metrological stage.- Once the system is within the strongly coupled phase, we can use the two-level system approximation discussed in the previous section. This is the part of the protocol where the measurement of δ is performed, and we require the quantum evolution to be sensitive to $N\delta$. Thus, for $t > t_i$, one can choose a second time scale for the evolution of the system, given by $\tau_{\rm ev}^{(2)}$,

$$\Omega_x(t) = \Omega_{x,i} e^{-(t-t_i)/\tau_{\rm ev}^{(2)}}. \tag{9.22}$$

Note that within the strongly coupled phase the gap follows the scaling given by Eq. (9.12), such that

$$\Delta_N(t) = \Delta_N(g,\omega,\Omega_x(t)) = \Delta_i e^{-\gamma(t-t_i)}, \tag{9.23}$$

with $\gamma = N/\tau_{\rm ev}^{(2)}$. The quantum metrological protocol will rely now on the quasi-adiabatic time evolution of the system, which is hold for

$$\gamma \ll \Delta', \tag{9.24}$$

where Δ' is the energy splitting from $|\Psi_+^{[\Omega_{\rm x}=0]}\rangle$ to the next excited energy level. The condition (9.24) ensures that the non-adiabatic transitions to the other excited states are suppressed. In the strongly coupled phase we have $\Delta' \approx \Omega_{x,{\rm c}}(1-1/N)$, which implies that the required condition reads $\gamma \ll \Omega_{x,{\rm c}}$, for large N.

Within the two-level approximation the state vector can be written as a superposition

$$|\Psi(t)\rangle = c_+(t)|\Psi_{{\rm gs},+}^{[\Omega_x=0]}\rangle + c_-(t)|\Psi_{{\rm gs},-}^{[\Omega_x=0]}\rangle, \tag{9.25}$$

where $c_\pm(t)$ are complex probability amplitudes. The condition $\Delta_i \gg N\delta$, ensures that the system is initially in an eigenstate of σ^x, with $c_+(t_i) = 1/\sqrt{2}$, and $c_-(t_i) = -1/\sqrt{2}$. The system evolves from $t = t_i$ up to a final time $t = t_f$, such that ends up in a phase

$$\Delta_N\left(g,\omega,\Omega_x(t_f)\right) = \xi\ N\delta, \tag{9.26}$$

with $\xi \ll 1$. In view of (9.23), the latter condition can be re-written as

$$t_m = t_f - t_i = \frac{1}{\gamma} \log\left(\frac{\Delta_i}{\xi N \delta}\right). \tag{9.27}$$

Thus, up to logarithmic corrections, the measurement time, $t_m = t_f - t_i$, is directly governed by the rate γ.

9.1.4 Quantum metrology protocol

In this section we focus on the description of the quasi-adiabatic evolution of the system during stage (ii) of the last section. We have to solve the quantum evolution of a two-level system with an exponentially decreasing transverse field, which turns out to be represented by the Demkov model with coupling $\Delta_N(t) = \Delta_i e^{-\gamma(t-t_i)}$ and detuning $N\delta$ [118]. Remarkably, the solution of the time-dependent Schrödinger equation $\mathrm{i}\frac{d}{dt}|\Psi\rangle = H_{\rm eff}|\Psi\rangle$ can be found exactly.

In the limit $xe^{-\gamma t_m} \ll 1$, with $x = (\Delta_i/2\gamma)$, we obtain

$$|c_+(t_f)|^2 = \frac{1}{2} + \mathrm{i}\frac{\pi}{4}\frac{x}{\cosh(\frac{\pi N\delta}{2\gamma})}\{J_\nu(x)J_{-\nu}(x) - J_{\nu-1}(x)J_{1-\nu}(x)\}, \tag{9.28}$$

where $J_\nu(x)$ is a Bessel function of the first-kind [119] with $\nu = 1/2 - \mathrm{i}N\delta/2\gamma$. For large $x \gg 1$ we can use the asymptotic expansion $J_\nu(x) \sim \sqrt{2/\pi x}\{\cos(x - \frac{\pi\nu}{2} - \frac{\pi}{4}) + O(x^{-1})\}$, which yields for the zth component of the total angular momentum,

$$\begin{aligned}\langle J_z(t_f)\rangle &= N\left(|c_+(t_f)|^2 - \frac{1}{2}\right) \\ &\approx -\frac{N}{2}\tanh\left(\frac{\pi N\delta}{2\gamma}\right) + O(x^{-1}).\end{aligned} \tag{9.29}$$

The result represents the measured signal at $t_f \gg \gamma^{-1}$, as a function of δ. For vanishing perturbation field $\delta = 0$ the final state is an equal superposition of the states (9.10), which yields $\langle J_z\rangle = 0$. However, for $\delta \neq 0$, the parity symmetry of $H_{\rm D}$ is broken and consequently of that the final probability amplitudes $c_\pm(t_f)$ are different, which allow us directly to estimate δ by measuring the collective spin population. Depending on the ratio between typical values of $N\delta$ and γ we have to distinguish the two following cases.

Quasi-adiabatic protocol

For $N\delta < \gamma$ the system evolution is a quasi-adiabatic in the sense that the dynamics is captured within the two-level subspace, but non-adiabatic effects within that subspace are used to estimate δ. Because the symmetry breaking term H_δ does not commute with the Dicke Hamiltonian $H_{\rm D}$ results in entangled superposition of the states (9.10) with probability amplitudes, depending the

sign and magnitudes of δ. The measured signal at time t_f is given by Eq. (9.29) and the variance of the signal is

$$\langle \Delta^2 J_z \rangle^{1/2} = \frac{N}{2\cosh\left(\frac{\pi N \delta}{2\gamma}\right)}. \tag{9.30}$$

The uncertainty in measuring δ is given by

$$\bar{\delta} = \frac{\langle \Delta^2 J_z \rangle^{1/2}}{|\partial \langle J_z \rangle / \partial \delta|} = \frac{2\gamma}{\pi N} \cosh\left(\frac{\pi N \delta}{2\gamma}\right), \tag{9.31}$$

which is approximated with the Heisenberg-limited precision, $\bar{\delta} \approx 2\gamma/\pi N$.

Finally, we present some numerical results to check the validity of the two-state approximation used for our quantum metrological protocol. We compare the analytical result for $\langle J_z \rangle$ obtained by the Demkov model with the exact numerical solution of the time-dependent Schrödinger equation with Hamiltonian (9.1). Figure 9.3a shows the measured signal as a function of δ for various γ. In a quasi-adiabatic region, the signal is well approximated with Eq. (9.29), while in the full adiabatic limit the signal tends to a step function. In Fig. 9.3b we have checked the expression (9.29) with the numerical exact result for various N. Finally, in Fig. 9.4 we plot the measured signal as a function of γ for various N. Remarkably, the exact solution follows for wide range of γ. In the limit $\gamma \gg N\delta$ the system dynamics become insensitive to δ in a sense that the signal $\langle J_z \rangle$ vanishes.

9.1.5 Conclusions and Outlook

We have studied the process of symmetry breaking of a discrete symmetry due to the presence of small perturbation field in a system described by the Dicke Hamiltonian. We have shown that quasi-adiabatic evolution in this system induces a quantum metrology protocol, which is Heisenberg limited. Our many-body Ramsey spectroscopy protocol can be implemented with linear ion crystal, where the symmetry breaking field is controlled by the laser detuning to the respective qubit transition. The realization of the proposed quantum metrology protocol is not restricted only to trapped ions but could be implemented with other experimental setups such as cavity [124] or circuit QED [125] systems.

We highlight a few advantages of our idea with respect to current approaches to quantum metrology: (i) Our method does not require quantum gates, since it is induced by always-on interactions. (ii) In principle, our work does not rely on effective spin-spin interactions mediated by auxiliary photonic or bosonic fields. On the contrary, our adiabatic process may also work in a regime in which $g \geq \omega$, such that the final state is not a pure state of qubits, but an entangled spin-boson state instead. (iii) Since our method mainly relies on symmetry considerations, it should be robust with respect to perturbations to H_{D} that respect the parity symmetry. (iv) We note that our method allows us to get information about δ with a single-shot measurement in the full adiabatic scheme.

We also remark that the scheme presented here share some of the limitations as standard protocols with quantum metrology with NOON states [126]. In particular, our method would not imply any advantage if the measurement time is limited by decoherence. Also, an important limitation of our scheme is the fact the spin-boson interactions have to be fully parity symmetric, being any deviation from that symmetry a potential source of error in the achieved accuracy.

We finish with an Outlook of possible research directions motivated by this work. We have presented a very specific study relying on a model belonging to the long-range Ising universality class. It would be very interesting to explore scalings related to similar quantum metrology protocols with different universality classes and symmetries, like those that can be simulated with trapped ions, for example [127]. Also, one could study quantum dissipative phase transitions [128, 129] in addition to the evolution of closed quantum systems presented here. Finally, although we have presented an example with trapped ions and frequency estimation, one could also think of applications to measure forces or magnetic fields, for example.

9.2 Quantum sensors assisted by spontaneous symmetry breaking for detecting very small forces

In this section we propose a quantum sensing scheme for measuring weak forces based on a symmetry-breaking adiabatic transition in the quantum Rabi model. We show that the system described by the Rabi Hamiltonian can serve as a sensor for extremely weak forces with sensitivity beyond the yN $/\sqrt{\text{Hz}}$ range. We propose an implementation of this sensing protocol using a single trapped ion. A major advantage of our scheme is that the force detection is performed by projective measurement of the population of the spin states at the end of the transition, instead of the far slower phonon number measurement used hitherto.

Using nanoscale mechanical oscillators as detectors of extremely weak forces has attracted considerable experimental interest [130]. Such systems allow to measure forces with sensitivity below the attonewton range which is beneficial for a broad range of applications. For example, a force detector with a nanomechanical oscillator coupled to a microwave cavity can reach sensitivity below one aN (10^{-18} N) per $\sqrt{\text{Hz}}$ [131]. Other sensors use mechanical oscillators made of carbon nanotubes for force detection with sensitivity in the zN (10^{-21} N) per $\sqrt{\text{Hz}}$ range [132]. Recently, the detection of ultra-weak forces as small as 5 yN (10^{-24} N) was experimentally demonstrated using injection locked ions [133]. Force measurement in an ensemble of ions in a Penning trap uses Doppler velocimetry technique to detect force with sensitivity of 170 yN$/\sqrt{\text{Hz}}$ [142]. Another approach uses high-precision ion position determination to measure light pressure forces [143]. In all cases the force sensing based on mechanical oscillators is carried out by converting the force into a displacement that is measured by electrical or optical means.

In this work, we introduce a different sensing protocol, which uses a system

described by the quantum Rabi (QR) model as a probe that is sensitive to extremely weak forces. The QR model consists of a single bosonic mode and an effective spin system which interact via dipolar coupling. We show that the effect of symmetry breaking of the underlying parity symmetry in the QR model due to the presence of external perturbation can be used in an efficient way for detection of classical oscillating forces. Our scheme relies on the adiabatic evolution of the ground-state of the QR model into the Schrödinger cat state, where the relevant force information is mapped in the respective probability amplitudes. The force sensing is performed simply by measuring the spin populations. Therefore our protocol, which demands a single population measurement, is considerably faster than previous protocols based on the detection of the motional degree of freedom via Rabi oscillations.

We consider a particular implementation of our sensing scheme using a coherently manipulated single trapped ion. The driving parameters of the QR model can be controlled and tuned by the laser detuning and intensity. The scheme, however, can be realized with various quantum optical systems such as nitrogen vacancy centers in diamond and superconducting qubits inside a microwave cavity [144, 145, 146]. We show that with the current ion trap technologies force sensitivity below one $\mathrm{yN}/\sqrt{\mathrm{Hz}}$ can be achieved. In addition, we show that our method can be applied for detection of spin-dependent forces which are created in magnetic-field gradients or Stark-shift gradients. Hence our method can be used for studying magnetic dipole moments of atomic or molecular ions [133, 147].

9.2.1 Adiabatic quantum metrology using the quantum Rabi model

Our system consists of a two-level atom with states $|\uparrow\rangle$ and $|\downarrow\rangle$ coupled to a single bosonic mode described by the quantum Rabi model,

$$\hat{H}_{\mathrm{R}} = \hbar\omega\hat{a}^{\dagger}\hat{a} + \frac{\hbar\Omega_y(t)}{2}\sigma_y + \hbar g\sigma_x(\hat{a}^{\dagger} + \hat{a}). \tag{9.32}$$

Here $\hat{a}^{\dagger}$ and $\hat{a}$ are the creation and annihilation operators of bosonic excitation with frequency ω and σ_β ($\beta = x, y, z$) are the respective Pauli matrices. The time-dependent Rabi frequency of the transverse field is given by $\Omega_y(t)$ and g is the spin-boson coupling. Recently, it was shown that the Rabi model permits exact integrability [148].

The quantum Rabi Hamiltonian (9.32) possesses a discrete symmetry revealed by the parity transformation $\hat{a} \to -\hat{a}$, $\sigma_y \to \sigma_y$ and $\sigma_x \to -\sigma_x$. In the following we consider the QR model in the regime $g \simeq \omega$ and study the effect of a small perturbation term $\hat{H}_{\mathrm{pert}}$, which breaks the underlying parity symmetry of the model. The total Hamiltonian including the perturbation term becomes

$$\hat{H} = \hat{H}_{\mathrm{R}} + \hat{H}_{\mathrm{pert}}. \tag{9.33}$$

As we will see, the symmetry-breaking process allows us to estimate the perturbation term very accurately.

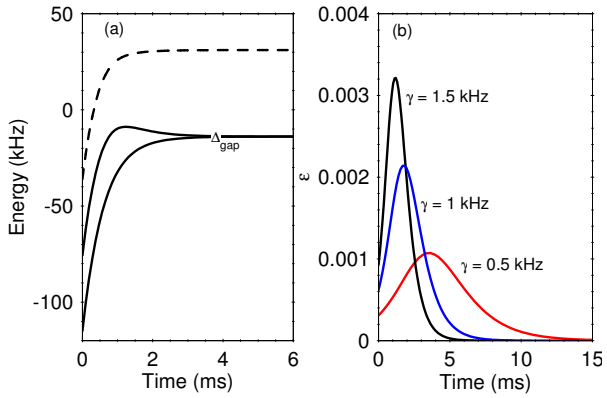

Fig. 9.5: (a) Low-energy spectrum of the quantum Rabi model as a function of time t. The two lowest lying states are separated by energy splitting $\Delta_{\rm gap}$. At the initial moment $t = 0$ the system is prepared in the ground-state with $\Omega_y(0) \gg g$ and then it evolves into the Schrödinger cat state (9.34). The energy difference between the third excited energy (dashed line) and the ground-state energy is $\Delta_{\rm ge}$. We assume $\gamma = 1.5$ kHz, $g = 25$ kHz, $\omega = 45$ kHz and $\Omega_y(0) = 225$ kHz. (b) Adiabatic parameter ϵ versus time t for $g = 25$ kHz and $\omega = 45$ kHz (solid lines), $\omega = 20$ kHz (dashed lines) and various values of γ.

The measurement protocol for $\hat{H}_{\rm pert}$ starts by preparing the system in the ground-state of the unperturbed Hamiltonian $\hat{H}_{\rm R}$ in the limit $\Omega_y(0) \gg g, 4g^2/\omega$ such that $|\psi_{\rm g}(0)\rangle = |-\rangle_y |0\rangle$ where $|-\rangle_y = (|\uparrow\rangle - {\rm i}\,|\downarrow\rangle)/\sqrt{2}$ and $|n\rangle$ is the Fock state of the bosonic mode with occupation number n. Then we adiabatically decrease the transverse field $\Omega_y(t)$ in time such that the system evolves into the Schrödinger cat state

$$|\psi_{\rm g}(t)\rangle = c_+(t)|\psi_+\rangle + c_-(t)|\psi_-\rangle, \tag{9.34}$$

where $c_\pm(t)$ are the respective probability amplitudes. Here $|\psi_+\rangle = |+\rangle_x |\alpha\rangle$ and $|\psi_-\rangle = |-\rangle_x |-\alpha\rangle$ form the ground-state multiplet with $|\pm\rangle_x = (|\uparrow\rangle \pm |\downarrow\rangle)/\sqrt{2}$ and $|\alpha\rangle$ stands for a coherent state with amplitude $\alpha = -g/\omega$. State (9.34) implies that for $\hat{H}_{\rm pert} = 0$ the parity symmetry is preserved by creating an entangled state with equal probabilities, $c_\pm = \pm 1/\sqrt{2}$. The effect of the perturbation is to break the parity symmetry of $\hat{H}_{\rm R}$ by creating a ground-state wavefunction (9.34) with unequal probability amplitudes, $|c_+|^2 \neq |c_-|^2$. By measuring the respective probabilities at the end of the process one can estimate the unknown perturbation.

In order to describe the creation of the symmetry-broken ground-state we represent the Hamiltonian (9.33) within the ground-state multiplet. Assuming that the parity-breaking perturbation does not couple different states in the ground-state manifold as in the case of force, we obtain an effective two-level

problem with the Hamiltonian

$$H_{\text{eff}} = \begin{bmatrix} \langle\psi_+|\,\hat{H}_{\text{pert}}\,|\psi_+\rangle & \hbar\Delta_{\text{gap}}/2 \\ \hbar\Delta_{\text{gap}}/2 & \langle\psi_-|\,\hat{H}_{\text{pert}}\,|\psi_-\rangle \end{bmatrix}. \tag{9.35}$$

Here Δ_{gap} is the energy gap of the ground-state multiplet $\Delta_{\text{gap}} = \Omega_y e^{-2(g/\omega)^2}$ which can be estimated by calculating the matrix elements of σ_y in quasi degenerate ground-state subspace which is valid even in the regime $g > \omega$ (see, Fig. 9.5a). Hereafter we assume an exponential decay of the transverse field $\Omega_y(t) = \Omega_y(0)e^{-\gamma t}$ with a characteristic slope γ which implies that $\Delta_{\text{gap}} \sim e^{-\gamma t}$. The latter reduces the two-state problem represented by the effective Hamiltonian (9.35) to the Demkov model. The adiabaticity of the process is characterized by the condition $\epsilon = |\langle\psi_{\text{g}}|\, d/dt\, |\psi_{\text{e}}\rangle / \Delta_{\text{ge}}| \ll 1$, which requires the coupling between the ground-state $|\psi_{\text{g}}\rangle$ to the first excited-state $|\psi_{\text{e}}\rangle$ to be much smaller that the energy gap between them Δ_{ge} at any instant of time. Note that because of the absence of fast driven oscillations in our system, the adiabatic condition $\epsilon \ll 1$ is sufficient. In Fig. 9.5(b) we show the adiabatic parameter ϵ during the creation of the Schrödinger cat state (9.34) for various γ. We observe that the non-adiabatic transitions become stronger for $g \geq \omega$ compared to the regime $g < \omega$. On the other hand the adiabaticity is fulfilled for lower γ.

9.2.2 Sensing weak forces and displacements

In the following we consider a harmonic oscillator represented by a single trapped ion with mass m confined in a Paul trap with an axial trap frequency ω_z. We assume that the effective spin system of the ion is implemented by two metastable atomic levels $|\uparrow\rangle$ and $|\downarrow\rangle$ with a transition frequency ω_0. We describe the small axial vibrations of the ion by the following motional Hamiltonian

$$\hat{H}_{\text{m}} = \hbar\omega\hat{a}^\dagger\hat{a}, \quad \hat{z} = z_0(\hat{a}^\dagger + \hat{a}), \tag{9.36}$$

where $\hat{a}^\dagger$ and $\hat{a}$ are the respective phonon creation and annihilation operators and $z_0 = \sqrt{\hbar/2m\omega_z}$ is the spread of the oscillator ground-state wave function.

Electric field sensing

The ability to control the motional and internal states with high accuracy makes the trapped ions a formidable experimental tool for electric-field sensing [149]. In contrast to the conventional methods which rely only on the detection of the motional degrees of freedom [149, 150, 151, 152, 153, 154], here the relevant information is transferred directly into the spin degrees of freedom due to the use of the symmetry-breaking adiabatic transition. In the following, we assume that a classical oscillating force $F(t) = F_{\text{d}}\cos(\omega_{\text{d}}t)$ with an amplitude F_{d} — the parameter we wish to estimate — and frequency $\omega_{\text{d}} = \omega_z - \omega$ shifted from the axial trap frequency ω_z by a small detuning ω ($\omega_z \gg \omega$) is applied to the ion. The action of the force is to displace the motional amplitude of the ion's

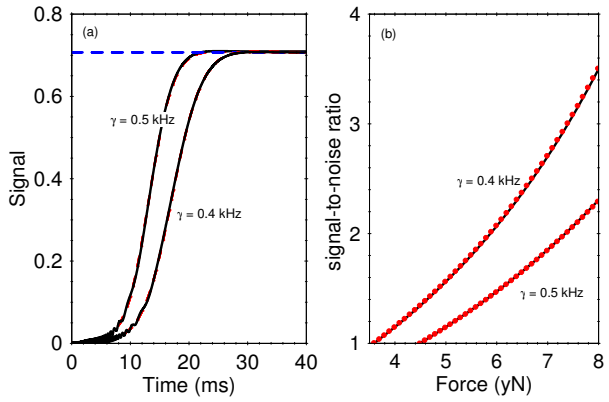

Fig. 9.6: (a) Time-evolution of the expectation value of σ_x (solid lines) for minimal detectable force (9.43) and different γ. The dashed curves correspond to the solution with the effective Hamiltonian and they are nearly indistinguishable with the exact solution. At $t_f \gg \gamma^{-1}$ the signal tends to the asymptotic formula (9.41) (blue dashed line). We assume a single $^{24}Mg^{+}$ trapped ion with an axial trap frequency $\omega_z = 6.3$ MHz. The other parameters are set to $g = 25$ kHz, $\omega = 110$ kHz, $\Omega_y(0) = 225$ kHz. (b) Signal-to-noise ratio versus $F_{\rm d}$. We compare the numerical solution of the time-dependent Schrödinger equation with the Hamiltonian (9.33) (dots) with the asymptotic expression given by $\mathrm{SNR} = \sinh(\pi g z_0 F_{\rm d}/(\hbar\gamma\omega))$ (solid lines).

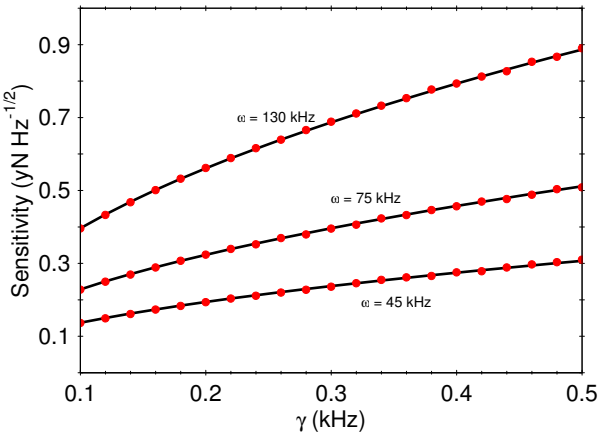

Fig. 9.7: The sensitivity $\eta_{\rm force}\sqrt{T}$ versus the slope γ for various values of ω. We assume a single $^{24}Mg^{+}$ ion with an axial trap frequency $\omega_z = 6.3$ MHz. The interaction time is set to $t_f = 14\gamma^{-1}$. The other parameters are $g = 25$ kHz, $\Omega_y(0) = 225$ kHz. The exact solution (dots) is compared with the analytical expression $\eta_{\rm force}\sqrt{T} = \sqrt{t_f}F_{\rm d}^{\rm min}$ (solid line) where $F_{\rm d}^{\rm min}$ is given by Eq. (9.43).

vibrational oscillator described by

$$\hat{H}_F = F(t)\hat{z}(t) = \frac{z_0 F_\mathrm{d}}{2}(\hat{a}^\dagger e^{\mathrm{i}\omega t} + \hat{a}e^{-\mathrm{i}\omega t}), \tag{9.37}$$

where we have neglected the fast-rotating terms. Note that in terms of motion and position the following discussion is restricted to 1D. In order to implement the spin-boson term in the quantum Rabi Hamiltonian we assume that the ion is simultaneously addressed by bichromatic laser fields in a Raman configuration with a wave vector difference $\Delta\vec{k}$ along the z direction, which induces a transition between the spin states via an auxiliary excited state. By setting the laser frequency beatnotes $\omega_\mathrm{r} = \omega_0 - \omega_z + \omega$ and $\omega_\mathrm{b} = \omega_0 + \omega_z - \omega$ close to the red- and blue-sideband transitions of the vibrational mode ω_z, the resulting Hamiltonian in the Lamb-Dicke limit ($\eta \ll 1$) becomes [202]

$$\hat{H}_{\mathrm{s-b}} = \hbar g\sigma_x(\hat{a}^\dagger e^{\mathrm{i}\omega t} + \hat{a}e^{-\mathrm{i}\omega t}), \tag{9.38}$$

where $g = \Omega\eta$ is the spin-phonon coupling with Ω being the two-photon Rabi frequency and η stands for the Lamb-Dicke parameter. The transverse field in (9.32) can be created by driving the resonant carrier transition between the internal spin states using a microwave or radio-frequency field, which yields

$$\hat{H}_y(t) = \frac{\hbar\Omega_y(t)}{2}\left(e^{\mathrm{i}\phi}\left|\uparrow\right\rangle\left\langle\downarrow\right| + \mathrm{h.c}\right) = \frac{\hbar\Omega_y(t)}{2}\sigma_y. \tag{9.39}$$

Here $\Omega_y(t)$ is the time-dependent Rabi frequency and we set the driving phase to $\phi = -\pi/2$. In the interaction picture rotating at the frequency ω the total Hamiltonian is $\hat{H} = \hat{H}_{\mathrm{s-b}} + \hat{H}_y + \hat{H}_F$ where the symmetry-breaking term is

$$\hat{H}_\mathrm{pert} = \frac{z_0 F_\mathrm{d}}{2}(\hat{a}^\dagger + \hat{a}). \tag{9.40}$$

The force sensing protocol starts by initialization of the spins along the y direction and laser cooling of the single ion vibrational mode to the motional ground state. Subsequently, the transverse field exponentially decays as $\Omega_y(t) = \Omega_y(0)e^{-\gamma t}$, which drives the system adiabatically into the superposition state $\left|\psi_\mathrm{g}(t)\right\rangle = c_+(t)\left|\psi_+\right\rangle + c_-(t)\left|\psi_-\right\rangle$. Here $c_\pm(t)$ are the respective probability amplitudes which are solutions of the time-dependent Schrödinger equation with the Hamiltonian (9.35). In our scheme the detection of the force is performed either by measuring the expectation value of σ_x or by measuring the position quadrature $\hat{Z} = \hat{a}^\dagger + \hat{a}$ of the bosonic field.

For vanishing force ($F_\mathrm{d} = 0$) the parity symmetry is restored by creating an entangled ground-state that is an equal superposition of states $\left|\psi_\pm\right\rangle$, which leads to $\langle\sigma_x(t_f)\rangle = 0$ and $\langle\hat{Z}(t_f)\rangle = 0$. For $F_\mathrm{d} \neq 0$, the parity symmetry of $\hat{H}_\mathrm{D}$ is broken, which allow us to estimate F_d by measuring σ_x or $\hat{Z}$. In Fig. 9.6(a) the time-evolution of the expectation value of σ_x in the presence of the symmetry-breaking term (9.40) is shown. At the interaction time $t_f \gg \gamma$ the signal and its variance are described by

$$\langle\sigma_x(t_f)\rangle = \tanh\left(\frac{\pi g z_0 F_\mathrm{d}}{\hbar\gamma\omega}\right),, \tag{9.41}$$

and

$$\langle \Delta^2 \sigma_x(t_f) \rangle = 1 - \langle \sigma_x(t_f) \rangle^2. \tag{9.42}$$

Note that compared to other schemes here the sign of the force in Eq. (9.40) is fully preserved due to the tanh dependence of the signal. The corresponding signal-to-noise ratio SNR $= \langle \sigma_x(t_f) \rangle / \langle \Delta^2 \sigma_x(t_f) \rangle^{1/2}$ is shown in Fig. 9.6(b). The minimum detectable force is determined by the condition that the signal-to-noise ratio is equal to one, which gives

$$F_{\rm d}^{\rm min} = \frac{\hbar \gamma \omega}{\pi g z_0} \sinh^{-1}(1). \tag{9.43}$$

We compare our minimal detectable force with those use a simple harmonic oscillator as a force sensor. In that case the signal-to-noise ratio of one gives $F_{\rm h.o.}^{\rm min} = 2\hbar/z_0 t$ [149]. Our scheme allows to overcome this limit by tuning the ratio ω/g. For example assuming $g = 44$ kHz, $\omega = 30$ kHz, $\gamma = 0.2$ kHz and evolution time of $t_f = 48$ ms we have verified numerically that $F_{\rm d}^{\rm min} \approx 0.92 F_{\rm h.o.}^{\rm min}$. The standard quantum limit derived by the time-energy uncertainty, however, gives $F_{\rm h.o.}^{\rm min}/2$ [153]. This limit can be approached by further decreasing ω/g. However, we note that decreasing ω/g can not increase the accuracy of the detection method indefinitely. Very low values of ω lead to longer evolution times required to stay within the adiabatic regime.

The sensitivity of the force measurement is defined as $\eta_{\rm force} = F_{\rm d}^{\rm min}/\sqrt{\nu}$, where $\nu = T/\tau$ is the repetition number with T being the total experimental time. The time τ includes the evolution time as well as the preparation and measurement times. Because our scheme relies on the projective measurement of the spin populations at the end of the adiabatic transition we have $\tau \approx t_f$. The sensitivity characterizes the minimal force difference, which can be discriminated within a total experimental time of one second. In Fig. 9.7 we show the sensitivity as a function of the slope γ for various values of ω. Lowering γ implies a longer interaction time t_f and thus better sensitivity. Using the parameters in Fig. 9.7 for $\omega = 45$ kHz and interaction time $t_f = 30$ ms we estimate force sensitivity of about 0.3 yN$/\sqrt{\rm Hz}$. Further increasing of the sensitivity to 0.16 yN$/\sqrt{\rm Hz}$ can be achieved with the interaction time of $t_f = 100$ ms.

Alternatively, the force estimation can be carried out by measuring the expectation value of the position quadrature $\langle \hat{Z}(t_f) \rangle$. We find

$$\begin{aligned} \langle \hat{Z}(t_f) \rangle &= -2\frac{g}{\omega} \tanh\left(\frac{\pi g z_0 F_{\rm d}}{\hbar \gamma \omega} \right), \\ \langle \Delta^2 \hat{Z}(t_f) \rangle &= 1 + 4\frac{g^2}{\omega^2} - \langle \hat{Z}(t_f) \rangle^2. \end{aligned} \tag{9.44}$$

Using Eq. (9.44) we obtain that for $\omega > 2g$ the uncertainty of the position quadrature is higher than the measured signal (SNR < 1). At $\omega = 2g$ and in the limit $F_{\rm d} \gg 2\gamma\hbar/(\pi z_0)$, the SNR tends asymptotically to one from below and thus no measurement is possible, whereas for $\omega < 2g$ the force estimation

is bounded by

$$F_{\mathrm{d}}^{\min} = \frac{\hbar\gamma\omega}{\pi g z_0} \tanh^{-1} \sqrt{\frac{1}{2} + \frac{\omega^2}{8g^2}}. \tag{9.45}$$

Comparing Eqs. (9.43) and (9.45) we conclude that the signal of σ_x provides better sensitivity. Moveover, the direct detection of quantum motional state requires additional operations after the sensing protocol. Such operations include the observation of the time evolution of the spin states under the influence of Jaynes-Cummings type interaction. Our scheme avoids those additional operations since it relies on simple fluorescence measurements of the spin states, and thus there is no requirement of additional time-evolution steps after the adiabatic process. This simplifies the experimental measurement procedure and can lead to the reduction of the total experimental time.

9.2.3 Conclusions

We have shown that the system described by the quantum Rabi Hamiltonian can serve as a detector of extremely small forces. The underlying physical mechanism is the process of symmetry-breaking adiabatic transition due to the presence of force perturbations. Our sensing protocols can be implemented using a trapped ion, where the parameters which drive the system across the adiabatic transition are controlled by external laser or microwave fields. We have shown that a system of a single trapped ion can be used as a probe for electric sensing with sensitivity about and even below 1 yN/$\sqrt{\mathrm{Hz}}$ range. Additionally, the proposed method can be extended for sensing magnetic fields. A major advantage of our protocol is that it demands a single population measurement, thereby achieving a considerably speed-up over previous protocols using phonon number measurement via Rabi oscillations.

10. HIGH-PRECISION FORCE SENSING USING A TRAPPED IONS

In this Chapter we introduce quantum sensing schemes for measuring very weak forces with a trapped ions. They use the spin-motional coupling induced by the laser-ion interaction to transfer the relevant force information to the spin-degree of freedom. Therefore, the force estimation is carried out simply by observing the Ramsey-type oscillations of the ion spin states. First, we consider three quantum probes, which are represented by systems obeying the Jaynes-Cummings, quantum Rabi (in 1D) and Jahn-Teller (in 2D) models. By using dynamical decoupling schemes in the Jaynes-Cummings and Jahn-Teller models, our force sensing protocols can be made robust to the spin dephasing caused by the thermal and magnetic field fluctuations. In the quantum-Rabi probe, the residual spin-phonon coupling vanishes, which makes this sensing protocol naturally robust to thermally-induced spin dephasing. We show that the proposed techniques can be used to sense the axial and transverse components of the force with a sensitivity beyond the yN $/\sqrt{\text{Hz}}$ range, i.e. in the xN$/\sqrt{\text{Hz}}$ (xennonewton, 10^{-27}). The Jahn-Teller protocol, in particular, can be used to implement a two-channel vector spectrum analyzer for measuring ultra-low voltages.

We then extend the force sensing protocols by using a linear ion chain which can operate beyond the quantum standard limit. We show that oscillating forces that are off resonance with the motional trap frequency can be detected very efficiently by using quantum probes represented by various spin-boson models. We demonstrate that the temporal evolution of a quantum probe described by the Dicke model can be mapped on the nonlinear Ramsey interferometry which allows us to detect far-detuned forces simply by measuring the collective spin populations. Moreover, we show that the measurement uncertainty can reach the Heisenberg limit by using initial spin-correlated states, instead of motional entangled states. An important advantage of the sensing technique is its natural robustness against the thermally induced dephasing, which extends the coherence time of the measurement protocol. Furthermore, we introduce a sensing scheme that utilizes the strong spin-phonon coupling to improve the force estimation. We show that for a quantum probe represented by the quantum Rabi model the force sensitivity can overcome the one achieved by the simple harmonic oscillator force sensor.

Finally, we introduce a quantum sensing protocol for detecting the parameters characterizing the phase-space displacement by using a single trapped ion as a quantum probe. We show that, thanks to the laser-induced coupling between the ion's internal states and the motion mode, the estimation of the two conju-

gated parameters describing the displacement can be efficiently performed by a set of measurements of the atomic state populations. Furthermore, we introduce a three-parameter protocol capable of detecting the magnitude, the transverse direction, and the phase of the displacement. We characterize the uncertainty of the two- and three-parameter problems in terms of the Fisher information and show that state projective measurement saturates the fundamental quantum Cramér-Rao bound.

10.1 Force Sensing with Spin-Boson Models

In this Section, we propose ion-based sensing schemes for measuring very rapidly varying forces, which follow an earlier proposal [174] wherein the relevant force information is mapped into the spin degrees of freedom of the single trapped ion. In contrast to [174], the techniques proposed here do not require specific adiabatic evolution of the control parameters but rather they rely on using Ramsey-type oscillations of the ion's spin states, which are detected via state-dependent fluorescence measurements. Moreover, we show that by using dynamical decoupling schemes, the sensing protocols become robust against dephasing of the spin states caused by thermal and magnetic-field fluctuations.

We consider a quantum system described by the Jaynes-Cummings (JC) model which can be used as a highly sensitive quantum probe for sensing of the axial force component. By applying an additional strong driving field [175, 176] the dephasing of the spin states induced by the residual spin-phonon interaction can be suppressed such that the sensing protocol does not require initial ground-state cooling of the ion's vibrational state. We show that the axial force sensing can be implemented also by using a probe represented by the quantum Rabi (QR) model. Because of the absence of residual spin-motional coupling in this case, the force estimation is robust to spin dephasing induced by the thermal motion fluctuations.

Furthermore, we introduce a sensing scheme capable to extract the two-dimensional map of the applied force. Here the quantum probe is represented by the Jahn-Teller (JT) model, in which the spin states are coupled with phonons in two spatial directions. We show that the two transverse components of the force can be measured by observing simply the coherent evolution of the spin states. In order to protect the spin coherence during the force estimation we propose a dynamical decoupling sequence composed of phonon phase-shift operators, which average to zero the residual spin-phonon interaction.

We estimate the optimal force sensitivity in the presence of motional heating and find that with current ion trap technologies force sensitivity better than 1 yN $\mathrm{Hz}^{-1/2}$ can be achieved. Thus, a single trapped ion may serve as a high-precision sensor of very weak electric fields generated by small needle electrodes with sensitivity as low as 1 μV/m $\mathrm{Hz}^{-1/2}$.

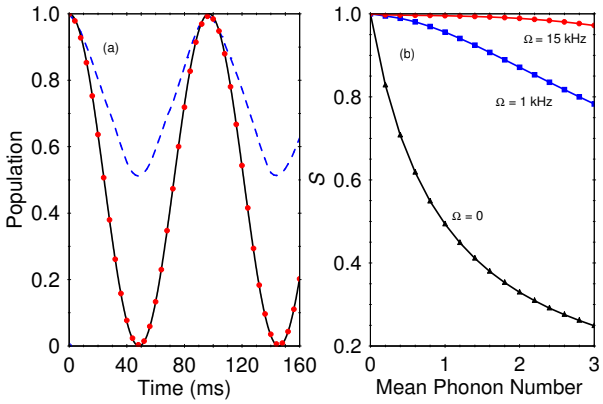

Fig. 10.1: a) Time-evolution of the probability to find the system in spin state $|\uparrow\rangle$ for the JC system. We compare the probabilities derived from the original Hamiltonian (10.3) (dots) and the effective Hamiltonian (10.4) (solid lines). We assume an initial thermal distribution with a mean phonon number $\bar{n} = 1.2$. The parameters are set to $g = 4$ kHz, $\omega = 170$ kHz, $\Delta = g^2/2\omega$, $z_{\rm ax} = 14.5$ nm, $F = 20$ yN and $\Omega = 10$ kHz. For the same initial state but in the absence of driving field ($\Omega = 0$), the signal loses contrast (blue dashed line). b) Contrast of the Rabi oscillations defined as $S = P_\uparrow(t_2) - P_\uparrow(t_1)$ with $t_1 = \pi/2\Omega_F$ and $t_2 = \pi/\Omega_F$ with $\Omega_F = 60$ kHz as a function of the mean phonon number $\bar{n}$.

10.1.1 1D Force Sensing

Jaynes-Cummings quantum probe

In our model we consider a single two-state ion with a transition frequency ω_0, in a linear Paul trap with an axial trap frequency ω_z. The small axial oscillation of the ion is described by the vibrational Hamiltonian $\hat{H}_{\rm ax} = \hbar\omega_z \hat{a}^\dagger \hat{a}$, where $\hat{a}^\dagger$ ($\hat{a}$) creates (annihilates) a phonon excitation. We assume that the ion interacts with a laser field with a frequency $\omega_{\rm L} = \omega_0 - \omega_z + \delta$, tuned near the red-sideband resonance with a detuning δ. The interaction Hamiltonian in the Lamb-Dicke limit and the rotating-wave approximation reads

$$\hat{H}_{\rm JC} = \hbar\omega\hat{a}^\dagger\hat{a} + \hbar\Delta\sigma_z + \hbar g(\sigma^-\hat{a}^\dagger + \sigma^+\hat{a}), \tag{10.1}$$

with $\delta = \Delta - \omega$, where Δ is the effective spin frequency and ω is the effective phonon frequency. Here, $\sigma_{x,y,z}$ are the Pauli matrices, $\sigma^\pm$ are the respective raising and lowering operators for the effective spin system, and g determines the strength of the spin-phonon coupling.

The external time-varying force with a frequency $\omega_d = \omega_z - \omega$, e.g., $F(t) = F\cos(\omega_d t)$, displaces the motional amplitude of the ion oscillator along the axial direction, as described by the term

$$\hat{H}_F = \frac{z_{\rm ax} F}{2}(\hat{a}^\dagger + \hat{a}). \tag{10.2}$$

Here $z_{\rm ax} = \sqrt{\hbar/2m\omega_z}$ is the spread of the zero-point wavefunction along the axial direction and F is the parameter we wish to estimate. The origin of the oscillating force can be a very weak electric field, an optical dipole force, spin-dependent forces created in a magnetic-field gradient or a Stark-shift gradient, etc. With the term (10.2) the total Hamiltonian becomes

$$\hat{H}_{\rm T} = \hat{H}_{\rm JC} + \hat{H}_F. \tag{10.3}$$

In the following, we consider the weak-coupling regime $g \ll \omega$, in which the phonon degree of freedom can be eliminated from the dynamics. This can be carried out by applying the canonical transformation $\hat{U} = e^{\hat{S}}$ to $\hat{H}_{\rm T}$ (10.3) such that $\hat{H}^{\rm JC}_{\rm eff} = e^{-\hat{S}}\hat{H}_{\rm T}e^{\hat{S}}$ with $\hat{S} = (g/\omega)(\sigma^+\hat{a} - \sigma^-\hat{a}^\dagger) + (\Omega_F/g)(\hat{a} - \hat{a}^\dagger)$. Keeping only the terms of order of g/ω we arrive at the following effective Hamiltonian,

$$\begin{aligned}\hat{H}^{\rm JC}_{\rm eff} &= \hbar\widetilde{\Delta}\sigma_z - \hbar\Omega_F\sigma_x - \hat{H}'_{\rm JC},\\ \hat{H}'_{\rm JC} &= \frac{\hbar g^2}{\omega}\sigma_z\hat{a}^\dagger\hat{a}.\end{aligned} \tag{10.4}$$

This result indicates that the spin-motional interaction in Eq. (10.3) shifts the effective spin frequency by the amount $\widetilde{\Delta} = \Delta - g^2/2\omega$, while the effect of the force term is to induce transitions between the spin states. The strength of the transition is quantified by the Rabi frequency $\Omega_F = gz_{\rm ax}F/2\hbar\omega$, which is proportional to the applied force F. Hence the force estimation can be carried out by observing the coherent evolution of the spin population that can be read out via state-dependent fluorescence. The last term $\hat{H}'_{\rm JC}$ in Eq. (10.4) is the residual spin-motional coupling. This term affects the force estimation because it can be a source of pure spin dephasing [177]. Indeed, the σ_z factor in $\hat{H}'_{\rm JC}$ induces transitions between the eigenstates $|\pm\rangle$ of the operator σ_x depending on the vibrational state of the oscillator. As long as the oscillator is prepared initially in an incoherent vibrational state at a finite temperature this would lead to a random component in the spin energy. As we will see below, by using dynamical decoupling the effect of the pure spin dephasing can be reduced.

The sensing protocol starts by preparing the system in state $\hat{\rho}(0) = |\uparrow\rangle\langle\uparrow| \otimes \hat{\rho}_{\rm osc}$, where $\hat{\rho}_{\rm osc}$ stands for the initial density operator of the oscillator. According to Eq. (10.4), the evolution of the system is driven by the unitary propagator $\hat{U}_{\rm JC}(t,0) = e^{-{\rm i}\hat{H}^{\rm JC}_{\rm eff}t/\hbar}$. Assuming for the moment that $\hat{\rho}_{\rm osc} = |0\rangle\langle 0|$ where $|n\rangle$ is the harmonic oscillator Fock state with n phonon excitations, the probability to find the system in state $|\uparrow\rangle$ is $P_\uparrow(t) = \cos^2(\Omega_F t)$, where for simplicity we set $\Delta = g^2/2\omega$, hence $\widetilde{\Delta} = 0$. In this case, the effect of $\hat{H}'_{\rm JC}$ automatically vanishes such that the signal exhibits a cosine behavior according to the effective Hamiltonian (10.4). An initial thermal phonon distribution, however, would introduce dephasing on the spin oscillations caused by thermal fluctuations. The spin coherence can be protected, for example, by applying a sequence of fast pulses, which flip the spin states and average the residual spin-motional interaction to zero during the force estimation [178]. On the other hand, because the relevant force information is encoded in the σ_x term in Eq. (10.4), continuously applying an additional strong driving field $\hat{H}_{\rm d} = \hbar\Omega\sigma_x$ in the same basis [175, 176],

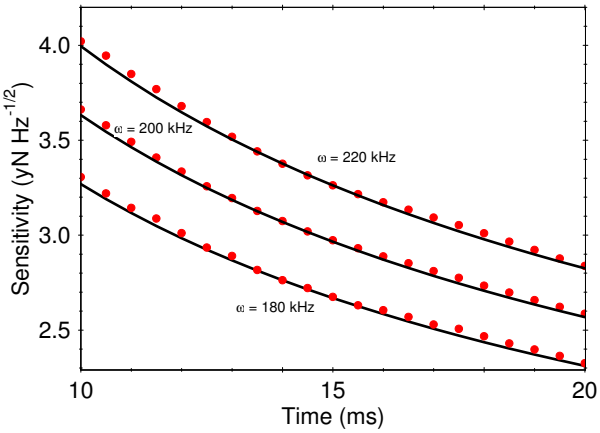

Fig. 10.2: The sensitivity of the force measurement versus time t for various values of ω. We assume an initial thermal vibrational state with a mean phonon number $\bar{n} = 1$. The solid lines represent the analytical result given by Eq. (10.7) while the dots are the exact numerical solution with the Hamiltonian (10.3) including the strong driving term. The other parameters are set to $g = 4$ kHz and $\Omega = 7$ kHz.

such that $\hat{H}_{\rm T} \to \hat{H}_{\rm T} + \hat{H}_{\rm d}$, would not affects the force estimation but rather will suppress the effect of the residual spin-motional coupling. Indeed, going in the interaction frame with respect to $\hat{H}_{\rm d}$, the residual spin-motional coupling becomes

$$\hat{H}'_{\rm JC}(t) = \frac{\hbar g^2}{\omega}(e^{2{\rm i}\Omega t}|+\rangle\langle -| + e^{-2{\rm i}\Omega t}|-\rangle\langle +|)\hat{a}^\dagger\hat{a}. \tag{10.5}$$

The latter result indicates that the off-resonance transitions between states $|\pm\rangle$ induced by $\hat{H}'_{\rm JC}$ are suppressed if $g^2/2\omega \ll \Omega$. By separating the pulse sequences from $t = 0$ to $t/2$ with a Hamiltonian $\hat{H}_{\rm T} + \hat{H}_{\rm d}$, and then from $t/2$ to t with a Hamiltonian $\hat{H}_{\rm T} - \hat{H}_{\rm d}$, the spin states are protected from the thermal dephasing and the signal depends only on the Rabi frequency Ω_F at the final time t. Note that the effect of the magnetic field fluctuations of the spin states is described by an additional σ_z term in Eq. (10.4), therefore the strong driving field used here suppresses the spin dephasing caused by the magnetic-field fluctuations, as was experimentally demonstrated [179, 180].

In Fig. 10.1(a) we show the time evolution of the probability $P_\uparrow(t)$ for an initial thermal vibrational state. Applying the driving field during the force estimation leads to reduction of the spin dephasing and hence protecting the contrast of the Rabi oscillations, see Fig. 10.1(b). We note that a similar technique using a strong driving carrier field for dynamical decoupling was proposed for the implementation of a high-fidelity phase gate with two trapped ions [181, 182].

The shot-noise-limited sensitivity for measuring Ω_F is

$$\delta\Omega_F = \frac{\Delta P_\uparrow(t)}{\frac{\partial P_\uparrow(t)}{\partial \Omega_F}\sqrt{\nu}}, \tag{10.6}$$

where $\Delta P_\uparrow(t)$ stands for the variance of the signal and $\nu = T/\tau$ is the repetition number. Here T is the total experimental time, and the time τ includes the evolution time as well as the preparation and measurement times. Because our technique relies on state-projective detection, such that the preparation and measurement times are much smaller than the other time scale, we assume $\tau \approx t$. From Eq. (10.6) we find that the sensitivity, which characterizes the minimal force difference that can be discriminated within a total experimental time of 1 s, is

$$F_{\min}\sqrt{T} = \frac{\hbar\omega}{g z_{\rm ax}\sqrt{t}}. \tag{10.7}$$

In Fig. 10.2 we show the sensitivity of the force estimation versus time t for different frequencies ω assuming an initial thermal vibrational state. For an evolution time of 20 ms, force sensitivity of 2 yN $\mathrm{Hz}^{-1/2}$ can be achieved.

Let us now estimate the effect of the motional heating which limits the force estimation. Indeed, the heating of the ion motion causes damping of the signal, which leads to

$$P_\uparrow(t) = \frac{1}{2}[1 + e^{-\gamma t}\cos(2\Omega_F t)], \tag{10.8}$$

where γ is the decoherence rate. We assume that $\gamma \sim \langle \dot{n}_{\rm ax}\rangle$ where $\langle \dot{n}_{\rm ax}\rangle$ stands for the axial ion's heating rate. Thus, the optimal force sensitivity is

$$F_{\min}\sqrt{T} = \frac{\hbar\omega}{g z_{\rm ax}}\sqrt{2\langle \dot{n}_{\rm ax}\rangle e}. \tag{10.9}$$

Using the parameters in Fig. 10.2 with $\omega = 180$ kHz and assuming $\langle \dot{n}_{\rm ax}\rangle = 0.01$ ms^{-1} we estimate force sensitivity of 2.4 yN $\mathrm{Hz}^{-1/2}$. For a cryogenic ion trap with heating rate in the range of $\langle \dot{n}_{\rm ax}\rangle = 1$ s^{-1} and evolution time of $t = 500$ ms, the force sensitivity would be 0.8 yN $\mathrm{Hz}^{-1/2}$.

Quantum Rabi model

An alternative approach to sense the axial component of the force is to use a probe described by the quantum Rabi model,

$$\hat{H}_{\rm QR} = \hbar\omega\hat{a}^\dagger\hat{a} + \hbar g\sigma_x(\hat{a}^\dagger + \hat{a}), \tag{10.10}$$

which includes it the counter-rotating wave terms. This Hamiltonian can be implemented by using a bichromatic laser field along the axial direction. In the weak-coupling regime, $g \ll \omega$, we find by using the unitary transformation $\hat{U} = e^{\hat{S}}$ with $\hat{S} = -(g/\omega)\sigma_x(\hat{a}^\dagger - \hat{a}) - (2\Omega_F/g)(\hat{a}^\dagger - \hat{a})$ that

$$\hat{H}_{\rm eff}^{\rm QR} = -2\hbar\Omega_F\sigma_x. \tag{10.11}$$

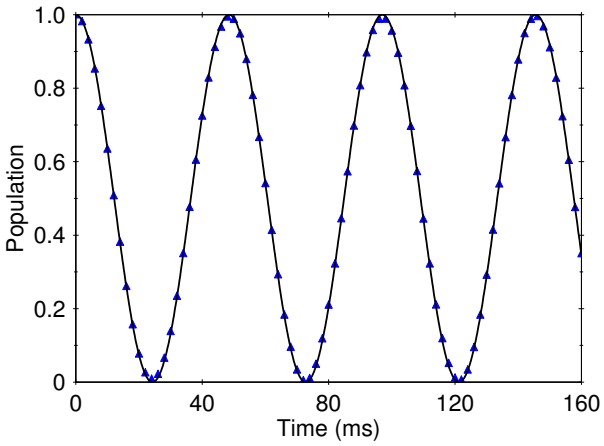

Fig. 10.3: Time-evolution of the probability to find the system in spin state $|\uparrow\rangle$ for the QR system. We assume an initial thermal vibrational state with a mean phonon number $\bar{n} = 1.2$. Due to the absence of residual spin-motion coupling the Rabi oscillations are robust with respect to the spin dephasing caused by the thermal fluctuations. We compare the probability derived from the Hamiltonian $\hat{H}_{\mathrm{T}} = \hat{H}_{\mathrm{QR}} + \hat{H}_F$ with the analytical solution $P_\uparrow = \cos^2(2\Omega_F)$. The parameters are set to $g = 4$ kHz, $\omega = 170$ kHz, $z_{\mathrm{ax}} = 14.5$ nm, $F = 20$ yN.

In contrast to Eq. (10.4), now the effective Hamiltonian (10.11) does not contain an additional residual spin-motional coupling, which implies that the spins are immune to dephasing caused by the thermal motion fluctuations, see Fig. 10.3. Thereby the force estimation can be carried out without additional strong driving field. We find that the optimal force sensitivity is similar to Eq. (10.9) but with extra factor of 2 in the denominator,

$$F_{\mathrm{min}}\sqrt{T} = \frac{\hbar\omega}{2gz_{\mathrm{ax}}}\sqrt{2\langle\dot{n}_{\mathrm{ax}}\rangle e}. \tag{10.12}$$

10.1.2 Summary and Outlook

We have proposed quantum sensing protocols, which rely on mapping the relevant force information onto the spin degrees of freedom of the single trapped ion. The force sensing is carried out by observing the Ramsey-type oscillations of the spin states, which can be detected via state-dependent fluorescence. We have considered quantum probes represented by the JC and QR systems, which can be used to sense the axial component of the force. We have shown that when using a JC system as a quantum probe, one can apply dynamical decoupling schemes to suppress the effect of the spin dephasing during the force estimation. When using a QR system as a probe, the absence of a residual spin-phonon coupling makes the sensing protocol robust to thermally-induced spin dephasing. Furthermore, we have shown that the transverse-force direction can be mea-

sured by using a system described by the JT model, in which the spin states are coupled with the two spatial phonon modes. Here the information of the magnitude of the force and the relative ratio can be extracted by observing the time evolution of the respective ion's spin states, which simplify significantly the experimental procedure.

Tuning the trap frequencies over the broad range, the force sensing methods proposed here can be employed to implement a spectrum analyzer for ultra-low voltages. Moreover, because in the force-field direction sensing the mutual ratio can be additionally estimated our method can be used to implement a two-channel vector spectrum analyzer. Finally, the realization of the proposed force sensing protocols are not restricted only to trapped ions but could be implemented with other quantum optical setups such as cavity-QED [185] or circuit-QED systems [186].

10.2 Force sensors with precision beyond the standard quantum limit

In this work we study the temporal evolution of the collective spin-boson Jahn-Teller model and show that it can be mapped on nonlinear Ramsey interferometer for measuring very weak forces. We consider force sensor protocols that utilize the laser induced coupling between the collective spin states and single vibrational mode and show that they can be used to detect very efficiently weak forces that are off-resonance with the ion's trap frequency. We demonstrate that low-frequency forces that are below the trapping frequency can be detected by using probe represented by the Dicke model. We show that for force detuning much higher than the spin-phonon coupling the relevant force information is mapped into the collective spin-degree of freedom. This allows to use the spin correlation instead of motional entangled states to improve the force sensitivity. We show that for initial uncorrelated spin states, the force sensitivity is short noise limited, while for the initial maximum entangled spin state the force sensitivity is Heisenberg limited. The main advantage of the proposed sensing protocol is its natural robustness against the thermally induced spin dephasing, which avoids the applications of additional dynamical decoupling techniques during the force estimation. The absence of residual spin-vibrational interaction extends the coherence time of the sensing protocol and allows to use ion chain which is not laser cooled to the vibrational ground state.

Furthermore, we introduce force sensor technique which is capable to detect time-varying forces with detuning smaller than the spin-phonon coupling by mapping the relevant force information into the vibrational degree of freedom. Here the quantum probe is represented by the quantum Rabi model describing the dipolar interaction between the single vibrational mode and effective spin states. We show that the force sensitivity of our technique can overcome the sensitivity which is achieved by using simple harmonic oscillator as a force sensor. Moreover, thanks to the strong spin-phonon coupling our sensitivity can overcome even the best sensitivity that can be achieved when the force oscillates

at resonance with the ion's trap frequency.

10.2.1 The model

We consider a model in which an ensemble of N two-state atoms interact with two boson modes via Jahn-Teller coupling

$$\begin{aligned}
&\hat{H} = \hat{H}_0 + \hat{H}_{\mathrm{JT}} + \hat{H}_F,\\
&\hat{H}_0 = \hat{H}_{\mathrm{b}} + \hat{H}_{\mathrm{s}} = \hbar\delta_x \hat{a}_x^\dagger \hat{a}_x + \hbar\delta_y \hat{a}_y^\dagger \hat{a}_y + \hbar\Delta \hat{J}_z,\\
&\hat{H}_{\mathrm{JT}} = \frac{2\hbar g_x}{\sqrt{N}} \hat{J}_x(\hat{a}_x^\dagger + \hat{a}_x) + \frac{2\hbar g_y}{\sqrt{N}} \hat{J}_y(\hat{a}_y^\dagger + \hat{a}_y),\\
&\hat{H}_F = \sqrt{N} F_x(\hat{a}_x^\dagger + \hat{a}_x) + \sqrt{N} F_y(\hat{a}_y^\dagger + \hat{a}_y).
\end{aligned} \tag{10.13}$$

Here $\hat{H}_0$ contains the free boson term where $a_\alpha^\dagger$, a_α ($\alpha = x, y$) are the creation and annihilation operators corresponding to oscillator with frequency ω_α. The term $\hat{H}_{\mathrm{s}}$ describes the interaction between the collection of spins and the external applied magnetic field with strength Δ. The second term in (10.13) is the Jahn-Teller spin-boson interaction with coupling strength g_α, where $\hat{J}_\beta = \frac{1}{2}\sum_{k=1}^{N} \sigma_k^\beta$ ($\beta = x, y, z$) are the collective spin operators with σ_k^β being the Pauli operator for spin k. The last term in (10.13) describes the action of force which displaces the two bosonic modes with strength F_α.

The collective spin basis consists of the set of the eigenvectors $\{|j, m\rangle\}$ of the two commuting operators $\hat{J}^2 |j, m\rangle = j(j+1) |j, m\rangle$ and $\hat{J}_z |j, m\rangle = m |j, m\rangle$ ($m = -j, \cdots, j$) with $j = \frac{N}{2}$. The total Hilbert space is spanned in the basis $\{|j, m\rangle \otimes |n_x, n_y\rangle\}$, where $|n_\alpha\rangle$ is the Fock state of the bosonic mode with occupation number n_α.

For general non-equal couplings $g_x \neq g_y$ and $F_x = F_y = 0$ the model possesses a discrete $\mathbb{Z}$ symmetry. Indeed, the parity operator defined by

$$\hat{\Pi} = \hat{\Pi}_{\mathrm{s}} \otimes \hat{\Pi}_{\mathrm{b}}, \quad \hat{\Pi}_{\mathrm{s}} = \sigma_1^z \otimes \cdots \otimes \sigma_N^z, \quad \hat{\Pi}_{\mathrm{b}} = (-1)^{\hat{a}_x^\dagger \hat{a}_x + \hat{a}_y^\dagger \hat{a}_y}, \tag{10.14}$$

transform $\hat{J}_{x,y} \to -\hat{J}_{x,y}$ and $\hat{a}_{x,y} \to -\hat{a}_{x,y}$ which implies that $\hat{H} \to \hat{H}$.

Let us discuss a few well known limits of our model. First, when either ($g_y = 0$, $g_x \neq 0$) or ($g_x = 0$, $g_y \neq 0$) the model is equivalent to the Dicke model [187]. For the particular case of single spin $j = 1/2$ it reduces to the quantum Rabi model [188]. In the symmetric case $\delta_x = \delta_y$ and $g_x = g_y$ the model (10.13) describes the U(1) invariant Jahn-Teller spin-boson interaction. In the limit of $N = 1$ the model reduces to $E \otimes e$ symmetrical Jahn-Teller model which has been shown to possesses an effective gauge potential description [189]. On the other hand in the semiclassical limit $N \gg 1$ the model exhibits a magnetic structural phase transition.

10.2.2 Sensing low-frequency forces

We begin by considering the weak coupling regime of our model (10.13) in which the detuning δ_α of the driving force is much higher than the spin-phonon

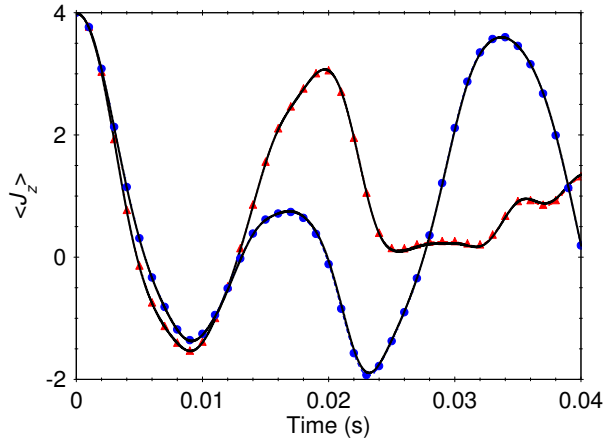

Fig. 10.4: Time-evolution of the expectation value of $\hat{J}_z$ operator for a system of $N = 8$ spins. We assume an initial state $|\Psi(0)\rangle = |j, j\rangle|0_x, 0_y\rangle$. We compare the numerical solution of the time-dependent Schrödinger equation with Hamiltonian (10.13) (solid lines) with the solution using effective Hamiltonian (10.16) for $\Delta = \chi_x\chi_y$ (blue circles) and $\Delta = 2\chi_x\chi_y$ (red triangles). The parameters are set to $g_x = 5$ kHz, $g_y = 3$ kHz, $\delta_x = -85$ kHz, $\delta_y = -80$ kHz, $f_{d,x} = 10$ yN and $f_{d,y} = 15$ yN.

coupling g_α ($|\delta_\alpha| \gg g_\alpha$). In that case the center-of-mass modes are only virtually excited, thereby they can be adiabatically eliminated from the dynamics. This can be carried out by applying the canonical transformation $\hat{U} = e^{\hat{S}}$ to the Hamiltonian (10.13) such that $\hat{H}_{\rm eff} = \hat{U}^\dagger \hat{H} \hat{U}$, where the anti-Hermitian operator $\hat{S}$ is given by

$$\begin{aligned}\hat{S} &= \frac{2g_x}{\delta_x\sqrt{N}}\hat{J}_x(\hat{a}_x - \hat{a}_x^\dagger) + \frac{2g_y}{\delta_y\sqrt{N}}\hat{J}_y(\hat{a}_y - \hat{a}_y^\dagger) \\ &\quad + \sqrt{N}\frac{F_x}{\delta_x}(\hat{a}_x - \hat{a}_x^\dagger) + \sqrt{N}\frac{F_y}{\delta_y}(\hat{a}_y - \hat{a}_y^\dagger). \end{aligned} \tag{10.15}$$

Keeping only the leading terms of order of g_α/δ_α the effective Hamiltonian becomes $\hat{H}_{\rm eff} = \hat{H}_0 + \frac{1}{2}[\hat{H}_{\rm JT} + \hat{H}_F, \hat{S}] + \hat{H}'$ which yields

$$\begin{aligned}&\hat{H}_{\rm eff} = \hat{H}_{\rm spin} + \hat{H}_{\rm res} + \hat{H}', \\ &\hat{H}_{\rm spin} = \hbar\Delta\hat{J}_z - \frac{4\hbar g_x^2}{N\delta_x}\hat{J}_x^2 - \frac{4\hbar g_y^2}{N\delta_y}\hat{J}_y^2 - \frac{4g_xF_x}{\delta_x}\hat{J}_x - \frac{4g_yF_y}{\delta_y}\hat{J}_y, \\ &\hat{H}_{\rm res} = \hat{H}_{\rm b} + \frac{2i\hbar g_x g_y}{N\delta_x\delta_y}\hat{J}_z\{(\delta_x + \delta_y)(\hat{a}_x^\dagger\hat{a}_y - \text{h.c.}) \\ &-(\delta_x - \delta_y)(\hat{a}_x^\dagger\hat{a}_y^\dagger - \text{h.c.})\}, \end{aligned} \tag{10.16}$$

where the we have omitted the constant terms. The result indicates that the phonon degree of freedom mediates an effective spin-spin interaction described

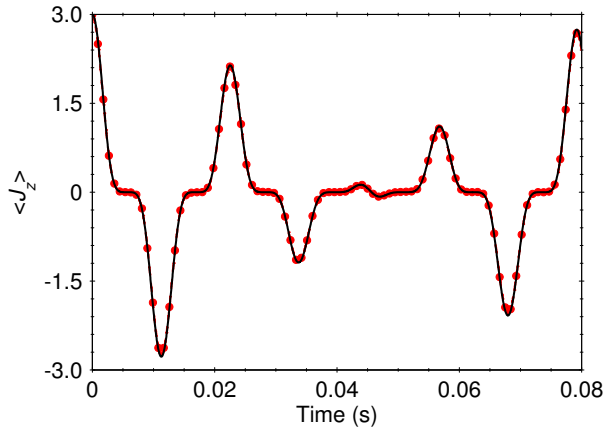

Fig. 10.5: Time-evolution of the expectation value of $\hat{J}_z$ operator for a system of $N = 6$ spins. We assume an initial thermal vibrational state with average phonon number $\bar{n} = 0.6$. We compare the numerical solution of the time-dependent Schrödinger equation with Hamiltonian (10.13) (solid lines) with the solution using effective Hamiltonian (10.18) (red circles). The parameters are set to $g_x = 5$ kHz, $\delta_x = 60$ kHz, $r_{0,x} = 14.5$ nm, $f_{d,x} = 1.5$ yN.

by the nonlinear quadratic collective spin operators in $\hat{H}_{\rm spin}$. In addition to it the effect of the symmetry-breaking term $\hat{H}_F$ is to induce transition between the individual spin states which are captured by the last two linear collective spin operators in $\hat{H}_{\rm spin}$. The term $\hat{H}_{\rm res}$ is the residual spin-phonon interaction, which does not couple spins at different sites, but rather describes processes in which phonon excitations are created and respectively reabsorbed by the same spin. Note that as long as the quantum oscillators are in their ground states the term $\hat{H}_{\rm res}$ does not affect the collective spin dynamics and thus it can be neglected. Finally, the term $\hat{H}' = \frac{1}{3}[[\hat{H}_{\rm JT} + \hat{H}_F, \hat{S}], \hat{S}] + \ldots$ contains high-order terms in the spin-phonon interaction which we neglected as long as $|\delta_\alpha| \gg g_\alpha$.

Hence, in the weak coupling regime the model (10.13) is mapped into the generalized Lipkin-Meshkov-Glick (LMG) Hamiltonian [190]. As can be seen from Eq. (10.16) the sign of the coupling strengths of the non-linear spin terms depend on the sign of the detunings δ_α, thus one could achieve ferromagnetic interaction $\delta_\alpha > 0$ or respectively anti-ferromagnetic interaction $\delta_\alpha < 0$. It is important to note that following the same line as in [191, 192] our effective Hamiltonian (10.16) in the anti-ferromagnetic regime possesses supersymmetric structure at the special point $\Delta = \chi_x\chi_y$ where we define $\chi_\alpha^2 = 4g_\alpha^2/(N|\delta_\alpha|)$. Indeed, it is straightforward to show that at this point the Hamiltonian (10.16) takes the form

$$\hat{H}_{\rm eff} = \hbar(\chi_x\hat{J}_x + i\chi_y\hat{J}_y + \gamma)(\chi_x\hat{J}_x - i\chi_y\hat{J}_y + \gamma^*) - \hbar|\gamma|^2, \tag{10.17}$$

where $\gamma = \mu_x\chi_x + i\mu_y\chi_y$ and $\mu_\alpha = F_\alpha N/2g_\alpha$. Figure (10.4) shows the time-evolution of the expectation value of $\hat{J}_z$ according the model (10.13) compared

with the effective Hamiltonian (10.16). As expected, the effective picture based on LMG model is very accurate in the weak coupling regime.

Let us now focus on the sensing protocol capable to detect only one of the force components, namely $f_{d,x}$. Thus in the following we set $\Delta = 0$, $g_y = 0$ such that the quantum probe is represented by the Dicke Hamiltonian describing the dipolar interaction between the ensemble of N atoms with the single vibrational mode. In the limit $|\delta_x| \gg g_x$ the effective Hamiltonian reduces to the one-axis twisting Hamiltonian

$$\hat{H}_{\text{eff}} = -\hbar\chi^2 \hat{J}_x^2 - \hbar\Omega_f \hat{J}_x, \tag{10.18}$$

where we define $\chi = \chi_x$ and $\Omega_f = 2g_x r_{0,x} f_{d,x}/\hbar\delta_x$. In that case as can be seen from Eq. (10.16) the residual spin-phonon term $\hat{H}_{\text{res}}$ vanishes automatically. Moreover, it is straightforward to show that even the high-order terms in the residual spin-phonon coupling vanishes such that we have $\hat{H}' = 0$ which indicates that for $|\delta_x| \gg g_x$ the model is exactly mapped into the one-axis twisting Hamiltonian (10.18).

The nonlinear Hamiltonian (10.18) has been proposed for practical applications to quantum metrology, since it can produce squeezed-spin states [193]. For example, such interaction is used to perform precision measurements of the s-wave scattering length between interacting atoms [194]. Here we study the potential application of the model to high-precision force sensing using linear ion crystal. In the following we wish to determine the force amplitude $f_{d,x}$ by measuring the expectation values of the collective spin operator $\hat{J}_z$. For this goal let us assume that the system is prepared in the product state $\hat{\rho}(0) = \hat{\rho}_{\text{spin}} \otimes \hat{\rho}_{\text{osc}}$ where $\hat{\rho}_{\text{osc}}$ is the density operator for the quantum oscillator and $\hat{\rho}_{\text{spin}} = |\Psi(0)\rangle\langle\Psi(0)|$ with $|\Psi(0)\rangle = \sum_{m=-j}^{j} d_m |j,m\rangle_x$ being the initial spin state where d_m is the reduced Wigner rotation matrix

$$d_m = \sqrt{\frac{(2j)!}{(j+m)!(j-m)!}} [\cos(\theta/2)]^{j+m} [\sin(\theta/2)]^{j-m}. \tag{10.19}$$

According to the effective model (10.18) the expectation value of $\hat{J}_z$ evolves in time as

$$\langle \hat{J}_z(t) \rangle = j \sin(\theta)(1 - \sin^2(\theta)\sin^2(\xi))^{2j-1} \cos[\varphi_f + (2j-1)\kappa], \tag{10.20}$$

where we define $\xi = \chi^2 t$, $\varphi_f = \Omega_f t$ and $\kappa = \tan^{-1}(\tan(\xi)\cos(\theta))$ [195]. Hence, in order to determine the force amplitude $f_{d,x}$ one needs to measure the phase φ_f. In Fig. (10.5) we show the signal as a function of time assuming initial thermal phonon state. Remarkably, due to vanishing the residual spin-phonon interaction, $\hat{H}' = 0$, the force sensing protocol does not dependent on the initial vibrational state of the linear ion crystal. As a result of that the measured signal ia naturally robust with respect to the thermally induced spin dephasing.

The uncertainty in the estimate of Ω_f from the measured signal $\langle \hat{J}_z(t) \rangle$ is given by

$$\delta\Omega_f = \frac{\langle \Delta^2 \hat{J}_z \rangle^{1/2}}{\frac{\partial \langle \hat{J}_z \rangle}{\partial \Omega_f} \sqrt{\nu}}, \tag{10.21}$$

where $\langle \Delta^2 \hat{J}_z \rangle^{1/2} = \sqrt{\langle \hat{J}_z^2 \rangle - \langle \hat{J}_z \rangle^2}$ is the variance of the signal and ν is the number of times the estimation is repeated. Assuming the particular value $\theta = \pi/2$ of the initial spin superposition state we have

$$\begin{aligned} \langle \Delta^2 \hat{J}_z \rangle &= \frac{j}{2} + \frac{j(2j-1)}{4} + \frac{j(2j-1)}{4} \cos^{2(j-1)}(2\xi) \cos(2\varphi_f) \\ &\quad -j^2 \cos^{2(2j-1)}(\xi) \cos^2(\varphi_f). \end{aligned} \tag{10.22}$$

Using Eqs. (10.20) and (10.22) one can show that the optimal sensitivity is achieved at the points $\chi^2 t = 2k\pi$ with k integer. At these points the force sensitivity scales as $\delta\Omega_f = 1/\sqrt{TtN}$ where we use that $\nu = T/t$, with T being the total experimental time. This is the standard quantum limit in accuracy for measurement of Ω_f using initial uncorrelated spin states.

The entangled motional states can be used to improve the force estimation accuracy at the Heisenberg limit. However, the physical implementation of such states is in practice difficult since they are very sensitive to motional heating. On the other hand the entangled spin states can be used to improve the sensitivity of frequency estimation using Ramsey fringe interferometry. Because our technique relies on the mapping the relevant force information into the spin-degree of freedom we may use the spin entanglement to increase the sensitivity of the force detection. Indeed, let us assume that the system is prepared initially in the maximally correlated N-particle Greenberger-Horne-Zeilinger (GHZ) spin state $|\Psi(0)\rangle = (|j,j\rangle_x + |j,-j\rangle_x)/\sqrt{2}$. The time evolution of the state according Eq. (10.18) will induce a phase shift proportional to the force. Subsequently, the parity operator $\hat{\Pi}_s$ (10.14) is measured which yields uncertainty in the force estimation

$$f_{d,x}\sqrt{T} = \frac{\hbar\delta_x}{2Ng_x r_{0,x}\sqrt{t}}. \tag{10.23}$$

Assume for example GHZ state with six ions, $\delta_x = 100$ kHz, $g_x = 5$ kHz, $r_{0,x} = 15$ nm and evolution time $t = 10$ ms and using Eq. (10.23) we estimate force sensitivity of order of 0.1 yN Hz$^{-1/2}$.

10.2.3 Strong coupling regime

Let us now discuss the case in which the spin-phonon coupling g_α is higher than the force detuning δ_α ($g_\alpha > \delta_\alpha$) which benefits the strong phonon excitations. In contrast to the previous force sensing protocol, the force estimation can now be performed by measuring the mean-phonon number. To this end we assume that the spin frequency Δ is much larger than the spin-phonon couplings ($\Delta \gg g_\alpha$). In this limit the spin dynamics become frozen, thus it can be decoupled from the phonon degree of freedom by using canonical transformation $\hat{U} = e^{\hat{S}}$ with

$$\hat{S} = \frac{2ig_y}{\sqrt{N}\Delta} \hat{J}_x(\hat{a}_y^\dagger + \hat{a}_y) - \frac{2ig_x}{\sqrt{N}\Delta} \hat{J}_y(\hat{a}_x^\dagger + \hat{a}_x). \tag{10.24}$$

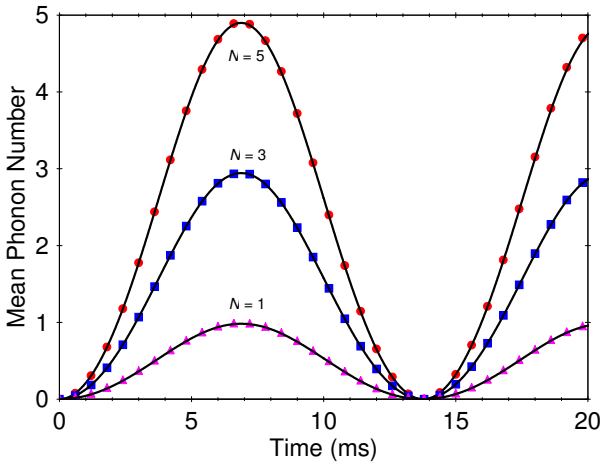

Fig. 10.6: Time-evolution of the expectation value of $\hat{a}_x^\dagger \hat{a}_x$ operator for various number of ions. We assume an initial $|j, -j\rangle|0_x\rangle$. We compare the numerical solution of the time-dependent Schrödinger equation with Hamiltonian (10.13) (solid lines) with the solution using effective Hamiltonian (10.25). The parameters are set to $g_x = 2.5$ kHz, $\Delta = 300$ kHz, $\delta_x = 0.5$ kHz, $r_{0,x} = 14.5$ nm, $f_{d,x} = 3$ yN.

The resulting effective Hamiltonian becomes

$$\begin{aligned}\hat{H}_{\text{eff}} &= \hat{H}_0 + \hat{H}_{\text{ph}} + \hat{H}_F + \hat{H}', \\ \hat{H}_{\text{ph}} &= \frac{2\hbar g_x^2}{N\Delta}\hat{J}_z(\hat{a}_x^\dagger + \hat{a}_x)^2 + \frac{2\hbar g_y^2}{N\Delta}\hat{J}_z(\hat{a}_y^\dagger + \hat{a}_y)^2,\end{aligned} \tag{10.25}$$

where $\hat{H}'$ contains high-order terms which can be neglected as long as $\Delta \gg g_\alpha$. The Hamiltonian (10.25) is diagonal in the collective spin basis, thereby the spin-degree of freedom can be traced out giving $N + 1$ orthogonal subspaces corresponding to each of the collective spin states $|j, m\rangle$. In addition to it, the Hamiltonian (10.25) is quadratic in the bosonic operators, thus it can be analytically diagonalized. Let us assume that the system is initially prepared in the spin state $|j, -j\rangle$. The corresponding bosonic Hamiltonian becomes

$$\begin{aligned}\hat{H}_{\text{eff}} &= \hat{H}_{x,\text{ph}} + \hat{H}_{y,\text{ph}} \\ \hat{H}_{\alpha,\text{ph}} &= \hbar\delta_\alpha \hat{a}_\alpha^\dagger \hat{a}_\alpha - \frac{\hbar g_\alpha^2}{\Delta}(\hat{a}_\alpha^\dagger + \hat{a}_\alpha)^2 + \frac{f_{d,\alpha} r_{0,\alpha}}{2}(\hat{a}_\alpha^\dagger + \hat{a}_\alpha),\end{aligned} \tag{10.26}$$

Note that the model (10.26) has been studied in the context of a quantum phase transition [271, 270] without the force symmetry breaking term $\hat{H}_F$. The unitary propagator corresponding to the Hamiltonian (10.26) can be written as $\hat{U}(t) = \hat{U}_x(t)\hat{U}_y(t)$, where

$$\hat{U}_\alpha(t) = \hat{D}^\dagger(\epsilon_\alpha)\hat{S}^\dagger(\nu_\alpha)e^{-i\upsilon_\alpha t \hat{a}_\alpha^\dagger \hat{a}_\alpha}\hat{S}(\nu_\alpha)\hat{D}(\epsilon_\alpha). \tag{10.27}$$

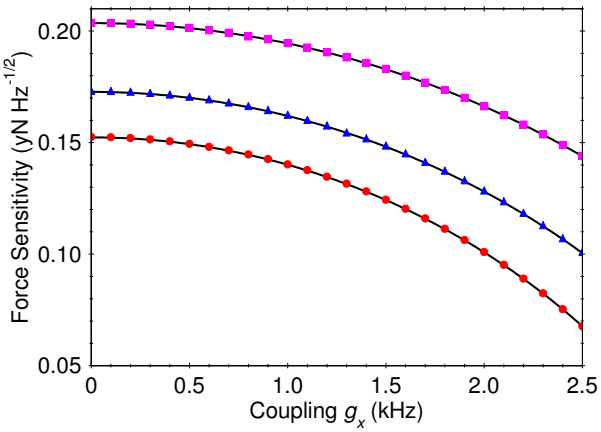

Fig. 10.7: Force sensitivity as a function of the coupling g_x for a single trapped ion. We compare the exact numerical solution for $\delta_x = 0.14$ kHz (dots), $\delta_x = 0.18$ kHz (triangles) and $\delta_x = 0.25$ kHz (squares) with the analytical expression (10.28) (solid line). The other parameters are set to $\Delta = 270$ kHz and $r_{0,x} = 14.5$ nm.

Here $\upsilon_\alpha = \delta_\alpha\sqrt{1-\lambda_\alpha^2}$ with $\lambda_\alpha^2 = 4g_\alpha^2/\delta_\alpha\Delta$. $\hat{D}(\epsilon_\alpha) = e^{\epsilon_\alpha(\hat{a}_\alpha^\dagger - \hat{a}_\alpha)}$ is a displacement operator with amplitude $\epsilon_\alpha = \sqrt{N} f_{d,\alpha} r_{0,\alpha}/\delta_\alpha(1-\lambda_\alpha^2)$ that is proportional to the external force, and respectively $\hat{S}(\nu_\alpha) = e^{\nu_\alpha(\hat{a}_\alpha^{\dagger 2} - \hat{a}_\alpha^\dagger)}$ is the squeeze operator with squeezing parameter $\nu_\alpha = -\frac{1}{4}\ln(1-\lambda_\alpha^2)$.

In Fig. (10.6) we show the time-evolution of $\langle \hat{a}_x^\dagger \hat{a}_x \rangle$. The corresponding signal-to-noise ratio SNR $= \langle \hat{a}_\alpha^\dagger \hat{a}_\alpha \rangle / \langle \Delta^2 \hat{a}_\alpha^\dagger \hat{a}_\alpha \rangle^{1/2}$ equals to one determines the minimal detectable force. We find that the optimal sensitivity is achieved at the points $\upsilon_\alpha t = k\pi$ with k odd number. At these points the signal becomes $\langle \hat{a}_\alpha^\dagger a_\alpha \rangle = 4\epsilon_\alpha^2$ with variance of the signal $\langle \Delta^2 \hat{a}_\alpha \hat{a}_\alpha \rangle^{1/2} = 2\epsilon_\alpha$. The minimal detectable force is given by

$$f_{d,\alpha}^{\min} = \frac{\hbar\pi\sqrt{1-\lambda_\alpha^2}}{t r_{0,\alpha}\sqrt{N}}. \tag{10.28}$$

The result (10.28) indicates that for a given force detuning δ_α one can improve the respective force sensitivity limit by increasing the coupling g_α and thus λ_α, while keeping the constrain $\Delta \gg g_\alpha$, see Fig. 10.7. Note that here we focus on the case $\lambda_\alpha \leq 1$. On the other hand, $\lambda_\alpha > 1$ leads to high phonon generation which however could break the Lamb-Dicke regime. Additionally, we find no major difference in the force sensitivity from the example with $\lambda_\alpha \leq 1$.

Let us compare our minimal detectable force assuming single trapped ion $N = 1$, with those using a simple harmonic oscillator as a force sensor. For simplicity we assume that the single ion force sensor is sensitive only to one of the force components, namely $f_{d,x}$ with detuning δ_x. In that case the quantum probe sensitive to the $f_{d,x}$ is represented by the Rabi Hamiltonian, so that we set

$g_y = 0$ in Eq. (10.26). The minimal detectable force for the harmonic oscillator force sensor is $f_{\rm HO}^{\rm min} = \hbar\pi/tr_{0,x}$ which is achieved at $\delta_x t = k\pi$ with k odd integer. Comparing with (10.28) we conclude that $f_{d,x}^{\rm min} < f_{\rm HO}^{\rm min}$, which indicates that this limit can be overcome within the evolution time $t = k\pi/\delta_x\sqrt{1-\lambda_x^2}$. Moreover, the best sensitivity is typically achieved when the time-varying force alternate with resonance with the motional frequency of the harmonic oscillator. In that case the minimal detectable force is $f_{\rm HO}^{\rm min} = 2\hbar/r_{0,x}t$. Tuning the ratio λ_x in Eq. (10.28) such that $\lambda_x > \sqrt{1-4/\pi^2}$ we can overcome this force sensitivity limit. For example, using the parameters in Fig. 10.7 with detuning $\delta_x = 0.14$ kHz and coupling $g_x = 2.5$ kHz the corresponding force sensitivity is 68 xN (10^{-27} N) per $\sqrt{\rm Hz}$ which is achieved approximately for evolution time $t = 40$ ms, while the force sensitivity for the simple harmonic oscillator at the same evolution time is 74 xN per $\sqrt{\rm Hz}$. However, in order to observe such high force sensitivity the evolution time must be short compared with the decoherence time due to the motional heating. For the latter example, this requires very low heating rate of order of $\langle\dot{n}\rangle = 1\ {\rm s}^{-1}$ which can be achieved for example in a cryogenic ion trap.

10.2.4 Conclusions

In conclusion, we have introduced sensing protocols capable to measure amplitude of the time-varying forces that are off-resonance with the trap frequencies of the ion chain. Using quantum probe described by the Dicke model, far-detuned forces with detuning much higher than the spin-boson coupling can be efficiently measured by mapping the relevant force information into the collective spin-degree of freedom. Thanks to that we have shown that the force sensitivity can be improved by using initial spin correlated states, leading to Heisenberg limited sensitivity. We have shown that the proposed force sensing protocol is robust with respect to the thermally induced dephasing, which prolong the coherence time and thus improves the force sensitivity. We have also considered sensing protocol capable to detect forces with detuning smaller that the spin-boson coupling. In that case, the relevant force information can be extracted by measuring the mean-phonon number. We have shown that thanks to the strong spin-phonon coupling in the quantum Rabi model the force sensitivity could overcome those using a simple harmonic oscillator as a force sensor.

11. ENHANCED PARAMETER ESTIMATION CLOSE TO DISSIPATIVE PHASE TRANSITION

We propose a scheme for detecting time-varying weak forces using quantum probe consisting of single spin and quantum oscillator under the effect of collective dissipation. We study the force estimation in the steady-state regime where the information of the force is extracted by measuring observable of the oscillator such as quadrature and mean phonon excitation. We quantify the force sensitivity in terms of quantum Fisher information and show that it diverges approaching the critical spin-boson coupling making the system sensitive to very small force perturbation. We show that close to the critical coupling the measurement of the oscillator quadrature is optimal in a sense that saturates the fundamental Cramer-Rao bound.

Furthermore, we propose a quantum sensor based on driven-dissipative quantum system for the joint estimation of two conjugated variables characterizing the phase space displacement. The quantum probe consists of lattice system with two level atoms and bosonic modes which interact via dipolar coupling. Interplay between the coherent dynamics and dissipative processes of losses of bosonic excitations leads to a steady-state which exhibits a non-analytical behaviour. we show that close to the dissipative phase transition the sensitivity of one of the conjugated parameters either the magnitude or the phase of the displacement can be significantly enhanced. Moreover, we show that the sum of the measurement uncertainties of the two parameters can overcome the standard quantum limit.

11.0.1 Motivation

Quantum sensing is one of the most promising application of quantum technologies. Usually quantum metrology task involves estimation of a single parameter. High-precision quantum estimation can be achieved by exploiting quantum critical systems which exhibit quantum phase transition as a probe. Indeed, as was shown in the sensitivity of single parameter estimation can be significantly improved close to a quantum critical point. Recently, high precision measurements of the control parameter at criticality was experimentally demonstrated using Bose-Einstein condensate [218, 219]. However, in general physical process can involve the simultaneous estimation of multiple parameters, which gives rise to the emergent field of multiparameter quantum metrology. A large class of quantum metrology problems involve joint estimation of more than one parameter, including for example enhanced estimation of multiple phases [220, 221, 222], phases

and noises [223, 224, 225], multidimensional field [226] as well as the estimation of the phase space displacement parameters [227, 228] (see the recent reviews on multiparameter quantum metrology [229, 230]). Moreover, an accessible and saturable lower bound to the multiparameter quantum Fisher information matrix was proposed in [231] which is based on mean values and variances of the measured observables. In analogous with enhanced single parameter estimation a natural task arises to quantify the sensitivity of the multiparameter estimation close to a quantum critical point.

In this section I discuss the estimation of two conjugated parameters characterizing the phase space displacement using quantum probe which exhibit dissipative phase transition. Such a new class of phase transitions emerges due to the interplay between the coupling with the environment and the driving mechanics in an open quantum systems. The dissipative phase transitions are characterized with a non-analytical change in the steady-state [232] and can be used as a potential resource for high-precision quantum metrology. Our dissipative quantum probe consists of one dimensional lattice system where at each site a single two level atom interact via dipolar coupling with a bosonic mode. The coupling between the bosons at different lattice sites is provided via hopping processes. The interplay between the coherent dynamics and dissipative processes which causes losses of bosonic excitations leads to a non-equilibrium regime where the information of the two parameters is imprinted in the *steady-state* density matrix elements. I consider the limit in which the spin excitations are highly suppressed such that the system approaches bosonic multimode Gaussian steady-state. Crucially, the effect of the phase space displacement is to break explicitly the parity symmetry of the lattice model which leads to a non-vanishing expectation values of the quadratures. First I discuss a single-mode case where critical point separates normal to superradiant dissipative phase transition. I show that close to the critical coupling the average quadratures are enhanced and essentially diverge approaching the dissipative phase transition, which can be used to improve the sensitivity in the single parameter displacement estimation. In order to quantify the uncertainty of the two-parameter estimation I use quantum Fisher information matrix (QFIM) which can be explicitly derived. I show that thanks to the spin-boson coupling the uncertainty of the joint estimation can be improved compared to the non-driven case. Moreover, for coupling close to the critical point the sensitivity of one of the conjugated parameters either the magnitude or the phase of the displacement can be significantly enhanced. As a result of that our two-parameter estimation technique can operate beyond the quantum standard limit.

Furthermore, I extend the quantum sensing technique by including the hopping between the bosons at different lattice sites. Approaching the steady-state the system is described by the multimode Gaussian state. I consider the two coupled lattice sites and show that the covariance matrix is independent on the parameters we wish to estimate which significantly simplifies the expression for the QFIM. All elements of the QFIM diverge for spin-boson coupling approaching the critical point signals the occurrence of dissipative phase transition. I show that the critical point is modified by the hopping and its value can be low-

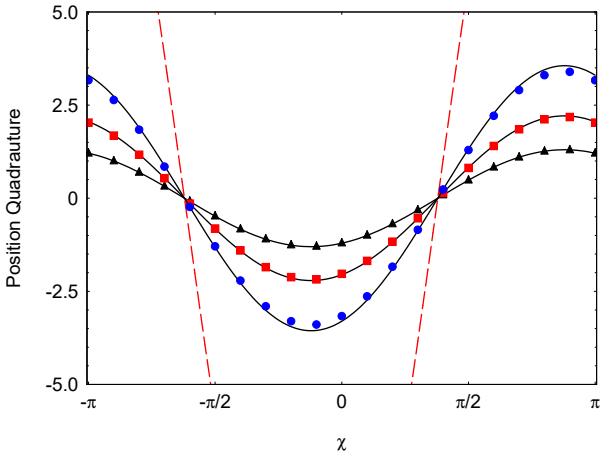

Fig. 11.1: Steady-state position quadrature versus the phase χ. We compare the exact solution derived from the original Hamiltonian (11.6) with $\lambda = 0.85$ (black triangle), $\lambda = 0.95$ (red squares), $\lambda = 1.0$ (blue circles) and the steady-state solution $\langle \hat{x} \rangle = 2\alpha \cos(\delta)$ (solid line). The dashed red line is the solution for $\lambda \to \lambda_c$. The other parameters are set to $\lambda_c = 1.077$ and $\tilde{F} = 0.53$.

ered compared to the single-mode case. Moreover, I show that the sensitivity of the two-parameter estimation can be improved compared to the achievable ultimate precision using two uncoupled quantum probes. Finally, I show that the saturation of the QFIM can be achieved by detecting linear quadrature observables.

11.0.2 Generalized Theoretical Framework for Multiparameter Quantum Estimation

In order to perform quantum multiparameter estimation of p unknown parameters $\theta = (\theta_1, \theta_2, \ldots, \theta_p)$ one needs a quantum probe described by a density matrix $\hat{\rho}_0$. Upon the action of the time-evolution the quantum probe evolves into the state $\hat{\rho}_\theta$ where the information of the parameters are imprinted in the density matrix elements. The sensitivity of the estimator is described by the estimator covariance matrix which elements are $\mathrm{Var}(\theta)_{ij} = \langle \theta_i \theta_j \rangle - \langle \theta_i \rangle \langle \theta_j \rangle$ where the diagonal elements quantifies the uncertainty of the estimation of the individual parameters while the off-diagonal elements indicates a possible correlation between the different parameters. The ultimate precision in the multiparameter estimation is quantified by the quantum Cramer-Rao bound

$$\mathrm{Var}(\theta) \geq (\nu \mathcal{F}_{\mathrm{Q}}(\hat{\rho}_\theta))^{-1}, \tag{11.1}$$

where ν is the number of experimental repetitions and $\mathcal{F}_{\mathrm{Q}}(\hat{\rho}_\theta)_{kl}$ is the $p \times p$ real-valued symmetric QFIM.

In order to calculate the multiparameter QFIM we define the hermitian symmetric logarithmic derivative (SLD) operator $\hat{\mathcal{L}}_{\theta_k}$ for each of the parameters

which obeys the operator equation

$$2\partial_{\theta_k}\hat{\rho}_\theta = \hat{\mathcal{L}}_{\theta_k}\hat{\rho}_\theta + \hat{\rho}_\theta\hat{\mathcal{L}}_{\theta_k}. \tag{11.2}$$

For the density matrix with spectral decomposition $\hat{\rho}_\theta = \sum_n p_n|\psi_n\rangle\langle\psi_n|$ the SLD can be expressed as

$$\hat{\mathcal{L}}_{\theta_k} = 2\sum_{n,m}\frac{\langle\psi_n|\partial_{\theta_k}\hat{\rho}_\theta|\psi_m\rangle}{p_n + p_m}|\psi_n\rangle\langle\psi_m|, \tag{11.3}$$

with $p_n + p_m \neq 0$. Then using the SLD operators one can express the real and symmetric QFIM elements as follows

$$(\mathcal{F}_{\mathrm{Q}}(\hat{\rho}_\theta))_{km} = \frac{1}{2}\mathrm{Tr}(\hat{\rho}_\theta\{\hat{\mathcal{L}}_{\theta_k}, \hat{\mathcal{L}}_{\theta_m}\}), \tag{11.4}$$

where $\{\cdot,\cdot\}$ is the anticommutator. We point out that QFIM can be interpreted as a measure of distinguishability of two quantum states with respect to an infinitesimal change of the parameters of interest. Indeed, one can define Bures distance between two infinitesimally close quantum states by $ds^2_{\mathrm{B}} = \sum_{k,m} g_{km}d\theta_k d\theta_m$ where $g_{km} = \frac{1}{4}(\mathcal{F}_{\mathrm{Q}}(\hat{\rho}_\theta))_{km}$ is the metric tensor [241]. This intimate relation between distance and QFIM indicates that the quantum parameter estimation can be substantially enhanced close to phase transition where infinitesimally small change of parameters give rise to huge change of the distance. Since the quantum Fisher information is equivalent to the inverse uncertainty of the measurement, the critical quantum dynamics enables significant enhancement in the measurement precision for single as well as for multiparameter estimations.

For single parameter estimation the optimal measurement is always achieved by the projective measurements composed by the eigenvectors of SLD operator. However, for multiparameter estimation the SLD operators corresponding to different physical observable may not commute and hence the ultimate precision is achieved by incompatible measurements. This is hold for conjugated variables for which a Heisenberg-type uncertainty relation applies. Defining

$$\hat{\mathcal{C}}_{\theta_k,\theta_m} = [\hat{\mathcal{L}}_{\theta_k}, \hat{\mathcal{L}}_{\theta_m}], \tag{11.5}$$

sufficient condition to exist an optimal measurement which saturates the quantum Cramer-Rao bound is the commutativity of all pairs of the SLD operators, $\hat{\mathcal{C}}_{\theta_k,\theta_m} = 0$. A weak condition for the saturation of the multiparameter quantum Cramer-Rao bound requires the commutativity of the SLD operators on average, $\mathrm{Tr}(\hat{\rho}_\theta\hat{\mathcal{C}}_{\theta_k,\theta_m}) = 0$. Recently, metrological multiparameter squeezing platform was introduced, which provides an accessible and saturable lower bound to the QFIM [231]. It is based on multiparameter moment matrix which approximates the sensitivity by means of first and second moments of the chosen measurement observables.

In the following I will discuss two-parameter estimation of the magnitude and the phase of unknown displacement using open quantum system as a probe,

which exhibits dissipative phase transition. The quantum probe consists of chain of dissipative coupled light-matter systems each of them described by the quantum Rabi model.

11.0.3 Quantum Sensing Protocol

Consider a quantum system of N spins which interact with N bosonic modes via dipolar interaction described by quantum Rabi model. The bosons at different lattice sites are coupled due to the hopping processes subject to the tight-binding model. The total Hamiltonian then is given by

$$\begin{aligned}\hat{H} &= \hbar\sum_{k=1}^{N}\{\omega\hat{a}_k^\dagger\hat{a}_k+\frac{\Omega}{2}\sigma_k^x+g(\hat{a}_k^\dagger+\hat{a}_k)\sigma_k^y \\ &\quad+\frac{F}{2}(\hat{a}_k^\dagger e^{i\chi}+\hat{a}_k e^{-i\chi})\}+\hbar\sum_{k>l}^{N}\kappa_{kl}(\hat{a}_k^\dagger\hat{a}_l+\hat{a}_k\hat{a}_l^\dagger),\end{aligned} \tag{11.6}$$

where ω is the frequency of the bosonic field, $\hat{a}_k^\dagger$ and $\hat{a}_k$ are creation and annihilation operators of the bosonic excitation at the kth site, $\sigma_k^{x,y}$ are the Pauli matrices associates with the kth spin and g is the coupling strength. Ω is the Rabi frequency of the transverse field and κ_{kl} is the hopping strength. Note that alternatively the bosonic system can be described in terms of collective modes such that each spin interacts with collection of bosonic modes [234].

The two conjugated parameters which we wish to estimate are the magnitude of the displacement $\theta_1 = F$ and respectively its phase $\theta_2 = \chi$. Such a displacement term can be created for example by applying a time-varying force with unknown magnitude and phase which displaces motion amplitude of the quantum oscillators. The effect of decay of bosonic excitation is described within the framework of master equation in Lindblad form,

$$\partial_t\hat{\rho}_\theta = -\frac{i}{\hbar}[\hat{H},\hat{\rho}_\theta]+\sum_{k=1}^{N}\gamma_k\hat{\mathcal{D}}[\hat{a}_k], \tag{11.7}$$

where the Lindblad term for each bosonic mode is $\hat{\mathcal{D}}[\hat{a}_k] = 2\hat{a}_k\hat{\rho}_\theta\hat{a}_k^\dagger-\{\hat{a}_k^\dagger\hat{a}_k,\hat{\rho}_\theta\}_+$ and γ_k is the decay rate.

In our quantum metrology scheme the system is prepared initially in state with density matrix $\hat{\rho}(0) = \hat{\rho}_{\rm spin}\otimes\hat{\rho}_{\rm b}$ and then evolves according to the master equation (11.7). Here $\hat{\rho}_{\rm spin} = \otimes_{k=1}^{N}|{\downarrow_k}\rangle\langle{\downarrow_k}|$, where $\sigma_k^x|{\downarrow_k}\rangle = -|{\downarrow_k}\rangle$ and respectively $\hat{\rho}_{\rm b} = \otimes_{k=1}^{N}|0_k\rangle\langle 0_k|$ with $|n_k\rangle$ being the Fock state for the kth boson. Defining the dimensionless coupling $\lambda = 2g/\sqrt{\omega\Omega}$ and consider the limit $\epsilon = \omega/\Omega\to 0$ one can trace out the spin degree of freedom. Indeed, making the unitary transformation $\hat{U} = \prod_k^N e^{-i\frac{g}{\Omega}(\hat{a}_k^\dagger+\hat{a}_k)\sigma_k^z}$ such that the effective Hamilto-

nian $\hat{H}_{\rm eff} = \hat{U}\hat{H}\hat{U}^{-1}$ becomes

$$\begin{aligned}\hat{H}_{\rm eff} &= \hbar\sum_{k=1}^{N}\{\omega\hat{a}_k^\dagger\hat{a}_k - \frac{\omega\lambda^2}{4}(\hat{a}_k^\dagger+\hat{a}_k)^2 + \frac{F}{2}(\hat{a}_k^\dagger e^{i\chi}+\hat{a}_k e^{-i\chi})\}\\ &\quad +\hbar\sum_{k>l}^{N}\kappa_{kl}(\hat{a}_k^\dagger\hat{a}_l+\hat{a}_k^\dagger\hat{a}_l). \end{aligned} \tag{11.8}$$

Interplay between the coherent and dissipative dynamics leads to a non-equilibrium steady-state of the system which can exhibits a non-analytical behaviour. Our quantum sensing protocol relies on the time-evolution of the system into the steady-state where the two-parameter estimation is performed. Since the dynamics is quadratic in the bosonic operators the steady-state of the system is of Gaussian form and the density operator can be reconstructed from the first and the second moments. In order to describes the N-mode Gaussian state of the system we define quadrature operator $\hat{\mathbf{q}} = \{\hat{x}_1, \hat{p}_1, \ldots, \hat{x}_N, \hat{p}_N\}^{\rm T}$ and mean displacement vector $\mathbf{d} = \langle\hat{\mathbf{q}}\rangle$ [235, 236]. Here $\hat{x}_k = (\hat{a}_k^\dagger + \hat{a}_k)$ and $\hat{p}_k = i(\hat{a}_k^\dagger - \hat{a}_k)$ are the position and momentum quadratures for kth oscillator. Then the covariance matrix becomes

$$V_{kl}(\hat{\rho}_\theta, \hat{\mathbf{q}}) = \frac{1}{2}\langle\hat{q}_k\hat{q}_l + \hat{q}_l\hat{q}_k\rangle - d_k d_l. \tag{11.9}$$

We quantify in the following the sensitivity of the two-parameter estimation in terms of QFIM. We focus on the single-mode case $N = 1$ and the two-mode case $N = 2$ where the effect of the hopping amplitude is discussed. For single-mode case one can derive explicit expression for the steady-state density matrix which allows direct evaluation of SLD operators and QFIM. For two-mode case it is more convenient to express the QFIM in terms of covariance matrix and mean displacement vector. We show that the covariance matrix (11.9) is independent on the parameters we wish to estimate which leads to significant simplification of the QFIM elements. Moreover, we show that the moment matrix which approximates the two-parameter sensitivity by means of first and second moments of the quadrature observables [231] coincide with the QFIM which leads to the saturation of the quantum Cramer-Rao bound.

11.0.4 Single-Mode Case

We begin by consider the non-equilibrium steady-state of the system for $\kappa_{kl} = 0$. This corresponds to a quantum probe, which is described by the dissipative quantum Rabi model. In that case the single-mode Gaussian steady-state can be expressed as $\hat{\rho}_\theta = \hat{R}(\delta)\hat{D}(\alpha)\hat{S}(\xi)\hat{\nu}\hat{S}^\dagger(\xi)\hat{D}^\dagger(\alpha)\hat{R}^\dagger(\delta)$, where $\hat{R}(\delta) = e^{i\delta\hat{a}^\dagger\hat{a}}$ is the rotation operator, $\hat{D}(\alpha) = e^{\alpha(\hat{a}^\dagger-\hat{a})}$ is the displacement operator, $\hat{S}(\xi) = e^{\frac{r}{2}(\hat{a}^2e^{-2i\phi}-\hat{a}^{\dagger 2}e^{2i\phi})}$ is the squeezing operator and $\hat{\nu} = \sum_n p_n|n\rangle\langle n|$ is the thermal state. Here $p_n = N_{\rm th}^n/(1+N_{\rm th})^{n+1}$ is the thermal state probability and $N_{\rm th}$ stand for the average number of thermal excitations. Note that $N_{\rm th}$ is independent on

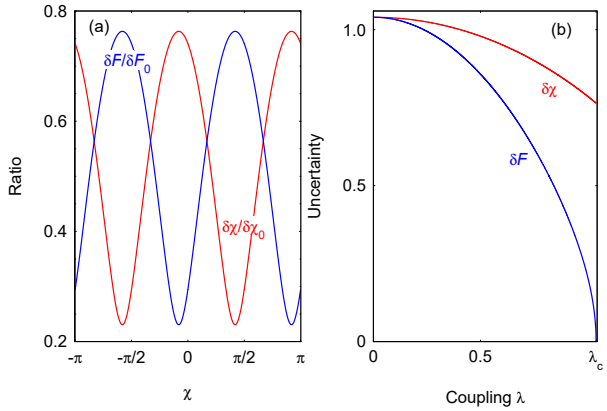

Fig. 11.2: (a) Ratio $\delta F/\delta F_0$ and $\delta\chi/\delta\chi_0$ as a function of phase χ. The parameters are set to $\lambda_c = 1.04$ and $\lambda = 0.95\lambda_c$. (b) Minimal detectable parameters δF in units of ω and $\delta\chi$ according Eq. (11.15) as a function of λ. The force sensitivity is improved for phase χ close to the optimal given by $\tan(2\chi_{\rm opt}) = 2\tilde{\gamma}/(\lambda_c^2 - 2)$.

the parameters we wish to estimate. I find that the displacement amplitude and rotation phase angle are given by

$$\alpha = \frac{\tilde{F}}{2(\lambda_c^2 - \lambda^2)}\sqrt{\lambda_c^2 - \lambda^2\tilde{\gamma}\sin(2\chi) + \lambda^2(\lambda^2 - 2)\sin^2(\chi)},$$
$$\tan(\delta) = \frac{(\lambda^2 - 1)\sin(\chi) - \tilde{\gamma}\cos(\chi)}{\tilde{\gamma}\sin(\chi) - \cos(\chi)} \tag{11.10}$$

and respectively the squeezing and its phase are

$$\tanh(2r) = \frac{\lambda^2}{\sqrt{4(\lambda_c^2 - \lambda^2) + \lambda^4}}, \quad \tan(2\phi + 2\delta) = \frac{2\tilde{\gamma}}{2 - \lambda^2}, \tag{11.11}$$

with $\tilde{F} = F/\omega$, $\tilde{\gamma} = \gamma/\omega$. Here $\lambda_c^2 = 1 + \tilde{\gamma}^2$ is the critical coupling which separates normal $\lambda \leq \lambda_c$ to superradiant $\lambda > \lambda_c$ dissipative phase transition. Note that the present estimation scheme is focused on the case $\lambda \leq \lambda_c$. We emphasize that the information of the two parameters we wish to estimate is encoded in three parameters, namely δ, α and ϕ which is in contrast with the standard two-parameter phase space estimation where the parameters are encoded respectively in the amplitude and the phase of the displacement [227]. In Fig. 11.1 is shown comparison between the exact and analytical results for the steady-state position quadrature for different phase χ. We see that by increasing λ the displacement amplitude is enhanced and respectively diverges approaching the dissipative phase transition at the critical coupling λ_c.

Having the expression for the non-equilibrium steady-state one can derive the expressions for the corresponding two SLD operators. Indeed, using (11.3)

it is straightforward to prove that

$$\hat{\mathcal{L}}_F = \frac{2\partial_F \alpha}{1+2N_{\rm th}} \hat{R}(\delta)\hat{D}(\alpha)\hat{S}(\xi)(\beta\hat{a}^\dagger + \beta^*\hat{a})\hat{S}^\dagger(\xi)\hat{D}^\dagger(\alpha)\hat{R}^\dagger(\delta), \tag{11.12}$$

with $\beta(r,\phi) = \cosh(r) + e^{2i\phi}\sinh(r)$ and respectively

$$\hat{\mathcal{L}}_\chi = \frac{2}{1+2N_{\rm th}} \hat{R}(\delta)\hat{D}(\alpha)\hat{S}(\xi)(\upsilon\hat{a}^\dagger + \upsilon^*\hat{a})\hat{S}^\dagger(\xi)\hat{D}^\dagger(\alpha)\hat{R}^\dagger(\delta), \tag{11.13}$$

with $\upsilon = (\partial_\chi \alpha)\beta(r,\phi) + i\alpha(\partial_\chi\delta)\beta(-r,\phi)$. In order to quantify the sensitivity of the two-parameter estimation we define the inverse QFIM

$$(\mathcal{F}_{\rm Q}(\hat{\rho}_\theta)^{-1})_{km} = \begin{pmatrix} \mathcal{F}_F^{-1} & \mathcal{F}_{F\chi}^{-1} \\ \mathcal{F}_{\chi F}^{-1} & \mathcal{F}_\chi^{-1} \end{pmatrix}. \tag{11.14}$$

The diagonal elements of the inverse QFIM provides achievable bounds for the sensitivity of the joint estimation. We find

$$\begin{aligned} \mathcal{F}_F^{-1} &= \frac{\omega^2}{4}\{4(\lambda_{\rm c}^2-\lambda^2)+\lambda^4+\lambda^2((\lambda^2-2)\cos(2\chi) \\ &\quad +2\tilde{\gamma}\sin(2\chi))\}, \\ \mathcal{F}_\chi^{-1} &= \frac{\omega^2}{4F^2}\{4(\lambda_{\rm c}^2-\lambda^2)+\lambda^4-\lambda^2((\lambda^2-2)\cos(2\chi) \\ &\quad +2\tilde{\gamma}\sin(2\chi))\}, \end{aligned} \tag{11.15}$$

Hence the ultimate achievable precision becomes $\delta F^2 \geq \frac{1}{\nu}\mathcal{F}_F^{-1}$ and $\delta\chi^2 \geq \frac{1}{\nu}\mathcal{F}_\chi^{-1}$. The off-diagonal elements of the matrix (11.14) describe the correlation between the two parameters. We obtain

$$\mathcal{F}_{F\chi}^{-1} = -\frac{\omega^2\lambda^2}{4F}\{(\lambda^2-2)\sin(2\chi) - 2\tilde{\gamma}\cos(2\chi)\}. \tag{11.16}$$

As a comparison I first discuss the ultimate precision by setting $g = 0$ and thus $\lambda = 0$. This correspond to a quantum probe consisting of a single dissipative harmonic oscillator sensitive to the magnitude and the phase of unknown displacement. Using Eq. (11.15) one can show that the uncertainty of the parameters estimation is given by $\delta F_0 \geq \frac{\omega}{\sqrt{\nu}}\lambda_{\rm c}$ and $\delta\chi_0 \geq \frac{\omega}{\sqrt{\nu}F}\lambda_{\rm c}$. Crucially enhancement of the joint sensitivity can be realized by increasing coupling λ. In Fig. 11.2(a) is shown the ratio $\delta F/\delta F_0$ and $\delta\chi/\delta\chi_0$ according to Eq. (11.15). We see that the ultimate joint sensitivity which is achieved by the driven-dissipative dynamics can be improved compared to the non-driven case with δF_0 and $\delta\chi_0$. In particular, when the phase χ is closed to the optimal phase given by $\tan(2\chi_{\rm opt}) = 2\tilde{\gamma}/(\lambda_{\rm c}^2-2)$ one can achieve significantly improve sensitivity of one of the parameters. Indeed, close to the critical coupling $\lambda_{\rm c}$ the two parameters correlations vanishes $\mathcal{F}_{F\chi}^{-1} \approx 0$ and the uncertainty of the joint estimation of the displacement magnitude and the phase becomes

$$\begin{aligned} \delta F^2 &\geq \frac{\omega^2}{4\nu}\{4(\lambda_{\rm c}^2-\lambda^2)+\lambda^4-\lambda^2\sqrt{4(\lambda_{\rm c}^2-\lambda^2)+\lambda^4}\}, \\ \delta\chi^2 &\geq \frac{\omega^2}{4\nu F^2}\{4(\lambda_{\rm c}^2-\lambda^2)+\lambda^4+\lambda^2\sqrt{4(\lambda_{\rm c}^2-\lambda^2)+\lambda^4}\}. \end{aligned} \tag{11.17}$$

Approaching the dissipative phase transition the joint sensitivity scales according to $\delta F \sim \frac{\omega}{\sqrt{\nu}}\sqrt{\lambda_c - \lambda}$ and $\delta\chi \sim \frac{\omega}{\sqrt{2\nu F}}\lambda_c^2$. Hence in this limit the quantum probe becomes sensitive to infinitely small force perturbation, see Fig. 11.2(b). Also we observe that as long as $\gamma < \omega$ we have $\delta\chi < \delta\chi_0$ such that the phase sensitivity is improved compared to $\delta\chi_0$. Note that for phase equal to $\chi = \chi_{\rm opt} + \pi/2$ one can show that $\delta F \sim \frac{\omega}{\sqrt{2\nu}}\lambda_c^2$ and $\delta\chi \sim \frac{\omega}{\sqrt{\nu F}}\sqrt{\lambda_c - \lambda}$ and thus one can enhance respectively the phase sensitivity.

Furthermore, we evaluate the commutator of the SLD operators corresponding to the two displacement parameters. Using Eqs. (11.12) and (11.13) we obtain

$$\hat{\mathcal{C}}_{F\chi} = \frac{8iF}{\omega^2}\frac{\hat{\mathbf{1}}}{4(\lambda_c^2 - \lambda^2) + \lambda^4}. \tag{11.18}$$

Since we deal with conjugate variables for which a Heisenberg uncertainty relation holds the two SLD operators do not commute even in an average. Using (11.18) one can estimate the commutator close to the dissipative phase transition, $\lambda \to \lambda_c$. We find

$$\hat{\mathcal{C}}_{F\chi} \sim \frac{8iF\omega^2}{(\omega^2 + \gamma^2)^2}\hat{\mathbf{1}}. \tag{11.19}$$

We note in order to satisfy the condition of weak commutativity $\langle\hat{\mathcal{C}}_{F\chi}\rangle = 0$ one can lower ω which on one hand will improve the sensitivity of one of the parameters, for example δF but on the other hand will spoil the phase estimation because $\delta\chi \sim 1/\omega$.

Finally, one can evaluate the sum of the measurement uncertainties of the two parameters. For this goal it is convenient to introduce dimensionless quantities $q = \tilde{F}\cos(\chi)$ and $p = \tilde{F}\sin(\chi)$. Then it is straightforward to show that the QFIM elements do not dependent on the values of the two parameters to be estimated. We find that both uncertainties becomes

$$\delta q^2 \geq \frac{1}{2\nu}(2\lambda_c^2 - 3\lambda^2 + \lambda^4), \quad \delta p^2 \geq \frac{1}{2\nu}(2\lambda_c^2 - \lambda^2) \tag{11.20}$$

and therefore

$$\delta q^2 + \delta p^2 \geq \frac{1}{2\nu}\{4(\lambda_c^2 - \lambda^2) + \lambda^4\}. \tag{11.21}$$

The quantum standard limit (SQL) requires $\delta q^2 + \delta p^2 \geq \frac{2}{\nu}$. The latter has simple explanation, namely it corresponds to the ultimate achievable precision for non-driven quantum probe with $\lambda = 0$ and $\lambda_c = 1$. Crucially the effect of the spin-boson coupling λ is to improve simultaneously the uncertainty of the two-parameter displacement estimation. Indeed, approaching the dissipative phase transition the sum of the variances becomes $\delta q^2 + \delta p^2 \sim \frac{\lambda_c^4}{2\nu}$ and thus as long as $\gamma < \omega$ one can overcome the SQL. Note that the beating of the SQL is equivalent that both uncertainties on the estimation of the parameters q and p are $\delta q < 1$ and $\delta p < 1$.

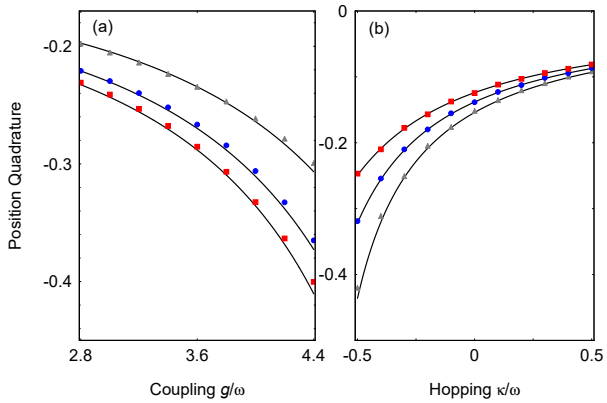

Fig. 11.3: (a) Average position quadrature as a function of the coupling g/ω for different hopping amplitude κ. We compare the exact solution of the master equation with Hamiltonian (11.6) with the steady-state result (11.22) (solid lines). The parameters are set to $\kappa/\omega = -0.4$ (red squares), $\kappa/\omega = -0.47$ (blue circles), and $\kappa/\omega = -0.5$ (grey triangles). The other parameters are $\epsilon = 4 \times 10^{-3}$, $\tilde{F} = 0.13$, $\tilde{\gamma} = 0.16$ and $\chi = \pi/7$. (b) The same but now vary the hopping amplitude for different couplings, $g/\omega = 3.1$ (black triangles), $g/\omega = 3.9$ (blue circles), $g/\omega = 4.5$ (red squares).

11.0.5 Two-Mode Case

Let's extend the two-parameter estimation by considering coupled system described with Hamiltonian (11.6) for $N = 2$. Again in the limit $\epsilon \to 0$ the model is transformed into the dissipative system of harmonic oscillators which interact via hopping dynamics. Note that depending on the physical realization of the scheme the sign of the hopping can vary. Indeed, for quantum probe based on trapped ion system the hopping can be positive (negative) depending on the either we use radial (axial) phonons as a bosonic degree of freedom. For realization with coupled cavity array the sigh of the hopping is negative.

In the steady-state the information of the two parameters is imprinted in the two-mode Gaussian state. Although the steady-state quadratures can be found for any number of sites the respective expressions are too complicated to be presented here. For the two-mode case the steady-state position quadrature is given by

$$\langle \hat{x}_k \rangle = -\tilde{F} \frac{(1+\tilde{\kappa})\cos(\chi) - \tilde{\gamma}\sin(\chi)}{(1+\tilde{\kappa})(\lambda_+^2(\kappa) - \lambda^2)}, \tag{11.22}$$

with $\tilde{\kappa} = \kappa/\omega$ and for simplicity we set $\gamma_k = \gamma$ $(k = 1, 2)$. Here $\lambda_+(\kappa) = \sqrt{\tilde{\gamma}^2 + (1+\tilde{\kappa})^2}/\sqrt{1+\tilde{\kappa}}$ is the critical coupling which is modified by the hopping κ compared to the single mode case with λ_c. As long as $\tilde{\kappa} > -1$, the critical coupling $\lambda_+(\kappa)$ is real such that the quadratures diverge in the limit $\lambda \to \lambda_+(\kappa)$ signal the existence of dissipative phase transition. For $\tilde{\kappa} < -1$ the

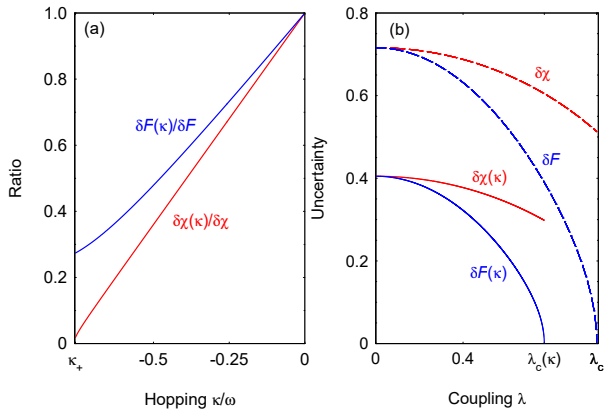

Fig. 11.4: (a) Ratios $\delta F(\kappa)/\delta F$ and $\delta\chi(\kappa)/\delta\chi$ as a function of the hopping according Eq. (11.24). The parameters are set to $\tilde{\gamma} = 0.16$, $\lambda = 0.59$ and $\chi = \pi/3$. (b) Minimal detectable force and phase versus the coupling λ (solid lines) for $\tilde{\kappa} = -0.45$. As a comparison is shown the results for $\kappa = 0$ (dashed lines).

coupling $\lambda_+(\kappa)$ becomes purely imaginary and thus no enhancement of the average quadratures is possible by increasing λ. We observe that as long as $\tilde{\kappa} < 0$ and $\tilde{\kappa} > \tilde{\kappa}_{\rm min}$ where $\tilde{\kappa}_{\rm min} = -1 + \tilde{\gamma}^2$, the critical coupling is smaller compared to $\lambda_{\rm c}$, namely $\lambda_+(\kappa) < \lambda_{\rm c}$. In Fig. 11.3(a) is shown comparison between the exact result with original Hamiltonian (11.6) and steady-state position quadrature (11.22) as a function of g/ω for different κ. We see that for $\epsilon \ll 1$ the exact dynamics is described very closely with the effective Hamiltonian (11.8). We observe that by increasing $|\kappa|$ the critical coupling λ_+ decreases which leads to higher average position quadrature $|\langle\hat{x}_k\rangle|$. As we will see below smaller value of $\lambda_+(\kappa)$ can leads to better sensitivity in a sense that for the same value of λ the two-parameter displacement estimation is improved compared to the single-mode case.

Furthermore, it is straightforward to show that the denominator in Eq. (11.22) can be rewritten as $(1 + \tilde{\kappa})(\lambda_+^2(\kappa) - \lambda^2) = (\kappa_+ - \tilde{\kappa})(\kappa_- - \tilde{\kappa})$. Here we define critical hopping amplitudes $\kappa_\pm = \frac{1}{2}\{\lambda^2 - 2 \pm \sqrt{\lambda^4 - 4\tilde{\gamma}^2}\}$ which are reals as long as $\lambda^4 \geq 4\tilde{\gamma}^2$. As is shown in Fig. 11.3(b) increasing the hopping amplitude κ the average position quadrature $|\langle\hat{x}_k\rangle|$ increases and eventually diverges in the limit $\tilde{\kappa} \to \kappa_+$. Note that in Fig. 11.3(b) the parameters are set such that $\kappa_+ > \kappa_-$ and $\kappa_\pm < 0$.

In order to describe the sensitivity of the two-parameter estimation in terms of QFIM one need to find the covariance matrix (11.9) for the two-mode Gaussian state. I find that all elements of V_{km} diverge near the critical point with $V_{km} \sim (\lambda_+ - \lambda)^{-1}(\lambda_- - \lambda)^{-1}$, where $\lambda_-(\kappa) = \sqrt{\tilde{\gamma}^2 + (1 - \tilde{\kappa})^2}/\sqrt{1 - \tilde{\kappa}}$. Moreover, all covariance matrix elements are *independent* on the parameters we wish to estimate which leads to significant simplification of the QFIM elements. In-

deed, we have

$$\mathcal{F}_{\mathrm{Q}}(\hat{\rho}_\theta)_{km} = (\partial_{\theta_k}\mathbf{d}^T)V(\hat{\rho}_\theta,\hat{\mathbf{q}})^{-1}(\partial_{\theta_m}\mathbf{d}). \tag{11.23}$$

Assuming that $\lambda_+(\kappa) < \lambda_-(\kappa)$ the ultimate uncertainty of the joint estimation becomes

$$\begin{aligned}\delta F^2(\kappa) &\geq \frac{\omega^2}{8\nu}\{4(1+\tilde{\kappa})(\lambda_+^2(\kappa)-\lambda^2)+\lambda^4+\lambda^2 Q(\kappa)\},\\ \delta\chi^2(\kappa) &\geq \frac{\omega^2}{8\nu F^2}\{4(1+\tilde{\kappa})(\lambda_+^2(\kappa)-\lambda^2)+\lambda^4-\lambda^2 Q(\kappa)\},\end{aligned} \tag{11.24}$$

where $Q(\kappa) = (\lambda^2-2-2\tilde{\kappa})\cos(2\chi)+2\tilde{\gamma}\sin(2\chi)$. As a comparison first I consider the case with $\kappa = 0$ which corresponds to two uncoupled driven-dissipative quantum probes. As can be expected in that case the additional factor of 2 in the denominator compared to Eq. (11.17) appears due to the additivity of the QFIM.

In Fig. 11.4(a) I show the ratio between the variances (11.24) and those obtained for $\kappa = 0$, namely $\delta F(\kappa)/\delta F$ and $\delta\chi(\kappa)/\delta\chi$. As can be seen the hopping $\kappa < 0$ improves simultaneously force and phase sensitivities. In Fig. 11.4(b) I plot the uncertainty in the estimation of F and χ where the phase is set $\chi = \chi_{\mathrm{opt}}$ with $\tan(2\chi_{\mathrm{opt}}) = 2\tilde{\gamma}(\lambda_+^2(\kappa)-2-2\tilde{\kappa})^{-1}$. For such phase and coupling λ close to the critical coupling $\lambda_+(\kappa)$ the off-diagonal elements of the QFIM vanishes, $\mathcal{F}_{F\chi} \approx 0$. Approaching the critical point both uncertainties scales according to $\delta F(\kappa) \sim \frac{\omega}{\sqrt{2\nu}}\sqrt{\lambda_+(\kappa)-\lambda}$ and $\delta\chi(\kappa) \sim \frac{\omega}{2\sqrt{\nu}F}\lambda_+^2(\kappa)$ or respectively $\delta F(\kappa) \sim \frac{\omega}{2\sqrt{\nu}}\lambda_+^2(\kappa)$ and $\delta\chi(\kappa) \sim \frac{\omega}{\sqrt{2\nu}F}\sqrt{\lambda_+(\kappa)-\lambda}$ for phase $\chi = \chi_{\mathrm{opt}}+\pi/2$. We see that for given λ and because $\lambda_+(\kappa) < \lambda_{\mathrm{c}}$ one can achieve better sensitivity for F and χ compared to the sensitivity which is achieved by using two uncoupled quantum probes with $\kappa = 0$.

Further, one can evaluate the sum of the uncertainties of the dimensionless quadratures q and p. I find

$$\delta q^2(\kappa)+\delta p^2(\kappa) \geq \frac{1}{4\nu}\{4(1+\tilde{\kappa})(\lambda_+^2(\kappa)-\lambda^2)+\lambda^4\}. \tag{11.25}$$

Since the displacement acts simultaneously on the two modes the SQL requires $\delta q^2(\kappa)+\delta p^2(\kappa) \geq \frac{1}{\nu}$. Close to the dissipative phase transition $\lambda \to \lambda_+(\kappa)$ we have $\delta q^2(\kappa)+\delta p^2(\kappa) \sim \frac{\lambda_{\mathrm{c}}^4(\kappa)}{4\nu}$. Hence in order to overcome the SQL we require that $\lambda_+^2(\kappa) < 2$. Moreover, the minimal value of right side of inequality (11.25) is $\tilde{\gamma}^2$ and thus as long as $\gamma < \omega$ the two parameters displacement estimation can operate beyond the SQL.

Finally, we discuss the saturation of the quantum Cramer-Rao bound. Recently, a moment-based method was proposed in Rev. [231] which provides the maximally achievable sensitivity for multimode displacements. In general, for a given set $\hat{\mathbf{X}}$ of measurement observables the estimator covariance matrix in the central limit is $\mathrm{Var}(\theta) = (\nu\mathcal{M}(\hat{\rho}_\theta,\hat{\mathbf{X}}))^{-1}$ [231]. Here $\mathcal{M}(\hat{\rho}_\theta,\hat{\mathbf{X}})$ is the moment matrix, which is given by

$$\mathcal{M}(\hat{\rho}_\theta,\hat{\mathbf{X}}) = D(\hat{\rho}_\theta,\hat{\mathbf{X}})^T V(\hat{\rho}_\theta,\hat{\mathbf{X}})^{-1} D(\hat{\rho}_\theta,\hat{\mathbf{X}}), \tag{11.26}$$

where $(D(\hat{\rho}_\theta, \hat{\mathbf{X}}))_{kl} = \partial_{\theta_l}\langle \hat{X}_k \rangle$ and $V(\hat{\rho}_\theta, \hat{\mathbf{X}})$ is the covariance matrix. Moreover, the moment matrix provides a saturable lower bound to the QFIM, namely $\mathcal{M}(\hat{\rho}_\theta, \hat{\mathbf{X}}) \leq \mathcal{F}_{\mathrm{Q}}(\hat{\rho}_\theta)$. As was shown in [231] the multimode displacement sensitivity using Gaussian probe states and unitary phase imprinting evolution the moment matrix is strictly equal to the QFIM for $\hat{\mathbf{X}} = \hat{\mathbf{q}}$, such that $\mathcal{M}(\hat{\rho}_\theta, \hat{\mathbf{q}}) = \mathcal{F}_{\mathrm{Q}}(\hat{\rho}_\theta)$. These linear quadrature observables can be detected by the standard homodyne measurement techniques. Remarkably, although our sensing technique is based on a driven-dissipative evolution the equality between the moment matrix (11.26) and the QFIM for single- as well as for two-mode cases is still hold. Indeed, because the covariance matrix $V(\hat{\rho}_\theta, \hat{\mathbf{q}})$ is independent on the two parameters we wish to estimate, the moment matrix (11.26) associated with the observables $\hat{\mathbf{X}} = \hat{\mathbf{q}}$ coincides with the QFIM.

11.0.6 Conclusion

In summary, I have discussed quantum sensor based on dissipative phase transition for the estimation of two displacement parameters. Our quantum probe consists of lattice system of two-level atoms and bosonic modes which interact via dipolar coupling. The interplay between the dissipation of bosonic excitations and the driven dynamics leads to a non-equilibrium steady-state which exhibits non-analytical behaviour at the critical coupling. I have examined the sensitivity of the two displacement parameters and show that thanks of the driven-dissipative dynamics one can achieve enhancement of the parameters estimation compared to the non-driven case. I have shown that close to the dissipative phase transition one can achieve significant improvement of the sensitivity of one of the conjugate parameters namely magnitude or the phase of the displacement. Moreover, I have shown that the total uncertainty of the two parameters displacement estimation can overcome the SQL. I have discussed the moment matrix which provides an accessible and saturable lower bound to the QFIM. I have shown that the moment matrix associated with the linear quadrature observables coincide with the QFIM which leads to he saturation of the multiparameter quantum Cramer-Rao bound.

12. QUANTUM THERMOMETRY WITH TRAPPED IONS

In this chapter we introduce the estimation protocol for detecting the temperature of the transverse vibrational modes of linear ion crystal. We show that thanks to the laser induced laser coupling between the vibrational modes and the collective spin states the estimation of the temperature is carried out by set of measurements of the spin populations. We show that temperature estimation protocol using single ion as a quantum probe is optimal in a sense that the set of state projective measurements saturate the fundamental Cramer-Rao bound. We find a plateau of the maximal temperature sensitivity using ion chain as a quantum probe. Moreover, we show that the non-classical part of the quantum Fisher information could leads to enhancement of the temperature sensitivity compared to the single ion case.

Furthermore, we propose an adiabatic method for optimal phonon temperature estimation using trapped ions which can be operated beyond the Lamb-Dicke regime. The quantum sensing technique relies on a time-dependent red-sideband transition of phonon modes, described by the non-linear Jaynes-Cummings model in general. A unique feature of our sensing technique is that the relevant information of the phonon thermal distributions can be transferred to the collective spin-degree of freedom. We show that each of the thermal state probabilities is adiabatically mapped onto the respective collective spin-excitation configuration and thus the temperature estimation is carried out simply by performing a spin-dependent laser fluorescence measurement at the end of the adiabatic transition. We characterize the temperature uncertainty in terms of the Fisher information and show that the state projection measurement saturates the fundamental quantum Cramér-Rao bound for quantum oscillator at thermal equilibrium.

12.0.1 Motivation

Over the last few years the devolvement of high-precision temperature sensing techniques has attracted considerable interest due to the broad and important applications ranging from medicine and biology [242] to quantum information processing and quantum thermodynamics [243, 244, 245]. The quantum thermometer in generally consists of a system called probe which is brought into thermal equilibrium with a sample of interest. Various quantum optical systems can be used as temperature probes including for example quantum dots [246, 247, 248], color centers in nanodiamonds [249, 250, 251], micromechanical resonators [239, 240] and trapped ions [252, 253, 255, 254, 256]. An accurate

strategy for temperature determination can be executed by measuring the populations in the energy basis of the quantum probe system [257, 258, 259, 260, 261]. Indeed, it turns out that this strategy is *optimal* with smallest temperature statistical uncertainty which saturates the fundamental Cramér-Rao bound for temperature estimation of any equilibrium system. However, the energy measurements are in general challenging as in case of a probe consisting of a quantum harmonic oscillator, where the number of basis states is typically large at thermal equilibrium, which limits the achievable temperature precision. Alternative approach is to use additional ancillary qubits to couple coherently with the probe. Then the information of the temperature is transferred to the qubit states which can be read-out with high-efficiency at the end of the interaction [239, 240]. Although this strategy is experimentally more convenient the statistical uncertainty of the temperature determination is usually higher than the optimal one given by the fundamental quantum Cramér-Rao bound.

In this work we propose an adiabatic method for optimal phonon temperature detection using trapped ions. Our technique relies on a global laser radiation which couples the internal spin states of ions to the vibrational mode via a red-sideband transition. This collective interaction is described by a non-linear Jaynes-Cummings type model in general. We show that by engineering time-dependent detuning and spin-motion coupling one can adiabatically transfer the relevant temperature information encoded in phonon distributions of vibrations onto the collective spin-excitation. Such a time-dependent control of the spin-phonon interaction has been extensively studied in creating of entangled spin and motion states [262, 263, 264, 265]. Recently, a rapid adiabatic passage was experimentally used to measure the electromagnetically-induced-transparency cooling dynamics in a string of trapped ions [266]. Here we show that each of the Fock states of the harmonic oscillator is adiabatically mapped on respective spin-excitation configuration. Thus the temperature determination is carried out by performing projection measurement of the spin populations at the end of the adiabatic transition. We show that our adiabatic sensing technique can be operated in and beyond the Lamb-Dicke limit and therefore is suitable for measuring a broad range of temperatures including a low temperature limit with mean thermal phonon excitations $\bar{n} \ll 1$ as well as the high temperature regime with $\bar{n} \gg 1$. We quantify the sensitivity of the temperature estimation using classical Fisher information. We show that the projection measurements in the original spin basis lead to an *equality* between the classical and quantum Fisher information for quantum harmonic oscillator at thermal equilibrium. Therefore, our quantum thermometry is optimal in the sense that the uncertainty of the temperature estimation is bounded by the quantum Cramér-Rao inequality. Moreover, we show that our adiabatic motion sensing technique can be applied for the measurement of various other quantum states such as coherent and squeezed motion states. In particular, we discuss the detection of the phase of the coherent cat state via single-shot measurements of the final spin populations. We show that the phase detection can be applied for ultra sensitive force measurement with Heisenberg limited precision [149, 153].

12.0.2 Principe of a Quantum Thermometry

We begin by considering a probe system which is represented by a simple quantum harmonic oscillator with Hamiltonian $\hat{H} = \hbar\omega\hat{a}^\dagger\hat{a}$, where $\hat{a}^\dagger$ and $\hat{a}$ are the creation and annihilation operators of bosonic excitation with frequency ω. We assume that the harmonic oscillator is prepared at thermal equilibrium and is described by a canonical Gibbs state with density matrix $\hat{\rho}_T = e^{-\beta\hat{H}}/Z = \sum_{n=0}^{\infty} p_n|n\rangle\langle n|$. Here $|n\rangle$ is the nth Fock state of the harmonic oscillator with eigenenergy $E_n = n\hbar\omega$, $p_n = Z^{-1}e^{-\beta E_n}$ are the corresponding thermal state probabilities, $Z = \mathrm{Tr}(e^{-\beta\hat{H}})$ the associated partition function, $\beta = 1/k_\mathrm{B}T$ with k_B being the Boltzmann constant and T is the temperature, the parameter we wish to estimate. Since, the temperature is not a direct observable its value can be extracted only by performing suitable measurements of other experimentally accessible observable. For this goal, consider a discrete set of measurements defined in terms of its corresponding positive-operator valued measure (POVM) $\{\hat{\Pi}_n\}$, with $\sum_n \hat{\Pi}_n = \mathbb{I}$. The corresponding classical Fisher information (CFI) which quantifies the amount of information on the temperature of the system is given by

$$F_\mathrm{C}(T) = \sum_n \frac{\left(\partial_T P_n(T)\right)^2}{P_n(T)}, \tag{12.1}$$

where $P_n(T) = \mathrm{Tr}(\hat{\Pi}_n\hat{\rho}_T)$ is the probability to get outcome n from the performed measurement. Furthermore, the variance δT of the temperature estimator is bounded by the Cramér-Rao inequality

$$\delta T \geq \frac{1}{\sqrt{\nu F_\mathrm{C}(T)}}, \tag{12.2}$$

where ν is the experimental repetitions.

The optimal strategy to measure the value of the temperature is however associated with a privileged observable which maximize the CFI and thus allows to determine the temperature with ultimate precision. Indeed, it is possible to show that the CFI is upper bounded by $F_\mathrm{C}(T) \leq F_\mathrm{Q}(T)$, where $F_\mathrm{Q}(T) = \mathrm{Tr}(\hat{\rho}_T\hat{L}^2)$ is the quantum Fisher information (QFI). Here $\hat{L}$ is the symmetrical logarithmic derivative (SLD) operator, which satisfies the operator equation $\partial_T\hat{\rho}_T = (\hat{\rho}_T\hat{L} + \hat{L}\hat{\rho}_T)/2$. Thus, the ultimate achievable precision of the temperature determination, optimized over all possible measurements is quantified by the quantum Cramér-Rao bound

$$\delta T \geq \frac{1}{\sqrt{\nu F_\mathrm{Q}(T)}}. \tag{12.3}$$

The eigenstates of the SLD operator $\hat{L}$ define the optimal measurement basis in which the quantum Cramér-Rao bound can be saturated. It is straightforward to show that for a Gibbs state with $\hat{\rho}_T$ the SLD operator can be written as $\hat{L} = \sum_n\{(E_n - \langle\hat{H}\rangle)/T^2\}|n\rangle\langle n|$, where $\langle\hat{H}\rangle = \mathrm{Tr}(\hat{H}\hat{\rho}_T)$ is the average energy [257].

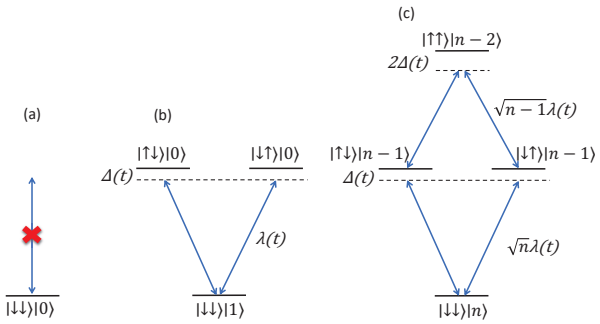

Fig. 12.1: Linkage pattern of the collective states of a string of two ions driven by red-sideband laser. Spins are initially prepared in their electronic ground state and the vibration center-of-mass mode is in thermal states. a) The state $|\downarrow\downarrow\rangle|0\rangle$ is not affected by the collective red-sideband interactions. b) and c) The states $|\downarrow\downarrow\rangle|1\rangle$ and $|\downarrow\downarrow\rangle|n\rangle$ $(n > 1)$ are coupled to the manifolds with the same number of total excitations.

The result emphasizes that the optimal temperature measurement is achieved in the Fock basis $|n\rangle$ of the harmonic oscillator, e.g., by measuring the probabilities p_n. Finally, the QFI for the harmonic oscillator at thermal equilibrium can be written as

$$F_{\mathrm{Q}}(T) = \frac{\hbar^2\omega^2}{4k_{\mathrm{B}}^2T^4}\mathrm{csch}^2\left(\frac{\hbar\omega}{2k_{\mathrm{B}}T}\right). \tag{12.4}$$

A question that arises is whether it is possible to saturate the fundamental quantum Cramér-Rao bound by performing different set of discrete measurements rather than measurements of the thermal state probabilities. For this goal we consider an auxiliary quantum system of N spin-1/2 particles which interacts coherently with the quantum harmonic oscillator. Using time-dependent unitary evolution one can map the information of the temperature into the respective spin state populations. We show that performing single-shot state projection measurements one can saturate the fundamental quantum Cramér-Rao bound and thus determine the temperature with the ultimate precision given by Eq. (12.3).

12.0.3 Ion Trap Realization of Quantum Thermometry

We discuss in the following the ion trap based quantum thermometer which is able to perform an optimal measurement of the phonon temperature by detecting the ions' spin populations. We consider a linear ion crystal of N ions confined in a Paul trap along the z axis with trap frequencies ω_χ $(\chi = x, y, z)$. We assume that the transverse frequencies are much larger than the axial trap frequency $\omega_{x,y} \gg \omega_z$ which leads to the formation of a linear ion crystal where the ions occupy equilibrium positions z_k^0 along the trap axis. The position operator of the lth ion can be expressed as $\hat{r}_l = \delta\hat{r}_{x,l}\vec{e}_x + \delta\hat{r}_{y,l}\vec{e}_y + (z_l^0 + \delta\hat{r}_{z,l})\vec{e}_z$,

where $\delta\hat{r}_{\chi,l}$ are the displacement operators around the ion's equilibrium positions, which can be written in terms of collective phonon modes as $\delta\hat{r}_{\chi,l} = \sum_{k=1}^{N} M_{l,k}^{\chi}\sqrt{\frac{\hbar}{2m\omega_{\chi,k}}}(\hat{a}_{\chi,k}^{\dagger} + \hat{a}_{\chi,k})$. Here $\hat{a}_{\chi,k}^{\dagger}$ and $\hat{a}_{\chi,k}$ are the creation and annihilation operators of the collective phonons with frequency $\omega_{\chi,k}$ along the spatial direction χ. The element $M_{l,k}^{\chi}$ is the amplitude of the normal mode k on ion l. We assume that each ion has two metastable internal levels $|\downarrow\rangle$ and $|\uparrow\rangle$ with a transition frequency ω_0. Then, the interaction-free Hamiltonian describing the linear ion crystal is given by

$$\hat{H}_0 = \hbar\omega_0\hat{S}_z + \hbar\sum_{k=1}^{N}\sum_{\chi=x,y,z}\omega_{\chi,k}\hat{a}_{\chi,k}^{\dagger}\hat{a}_{\chi,k}, \tag{12.5}$$

where $\hat{S}_z = \frac{1}{2}\sum_{l=1}^{N}\sigma_l^z$ and $\hat{S}^{+} = \sum_{l=1}^{N}\sigma_l^{+}$ ($\hat{S}^{-} = (\hat{S}^{+})^{\dagger}$) are the collective spin operators with σ_l^z being the Pauli operator for the lth spin and respectively $\sigma_l^{+} = |\uparrow_l\rangle\langle\downarrow_l|$ is the spin raising operator.

After performing a Doppler cooling of the linear ion crystal each collective vibrational mode is in a thermal state of motion with mean thermal phonon excitation $\bar{n}_{\chi,k}$. Since the oscillations of the ions in all three directions are decoupled one can determine the temperature of each vibrational mode independently [252]. For concreteness we consider the temperature estimation of the collective center-of-mass mode along the spatial transverse direction x. This mode has the highest vibrational frequency $\omega_{x,1} = \omega_x$ in which the ions oscillate in phase with equal amplitude. The total Hilbert space is spanned by the basis $\{|S,m\rangle\otimes|n\rangle\}$ where $|n\rangle$ is the Fock state of the center-of-mass vibrational mode with n phonons. The states $|S,m\rangle$ are the eigenvectors of the two commuting operators $\hat{S}^2|S,m\rangle = S(S+1)|S,m\rangle$ and $\hat{S}_z|S,m\rangle = m|S,m\rangle$ ($m = -S,\ldots,S$) with $S = \frac{N}{2}$. In the computational basis the state $|D_l\rangle = |S,-S+l\rangle$ with l spin excitations ($l = 0,1,\ldots,2S$) can be expressed as

$$|D_l\rangle = \sqrt{\frac{l!(2S-l)!}{2S!}}\sum_{x}P_x\,|\uparrow_1\ldots\uparrow_l\downarrow_{l+1}\ldots\downarrow_N\rangle\,, \tag{12.6}$$

where the sum subscript x runs over all distinct permutations P_x of the ions' internal states with l spins in excited state $|\uparrow\rangle$ and respectively $N-l$ in the ground state $|\downarrow\rangle$.

In order to create a coupling between the collective vibrations and the ion spin states we assume that the linear ion crystal is globally addressed by laser field with laser wave vector $\vec{k}$ pointing along the x direction ($|\vec{k}| = k_x$) and laser frequency $\omega_{\mathrm{L}}(t) = \omega_0 - \omega_x + \Delta(t)$ tuned near the center-of-mass red-sideband resonance with time-dependent detuning $\Delta(t)$ ($\omega_x \gg \Delta(t)$). After performing an optical rotating-wave approximation, the interaction Hamiltonian becomes

$$\begin{aligned}\hat{H}_I(t) \;=\; & \hbar\Omega(t)\sum_{l=1}^{N}\{\sigma_l^{+}e^{i(\sum_{k=1}^{N}\eta_{l,k}^{x}(\hat{a}_{x,k}^{\dagger}e^{i\omega_{x,k}t}+\hat{a}_{x,k}e^{-i\omega_{x,k}t})}\\ & \times e^{i(\omega_x t-\int_{t_i}^{t}\Delta(\tau)d\tau)} + \text{h.c.}\},\end{aligned} \tag{12.7}$$

where $\Omega(t)$ is the time-dependent Rabi frequency and $\eta^x_{l,k} = k_x\sqrt{\frac{\hbar}{2m\omega_{x,k}}}M^x_{l,k}$ is the Lamb-Dicke parameter. Moreover, since the laser field frequency is close to the red-sideband resonance of the center-of-mass mode one can perform vibrational rotating-wave approximation, in which the contribution of the other spectator phonon modes is neglected. Transforming the Hamiltonian in the rotating-frame with respect to $\hat{U}_{\rm R} = e^{i\int_{t_i}^{t}\Delta(\tau)d\tau\hat{S}_z}$ such that $\hat{H}_{\rm JC}(t) = \hat{U}_R^\dagger\hat{H}_I(t)\hat{U}_R - i\hbar\hat{U}_R^\dagger\partial_t\hat{U}_R$, we arrive to

$$\hat{H}_{\rm nJC}(t) = \hbar\Delta(t)\hat{S}_z + \hbar\lambda(t)(\hat{S}^+\hat{F}(\hat{n})\hat{a} + \hat{S}^-\hat{a}^\dagger\hat{F}(\hat{n})), \tag{12.8}$$

where $\lambda(t) = \Omega(t)\eta^x_{l,1}$ is the time-dependent spin-phonon coupling and $\eta^x_{l,1} = \eta$ being the Lamb-Dicke parameter for the center-of-mass vibrational mode and $\hat{a}^\dagger$ and $\hat{a}$ are respectively the phonon creation and annihilation operators corresponding to an oscillator with frequency ω_x. The Hamiltonian (12.8) describes the non-linear Jaynes-Cummings (nJC) model, where the non-linear operator function can be expressed as

$$\hat{F}(\hat{n}) = e^{-\eta^2/2}\sum_{n=0}^{\infty}\frac{(-\eta^2)^n}{n!(n+1)!}\hat{a}^{\dagger n}\hat{a}^n. \tag{12.9}$$

Assuming the Lamb-Dicke limit $\eta\langle(\hat{a}^\dagger+\hat{a})^2\rangle^{1/2} \ll 1$ in which the amplitudes of oscillations of the ions around their equilibrium positions are small compared to optical wavelength one can approximate the Hamiltonian (12.8) to

$$\hat{H}_{\rm JC}(t) = \hbar\Delta(t)\hat{S}_z + \hbar\lambda(t)(\hat{S}^+\hat{a} + \hat{S}^-\hat{a}^\dagger), \tag{12.10}$$

which describes the linear Jaynes-Cummings (JC) model. We note that the Lamb-Dicke approximation is justified for low temperatures and small $\eta \ll 1$. However, with increasing temperature one would need to consider the nJC Hamiltonian (12.8) as the effect of the non-linear term (12.9) becomes significant.

Since the collective spin excitation can be created (annihilated) by absorption (emission) of collective center-of-mass phonon, the linear as well as the non-linear Jaynes-Cummings Hamiltonian commutes with the operator of the total number of excitations defined by $\hat{N} = \hat{S}_z + \hat{a}^\dagger\hat{a}$. Consequently, the Hilbert space is decomposed into the subspaces with well defined total number of excitations $N = n_{\rm s} + n$ with $n_{\rm s} = 0, 1, \ldots, 2S$ being the number of spin excitations.

Temperature sensing protocol

The temperature estimation scheme begins by preparing the system initially in the product state $\hat{\rho}_i = \hat{\rho}_{\rm spin}\otimes\hat{\rho}_{\rm th}$ where $\hat{\rho}_{\rm th} = \sum_{n=0}^{\infty}p_n\left|n\right\rangle\left\langle n\right|$ is the thermal state density operator for the center-of-mass mode with $p_k = \frac{\bar{n}^k}{(1+\bar{n})^{k+1}}$ and $\bar{n} = (e^{\beta\hbar\omega_x}-1)^{-1}$ being the average number of thermal excitations. We assume that the spins are initially polarized along the z-direction in a pure state with density matrix $\hat{\rho}_{\rm spin} = \left|D_0\right\rangle\left\langle D_0\right|$. Therefore, the initial total number of

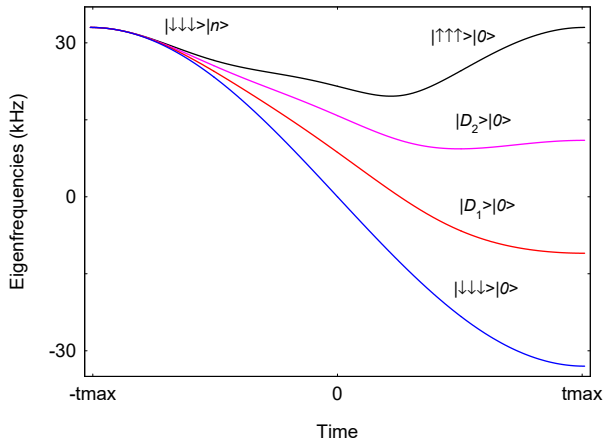

Fig. 12.2: Lowest eigenfrequencies of Hamiltonian (12.10) for three spins and for different phonon number n as a function of time. We assume time-dependent detuning and spin-phonon coupling are given by Eq. (12.13). In the adiabatic limit each of the initial states $|\psi_n(t_i)\rangle = |\downarrow\downarrow\downarrow\rangle\,|n\rangle$ $(n = 0, 1, 2, 3)$ is transformed into $|\psi_n(t_i)\rangle \to |D_n\rangle|0\rangle$.

excitations is determined by the number of center-of-mass phonons n, namely $N = n$ $(n = 0, 1, 2, \ldots)$. Then the system evolves according the time-dependent red-sideband interaction such that the relevant temperature information is distributed over and stored in the collective spin degrees-of-freedom. In Fig. 12.1 the linkage pattern of the collective states of linear crystal of two ions is shown where for concreteness we assume linear JC interaction described by Hamiltonian (12.10). As it can be seen a collective spin excitation can be only created by the annihilation of center-of-mass phonon and vice versa. Thus the motional ground state is not affected by the red-sideband interaction, while states with $n > 0$ phonons are coupled to the manifolds with the same number of total excitations. Since we deal with thermal motional states each of these three independent transitions is realized with probability p_n.

Adiabatic Transition

Our goal is to determine the probabilities p_n to observe a Fock state $|n\rangle$ by execute a projection spin-dependent measurements. First, we emphasize that due to the off-resonant transitions the application of π laser pulse is not capable to distinguish the probabilities p_n by measuring the spin population. For this reason we adopt the adiabatic technique for detecting p_n which is slower in time but more robust with respect to parameter fluctuation. In Fig. 12.2 we show the lowest eigenfrequencies of Hamiltonian (12.10) for three spins and different phonon numbers $(n = 0, 1, 2, 3)$. Assume that at the initial moment the laser detuning is much higher than the spin-phonon coupling, $|\Delta(t_i)| \gg \lambda(t_i)$ and $\Delta(t_i) < 0$. Then the state vectors $|\psi_n(t_i)\rangle = |D_0\rangle\,|n\rangle$ are an eigenstates

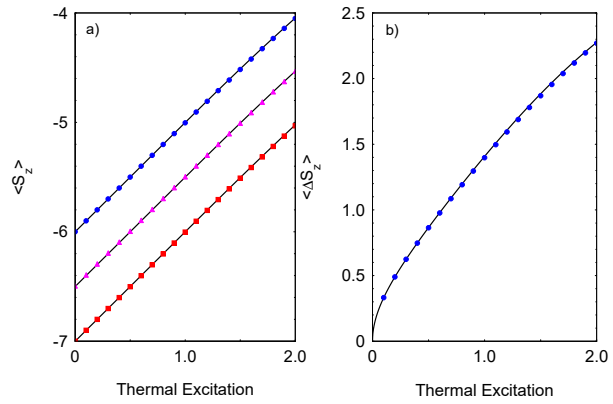

Fig. 12.3: a) Average $\langle \hat{S}_z \rangle$ at $t_{\max}$ as a function of the thermal phonon excitation. We compare the numerical result derived from the Hamiltonian $\hat{H}_{\rm JC}$ with the analytical solution (12.14) (solid line) for $S = 6$ (blue circles), $S = 13/2$ (purple triangles) and $S = 7$ (red squares). The other parameters are set to $\lambda_0/2\pi = 5$ kHz, $\Delta_0/2\pi = 22$ kHz, and $\gamma/2\pi = 5.5$ kHz. b) The variance $\Delta\hat{S}_z$ at $t_{\max}$ for $S = 6$. The blue circles are the exact solution and the solid line is the analytical expression (12.15).

of Hamiltonian (12.10) such that $\hat{H}_{\rm JC}(t_i)\,|\psi_n(t_i)\rangle = -S\Delta(t_i)\,|\psi_n(t_i)\rangle$. Adiabatically varying the detuning $\Delta(t)$ such that we end up with $\Delta(t_f) \gg \lambda(t_f)$ and $\Delta(t_f) > 0$. In the adiabatic limit, the system remains in the same eigenstate of the Hamiltonian (12.10) at all times. Since the total number of excitations is preserved the initial state $|\psi_n(t_i)\rangle$ is adiabatically transformed into the final state $|\psi_n(t_f)\rangle = |D_l\rangle|0\rangle$ where we assume $n \leq 2S$ and $n = l$ emphasizing that the initial number of phonons is transferred into the collective spin excitations. Since the maximal number of spin excitations is $n_{\rm s} = 2S$ in which all spins are in the excited levels, the initial state $|\psi_n(t_i)\rangle$ with $n > 2S$ adiabatically evolves into $|\psi_n(t_f)\rangle = |D_{2S}\rangle|n - 2S\rangle$. Therefore, for a state with N spins and thermal motion state this implies the following transition

$$\hat{\rho}_i \to \hat{\rho}_f = \sum_{l=0}^{2S} p_l |D_l\rangle\langle D_l| \otimes |0\rangle\langle 0| + \hat{\rho}_{\rm res}. \tag{12.11}$$

Hence, the maximally mixed thermal motion state is adiabatically transformed into the maximally mixed spin state in which one can observe state $|D_l\rangle$ with probability p_l. Finally, the residual density matrix in (12.11) is given by

$$\hat{\rho}_{\rm res} = |D_{2S}\rangle\langle D_{2S}| \otimes \sum_{n=2S+1}^{\infty} p_n |n - 2S\rangle\langle n - 2S|. \tag{12.12}$$

A convenient choice of the time-dependent detuning and spin-boson cou-

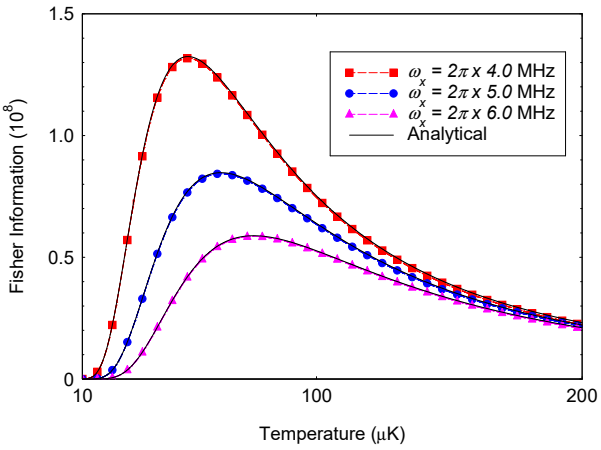

Fig. 12.4: Classical Fisher information for the observables $P_{s_1,\ldots,s_N}$ at $t_{\max}$ as a function of the temperature for ion chain with four ions. The numerical result for different transverse trap frequencies ω_x is compared with the QFI (12.4) (solid lines). The other parameters are set to $\lambda_0/2\pi = 5$ kHz, $\Delta_0/2\pi = 25$ kHz, and $\gamma/2\pi = 5.5$ kHz.

pling, which can be used to drive the adiabatic transition, is

$$\Delta(t) = \Delta_0 \sin\left(\frac{\gamma t}{2}\right), \quad \lambda(t) = \lambda_0 \cos^2\left(\frac{\gamma t}{2}\right), \tag{12.13}$$

where $\Delta_0 > 0$, $\lambda_0 > 0$ and γ is a characteristic parameter which controls the adiabaticity of the transition. The interaction time varies as $t \in [-t_{\max}, t_{\max}]$ with $t_{\max} = \pi/\gamma$ which ensures that $|\Delta(-t_{\max})| \gg \lambda(-t_{\max})$ and respectively $\Delta(t_{\max}) \gg \lambda(t_{\max})$.

In Fig. 12.3(a) we show the exact result for the average spin magnetization $\langle \hat{S}_z(t_f)\rangle = \mathrm{Tr}(\hat{\rho}_f \hat{S}_z)$ compared with the analytical result given by

$$\langle \hat{S}_z(t_f)\rangle = \bar{n} - S - \left(\frac{\bar{n}}{1+\bar{n}}\right)^{2S+1} (\bar{n} + S + 1), \tag{12.14}$$

where very good agreement is observed. We see that the time-dependent red-sideband interaction rotates the initial spin magnetization which varies with the thermal phonon excitations and thus the observable $\langle \hat{S}_z(t_f)\rangle$ can be used for detecting the temperature. Indeed, the shot-noise limited sensitivity in the temperature estimation from the measured signal $\langle \hat{S}_z(t_f)\rangle$ is given by the error propagation formula $\delta T^2 = (\nu F_{S_z})^{-1}$ where $F_{S_z} = \frac{1}{\langle \Delta \hat{S}_z\rangle^2}\left(\frac{\partial \langle \hat{S}_z\rangle}{\partial T}\right)^2$ is the fidelity susceptibility and $\langle \Delta \hat{S}_z\rangle^2 = \langle \hat{S}_z^2\rangle - \langle \hat{S}_z\rangle^2$ is the variance of $\hat{S}_z$. Using

(12.11) it is straightforward to show that (see Fig. 12.3(b))

$$\langle \Delta \hat{S}_z(t_f)\rangle^2 = \frac{\bar{n}}{(1+\bar{n})^{4S+2}}\{(1+\bar{n})^{4S+3} - \bar{n}^{4S+1}(1+S+\bar{n})^2 - \bar{n}^{2S}(1+\bar{n})^{2S+1}[1+\bar{n}+S(4+3S+2\bar{n})]\}. \quad (12.15)$$

However, a more convenient approach for temperature estimation is to detect the spin populations $P_{s_1,\ldots,s_N} = \mathrm{Tr}(\hat{\rho}_f \hat{\Pi}_{s_1,\ldots,s_N})$, where $\hat{\Pi}_{s_1,\ldots,s_N} = |s_1,\ldots,s_N\rangle\langle s_N,\ldots,s_1|$ is the projection operator with $s_l = \uparrow_l, \downarrow_l$. Indeed, the magnetization of each spin after the adiabatic transition can be measured by illuminating the ions with a global laser radiation and collecting the state-dependent fluorescence on a camera.

In Fig. 12.4 we show the exact result for the CFI (12.1) for the spin probabilities $P_{s_1,\ldots,s_N}$ compared with the QFI (12.4). We see that the CFI associated with the observables $P_{s_1,\ldots,s_N}$ is equal to the QFI (12.4) for quantum harmonic oscillator at thermal equilibrium. Therefore, the detection of the orientation of each spin is optimal for the temperature estimation in the sense that the temperature uncertainty is bounded by the quantum Cramér-Rao bound (12.3). In Fig. 12.5 it is shown comparison between the numerical result for the CFI and the QFI (12.4) for different number of ions and high temperature. As the mean thermal phonon excitation increases the residual density matrix term $\hat{\rho}_{\mathrm{res}}$ (12.12) limits temperature sensitivity. Indeed, the probability to observe a collective state with all spins in the excited levels is not equal to p_{2S} but other highly excited thermal phonon states with probabilities p_n ($n > 2S$) are also contributed, which spoil the optimal temperature estimation. However, as we can see from the Fig. 12.5 the effect of the residual term can be suppressed by increasing the number of ions. Indeed, for higher number of ions the probability to observe all spins in the excited states after the adiabatic transition becomes negligibly small, so that the effect of the residual term $\hat{\rho}_{\mathrm{res}}$ can be suppressed which ultimately improves the temperature sensitivity.

Finally, we point out that the optimal temperature estimation of other vibrational modes can be carried out by individual addressing each ion. Indeed, laser addressing of the other vibrational modes leads to a site-dependent coupling between the ion states and the respective phonon mode. This will affect the adiabatic transition which relies on the collective nature of the spin-phonon coupling. However, depending on the mode shape one can address locally each ion such that by tuning the relative amplitude of each individual laser it is possible to produce Hamiltonian (12.10).

In the following we examine the effect of the non-adiabatic transitions which limit the efficiency of the temperature determination. We discuss the red-sideband interaction beyond the Lamb-Dicke approximation by including the non-linear terms (12.9), which becomes significant in the high temperature limit. Since the nJC Hamiltonian (12.8) preserves the total number of excitations the adiabatic transition (12.11) still holds. We show that the effect of the non-linear terms is merely to modify the adiabaticity of the transition.

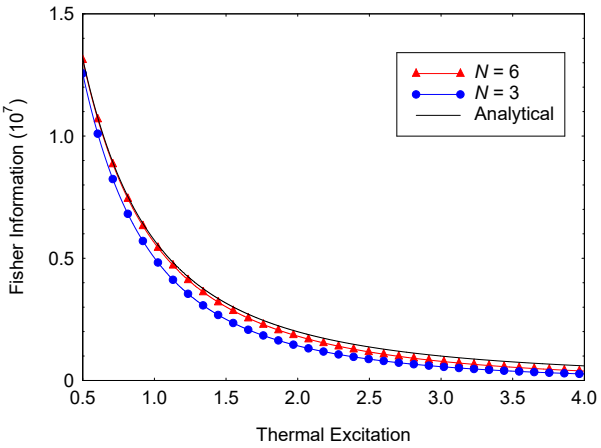

Fig. 12.5: Classical Fisher information as a function of the thermal phonon excitation $\bar{n}$. The numerical result for $\omega_x/2\pi = 6$ MHz and different number of ions is compared with the analytical expression for QFI (12.4) (solid line).

12.0.4 Physical Imperfections

As a figure of merit for the efficiency of the adiabatic transition we use the fidelity between two density matrices defined by

$$F(\hat{\rho}_f, \hat{\rho}(t)) = \frac{\mathrm{Tr}(\hat{\rho}_f \hat{\rho}(t))}{\sqrt{\mathrm{Tr}(\hat{\rho}_f^2)\mathrm{Tr}(\hat{\rho}(t)^2)}}. \tag{12.16}$$

Here $\hat{\rho}_f$ is the desired density matrix (12.11) and $\hat{\rho}(t)$ is the actual one. In Fig. 12.6(a) we show the numerical result for the fidelity (12.16) as a function of the controlling parameter γ using the nJC Hamiltonian (12.8). As the temperature increases the Lamb-Dicke approximation is not fulfilled and thus one needs to include the high-order terms in the Lamb-Dicke expansion given by Eq. (12.9). We observe that on one hand the non-adiabatic transitions become stronger for higher values of $\bar{n}$ and the fidelity decreases slightly when $\bar{n}$ increases toward high temperature limit. On the other hand the adiabaticity is improved for lower value of γ and thus longer interaction time. For example, assuming the mean thermal phonon excitations $\bar{n} = 15$ and $\gamma/2\pi = 2.4$ kHz such that the total interaction time is $\tau = 2t_{\max} \approx 417$ μs, we estimate fidelity $F(\hat{\rho}_f, \hat{\rho}(t_{\max})) > 0.99$. Increasing the interaction time improves the fidelity until the random noise compromises the signal. For example, the electric fluctuations of the trap electrodes affect the motional phonon population during the adiabatic transition. Consider heating rate $\langle \dot{n} \rangle = 1/t_{\mathrm{dec}}$, where t_{dec} is the characteristic decoherence time we require $t_{\mathrm{dec}} \gg \tau$. For heating rate of 0.1 ms^{-1}, which corresponds to typical heating rate in linear ion Pual traps and interaction time of order of $\tau \approx 0.4$ ms this condition is satisfied. Other possible source of errors are spontaneous spin flip from the excited state during the adiabatic transition and magnetic field

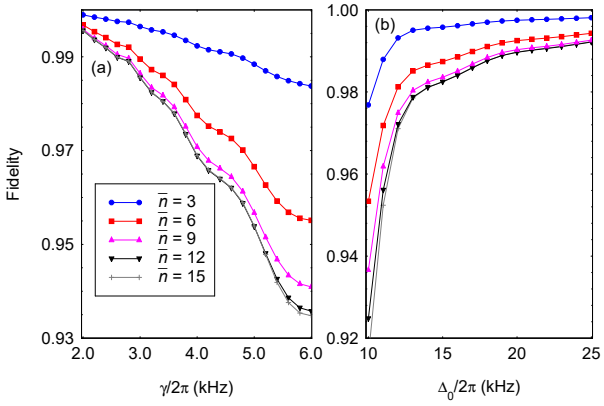

Fig. 12.6: (a) Fidelity (12.16) at $t_{\max}$ for different characteristic rate γ. We integrate numerically the Liouville equation with Hamiltonian (12.8). The other parameters are set to $\lambda_0/2\pi = 5$ kHz, $\Delta_0/2\pi = 22$ kHz, $\eta = 0.2$ and $N = 6$. (b) The same but we vary the detuning Δ_0 for $\gamma/2\pi = 2.5$ kHz.

fluctuations which cause spin dephasing. Usually the spontaneous decay of the upper level takes too long time of order of 1 s and thus it can be neglected. The coherence time is often limited by ambient magnetic field fluctuations which can be suppressed by using magnetic field insensitive transitions.

In Fig. 12.6(b) we show the fidelity as a function of the detuning Δ_0 and for fixed γ. On one hand, as can be seen by increasing Δ_0 the adiabaticity of the transition is improved which leads to higher fidelity. On the other hand in order to resolve the vibrational center-of-mass mode the energy splitting to the energetically nearest rocking mode with frequency $\omega_{\rm roc} = \sqrt{\omega_x^2 - \omega_z^2}$ has to be sufficiently large compared to the spin-phonon coupling λ_0 and laser detuning Δ_0, namely $\Delta_{\rm gap} \gg \lambda_0, \Delta_0$ where $\Delta_{\rm gap} = \omega_x - \omega_{\rm roc}$. Increasing the number of ions however makes the vibrational modes closer, such that the laser addressability of the center-of-mass mode imposes a restriction on N. Moreover, for given aspect ratio ω_z/ω_x there is a maximal number of ions for which the system undergoes structural phase transition to a zigzag configuration. Thus the energy gap scales with the number of ions as $\Delta_{\rm gap}/\omega_x \approx 0.6228\ln(6N)/N^2$. Consider $N = 12$ and $\omega_x/2\pi = 8$ MHz we find $\Delta_{\rm gap}/2\pi \approx 148$ kHz. For $\gamma/2\pi = 2.3$ kHz, $\bar{n} = 6$ and $\Delta_0/2\pi = 15$ kHz we estimate fidelity $F(\hat{\rho}_f, \hat{\rho}(t_{\max})) > 0.99$.

12.0.5 Detection of the relative phase of the coherent cat state

Let us extend the discussion by considering various initial motion states. In Fig. 12.7(a) we show the time-evolution of the collective spin populations $P_{D_l}(t) = {\rm Tr}(|D_l\rangle\langle D_l|\hat{\rho}(t))$ for initial state $\hat{\rho}_i = |D_0\rangle\langle D_0| \otimes \hat{\rho}_\alpha$ where $\hat{\rho}_\alpha = |\alpha\rangle\langle\alpha|$ is the coherent density operator with Fock state distribution given by $p_n = e^{-|\alpha|^2}|\alpha|^{2n}/n!$. The adiabatic evolution drives the system into the final density matrix given by Eq. (12.11) such that at $t_{\max}$ the collective spin probabilities are equal to

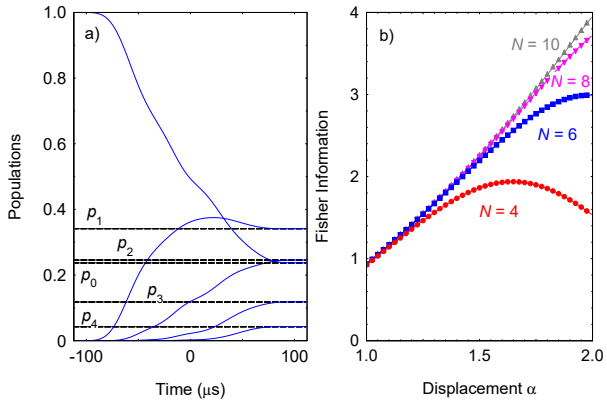

Fig. 12.7: (a) First four collective spin populations $P_{D_l}(t)$ (blue solid lines) as a function of time for ion chain with six ions. We assume that the system is prepared in motion coherent state with density matrix operator $\hat{\rho}_\alpha = |\alpha\rangle\langle\alpha|$ with $\alpha = 1.2$ and coherent Fock state distribution $p_n = e^{-|\alpha|^2}|\alpha|^2/n!$ (dashed lines). Approaching $t_{\max}$ the collective spin populations are equal to $P_{D_l}(t_{\max}) = p_l$. The parameters are set to $\lambda_0/2\pi = 5$ kHz, $\Delta_0/2\pi = 20$ kHz and $\gamma/2\pi = 4.5$ kHz b) Classical Fisher information for the estimation very weak force ϵ for initial coherent cat state as a function of the displacement amplitude α. The spin observables are measured at $t_{\max}$. We numerically integrate the Liouville equation with Hamiltonian (12.10) for different number of ions. The other parameters are set to $\Delta_0/2\pi = 22$ kHz and $\gamma/2\pi = 2.2$ kHz.

$P_{D_l}(t_{\max}) = p_l$. Thus, the relevant information of the magnitude of the displacement amplitude is mapped onto the collective spin-excitations and thereby it can be measured by detecting the spin populations at the end of the adiabatic transition. Furthermore, our adiabatic technique can be applied also for detecting the relative phase of the coherent cat state. Consider a motional density matrix $\hat{\rho}_{\rm cat} = |\psi_{\rm cat}\rangle\langle\psi_{\rm cat}|$, where $|\psi_{\rm cat}\rangle = (|\alpha\rangle + |-\alpha\rangle)/\sqrt{2}$ is a coherent cat state ($\alpha \gg 1$) such that we have $\hat{\rho}_i = |D_0\rangle\langle D_0| \otimes \hat{\rho}_{\rm cat}$. We assume that a time-varying force is applied which is on resonance with the frequency of the center-of-mass mode. The effect of the force is to displace a small motion amplitude with $\hat{D}(\epsilon) = e^{i\epsilon(\hat{a}^\dagger - \hat{a})}$ where ϵ is the parameter we wish to estimate. The information of ϵ ($\epsilon \ll 1$) is imprinted in the relative phase of the coherent cat state, namely $|\psi_{\rm cat}\rangle \approx (e^{i\theta}|\alpha\rangle + e^{-i\theta}|-\alpha\rangle)/\sqrt{2}$, where $\theta = \alpha\epsilon$ [153]. Then the system evolves according the time-dependent detuning $\Delta(t)$ and spin-phonon coupling $\lambda(t)$ (12.13) such that the relevant phase information is encoded in the collective spin populations which are measured at $t_{\max}$. In Fig. 12.7(b) we show the numerical result for the CFI for estimating ϵ as a function of the initial displacement amplitude α and for different number of ions. Crucially, using a coherent cat state, the precision in estimating ϵ grows quadratically with α which corresponds to a Heisenberg limit, namely $\delta\epsilon^2 \geq 1/\alpha^2$ [153]. As is shown in Fig. 12.7(b) increasing α results in more phonon states being populated which in turn requires the increase of the number of ions.

12.0.6 Conclusions

We have proposed an efficient adiabatic method for temperature measurement with trapped ions which can be operated beyond the Lamb-Dicke limit. The technique is based on an adiabatic evolution which transfer the relevant phonon temperature information onto the spin populations which can be measured by state-dependent fluorescence at the end of the adiabatic transition with high efficiency. We have characterized the amount of temperature information which can be extracted for such a spin detection in terms of classical Fisher information. We have shown that the state-projection measurements lead to equality between the classical and quantum Fisher information for harmonic oscillators at thermal equilibrium. Thus the temperature is determined with ultimate precision given by the quantum Cramér-Rao bound.

Furthermore, we have discussed the application of our method for the detection of the relative phase of the coherent cat state. Such a phase can be generated by the application of very weak time-varying force which displaces the initial motional coherent cat state. We have shown that by executing a state projective measurement one can determine the unknown displacement with Heisenberg limited precision.

13. QUANTUM CHAOS IN QUANTUM OPTICAL SYSTEMS

In this chapter we investigate signatures of chaos and equilibration in quantum Rabi models, which exhibits a quantum phase transition when the ratio of the atomic level-splitting to bosonic frequency grows to infinity. We show that out-of-time-order correlator derived from the Loschmidt echo signal quickly saturates in the normal phase and reveals exponential growth in the superradiant phase which is associated with the onset of quantum chaos. Furthermore, we show that the effective time-averaged dimension of quantum Rabi model can be large compared to the spin system size which leads to suppression of the temporal fluctuations and equilibration of the spin system.

13.0.1 Motivation

The quantum Rabi (QR) model is one of the simplest and most fundamental models describing quantum light-matter interaction. It consists of a single bosonic field mode and an effective spin system which interact via dipolar coupling [267]. Various quantum-optical regimes of the QR model have been studied, including the ultra-strong coupling and deep strong coupling regimes, where the coupling strength is comparable to or larger than the bosonic mode frequency [268, 269]. Recently, it was shown that the QR model exhibits a finite-size quantum phase transition when the ratio of level-splitting Δ to bosonic frequency ω grows to infinity $\eta = \Delta/\omega \to \infty$ [270]. The latter corresponds to the classical oscillator limit $\omega \to 0$ that also unveils a finite-size criticality in its generalized

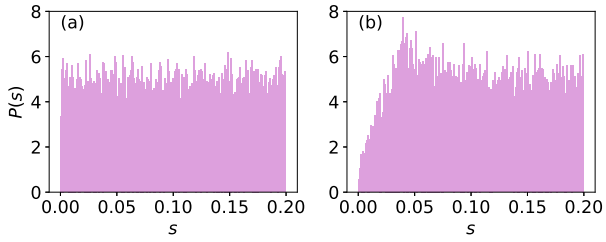

Fig. 13.1: Distribution $p(s)$ of the nearest-neighbor energy spacing $s_n = E_{n+1} - E_n$ for the QR model with Hamiltonian (13.1). (a) Normal phase with spin-boson copling $g = 3$. (b) Superradiant phase with $g = 7$. The other parameters are set to $\eta = 200$ with critical coupling $g_c = 5$. The bosonic Hilbert space is truncated at $n_{\max} = 120000$.

counterpart of N two-level systems, the Dicke model [271]. The second-order quantum phase transition in the QR model occurs at a critical spin-boson interaction strength $g = g_c$ between a normal $g < g_c$ and a superradiant phase $g > g_c$. The recent experimental realization of such a quantum phase transition in a trapped-ion system opened fascinating prospects for exploring critical behaviour in finite-size quantum optical systems [272].

Critical behaviour in quantum many-body systems has been associated with the onset of chaos [274, 275, 277, 273, 276]. In light of this we investigate signatures of chaos in the QR model as we approach the effective thermodynamic limit $\eta \to \infty$. One such measure is the nearest-neighbour level-spacing distribution of the Hamiltonian eigenenergies. While for non-chaotic systems we expect a Poissonian distribution [278], the onset of chaos is associated with a crossover to Wigner-Dyson statistics, as described by Random Matrix Theory [279]. We show that neither of these distributions is observed in the QR model, due to it being finite-size [280], however, the spectrum exhibits level-crossings in the normal phase and level-repulsions in the superradiant phase, the latter being associated with chaotic behaviour of non-integrable systems.

Furthermore, we use a double commutator out-of-time-order correlation function (OTOC) which measures the scrambling of quantum information across the system's degrees of freedom [281]. The OTOC is presented as an indicator of quantum chaos, with its growth rate being associated with the classical Lyapunov exponent [282, 283, 284]. Moreover, the OTOC has been measured in a system of trapped ions [285, 286, 287, 288] and in a nuclear magnetic resonance quantum simulator [289]. Recently, the thermally averaged OTOC with infinite temperature has been studied in quantum Rabi and Dicke models [290]. Here we explore the OTOC derived from the Loschmidt echo signal [291] to study the variance of an observable under imperfect time reversal. We show that in the normal phase the OTOC quickly saturates to a value independent of η. In the superradiant phase, however, it displays *exponential growth* which becomes larger as η is increased and allows for numerical extraction of the Lyuapunov exponent $\lambda_Q(g, \omega, \Delta)$ [292, 293, 294, 295]. We find that the relation $\lambda_Q t^* \sim \log \eta$, that is characteristic of chaotic systems with a classical limit of $1/\eta \sim \omega \to 0$ [296], holds for the QR model, with $t^*(g, \omega, \Delta)$ being the saturation time of the OTOC. Similarly, $\lambda_Q t^* \sim \log N$ has been proven to hold for a variety of quantum many-body systems [297, 277, 298, 299]. Moreover, we find similar exponential growth of the OTOC in other non-integrable critical quantum systems such as perturbed QR model and quantum Jahn Teller (QJT) model which indicates that the onset of chaos is closely related to the existence of a finite-size quantum phase transition.

Finally, we investigate the connection to equilibration and thermalization. We show that the long-time average of observables in the QR model relaxes to a value solely determined by the initial energy. We show that the observables of the QR model don't thermalize in general. However, we find a regime in which the effective dimension of the time-averaged density operator is larger than the spin system dimension which drives the spin system towards equilibrium [301, 302].

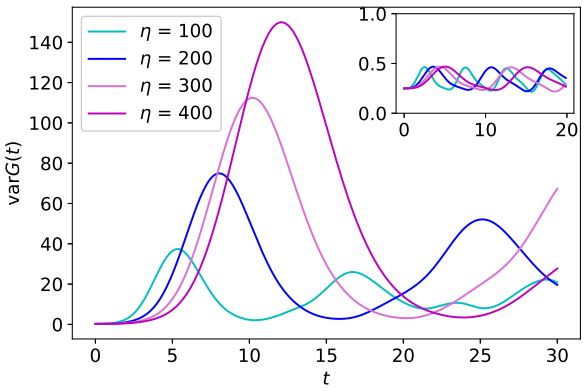

Fig. 13.2: Exact time-evolution of FOTOC for the QR model with Hamiltonian (13.1). We set $g_c = 5$, and vary η. In normal phase with $g = 4$ the FOTOC oscillates with amplitude independent of η (inset). In the superradiant phase with $g = 7$ the FOTOC exponentially grows with quantum Lyapunov exponent $\lambda_Q(g, \omega, \Delta)$ and saturation time t^*. The initial state is $|\psi_0\rangle = |+, 0\rangle$.

13.0.2 Quantum Rabi Model

Finite size quantum phase transition

The QR Hamiltonian is given by

$$\hat{H}_{\mathrm{QR}} = \omega \hat{a}^\dagger \hat{a} + \frac{\Delta}{2}\sigma_z + g\sigma_x(\hat{a}^\dagger + \hat{a}), \tag{13.1}$$

where Δ is the level-splitting of the two-level system and $\hat{a}^\dagger$, $\hat{a}$ are respectively the creation and annihilation operators of the bosonic mode, corresponding to an oscillator with frequency ω. The coupling g characterizes the strength of the dipolar spin-boson interaction. The QR model exhibits a finite-size quantum phase transition at the critical coupling $g_c = \sqrt{\Delta\omega}/2$ in the effective thermodynamic limit $\eta \to \infty$. The two phases of the system are a normal phase for $g < g_c$ characterized by zero mean-field bosonic excitations and polarized spin along the z-axis, and a superradiant phase for $g > g_c$ with non-zero magnetization along the x-axis and a macroscopically excited bosonic state [270, 272].

Level-spacing distribution

Usually the cross-over between integrable and chaotic behaviour in quantum systems is related to the change of energy level statistics from Poissonian $p_{\mathrm{P}}(s) = e^{-s}$ to the Wigner-Dyson distribution $p_{\mathrm{WD}}(s) = (\pi s/2)e^{-\pi s^2/2}$, which in random-matrix theory describes a chaotic system [279, 303]. In the core of this method lies the observation of level crossing for integrable systems and level repulsion for chaotic ones.

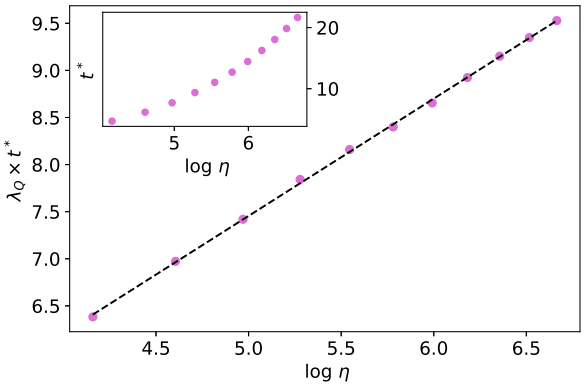

Fig. 13.3: Lyapunov exponent times the scrambling time $\lambda_Q(g, \omega, \Delta)t^*$ as a function of η. The parameters are set to $g = 6$, $g_c = 5$. The relation is well approximated by a logarithmic function $\lambda_Q(g, \omega, \Delta)t^* \sim \log \eta$ (dashed line). (Inset) Scrambling time t^* as a function of η in the superradiant phase.

In order to consider the level-spacing statistics of the QR model one needs to first unfold the energy spectrum, so that the resulting distribution includes only transitions within a subspace of states that is invariant under the parity transformation. In Fig. 13.1 we show the level statistics distribution for the QR Hamiltonian (13.1). Although the level statistics distribution is neither Wigner-Dyson nor Poissonian, if we focus on small scales for the energy difference s, one can see that the QR model indeed exhibits level crossing in the normal phase ($g < g_c$) and level-repulsions in the superradiant phase ($g > g_c$). The QR Hamiltonian was shown to have a regular spectrum and was deemed integrable in [148], however, the spacing between adjacent eigenenergies is dependent on ω, which in our effective thermodynamic limit tends to zero, thus indicating possible level-clustering as long as $\eta \to \infty$.

Furthermore, we investigate the level spacing distribution in the QJT model with Hamiltonian $\hat{H}_{\mathrm{JT}} = \hat{H}_{\mathrm{QR}} + \hat{H}_b$, where $\hat{H}_b = \omega \hat{b}^\dagger \hat{b} + g\sigma_y(\hat{b}^\dagger + \hat{b})$ which describes the U(1) symmetric interaction between a single spin and two bosonic modes [300]. To the best of our knowledge the QJT model is not integrable. Similarly to the QR model, the QJT model exhibits a finite-size quantum phase transition in the limit $\eta \to \infty$ between a normal phase and a U(1) symmetry-broken supperadiant phase. We observe neither Poissonian nor Wigner-Dyson nearest-neighbourgh distribution in both phases of the QJT system. However, focusing on a smaller scale for the energy difference, one can see that level-crossings are present in the normal phase, and level-repulsions in the supperradiant phase.

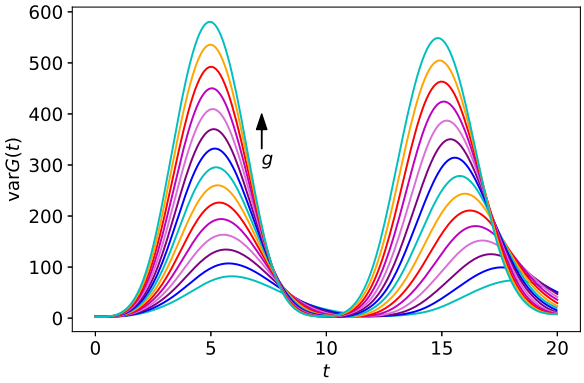

Fig. 13.4: Time evolution of the FOTOC for the QR model from the initial state $|\psi_0\rangle = |+, 5\rangle$. The coupling is varied from $g = 7$ to $g = 14$ in steps of 0.5, $\eta = 200$.

13.0.3 Fidelity out-of-time-order correlators

To further investigate signatures of chaos in QR model, we employ out-of-time-order correlation functions (OTOCs)

$$F(t) = \langle \hat{W}^\dagger(t)\hat{V}^\dagger\hat{W}(t)\hat{V}\rangle, \tag{13.2}$$

where the angular brackets denote averaging over the initial state $|\psi_0\rangle$. The OTOCs quantify the degree of non-commutativity in time between two initally ($t = 0$) commuting operators $[\hat{W}, \hat{V}] = 0$, whose time-evolution is governed by the system Hamiltonian as $\hat{W}(t) = e^{i\hat{H}t}\hat{W}e^{-i\hat{H}t}$. Moreover, it can be regarded as a natural extension of the idea of classical chaos via the correspondence between the phase space Poisson brackets and the commutator in quantum mechanics since $1 - \Re[F(t)] = \langle[\hat{V}^\dagger, \hat{W}^\dagger(t)][\hat{W}(t), \hat{V}]\rangle/2 \sim e^{\lambda_Q t}$, where λ_Q is a quantum Lyuapunov exponent, associated with the onset of chaos. In the following we choose $F(t)$ to be a fidelity OTOC (FOTOC) with the condition that the initial state $|\psi_0\rangle$ is an eigenstate of $\hat{V}$ and $\hat{W}_G = e^{i\delta\phi\hat{G}}$ for a Hermitian operator $\hat{G}$, where $\delta\phi$ is a small perturbation. Such a choice has been considered for studying the irreversibility of the dynamics in the Sachdev-Ye-Kitaev model due to imperfect time reversal [291], and for quantifying scrambling and quantum chaos in the Dicke model [277]. We choose $\hat{V}$ to be a projector on the initial state $\hat{V} = \hat{\rho}(0) = |\psi_0\rangle\langle\psi_0|$ where $|\psi_0\rangle = |+, 0\rangle$ ($\sigma_x |+, 0\rangle = |+, 0\rangle$). Note that alternatively one can set $\hat{V} = \sigma_x$. Since $\delta\phi$ is a small perturbation one can expand the FOTOC $F_G(t) = \langle \hat{W}_G^\dagger(t)\hat{\rho}(0)\hat{W}_G(t)\hat{\rho}(0)\rangle$ in power series of $\delta\phi$ which yields

$$1 - F_G(t) = \delta\phi^2(\langle\hat{G}^2(t)\rangle - \langle\hat{G}(t)\rangle^2) = \delta\phi^2 \mathrm{var}\hat{G}(t). \tag{13.3}$$

In Fig. 13.2 we plot the the variance of $\hat{G} = (\hat{a}^\dagger + \hat{a})/2$. We observe a clearly distinguishable difference in the behaviour of FOTOC in the two quan-

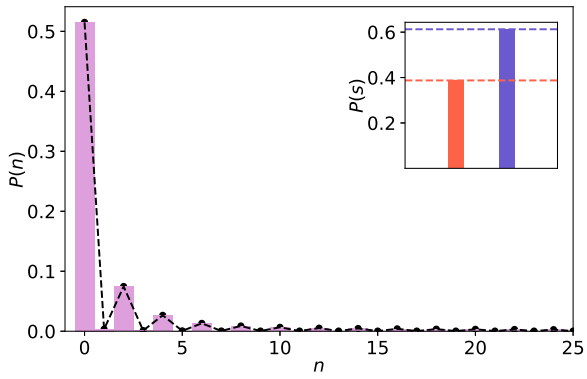

Fig. 13.5: Numerical result for the time-average mean boson occupation distribution $P(n)$ (pink bars) compared with its diagonal ensemble average with density operator $\hat{\rho}_{\mathrm{DE}}$ (dashed line). (Inset) The time-average spin population $P(\downarrow)$ (red bar) and $P(\uparrow)$ (blue bar) compared with its diagonal ensemble average (dashed lines). The parameters are set to $g = 10$, and $\eta = 200$.

tum phases. In the normal phase ($g < g_{\mathrm{c}}$) the FOTOC oscillates with an amplitude independent of η, see Fig. 13.2 (inset). In the superradiant phase ($g > g_{\mathrm{c}}$) we observe exponential growth of the FOTOC in the beginning of the time evolution, which is associated with the onset of quantum chaos via the relation (13.3).

The exponential growth is observed after a short time of slow dynamics with no perceivable growth of the FOTOC. From here we can extract the quantum Lyapunov exponent $(1 - F_G(t))/\delta\phi^2 \sim e^{\lambda_Q(g,\omega,\Delta)t}$. We observe that as η increases the FOTOC grows larger and reaches its maximal value at the scrambling time t^*, beyond which any initial local information about the system is globally spread among its degrees of freedom. After the scrambling time t^* the FOTOC displays oscillatory behaviour characterized by periodically occurring maximal saturation. In Fig. 13.3(inset) we show the exact result for the scrambling time t^* as a function of the parameter η. We find that t^* behaves as $t^* \sim a\log(\eta) + b\log^2(\eta)$ with a and b being fit parameters. Moreover, we find the relation $\lambda_Q(g,\omega,\Delta)t^* \sim \log\eta$ as shown in Fig. 13.3. Finally, we note that the FOTOC and the Lyapunov exponent increase with g, while the saturation time t^* stays nearly constant which makes the QR system more chaotic for stronger spin-boson interaction, see Fig. 13.4.

13.0.4 Equilibration

The emergence of quantum statistical mechanics in a closed system has been connected to chaotic behaviour, therefore investigation of equilibration and thermalization is a natural continuation of our discussion [279]. The *Eigenstate Thermalization Hypothesis* (ETH) [304, 305] states that the expectation value of a

thermalizing observable in a Hamiltonian eigenstate is equal to the microcanonical prediction for that observable at the corresponding eigenenergy. As our system exhibits temporal fluctuations, we focus on the long-time average of observables, rather that their true value. Given an initial state $|\psi_0\rangle = \sum_\alpha c_k|E_k\rangle$, where $\hat{H}|E_k\rangle = E_k|E_k\rangle$ and $c_k = \langle E_k|\psi_0\rangle$, evolving under the system Hamiltonian as $|\psi(t)\rangle = e^{-i\hat{H}t}|\psi_0\rangle = \sum_k c_k e^{-iE_k t}|E_k\rangle$, the long-time average of an observable $\hat{O}$ reads

$$\langle\bar{O}\rangle = \sum_k |c_k|^2 O_{kk} = \mathrm{Tr}[\hat{\rho}_{\mathrm{DE}}\hat{O}], \tag{13.4}$$

where $\hat{\rho}_{\mathrm{DE}}$ is the density matrix of the so-called diagonal ensemble (DE) $\hat{\rho}_{\mathrm{DE}} = \sum_k |c_k|^2|E_k\rangle\langle E_k|$ and $O_{kk} = \langle E_k|\hat{O}|E_k\rangle$. The statement of the ETH translates to the fact that the predictions for $\langle\bar{O}\rangle$ given by the diagonal and microcanonical ensemble (ME) at energy $E_0 = \langle\psi_0|\hat{H}|\psi_0\rangle$ coincide, where the latter is given by

$$\langle\hat{O}\rangle_{\mathrm{ME}}(E_0) = \mathrm{Tr}[\hat{\rho}_{\mathrm{ME}}\hat{O}] = \frac{1}{\mathcal{N}} \sum_{k:|E_k - E_0|<\delta E} O_{kk}. \tag{13.5}$$

The sum runs through the $\mathcal{N}$ eigenstates of $\hat{H}$ that are inside an energy shell of width $2\delta E$ around E_0.

In Fig. 13.5 we show that (13.4) holds for the QR model. We have chosen our observables to be the projectors onto the bosonic Fock states $\hat{P}(n) = |n\rangle\langle n|$ and σ_z eigenstates $\hat{P}(s) = |s\rangle\langle s|$, $(s = \uparrow, \downarrow)$. To find the long-time average value we use $\langle\bar{P}\rangle = \frac{1}{\Delta t}\int_t^{t+\Delta t} d\tau \mathrm{Tr}[\hat{P}\hat{\rho}(\tau)]$ for all of the respective projector operators, where $\hat{\rho}(t)$ is the density matrix of the system.

The DE prediction depends on the initial state of the system through the amplitudes c_k, however, agreement between the DE and ME predictions implies a thermodynamical universality, namely the (averaged) relaxation value of an observable should only depend on the initial energy, and should hold true for a variety of initial states of the same energy [306]. We test this for the QR model for initial states of the type $|\psi_0\rangle = (|\downarrow\rangle + e^{i\phi}|\uparrow\rangle)|0\rangle/\sqrt{2}$ which have the same E_0 for any value of ϕ. The results presented in Fig. 13.6(b) show that (13.4) leads to such universality, i.e. we have that $\sum_k |c_k|^2 O_{kk} = \langle\bar{O}\rangle_{E_0}$. In Fig. 13.6(a) we compare $\langle\bar{O}\rangle_{E_0}$ with $\langle\hat{O}\rangle_{\mathrm{ME}}(E_0)$, as well as the non-averaged time-evolution $\langle\psi(t)|\hat{O}|\psi(t)\rangle$ for $\hat{O} = \{\hat{P}(\uparrow), \hat{P}(\downarrow)\}$. The microcanonical energy shell is chosen with robustness in mind, meaning that the ME prediction gives nearly the same result regardless of small fluctuations around the value of δE. This is in accordance with the implication of the ETH that the expectation values O_{kk} of $\hat{O}$ for states $|E_k\rangle$ inside the energy shell are nearly independent of k. However, we see that in the general case the DE and ME averages do not agree, despite the aforementioned universality.

Furthermore, we investigate the condition of equilibration of the spin system which requires the effective dimension of the time-averaged density matrix defined by $d_{\mathrm{eff}} = (\sum_k |c_k|^4)^{-1}$ to be much larger than d_{s}^2 ($d_{\mathrm{eff}} \gg d_{\mathrm{s}}^2$) where $d_{\mathrm{s}} = 2$ is the spin system dimension [301, 302]. This condition ensures that the initial state is composed of a large number of energy eigenstates so that the bosonic

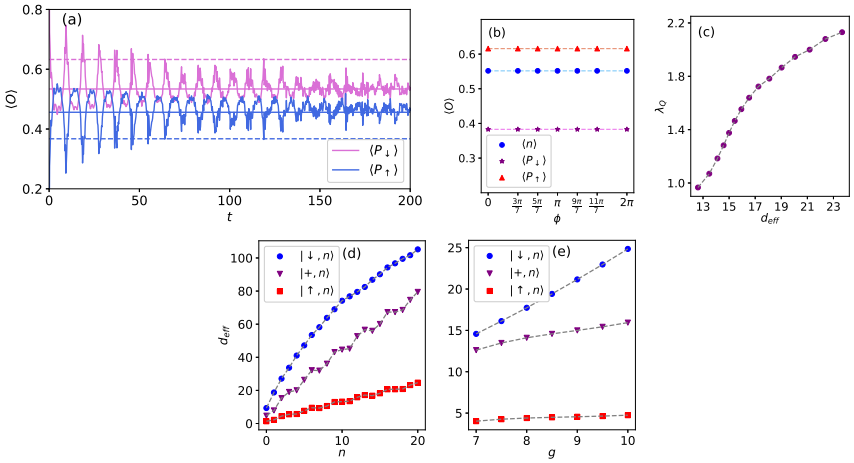

Fig. 13.6: (a) Time-evolution of the spin populations from $|\psi_0\rangle = |\downarrow, 20\rangle$ compared to the DE (solid lines) and ME (dashed lines) predictions in the superradiant phase for $\omega\Delta = 100$, $\eta = 200$, $g = 15$. (b) Long-time average of the spin populations (red triangles and purple stars) and mean boson number (blue dots) for various initial states and $\eta = 100$, $g = 10$. (c) Quantum Lyapunov exponent as a function of d_{eff} through varying g, $\omega\Delta = 100$, $\eta = 200$, $|\psi_0\rangle = |+, 5\rangle$. (d) Effective dimension of the time-averaged density operator d_{eff} as a function of n for $\eta = 200$, $g = 15$. (e) The same but as function of g for $n = 5$.

degree of freedom acts as an effective bath coupled to the spin. In Figs. 13.6(c) and 13.6(d) we show d_{eff} for different initial spin and Fock states. We see that for all initial states d_{eff} increases with the number of bosons n [307]. This leads to suppression of the temporal fluctuations and hence equilibration of the spin obsevable which remains close to its time average as is shown in Fig. 13.6(a). Finally, we note that for large effective dimension d_{eff} the initial local information is spread between large number of eigenstates which increases $\lambda_Q(g, \omega, \Delta)$ and thus makes the QR system more chaotic, see Fig. 13.6(c).

13.0.5 Summary

We have shown that the critical QR model exhibits signatures of quantum chaos in the superradiant phase that become more apparent as we approach the effective thermodynamic limit $\eta \to \infty$. This is most clearly seen in the behaviour of the FOTOC which also quantifies chaos via the quantum Lyuapunov exponent. Furthermore, we investigate the equilibration of the spin degree of freedom in the QR model. We see that the system doesn't thermalize in general, but exhibits relaxation due to dephasing, characterized by the long-time average of observables that can be described using the diagonal density ensemble. We also have shown that the effective dimension of the time-averaged density matrix can be much larger than the spin system dimension which leads to equilibration of the spin observables.

BIBLIOGRAPHY

[1] K. Singer, U. Poschinger, M. Murphy, **P. Ivanov**, F. Ziesel, T. Calarco and F. Schmidt-Kaler, Rev. Mod. Phys. **82**, 2609 (2010).

[2] D. Leibfried, R. Blatt, C. Monroe, and D. Wineland, Rev. Mod. Phys. **75**, 281 (2003).

[3] D. F. V. James, Appl. Phys. B: Lasers Opt. **66**, 181 (1998).

[4] C. Marquet, F. Schmidt-Kaler, and D. F. V. James, Appl. Phys. B **76**, 199 (2003).

[5] D. J. Wineland *et al.*, J. Res. Natl. Inst. Technol. **103**, 259 (1998).

[6] C. Schneider, D. Porras, and T. Schaetz, Rep. Prog. Phys. **75**, 024401 (2012).

[7] J. I. Cirac and P. Zoller, Phys. Rev. Lett. **74**, 4091 (1995).

[8] R. P. Feynman, Int. J. Theor. Phys. **21**, 467 (1982).

[9] D. Kielpinski *et al.*, Nature (London) **417**, 709 (2002).

[10] A. D. Greentree *et al.*, Nat. Phys. **2**, 856 (2006).

[11] M. J. Hartmann *et al.*, Nat. Phys. **2**, 849 (2006).

[12] D. G. Angelakis, M. F. Santos, and S. Bose, Phys. Rev. A **76**, 031805(R) (2007).

[13] M. I. Makin, J. H. Cole, C. Tahan, L. C. L. Hollenberg, and A. D. Greentree, Phys. Rev. A **77**, 053819 (2008).

[14] D. Rossini and R. Fazio, Phys. Rev. Lett. **99**, 186401 (2007).

[15] J. Hubbard, Proc. R. Soc. London, Ser. A **276**, 238 (1963).

[16] D. Porras and J. I. Cirac, Phys. Rev. Lett. **93**, 263602 (2004).

[17] A. Imamoglu, H. Schmidt, G. Woods, and M. Deutsch, Phys. Rev. Lett. **79**, 1467 (1997).

[18] E. K. Irish, C. D. Ogden, and M. S. Kim, Phys. Rev. A **77**, 033801 (2008).

[19] A. Mering, M. Fleischhauer, P. A. Ivanov, and K. Singer, Phys. Rev. A **80**, 053821 (2009).

[20] S. Schmidt and G. Blatter, Phys. Rev. Lett. **103**, 086403 (2009).

[21] M. J. Hartmann, F. G. S. L. Brandao, and M. B. Plenio, Laser Photonics Rev. **2**, 527 (2008).

[22] D. J. Klein, J. Chem. Phys. **61**, 786 (1974).

[23] S. Trotzky *et al.*, Science **319**, 295 (2008).

[24] A. B. Kuklov and B. V. Svistunov, Phys. Rev. Lett. **90**, 100401 (2003).

[25] H. Häffner, C. F. Roos, and R. Blatt, Phys. Rep. **469**, 155 (2008).

[26] C. Ospelkaus *et al.*, Phys. Rev. Lett. **101**, 090502 (2008).

[27] C. Ospelkaus *et al.*, Nature (London) **476** 181 (2011).

[28] A. Kay and D. G. Angelakis, Europhys. Lett. **84**, 20001 (2008).

[29] S. Schmidt, G. Blatter, and J. Keeling, J. Phys. B **46**, 224020 (2013).

[30] A. Tomadin and R. Fazio, J. Opt. Soc. Am. **B** 27, A130 (2010).

[31] A. Auerbach, *Interacting Electrons and Quantum Magnetism* (Springer-Verlag, New York, 1994).

[32] J. P. Kestner *et. al.*, Phys. Rev. B **83**, 174409 (2011).

[33] M. Dalmonte et al., Phys. Reb. B **83**, 155110 (2011).

[34] Z.-C. Gu and X.-G. Wen, Phys. Rev. B **80**, 155131 (2009).

[35] F. Pollmann *et al.*, Phys. Rev. B **81**, 064439 (2010).

[36] F. Pollmann *et al.*, Phys. Rev. B **81**, 075125 (2012).

[37] F. D. M. Haldane, Phys. Rev. Lett. **50**, 1153 (1983).

[38] J. J. Garcia-Ripoll, M. A. Martin-Delgado, and J. I. Cirac, Phys. Rev. Lett. **93**, 250405 (2004).

[39] R. Englman, *The Jahn-Teller Effect in Molecules and Crystals* (Wiley, 1972).

[40] I. B. Bersuker, *The Jahn-Teller Effect*, (Cambridge University Press, Cambridge 2006).

[41] R. Englman and B. Halperin, Phys. Rev. B **2**, 75 1970; B. Halperin and R. Englman, Phys. Rev. B **3**, 1698 (1971).

[42] A. J. Millis, Boris. I. Shraiman, and R. Mueller, Phys. Rev. Lett. **77**, 175 (1996).

[43] Y. Tokura and N. Nagaosa, Science **288**, 462 (2000).

[44] J. Larson, Phys. Rev. A **78**, 033833 (2008).

[45] J. Larson and Sjöqvist, Phys. Rev. A **79**, 043627 (2009).

[46] A. P. Hines, C. M. Dawson, R. H. McKenzie, and G. J. Milburn, Phys. Rev. A **70**, 022303 (2004).

[47] G. Liberti, R. L. Zaffino, F. Piperno, and F. Plastina, Phys. Rev. A **76**, 042332 (2007).

[48] J. Larson and S. Levin, Phys. Rev. Lett. **103**, 013602 (2009).

[49] E. Majernikova and S. Shpyrko, J. Phys. A: Math. Theor. **44**, 065101 (2011).

[50] C. Emary and T. Brandes, Phys. Rev. Lett. **90**, 044101 (2003); C. Emary and T. Brandes, Phys. Rev. E **67**, 066203 (2003).

[51] K. Baumann, C. Guerlin, F. Brennecke and T. Esslinger, Nature **464**, 1301 (2010).

[52] K. Baumann, R. Mottl, F. Brennecke, and T. Esslinger, Phys. Rev. Lett. **107**, 140402 (2011).

[53] M. Johanning, A. Braun, N. Timoney, V. Elman, W. Neuhauser, and Chr. Wunderlich, Phys. Rev. Lett. **102**, 073004 (2009).

[54] N. Timoney, I. Baumgart, M. Johanning, A. F. Varom, M. B. Plenio, A. Retzker and Ch. Wunderlich, Nature **476**, 185 (2011).

[55] A. Bermudez, M. A. Martin-Delgado and A. Luis, Phys. Rev. A **77**, 063815 (2008).

[56] P. Navado and D. Porras, arXiv:1212.4709.

[57] J. Larson, Phys. Rev. A **78**, 033833 (2008).

[58] J. Larson and E. Sjöqvist, Phys. Rev. A **79**, 043627 (2009).

[59] S. Fishman, G. De Chiara, T. Calarco, and G. Morigi, Phys. Rev. B **77**, 064111 (2008).

[60] Chr. Wunderlich, Th. Hannemann, T. Körber, H. Häffner, Ch. Roos, W. Hänsel, R. Blatt, and F. Schmidt-Kaler, J. Mod. Opt. **54**, 1541 (2007).

[61] A. Auerbach, *Interaction Electrons and Quantum Magnetism* (Springer, New York, 1994).

[62] J. Sinova, D. Culcer, Q. Niu, N. A. Sinitsyn, T. Jungwirth, and A. H. MacDonald, Phys. Rev. Lett. **92**, 126603 (2004).

[63] L. Balents, Nature **464**, 199 (2010).

[64] A. V. Gorshkov, M. Hermele, V. Gurarie, C. Xu, P. S. Julienne, J. Ye, P. Zoller, E. Demler, M. D. Lukin and A. M. Rey , Nature Phys. **6**, 289 (2010).

[65] A. Metavitsiadis, Phys. Rev. B **83**, 054409 (2011).

[66] T. Rosenband, et al., Science **319**, 1808 (2008).

[67] C. W. Chou, D. B. Hume, M. J. Thorpe, D. J. Wineland, and T. Rosenband, arXiv:1101.3766 (2011).

[68] T. Rosenband et al., Phys. Rev. Lett. **98**, 220801 (2007).

[69] T. Lahaye, T. Koch, B. Frohlich, M. Fattori, J. Metz, A. Griesmaier, S. Giovanazzi and T. Pfau, Nature **448**, 672 (2007).

[70] J. Metz, T. Lahaye, B. Frohlich, A. Griesmaier, T. Pfau, H. Saito, Y. Kawaguchi and M. Ueda, New J. Phys. **11**, 055032 (2009).

[71] J. D. Jost, J. P. Home, J. M. Amini, D. Hanneke, R. Ozeri, C. Langer, J. J. Bollinger, D. Leibfried and D. J. Wineland, Nature **459**, 683 (2009).

[72] J.-Willem, G. Bos, C. V. Colin, and T. T. M. Palstra, Phys. Rev. B **78**, 094416 (2008).

[73] L. Lamata, J. Leon, T. Schätz, and E. Solano, Phys. Rev. Lett. **98**, 253005 (2007).

[74] S. Dutta and E. J . Mueller, arXiv:1711.08059 (2017).

[75] Saffman, M., Walker, T. G. & Mölmer, K. Quantum information with Rydberg atoms. *Rev. Mod. Phys.* **82**, 2313 (2010).

[76] Killian, T. C., Pattard, T., Pohl, T. & Rost, J. M. Ultracold neutral plasmas. *Phys. Rep.* **449**, 77 (2007).

[77] Naguyen, T. L. *et al.* Towards quantum simulation with circular Rydberg atoms. *Phys. Rev. X* **8**, 011032 (2018).

[78] Beterov, I. I. *et al.* Adiabatic passage of radio-frequency-assisted Föster resonances in Rydberg atoms for two-qubit gates and the generation of Bell states. *Phys. Rev. A* **97**, 032701 (2018).

[79] Tauschinsky, A. *et al.* Radio-frequency-driven dipole-dipole interactions in spatially separated volumes. *Phys. Rev. A* **78**, 063409 (2008).

[80] Tretyakov, D. B. *et al.* Controlling the interactions of a few cold Rb Rydberg atoms by radio-frequency-assisted Föster resonances. *Phys. Rev. A* **90**, 041403(R) (2014).

[81] Feldker, T. *et al.* Rydberg excitation of a single trapped ion. *Phys. Rev. Lett.* **115**, 173001 (2015).

[82] Higgins G. *et al.* Single Strontium Rydberg ion confined in a Paul trap. *Phys. Rev. X* **7**, 021038 (2017).

[83] Bachor, P., Feldker, T., Walz, J. & Schmidt-Kaler, F. Addressing single trapped ions for Rydberg quantum logic. *J. Phys. B* **49**, 154004 (2016).

[84] Müller, M., Liang, L., Lesanovski, I. & Zoller, P. Trapped Rydberg ions: from spin chains to fast quantum gates. *New. J. Phys.* **10**, 093009 (2008).

[85] Schmidt-Kaler, F. *et al.* Rydberg Excitation of Trapped Cold Ions: A Detailed Case Study. *New. J. Phys.* **13**, 075014 (2011).

[86] James, D. F. V. & Jerke, J. Effective Hamiltonian theory and its applications in quantum information. *Can. J. Phys.* **85**, 625 (2007).

[87] Goldman, N. & Dalibard, J. Periodically driven quantum systems: effective Hamiltonians and engineered gauge fields. *Phys. Rev. X*, **4**, 031027 (2014).

[88] Rahav, S., Gilary, I. & Fishman, S. Effective Hamiltonians for periodically driven systems. *Phys. Rev. A* **68**, 013820 (2003).

[89] J. D. Pritchard, D. Maxwell, A. Gauguet, K. J. Weatherill, M. P. A. Jones, and C. S. Adams, Phys. Rev. Lett. **105**, 193603 (2010).

[90] D. Petrosyan, J. Otterbach, and M. Fleischhauer, Phys. Rev. Lett. **107**, 213601 (2011).

[91] N. Schine, A. Ryou, A. Gromov, A. Sommer and J. Simon, Nature **534**, 671 (2016).

[92] A. Sommer and J. Simon, New J. Phys. **18**, 035008 (2016).

[93] M. Fleischhauer, A. Imamoglu, and J. P. Marangos, Rev. Mod. Phys. **77**, 633 (2005).

[94] R. B. Laughlin, Phys. Rev. B **23** 5632–5633 (1981).

[95] M. F. Andersen, C. Ryu, Pierre Cladé, Vasant Natarajan, A. Vaziri, K. Helmerson, and W. D. Phillips, Phys. Rev. Lett. **97**, 170406 (2006).

[96] F. Grusdt, F. Letscher, M. Hafezi, and M. Fleischhauer, Phys. Rev. Lett. **113**, 155301 (2014).

[97] F. Letscher, F. Grusdt, and M. Fleischhauer, Phys. Rev. B **91**, 184302 (2015).

[98] J. Ningyuan, Al. Georgakopoulos, A. Ryou, N. Schine, A. Sommer, and J. Simon, Phys. Rev. A **93**, 041802(R) (2016).

[99] N. Jia, N. Schine, A. Georgakopoulos, A. Ryou, A. Sommer, and J. Simon, Nat. Phys. **14**, 550 (2018).

[100] F. Grusdt, and M. Fleischhauer, Phys. Rev. B **87**, 043628 (2013).

[101] J. K. Jain, *Composite Fermions* (Cambridge University Press, Cambridge, UK, 2007).

[102] J. I. Cirac and P. Zoller, Nat. Phys. **8**, 264 (2012).

[103] R. Blatt and C. F. Roos, Nat. Phys. **8**, 277 (2012).

[104] A. Friedenauer *et. al.*, Nat. Phys. **4**, 757 (2008).

[105] R. Islam *et al.*, Nat. Comm. **2**, 377 (2011).

[106] J. W. Britton *et al.*, Nature (London) **484**, 489 (2012).

[107] A. Bermudez and M. B. Plenio, Phys. Rev. Lett. **109**, 010501 (2012).

[108] V. Giovannetti, S. Lloyd, and L. Maccone, Nat. Photon. **5**, 222 (2011).

[109] V. Giovannetti, S. Lloyd, and L. Maccone, Phys. Rev. Lett. **96**, 010401 (2006).

[110] D. J. Wineland, J. J. Bollinger, W. M. Itano, and D. J. Heinzen, Phys. Rev. A **50**, 67 (1994).

[111] J. J. Bollinger, W. M. Itano, D. J. Wineland, and D. J. Heinzen, Phys. Rev. A **54**, R4649 (1996).

[112] D. Leibfried *et al.*, Science **304**, 1476 (2004).

[113] C. F. Roos, M. Chwalla, K. Kim, M. Riebe, and R. Blatt, Nature **443**, 316 (2006).

[114] S. Sachdev, *Quantum Phase Transitions* (Cambridge University Press, Cambridge, 2001).

[115] R. H. Dicke, Phys. Rev. **93**, 99 (1954).

[116] K. Hepp and E. H. Lieb, Phys. Rev. A **8**, 2517 (1973).

[117] C. Emary and T. Brandes, Phys. Rev. Lett. **90**, 044101 (2003).

[118] N. V. Vitanov, J. Phys. B: At. Mol. Opt. Phys. **26**, L53 (1993).

[119] M. Abramowitz and I. A. Stegun, *Handbook of Mathematical Functions* (Dover, New York, 1964).

[120] J. Benhelm, G. Kirchmair, C. F. Roos, and R. Blatt, Nat. Phys. **4**, 463 (2008).

[121] T. Monz *et al.*, Phys. Rev. Lett. **106**, 130506 (2011).

[122] L. Aolita, K. Kim, J. Benhelm, C. F. Roos, and H. Häffner, Phys. Rev. A **76**, 040303(R) (2007).

[123] M. J. Biercuk, H. Uys, J. W. Britton, A. P. Vandevender, and J. J. Bollinger, Nat. Nanotechnol. **5**, 646 (2010).

[124] F. Dimer, B. Estienne, A. S. Parkins, and H. J. Carmichael, Phys. Rev. A **75**, 013804 (2007).

[125] P. Nataf and C. Ciuti, Nat. Commun. **1**, 72 (2010).

[126] S. F. Huelga *et al.*, Phys. Rev. Lett. **79**, 3865 (1997).

[127] P. A. Ivanov, S. S. Ivanov, N. V. Vitanov, A. Mering, M. Fleischhauer, and K. Singer, Phys. Rev. A **80**, 060301 (2009).

[128] B. Horstmann, J. I. Cirac, and G. Giedke, Phys. Rev. A **87**, 012108 (2013).

[129] M. Müller, S. Diehl, G. Pupillo, and P. Zoller, Adv. At. Mol. Opt. Phys. **61**, 1 (2012).

[130] H. J. Mamin and D. Rugar, Appl. Phys. Lett. **79**, 3358 (2001).

[131] J. D. Teufel, T. Donner, M. A. Castellanos-Beltran, J. W. Harlow, K. W. Lehnert, Nature Nanotech. **4**, 820 (2009).

[132] J. Moser, J. Güttinger, A. Eichler, M. J. Esplandiu, D. E. Liu, M. I. Dykman, and A. Bachtold, Nature Nanotech. **8**, 493 (2013).

[133] S. Knünz, M. Herrmann, V. Batteiger, G. Saathoff, T. W. Hänsch, K. Vahala, and Th. Udem, Phys. Rev. Lett. **105**, 013004 (2010).

[134] Pezzé, L.; Smerzi, A.; Oberthaler, M. K.; Schmied, R; Treutlein, P. Quantum metrology with nonclassical states of atomic ensembles. *Rev. Mod. Phys.* **90**, 035005 (2018).

[135] Garbe, L.; Bina, M.; Keller, A.; Paris, M. G. A.; Felicetti, S. Critical Quantum Metrology with a Finite-Component Quantum Phase Transition. *Phys. Rev. Lett.* **124**, 120504 (2020).

[136] Chu, Y.; Zhang, S.; Yu, B. ; Cai, J. Dynamic Framework for Criticality-Enhanced Quantum Sensing. *Phys. Rev. Lett.* **126**, 010502 (2021).

[137] Cai, M.-L. *et al.* Observation of a quantum phase transition in the quantum Rabi model with a single trapped ion. *Nature Commun.* **12**, 1126 (2021).

[138] Ivanov, P. A. Force sensors with precision beyond the standard quantum limit. *Phys. Rev. A* **94**, 022330 (2016).

[139] Ivanov, P. A. Efficient approach for quantum sensing field gradients with trapped ions. *Optics Commin.* **405**, 355 (2017).

[140] Ivanov, P. A. Steady-state force sensing with single trapped ion. *Phys. Scr.* **95**, 025103 (2020).

[141] Ikeda, T. N.; Sato, M. General description for nonequilibrium steady states in periodically driven dissipative quantum systems. *Sci. Adv.* **6**, eabb4019 (2020).

[142] M. J. Biercuk, H. Uys, J. W. Britton, A. P. VanDevender and J. J. Bollinger, Nature Nanotech. **5**, 646 (2010).

[143] T. F. Gloger, P. Kaufmann, D. Kaufmann, M. T. Baig, T. Collath, M. Jojanning and C. Wunderlich, arXiv:1503.07031.

[144] T. Niemczyk, F. Deppe, H. Huebl, E. P. Menzel, F. Hocke, M. J. Schwarz, J. J. Garcia-Ripoll, D. Zueco, T. Hümmer, E. Solano, A. Marx and R. Gross, Nature Phys. **6**, 772 (2010).

[145] D. Ballester, G. Romero, J. J. Garcia-Ripoll, F. Deppe, and E. Solano, Phys. Rev. X **2**, 021007 (2012).

[146] L. J. Zou, D. Marcos, S. Diehl, S. Putz, J. Schmiedmayer, J. Majer, P. Rabl, Phys. Rev. Lett. **113**, 023603 (2014).

[147] H. Loh, S. Ding, R. Hablutzer, G. Maslennikov, and D. Matsukevich, Phys. Rev. A **90**, 061402(R) (2014).

[148] D. Braak Phys. Rev. Lett. **107**, 1000401 (2011).

[149] R. Maiwald, D. Leibfried, J. Britton, J. C. Bergquist, G. Leuchs and D. J. Wineland, Nature Phys. **5**, 551 (2009).

[150] G. Binnig, C. F. Quate and Ch. Gerber, Phys. Rev. Lett. **56**, 930 (1986).

[151] C. M. Caves, K. S. Thorne, R. W. P. Drever, V. D. Sandberg, and M. Zimmermann, Rev. Mod. Phys. **52**, 341 (1980).

[152] D. Rugar, R. Budakian, H. J. Mamin and B. W. Chui, Nature **430**, 329 (2004).

[153] W. J. Munro, K. Nemoto, G. J. Milburn, and S. L. Braunstein, Phys. Rev. A **66**, 023819 (2002).

[154] A. Ourjoumtsev, H. Jeong, R. Tualle-Brouri and P. Grangier, Nature **448**, 784 (2007).

[155] P. J. Lee, K.-A. Brickman, L. Deslauriers, P. C. Haljan, L.-M. Duan, and C. Monroe, J. Opt. B: Quantum Semiclass. Opt. **7**, 371 (2005).

[156] J. Chiaverini and J. M. Sage, Phys. Rev. A **89**, 012318 (2014).

[157] N. Timoney, I. Baumgart, M. Johanning, A. F. Varon, M. B. Plenio, A. Retzker and Ch. Wunderlich, Nature **476**, 185 (2011).

[158] S. C. Webster, S. Weidt, K. Lake, J. J. McLoughlin, and W. K. Hensinger, Phys. Rev. Lett. **111**, 140501 (2013).

[159] F. Mintert and C. Wunderlich, Phys. Rev. Lett. 87, 257904 (2001).

[160] D. B. Hume, C. W. Chou, D. R. Leibrandt, M. J. Thorpe, D. J. Wineland, and T. Rosenband, Phys. Rev. Lett. **107**, 243902 (2011).

[161] S. Haze, Y. Tateishi, A. Noguchi, K. Toyoda, S. Urabe, Phys. Rev. A **85**, 031401(R) (2012).

[162] M. Harlander, R. Lechner, M. Brownnutt, R. Blatt, and W. Hänsel, Nature (London) **471**, 200 (2011).

[163] K. R. Brown, C. Ospelkaus, Y. Colombe, A. C. Wilson, D. Leibfried, and D. J. Wineland, Nature (London) **471**, 196 (2011).

[164] K. Toyoda, Y. Matsuno, A. Noguchi, S. Haze, and S. Urabe, Phys. Rev. Lett. **111**, 160501 (2013).

[165] A. Abdelrahman, O. Khosravani, M. Gessner, H.-P. Breuer, A. Buchleitner, D. J. Gorman, R. Masuda, T. Pruttivarasin, M. Ramm, P. Schindler, and H. Häffner, arXiv:1610.04927.

[166] K. A. Gilmore, J. G. Bohnet, B. C. Sawyer, J. W. Britton, and J. J. Bollinger, arXiv:1703.05369 (2017).

[167] M. Johanning, A. Braun, N. Timoney, V. Elman, W. Neuhauser, and Chr. Wunderlich, Phys. Rev. Lett. **102**, 073004 (2009).

[168] M. D. Vidrighin, G. Donati, M. G. Genoni, X.-M. Jin. W. S. Kolthammer, M. S. Kim, A. Datta, M. Barbieri, I. A. Walmsley, Nat. Commun. **5**, 3532 (2014).

[169] G. Toth and I. Apellaniz, J. Phys. A:Math. Theor. **47**, 424006 (2014).

[170] M. G. A. Paris, Int. J. Quantum. Inf. **7**, 125 (2009).

[171] P. Zanardi, M. G. A. Paris, and L. C. Venuti, Phys. Rev. A **78**, 042105 (2008).

[172] M. Bina, I. Amelio, and M. G. A. Paris, Phys. Rev. E **93**, 052118 (2016).

[173] G. Salvatori, A. Mandarino, and M. G. A. Paris, Phys. Rev. A **90**, 022111 (2014).

[174] P. A. Ivanov, K. Singer, N. V. Vitanov and D. Porras, Phys. Rev. Appl. **4**, 054007 (2015).

[175] Shi-Biao Zheng, Phys. Rev. A **66**, 060303(R) (2002).

[176] E. Solano, G. S. Agarwal, and H. Walther, Phys. Rev. Lett. **90**, 027903 (2003).

[177] L. Viola, E. Knill, and S. Lloyd, Phys. Rev. Lett. **82**, 2417 (1999).

[178] W. Yang, Z.-Y. Wang, and R.-B. Liu, Front. Phys. **6**, 1 (2010).

[179] N. Timoney, I. Baumgart, M. Johanning, A. F. Varon. M. B. Plenio, A. Retzker, and Ch. Wunderlich, Nature **476**, 185 (2011).

[180] S. C. Webster, S. Weidt, K. Lake, J. J. McLoughlin, and W. K. Hensinger, Phys. Rev. Lett. **111**, 140501 (2013).

[181] T. R. Tan, J. P. Gaebler, R. Bowler, Y. Lin, J. D. Jost, D. Leibfried, and D. J. Wineland, Phys. Rev. Lett. **110**, 263002 (2013).

[182] A. Bermudez, P. O. Schmidt, M. B. Plenio, and A. Retzker, Phys. Rev. A **85**, 040302(R) (2012).

[183] H. Carr and E. M. Purcell, Phys. Rev. **94**, 630 (1954).

[184] S. Meiboom and D. Gill, Rev. Sci. Instrum. **29**, 688 (1958).

[185] F. Dimer, B. Estienne, A. S. Parkins, H. J. Carmichael, Phys. Rev. A **75**, 013804 (2007).

[186] D. Ballester, G. Romero, J. J. Garcia-Ripoll, F. Deppe, E. Solano, Phys. Rev. X **2**, 021007 (2012).

[187] R. H. Dicke, Phys. Rev. **93**, 99 (1954).

[188] I. I. Rabi, Phys. Rev. **49**, 324 (1936).

[189] J. Larson and S. Levin, Phys. Rev. Lett. **103**, 013602 (2009).

[190] H. J. Lipkin, N. Meshkov, and A. Glick, Nucl. Phys. **62**, 188 (1965).

[191] R. G. Unanyan and M. Fleischhauer, Phys. Rev. Lett. **90**, 133601 (2003).

[192] R. G. Unanyan, C. Ionescu, and M. Fleischhauer, Phys. Rev. A **72**, 022326 (2005).

[193] J. Ma, H. Wang, C. P. Sun, and F. Nori, Phys. Rep. **509**, 89 (2011).

[194] A. M. Rey, L. Jiang, and M. D. Lukin, Phys. Rev. A **76**, 053617 (2007).

[195] S. Boixo, A. Datta, S. T. Flammia, A. Shaji, E. Bagan, and C. M. Caves, Phys. Rev. A **77**, 012317 (2008).

[196] L. Bakemeier, A. Alvermann, and H. Fehske, Phys. Rev. A **85**, 043821 (2012).

[197] M.-J. Hwang, R. Puebla, and M. Plenio, Phys. Rev. Lett. **115**, 180404 (2015).

[198] G. Toth and I. Appelaniz, J. Phys. A: Math. Theor. **47**, 424006 (2014).

[199] S. L. Braunstein and C. M. Caves, Phys. Rev. Lett. **72**, 3439 (1994).

[200] M. G. A. Paris, Int. J. Quantum. Inf. **7**, 125 (2009).

[201] K. Matsumoto, J. Phys. A **35**, 3111 (2002).

[202] P. J. Lee, K.-A. Brickman, L. Deslauriers, P. C. Haljan, L.-M. Duan, and C. Monroe, J. Opt. B **7**, 371 (2005).

[203] M. G. Genoni, M. G. A. Paris, G. Adesso, H. Nha, P. L. Knight, and M. S. Kim, Phys. Rev. A **87**, 012107 (2013).

[204] L. Pezze, M. A. Ciampini, N. Spagnolo, P. C. Humphreys, A. Datta, I. A. Walmsley, M. Barbieri, F. Sciarrino, and A. Smerzi, Phys. Rev. Lett. **119**, 130504 (2017).

[205] P. Rabl, P. Cappellaro, M. V. Gurudev Dutt, L. Jiang, J. R. Maze, and M. D. Lukin, Phys. Rev. B **79**, 041302(R) (2009).

[206] P. Rabl, A. Shnirman, and P. Zoller, Phys. Rev. B **70**, 205304 (2004).

[207] G. Vacanti, M. Paternostro, G. M. Palma, M. S. Kim, and V. Vedral, Phys. Rev. A **88**, 013851 (2013); G. Vacanti, R. Fazio, M. S. Kim, G. M. Palma, M. Paternostro, and V. Vedral, Phys. Rev. A **85**, 022129 (2012).

[208] D. Lv, S. An, Z. Liu, J.-N. Zhang, J. S. Pedernales, L. Lamata, E. Solano, and K. Kim, Phys. Rev. X **8**, 021027 (2018).

[209] A. Lemmer, C. Cormick, D. Tamascelli, T. Schaetz, S. F. Huelga, and M. B. Plenio, New J. Phys. **20**, 073002 (2018).

[210] M.-J. Hwang, R. Puebla, and M. B. Plenio, Phys. Rev. Lett. **115**, 180404 (2015).

[211] M.-J. Hwang, P. Rabl, and M. B. Plenio, Phys. Rev. A **97**, 013825 (2018).

[212] M. G. Genoni, M. Bina, S. Olivares, G. De Chiara, and M. Paternostro, New J. Phys. **17**, 013034 (2015).

[213] S. P. Nolan S. A. Haine, Phys. Rev. A. **95**, 043642 (2017).

[214] C. Weedbrook, S. Pirandola, R. Garcia-Patron, N. J. Cerf, J. H. Shapiro, S. Lloyd, Rev. Mod. Phys. **84**, 621 (2012).

[215] A. Monras, arXiv:1303.3682.

[216] O. Pinel, P. Jian, N. Treps, C. Fabre, and D. Braun, Phys. Rev. A **88**, 040102(R) (2013).

[217] S. Fernandez-Lorenzo and D. Porras, Phys. Rev. A **96**, 013817 (2017).

[218] L. Rezze, A. Trenkwalder, and M. Fattori, arXiv:1906.01447.

[219] S. S. Mirkhalaf, E. Witkowska, and L. Lepori, Phys. Rev. A **101**, 043609 (2020).

[220] P. C. Humphreys, M. Barbieri, A. Datta, and I. A. Walmsley, Phys. Rev. Lett. **111**, 070403 (2013).

[221] M. Gessner, L. Pezze, and A. Smerzi, Phys. Rev. Lett. **121**, 130503 (2018).

[222] L. Pezze, *et.al.*, Phys. Rev. Lett. **119**, 130504 (2017).

[223] M. D. Vidrighin, *et.al.*, Nat. Commun. **5**, 3532 (2014).

[224] J.-D. Yue, Y.-R. Zhang, and H. Fan, Scient. Rep. **4**, 5933 (2014).

[225] M. G. Genoni, S. Olivares, and M. G. Paris, Phys. Rev. Lett. **106**, 153603 (2011).

[226] T. Baumgratz and A. Datta, Phys. Rev. Lett. **116**, 030801 (2016).

[227] M. G. Genoni, M. G. A. Paris, G. Adesso, H. Nha, P. L. Knight, and M. S. Kim, Phys. Rev. A **87**, 012107 (2013).

[228] M. Bradshaw, P. K. Lam, and S. M. Assad, Phys. Rev. A **97**, 012106 (2018).

[229] M. Szczykulska, T. Baumgratz, and A. Datta, Adv. Phys. X 1, 621 (2016).

[230] F. Albarelli, M. Barbieri, M. G. Genoni, and I. Gianani, Phys. Lett. A, 126311 (2020).

[231] M. Gessner, A. Smerzi, and L. Pezze, Nature Commun. **11**, 3817 (2020).

[232] F. Minganti, A. Biella, N. Bartolo, and C. Ciuti, Phys. Rev. A **98**, 042118 (2018).

[233] S. Braunstein, and C. M. Caves, Phys. Rev. Lett. **72**, 3439 (1994).

[234] S. Gopalakrishnam, B. L. Lev, and P. M. Goldbart, Phys. Rev. Lett. **107**, 277201 (2011).

[235] C. Weedbrook, S. Pirandola, R. Garcia-Patron, N. J. Cerf, J. H. Shapiro, and S. Lloyd, Rev. Mod. Phys. **84**, 621 (2012).

[236] O. Pinel, P. Jian, N. Treps, C. Fabre, and D. Braun, Phys. Rev. A **88**, 040102(R) (2013).

[237] C. Noh and D. G. Angelakis, Rep. Prog. Phys. **80**, 016401 (2017).

[238] S. Fernandez-Lorenzo, J. A. Dunningham, and D. Porras, Phys. Rev. A **97**, 023843 (2018).

[239] M. Brunelli, S. Ovivares, and M. G. A. Paris, Phys. Rev. A **84**, 032105 (2011).

[240] M. Brunelli, S. Ovivares, M. Paternistro, and M. G. A. Paris, Phys. Rev. A **86**, 012125 (2012).

[241] S. L. Braunstein and C. M. Caves, Phys. Rev. Lett. **72**, 3439 (1994).

[242] B. Kinkert, and F. Narberhaus, Cell. Mol. Life Sci. **66**, 2661 (2009).

[243] M. Mehboudi, A. Sanpera, and L. A. Correa, J. Phys. A **52**, 303001 (2019).

[244] A. De Pasquale, D. Rossini, R. Fazio, and V. Giovannetti, Nat. Comm. **7**, 12782 (2016).

[245] J. Gemmer, M. Michel, and G. Mahler, *Quantum Thermodynamics* (Springer, Berlin/Heidelberg, 2009).

[246] F. Seilmeier, M. Hauck, E. Schubert, G. J. Schinner, S. E. Beavan, and A. Högele, Phys. Rev. Applied **2**, 024002 (2014).

[247] F. Haupt, A. Imamoglu, and M. Kroner, Phys. Rev. Applied **2**, 024001 (2014).

[248] C. Sabin, A. White, L. Hackermuller, and I. Fuentes, Sci. Rep. **4**, 6436 (2014).

[249] P. Neumann, *et al.*, Nano Lett. **13**, 2738 (2013).

[250] G. Kucsko, *et al.*, Nature (London) **500**, 54 (2013).

[251] D. M. Toyli, *et al.*, Proc. Natl. Acad. Sci. U.S.A. **110**, 8417 (2013).

[252] D. M. Meekhof, C. Monroe, B. E. King, W. M. Itano, and D. J. Wineland, Phys. Rev. Lett. **76**, 1796 (1996).

[253] J. Roßnagel, K. N. Tolazzi, F. Schmidt-Kaler, and K. Singer, New J. Phys. **17**, 045004 (2015).

[254] Y. Wan, F. Gebert, F. Wolf, and P. O. Schmidt, Phys. Rev. A **91**, 043425 (2015).

[255] F. Gebert, Y. Wan, F. Wolf, J. C. Heip, and P. O. Schmidt, New J. Phys. **18**, 013037 (2016).

[256] A. Levy, M. Göb, Bo Deng, K. Singer, E. Torrontegui, and D. Wang, New J. Phys. **22**, 093020 (2020).

[257] M. G. A. Paris, J. Phys. A **03LT02** (2016).

[258] U. Marzolino and D. Braun, Phys. Rev. A **88**, 063609 (2013).

[259] L. A. Correa, M. Mehboudi, G. Adesso, and A. Sanpera, Phys. Rev. Lett. **114**, 220405 (2015).

[260] S. Campbell, M. Mehboudi, G. De Chiara, and M. Paternostro, New J. Phys. **19**, 103003 (2017).

[261] S. Campbell, M. G. Genoni, S. Daffner, Quantum Sci. Technol. **3**, 025002 (2018).

[262] I. E. Linington and N. V. Vitanov, Phys. Rev. A **77**, 010302(R) (2008).

[263] I. E. Linington, P. A. Ivanov, N. V. Vitanov, and M. B. Plenio, Phys. Rev. A **77**, 063837 (2008).

[264] D. B. Hume, C. W. Chou, T. Rosenband, and D. J. Wineland, Phys. Rev. A **80**, 052302 (2009).

[265] K. Toyoda, T. Watanabe, T. Kimura, S. Nomura, S. Haza, and S. Urabe, Phys. Rev. A **83**, 022315 (2011).

[266] R. Lechner, C. Maier, C. Hempel, P. Jurcevic, B. P. Lanyon, T. Monz, M. Brownnutt, R. Blat, and C. F. Roos, Electromagnetically-induced-transparency groun-state cooling of long ion string, Phys. Rev. A **93**, 053401 (2016).

[267] Q. Xie, H. Zhong, M. T. Batchelor, and C. Lee, J. Phys. A: Math. Theor. **50**, 113001 (2017).

[268] J. S. Pedernales, I. Lizuain, S. Felicetti, G. Romero, L. Lamata, and E. Solano, Sci. Rep. **5**, 15472 (2015).

[269] D. Lv, S. An, Z. Liu, J.-N. Zhang, J. S. Pedernales, L. Lamata, E. Solano, and K. Kim, Phys. Rev. X **8**, 021027 (2018).

[270] M. Hwang, R. Puebla, M. B. Plenio, Phys. Rev. Lett. **115**, 180404 (2015).

[271] L. Bakemeier, A. Alvermann, H. Fehske, Phys. Rev. A **85**, 043821 (2012).

[272] M.-L. Cai *et al.*, Nature Commun. **12**, 1126 (2021).

[273] P. Pérez-Fernández *et al.*, Phys. Rev. E **83**, 046208 (2011).

[274] C. Emary, T. Brandes, Phys. Rev. Lett. **90**, 044101 (2003).

[275] C. Emary, T. Brandes, Phys. Rev. E **67**, 066203 (2003).

[276] B. Georgeot, D. Shepelyansky, Phys. Rev. Lett. **81**, 5129 (1998).

[277] R. J. Lewis-Swan, A. Safavi-Naini, J. J. Bollinger, A. M. Rey, Nature Commun. **10**, 1581 (2019).

[278] M. Berry, M. Tabor, Proc. R. Soc. Lond. A **356** 375 (1977).

[279] L. D'Alessio, Y. Kafri, A. Polkovnikov, M. Rigol, Adv. Phys. **65**, 239 (2016).

[280] M. Kuś, Phys. Rev. Lett. **54**, 1343 (1985).

[281] B. Swingle, Nature Phys. **14**, 988 (2018).

[282] S. H. Shenker, D. Stanford, J. High Energ. Phys. **2014**, 67 (2014).

[283] A. Bohrdt, C. B. Mendl, M. Endres, and M. Knap, New J. Phys. **19**, 063001 (2017).

[284] H. Shen, P. Zhang, R. Fan, and H. Zhai, Phys. Rev. B **96**, 054503 (2017).

[285] M. Gärttner, J. G. Bohnet, A.S.-Naini, M. L. Wall, J. J. Bollinger, and A. M. Rey, Nature Phys. **13**, 781 (2017).

[286] K. A. Landsman, C. Figgtt, T. Schuster, N. M. Linke, B. Yoshida, N. Y. Yao, and C. Monroe, Nature **567**, 61 (2019).

[287] M. K. Joshi, A. Elben, B. Vermersch, T. Brydges, C. Maier, P. Zoller, R. Blatt, and C. F. Roos, Phys. Rev. Lett. **124**, 240505 (2020).

[288] A. M. Green, A. Elben, C. H. Alderete, L. K. Joshi, N. H. Nguyen, T. V. Zache, Y. Zhu, B. Sundar, and N. M. Linke, arXiv:2112,02068 (2021).

[289] J. Li, R. Fan, H. Wang, B. Ye, B. Zeng, H. Zhai, X. Peng, and J. Du, Phys. Rev. X **7**, 031011 (2017).

[290] Z.-H. Sun, J.-Q. Cai, Q.-C. Tang, Y. Hu, and H. Fan, Ann. Phys. (Berlin) **532**, 1900270 (2019).

[291] M. Schmitt, D. Sels, S. Kehrein, A. Polkovnikov, Phys. Rev. B **99**, 134301 (2019).

[292] J. Maldacena, S. Shenker, D. Stanford, J. High Energ. Phys. **2016**, 106 (2016).

[293] A. Bohrdt, C. B. Mendl, M. Endres, M. Knap, New J. Phys. **19**, 063001 (2017).

[294] J. C.-Carlos *et al.,* Phys. Rev. Lett. **122**, 024101 (2019).

[295] A. Keselman, L. Nie, E. Berg, Phys. Rev. B **103**, 121111 (2021).

[296] J. Rammensee, J.-D. Urbina, K. Richter, Phys. Rev. Lett. **121**, 124101 (2018).

[297] Y. Sekino, L. Susskind, J. High Energy Phys. **2008**, 065 (2008).

[298] X. Chen, T. Zhou, arXiv:1804.08655.

[299] H. Gharibyan, M. Hanada, B. Swingle, M. Tezuka, J. High Energy Phys. **2019**, 82 (2019).

[300] D. Porras, P. A. Ivanov, and F. Schmidt-Kaler, Phys. Rev. Lett. **108**, 235701 (2012).

[301] N. Linden, S. Popescu, A. J. Short, and A. Winter, Phys. Rev. E **79**, 061103 (2009).

[302] C. Gogolin, M. P. Müller, and J. Eisert, Phys. Rev. Lett. **106**, 040401 (2011).

[303] C. Gogolin and J. Eisert, Reports on Progress in Physics **79**, 056001 (2016).

[304] M. Srednicki, Phys. Rev. E **50**, 888 (1994).

[305] J. Deutsch, Phys. Rev. A **43**, 2046 (1991).

[306] M. Rigol, V. Dunjko, M. Olshanii, Nature **452**, 854 (2008).

[307] G. Clos, D. Porras, U. Warring, and T. Schaetz, Phys. Rev. Lett. **117**, 170401 (2016).

LIST OF PUBLICATIONS USED IN THIS THESIS

[1] K. Singer, U. Poschinger, M. Murphy, **P. Ivanov**, F. Ziesel, T. Calarco and F. Schmidt-Kaler, "*Colloquium: Trapped ions as quantum bits: Essential numerical tools*". Rev. Mod. Phys. **82**, 2609 (2010).

[2] **P. A. Ivanov**, S. S. Ivanov, N. V. Vitanov, A. Mering, M. Fleischhauer, and K. Singer "*Simulation of a quantum phase transition of polaritons with trapped ions*". Phys. Rev. A **80**, 060301(R) (2009).

[3] A. Mering, M. Fleischhauer, **P. A. Ivanov**, and Kilian Singer, "*Analytic approximations to the phase diagram of the Jaynes-Cummings-Hubbard model*". Phys. Rev. A **80**, 053821 (2009).

[4] **P. A. Ivanov**, N. I. Karchev, N. V. Vitanov, and D. G. Angelakis, "*Quantum simulation of superexhange magnetism in linear ion crystals*". Phys. Rev. A **90**, 012325 (2014).

[5] **P. A. Ivanov**, D. Porras, S. S. Ivanov, and F. Schmidt-Kaler, "*Simulation of the Jahn-Teller-Dicke magnetic structural phase transition with trapped ions*". J. Phys. B: At. Mol. Opt. Phys. **46**, 104003 (2013).

[6] D. Porras, **P. A. Ivanov**, and F. Schmidt-Kaler, "*Quantum Sumulation of the Cooperative Jahn-Teller Transition in 1D Ion Crystals*", Phys. Rev. Lett. **108**, 235701 (2012).

[7] **Peter A. Ivanov**, "*Collective Modes in the Cooperative Jahn-Teller Model: Path Integral Approach*". J. Low Temp. Phys. **179**, 375 (2015).

[8] **Peter A. Ivanov** and Ferdinand Schmidt-Kaler, "*Simulation of quantum magnetism in mixed-spin systems with impurity-doped ion crystals*". New Journal of Physics **13**, 125008 (2011).

[9] T. G. Tenev, **P. A. Ivanov**, and N. V. Vitanov, "*Proposal for trapped-ion emulation of the electric dipole moment of neutral relativistic particles*". Phys. Rev. A **87**, 022103 (2013).

[10] **P. A. Ivanov**, F. Letscher, J. Simon, and M. Fleischhauer, "*Adiabatic flux insertion and growing of Laughlin states of cavity Rydberg polaritons*". Phys. Rev. A **98**, 013847 (2018).

[11] L. S. Simeonov, N. V. Vitanov, and **P. A. Ivanov**, "*Compenstation of the trap-induced quadrupole interaction in trapped Rydberg ions*". Scientific Reports **9**, 7340 (2019).

[12] **Peter A. Ivanov** and Diego Porras, "*Adiabatic quantum metrology with strongly correlated quantum optical systems*". Phys. Rev. A **88**, 023803 (2013).

[13] **P. A. Ivanov**, K. Singer, N. V. Vitanov and D. Porras, "*Quantum Sensors Assisted by Spontaneous Symmtery Breaking for Detecting Very Small Forces*". Phys. Rev. Applied **4**, 054007 (2015).

[14] **Peter A. Ivanov**, "*Enhanced Parameter Estimation with Periodically Driven Quantum Probe*" Entropy **23**, 1333 (2021).

[15] **Peter A. Ivanov**, "*Efficient approach for quantum sensing field gradients with trapped ions*". Optics Communications **405**, 355 (2017).

[16] **P. A. Ivanov**, N. V. Vitanov, and K. Singer, "*High-precision force sensing using a single trapped ion*". Scientific Reports **6**, 28078 (2016).

[17] **Peter A. Ivanov**, "*Force sensors with precision beyond the standard quantum limit*", Phys. Rev. A **94**, 022330 (2016).

[18] **Peter A. Ivanov** and Nikolay V. Vitanov, "*Quantum sensing of the phase-space-displacement parameters using a single trapped ion*". Phys. Rev. A **97**, 032308 (2018).

[19] **Peter A. Ivanov**, "*Steady-State Force Sensing with Single Trapped Ion*". Phys. Scr. **95**, 025103 (2020).

[20] **Peter A. Ivanov**, "*Enhanced two-parameter phase-space-displacement estimation close to a dissipative phase transition*". Phys. Rev. A **102**, 052611 (2020).

[21] **Peter A. Ivanov**, "*Quantum thermometry with trapped ions*". Optics Communications **436**, 101 (2019).

[22] A. V. Kirkova, W. Li, and **P. A. Ivanov**, "*Adiabatic sensing technique for optimal temperature estimation using trapped ions*". Phys. Rev. Research **3**, 013244 (2021).

[23] Aleksandrina V. Kirkova, Diego Porras, and **Peter A. Ivanov**, "*Out-of-time-order correlator in the quantum Rabi model*", arXiv:2201.06340.